Deliverable 15.14: ConCorD Synthesis Report

Work Package: 15

This project has received funding from the European Union's Horizon 2020 research and innovation programme 2014-2018 under grant agreement N°847593.

Document information

Project Acronym	**EURAD**
Project Title	**European Joint Programme on Radioactive Waste Management**
Project Type	**European Joint Programme (EJP)**
EC grant agreement No.	**847593**
Project starting / end date	**1st June 2019 – 30th May 2024**
Work Package No.	**15**
Work Package Title	**Container Corrosion under Disposal conditions**
Work Package Acronym	**ConCorD**
Deliverable No.	**D15.14**
Deliverable Title	**ConCorD Synthesis Report**
Lead Beneficiary	**Jacobs**
Contractual Delivery Date	**31/5/2024**
Actual Delivery Date	**31/5/2024**
Type	**Document**
Dissemination level	**Public**
Authors	**Amphos 21:** Andrés Idiart, Arnau Pont, Olga Riba; **ANDRA:** Aurélien Debelle; **CIEMAT:** Ursula Alonso, Mikel Diéguez, Ana María Fernández, Miguel García-Gutiérrez, Manuel Mingarro, Tiziana Missana, Paula Nieto, Carla Soto, Pedro Valdivieso; **EMSE:** Cedric Bosch, Rita De Cassia Costa Dias, Patrick Ganster; **EPFL:** Rizlan Bernier-Latmani; **GRS:** Andres Muñoz; **HZDR:** Andrea Cherkouk; **Jacobs:** Clayton Bevas, James Hesketh, Cristiano Padovani, Ben Pateman, Andy Rance, Nick Smart, Leigh-Anne Stevenson, Shorubhi Uthayakumaran; **KIPT:** Alex Kuprin, Sergey Sayenko; **KIT-INE:** Nicolas Finck, Natalie Müller, Dieter Schild, Ashutosh R. Singh; **Nagra:** Nikitas Diomidis; **ONDRAF/NIRAS:** Roberto Gaggiano; **SCK-CEN:** Kristel Mijnendonkx, Vanessa Montoya; **Subatech:** Abdesselam Abdelouas, Lola Sarrasin, Muhammad Faiz Al Rasyid Tisyadi; **SURAO:** Michaela Matulová; **TUL:** Katerina Cerná; **U. Bern:** Jin Ma, Paul Wersin; **U. Granada:** Mohamed Merroun; **UFZ:** Olaf Kolditz, Matthias Schmidt, Haibing Shao, Marc Tamisier, Carsten Vogt; **UJV:** David Dobrev, Daniel Götz, Vlastislav Kašpar, Kateřina Kolomá, Šárka Šachlová, Petr Večerník, Milan Zuna; **Unilim:** Inaki Cornu, Fabrice Rossignol; **VTT:** Janne Pakarinen, Andressa Trentin.

To be cited as:

Smart N. (ed.), Abdelouas A., Alonso De los Rios U., Bernier-Latmani R., Bevas C., Bosch C., Cerná K., Cherkouk A., Cornu I., De Cassia Costa Dias R., Debelle A., Diéguez M., Diomidis N., Dobrev D., Fernández A. M., Finck F., Gaggiano R., Ganster P., García-Gutiérrez M., Götz D., Hesketh J., Idiart A., Kašpar V., Kolditz O., Kolomá K., Kuprin A., Ma J., Matulová M., Merroun M., Mijnendonkx K., Mingarro M., Missana T., Montoya V., Müller N., Muñoz A., Nieto P., Padovani C., Pakarinen J., Pateman B., Pont A., Rance A., Riba O., Rossignol F., Šachlová S., Sarrasin L., Sayenko S., Schild D., Schmidt M., Shao H., Singh A. R., Soto C., Stevenson L.A., Tamisier M., Tisyadi M. F. A., Trentin A., Uthayakumaran S., Valdivieso P., Večerník P., Vogt C., Wersin P., Zuna M. (2024): ConCorD Synthesis Report. Final version as of 31.05.2024 of deliverable D15.14 of the HORIZON 2020 project EURAD. EC Grant agreement no: 847593.

Disclaimer

Acknowledgement

This document is a deliverable of the European Joint Programme on Radioactive Waste Management (EURAD). EURAD has received funding from the European Union's Horizon 2020 research and innovation programme under grant agreement No 847593.

Status of deliverable		
	By	Date
Delivered (Lead Beneficiary)	J. Hesketh (Jacobs)	
Verified (WP Leader)	Nikitas Diomidis	
Reviewed (Reviewers)		
Approved (PMO)		
Submitted to EC	Andra (Coordinator)	31/05/2024

Executive Summary

The concept of a sealed container (or canister) for the disposal of high-level radioactive waste (HLW) and spent fuels (SF) is intended for use in applied in all deep geological repository programmes in nations that operate nuclear power plants. The container constitutes one of the main barriers in the overall multi-barrier disposal system which provides a complete confinement of radionuclides. Therefore, attention is frequently focused on the performance of the canister, especially concerning the length of time during which the material stability and thus the barrier function can be guaranteed. This was the subject of the research carried out in the multi-national EURAD project entitled 'Container Corrosion under Disposal conditions (ConCorD)'. The work programme was divided into a set of separate tasks as described below. The aim of the current synthesis report was to draw together a summary of the work carried out in the various tasks of the project and to identify the key aspects and outcomes that may be applied in the preparation of future performance assessments and safety cases by the national waste management organisations.

Task 1 encompassed the overall management and review of the project, including scientific-technical coordination and integration, and preparation of a State-of-the-Art report (SotA), which was published separately.

Novel materials: The understanding of degradation mechanisms and the resulting container durability estimates is well developed and has been demonstrated for already existing disposal concepts envisaging the use of copper and carbon steel in clay-based environments. These are the archetypal 'corrosion allowance' materials (i.e. materials that corrode slowly and in a uniform and predictable manner). The second type of materials under consideration are the 'novel materials', which are typically subject to very low corrosion rates (e.g. stainless steel, nickel- and titanium-based alloys). This category also includes ceramic materials. This topic was investigated under Task 2 of the project.

Despite the significant knowledge base on traditional materials, which is thought to be sufficient to support license applications, several uncertainties that are linked to coupled processes remain and these may impact the preparation of safety cases, as described below.

Radiation: In general, it is assumed that one of the specific driving forces for any acceleration of corrosion of radioactive waste containers is likely to be the presence of radiolysis products, either dissolved in solution or in the gas phase. From the point of view of long-term safety, it is important to know to what extent the lifetime of the container and the properties of bentonite will be affected by radiation. This was the subject of the work carried out in Task 3.

Influence of microbial activity: Microbially influenced corrosion (MIC) entails the acceleration of corrosion as a consequence of microbial metabolism. MIC often results from the establishment of microbial communities that utilise electrons from the metal (directly or via H_2) to reduce electron acceptors, such as sulphate, which leads to the production of sulphide. Often, a safety function of the bentonite buffer is to minimise microbial activity (e.g. dry density, adsorbed O_2). In Task 4, the microbial activity in highly compacted bentonite was evaluated and the potential for MIC was assessed.

Corrosion during transients: The evolution of the repository environment after its closure will depend on a number of factors including the properties of the engineered barriers, the composition of the groundwater, the thermal profile, the saturation rate of the bentonite barrier leading to swelling and the development of mechanical stresses on the container. The corrosion of container materials has generally been studied under constant conditions and the application of the experimental results obtained to assessing the time-dependent chemical, mechanical and redox conditions of the early post-closure period needs to be verified and complemented. The effect of transients on corrosion behaviour was the subject of the work performed under Task 5.

Predictive modelling: An additional important aspect of disposal container development is the ability to confidently evaluate and predict their long-term performance. The research programme therefore included a task to extend the development of predictive models (Task 6).

The output from Tasks 2 to 5 above was presented in a series of detailed deliverables, which are referenced from the current report, but the work undertaken from Task 6, is included in the present synthesis report. An overview of the outcomes from each task is given below.

Task 2 – Novel materials

Task 2 of the ConCorD project aimed to explore the potential of novel materials and processes for the optimisation of long-term container performance for high-level waste disposal. The task focused on the experimental work on ceramic and metallic materials for bulk containers and coatings. The main achievements of the project include the development of new alumina-based materials for sealing bulk ceramic containers by microwave heating, the determination of the optimal parameters for sintering high-density silicon carbide, the comparison of the performance of different copper grades in simulated groundwater, and the production and testing of various ceramic and metallic coatings by cathodic arc evaporation and cold spray processes.

The task also outlined future research directions for the development of novel materials for containers. Ceramic materials have high corrosion resistance and low gas formation, but their mechanical strength and sealing processes need to be improved. Metallic materials can offer corrosion resistance depending on the alloy composition and the coating technology, but the overall understanding of their degradation mechanisms under repository conditions requires further work. Alumina-based ceramics can be sealed by microwave heating with specially designed sealing materials, and hetero-aggregation can be used to improve the microwave coupling of the sealing material via a nano-structuration process. SiC-based ceramics can be doped with Cr to increase their fracture toughness and corrosion resistance and can be joined by laser or glass-ceramic methods. CrN-based and TiO_2-based coatings, whose properties can be tailored by varying the deposition parameters, can provide high corrosion protection for steel substrates. The participants in Task 2 were KIPT, IRCER, ANDRA, VTT and EMSE.

Task 3 – Corrosion under radiation

Task 3 focused on the effects of radiation on corrosion behaviour. The experiments were designed to represent the conditions expected in the repository with the inclusion of tests in representative bulk solutions and buffer materials at different saturation levels, groundwater compositions, temperatures, and redox conditions. The experiments were conducted using carbon steel and copper.

The results from tests conducted in bulk solutions (Jacobs) demonstrated that for copper, the presence of radiation results in an increase in corrosion rate measured under all dose rates investigated (0.1 to 10 Gy hr^{-1}), with an increasing effect at higher dose rates. The increase in corrosion rate due to the presence of radiation varied from 0.03 to 1.15 µm yr^{-1}, for dose rates from 0.1 to 10 Gy hr^{-1}, respectively. However, due to the very low corrosion rate of copper in the absence of radiation of 0.02 µm yr^{-1}, the additional corrosion loss due to radiation, reflected a large relative increase compared to unirradiated conditions. For carbon steel, the influence of radiation on corrosion rate was less substantial than for copper. A significant increase in corrosion rate was only detected above 10 Gy hr^{-1}. At 10 Gy hr^{-1} the presence of radiation led to an increase in corrosion rate by 0.90 and 1.41 µm yr^{-1}, following exposure durations of 10,000 and 5,000 hours respectively. However, since the corrosion rate of carbon steel in the absence of radiation was between 1.57 and 3.51 µm yr^{-1}, the increase in corrosion loss due to radiation was modest relative to the corrosion rate in unirradiated conditions.

It was found that at 150°C, the presence of radiation resulted in a significant inhibition of the corrosion rate for all durations tested and in both types of bentonite. A more modest inhibition was also observed for tests performed in BCV (Bentonite Cerny Vrch) bentonite at 90°C, but in MX-80 bentonite the influence of radiation on corrosion rate was negligible.

The work undertaken provided additional information on the potential influence of the type of bentonite used, the nature of the irradiation source (Co-60, Cs-137), the effect of water saturation (63%-100% relative humidity), and the dose rate (0.4-657 Gy hr^{-1}).

Contrasting results were obtained about the effect of γ-irradiation on steel corrosion, where the corrosion was enhanced in experiments conducted by SUBATECH and CIEMAT while the steel corrosion decreased under irradiation at high temperature (150°C) in experiments conducted by UJV. Experiments conducted under controlled water saturation at 25°C (SUBATECH) showed a strong effect of radiation, which enhanced steel

corrosion compared to reference non-irradiated samples. Nevertheless, the lowest percentage of relative humidity (63% RH) showed the highest corrosion rate (as high as 250 µm yr^{-1}), which then decreased with increasing water saturation (100%). In the case of experiments using carbon steel contacting compacted MX-80 bentonite at different saturation levels (60% and 100%) (CIEMAT), the corrosion rate of carbon steel was higher in the presence of gamma irradiation relative to reference samples and increased with increasing saturation from 60% to 100% (in contrast to experiments conducted by SUBATECH). Similar experiments by CIEMAT using copper showed only minor corrosion under irradiation. Experiments with steel and fully saturated MX-80 or BCV bentonite conducted by UJV showed lower corrosion rates under irradiation compared to reference experiments at 150°C, while gamma radiation had no significant effect on steel corrosion at lower temperatures (90°C and room temperature). The lower corrosion rate of carbon steel heated at 150°C and irradiated in the BCV bentonite was explained mainly by temperature and possibly lower saturation considerations. The effect of irradiation was minor due to low dose rates. Nevertheless, similarities were found for all experimental configurations such as the decrease of corrosion rate with increasing time or typical corrosion products such as siderite, magnetite or iron hydroxides. Furthermore, no clear impact of the dose rate or the type of irradiation (Co-60 vs Cs-137) on the steel corrosion was found. Finally, it is concluded that the radiation effect on steel corrosion should be investigated further to elucidate the mechanisms governing the corrosion process (corrosion rate and corrosion products) under the anticipated repository conditions. Among the subjects to be developed, the work highlighted the role of humid air radiolysis, in particular the yield of radiolysis products as a function of relative humidity, which impacts the corrosion kinetics. This could be achieved both experimentally and by modelling. Also, the combined effect of temperature and radiolysis on steel corrosion needs to be better understood.

Task 4 – Microbial effects

The work performed in WP ConCorD's Subtasks 4.1 and 4.2 focused on the effect of irradiation and other repository-relevant stressors, such as heat and bentonite density, on indigenous microorganisms in bentonite, and their effect on the corrosion of canister materials. The results obtained demonstrated that the initially high temperature and γ-radiation have the potential to exhaust most microbial activity in the bentonite zones subjected to temperatures of at least 90°C. As a consequence of the suppression of microbial activity in the buffer, biofilm formation on the canister surface does not need to be considered. However, further microbiological studies combined with mathematical modelling of temperature evolution in a DGR are necessary to predict the size and spatial distribution as well as the long-term persistence of such microbially depleted zones in the bentonite buffer around the metal canisters. When full saturation is reached, microbial activity will be further suppressed by compacted bentonite where the threshold dry density depends on the bentonite (their physical-chemical properties and the indigenous microbial communities). The current results indicate that the methodologies and experimental setups developed within ConCorD can be used as a standard method for investigating threshold densities for buffer candidates. It was shown by batch microcosm experiments that the Calcigel bentonite is a good candidate for studying the impact of dry density on microbial activity and corrosion because this bentonite has a low sulphate content and contains natural sulphate-reducing bacteria that have the potential to contribute to corrosion.

It is expected that the only form of microbially influenced corrosion that needs to be considered is that due to the diffusion of aggressive metabolic by-products (invariably sulphide) to the canister surface from locations at which microbial activity is deemed to be possible. In accordance with this assumption, the compacted bentonite samples from UGR that were supplemented with SRB and IRB showed the highest alteration of the metal surface (at 1.6 g cm^{-3}). This shows that introduced microorganisms can affect the corrosion even in bentonite compacted at a high dry density. The non-irradiated compacted bentonite samples without additional bacteria showed that the metal surface was covered with copper oxides and the coupons had a low corrosion rate (as studied in detail in Task 3). Results from UGR/CIEMAT also showed that the porewater used and the method of compaction (first saturated then compacted, or first compacted then saturated) can have an influence on the corrosion behaviour.

One of the objectives of this project was to enable cross-comparison between the results obtained, in order to optimise future research methods. This is important as it is known that DNA extraction plays a crucial role in determining the variability of results obtained through 16S rRNA amplicon sequencing. In particular, bentonite

and other clay samples can impede the efficiency of standard cultivation-independent techniques. These samples often contain low biomass, further complicating the extraction process. To address these concerns, an inter-laboratory comparison study was conducted to thoroughly assess the efficacy of two published DNA extraction methods specifically designed for bentonite samples. Notably, our findings indicate that the selection of one or other method is not critical, but rather depends on the specific analysis requirements. However, it is crucial to maintain consistency in the chosen method, as comparing results becomes challenging, particularly in the presence of bentonite. Additionally, we discovered that slight modifications to one of the extraction methods can enhance its efficiency. In summary, the study emphasises the importance of standardised DNA extraction methods and underscores the importance of validating these methods using appropriate controls when studying microbial communities with 16S rRNA amplicon sequencing, particularly in environments characterized by low biomass and clay-rich compositions.

Task 5 – Corrosion under transients

Task 5 aimed to identify the role of transient conditions on the corrosion of materials selected for disposal canisters in deep geological repositories for high-level radioactive waste. Experimental work was carried out by four separate organisations, namely CIEMAT, GRS, KIT-INE and UJV-SURAO.

CIEMAT analysed the impact of redox, hydraulic and thermal near-field transients on the corrosion and bentonite interactions, simulating the canister / bentonite interface of a deep geological repository. Both laboratory scale and in situ experiments, carried out at the Äspö Underground laboratory (Sweden), were analysed. The samples from the Äspö-ABM5 in situ experiment were hydrated for 4.4 years with Äspö granitic groundwater at temperatures up to 250°C. Thus, these samples were representative of coupled hydration, temperature, redox and chemical transients. Analyses of different bentonite samples revealed that all bentonites analysed preserved their hydro-geochemical properties after being subjected to saline groundwater infiltration, heating and interaction with corroding metals for 4.4 years. The main changes observed in all the bentonite samples were the modification of exchangeable cation composition and an increase in the iron in the bentonite as a function of the distance to the contact point with the heater, due to corrosion of the heater. The main corrosion products were goethite, haematite and siderite.

CIEMAT laboratory experiments were representative of coupled thermo-hydraulic gradients and thermo-hydraulic-chemical interactions. CIEMAT's activities covered a range of transient conditions affecting corrosion of metals, such as resaturation of compacted bentonite, convective water vapour saturation fluxes, ambient and high temperature (80°C), different salinity of the infiltrating waters and variations in oxic/anoxic conditions. The corrosion rates measured for all carbon steel coupons in contact with the bentonite, hydrated with different waters and subjected to 80°C, ranged between 28 µm yr^{-1} and 413 µm yr^{-1}, with the highest corrosion rate observed for the Nagra carbon steel coupon tested with FEBEX bentonite compacted at 1.4 g cm^{-3}. The corrosion rates of Cu-OFP coupons subjected to the same conditions were significantly lower, ranging from 3 to 9 µm yr^{-1}.

GRS analysed the effects of the consumption of oxygen enclosed in saturated bentonite on the first stages of corrosion. Electrochemical techniques, such as polarisation curves (current-voltage curves) and electrochemical impedance, were used to monitor the evolution of the corrosion rate for a period of about 3 months. The electrochemical experiments were performed in a dedicated cell containing the oversaturated Wyoming bentonite slurry (Na-bentonite like the MX-80) prepared with artificial Opalinus Clay water with a ratio of 1:10 w/w. The experiments were complemented using surface analysis techniques, including SEM-EDX and localised XPS to identify the nature of the corrosion products formed. Electrochemical experiments in Opalinus Clay water with different oxygen contents at different temperatures were performed in order to obtain additional information on the corrosion kinetics. The middle-term runs were performed at temperatures of 30°C and 50°C. A miniaturised Pt-sensor was tested to follow pH-changes in close proximity to the corroding surfaces by running cyclic voltammetry measurements from time to time. Comparative experiments were carried out under γ-irradiation conditions.

The corrosion rates measured by GRS for GGG40 cast iron in contact with a slurry of bentonite hydrated with synthetic Opalinus clay were 6 µm yr^{-1} and 13 µm yr^{-1} for 30°C and 50°C, respectively. The electrochemical investigations showed that at the corrosion potential, oxygen reduction was mass-transport controlled, the

diffusion of oxygen being restrained by the slurry, indicating that kinetically controlled water reduction seemed to predominate. A γ-radiation dose 130 Gy hr^{-1} on GGG40 in the same bentonite slurry at 50°C increased the mean corrosion rate to 52 µm yr^{-1}.

KIT-INE performed corrosion experiments with spheroidal graphite cast iron (SGI) and cupronickel alloy (CuNi) in contact with a bentonite slurry hydrated with granitic groundwater. Ex situ experiments were carried out in the laboratory under anoxic conditions in a N_2- or Ar-filled glovebox, under static and dynamic conditions, and for contact times lasting up to 12 months. The purpose of these experiments was to provide information about the effect of porewater renewal on the investigated processes and performed experiments in closed vessels at 25°C and at 50°C. Experiments under dynamic conditions were carried out using cylindrical vessels and the flow rate was applied by using a peristaltic pump. The applied transient conditions were specific for each selected material. In the case of spheroidal graphite cast iron (SGI), a layer of a ferric compound was inserted between the metallic coupon and the bentonite. In experiments involving cupronickel coupons, the porewater was spiked with sulphide once corrosion processes had already started. Reference experiments were performed separately in the absence of ferric compounds or added sulphide, in order to identify the effect of these parameters on the corrosion behaviour of the metallic materials.

The KIT results showed that SGI corroded upon exposure to the bentonite suspension hydrated with low saline granitic water, where the redox potential decreased in all experiments, suggesting the formation of Fe(II)-bearing secondary phases. Comparative experiments performed in the presence of haematite did not significantly alter the steel degradation mechanism. After 3 months at 25°C in contact with the bentonite suspension, the corrosion rate was 4.8 µm yr^{-1}, favoured by the larger amount of water available. Increasing the temperature to 50°C significantly increased the corrosion rate to 10.6 µm yr^{-1}. Corrosion rates decreased systematically with increasing reaction time. In comparison, CuNi corrosion was significantly lower, with the highest value being 2.7 µm yr^{-1} at 50°C. The presence of added sulphide had no significant effect on corrosion but may have had an effect at longer exposure times, or higher sulphide concentrations.

UJV-SURAO studied the effect of increased temperature and γ-irradiation on the acceleration of corrosion of carbon steel in compacted Ca-Mg bentonite, including MX-80 in a limited number of tests, to gain an insight into the chemical evolution and its influence on the development of the carbon steel canister / bentonite interface. Results showed that the carbon steel samples heated at 150°C in the BCV bentonite had lower corrosion rates when irradiated compared to unirradiated samples, ranging from around 2 µm yr^{-1} to 24.3 µm yr^{-1} at 150°C with irradiation. Unirradiated samples heated to 150°C showed the highest corrosion rate after 6 months but they decreased when the loading period was prolonged to 18 months. A decreasing corrosion rate was observed in both irradiated and unirradiated steel samples heated at 90°C with increasing exposure period.

Task 6 – modelling

Three modelling tasks were undertaken to cover (i) reactive transport modelling of the corrosion behaviour of steel in bentonite, (ii) the inclusion of microbial activity in geochemical models of repository behaviour, and (iii) repository scale modelling of sulphide in a repository. The report describes how the models were set up and provides some preliminary results from the modelling activities. Sub-task 6.1 focused on creating a numerical tool that can take account of modelling water and chloride radiolysis and their consequent effect on corrosion behaviour based on their effect on electrochemical processes. The results of the modelling were compared to experimental results from a radiation-corrosion experiment for steel in bentonite.

Sub-task 6.2 outlines a mathematical description of microbial activity based on treating microbes as colloid-like chemically reactive particles. Some examples of applying the model to a common sulphate-reducing bacteria system are given.

Sub-task 6.3 involved development of a previous 1D model for the sulphide evolution in the near-field and sulphide corrosion on copper canisters in the Swiss DGR to create a 2D model. It was also extended to estimate sulphide corrosion on both copper and steel canisters under different repository settings, including the effect of badly-emplaced" buffer and high pH plumes from a concrete liner. The model was used to predict the corrosion depth after 1 Myr for copper and steel canisters in various scenarios.

For each task, as a section is included which reflects on the significance of the results obtained and how they might be applied to future performance assessments. The report concludes with an overview of the significance of the results from the various tasks and their relevance to the preparation of future performance assessments.

Table of Contents

List of figures

List of Tables

Glossary

ABM	Alternative Buffer Material
ANSTO	Australian Nuclear Science and Technology Organisation
ARWA	Australian Radioactive Waste Agency
BCLT	Buffer Coupon Long-term Test
BCV	Bentonite Cerny Vrch
BFS	Blast Furnace Slag
C/S	CaO/SiO_2 ratio
CIEMAT	Centro de Investigaciones Energéticas, Medioambientales y Tecnológicas (Spain)
CRH	Critical Relative Humidity
CRT	Canister Retrieval Test
C-S-H	Calcium Silicate Hydrates
CSIRO	Commonwealth Scientific and Industrial Research Organisation
Cu-OFP	Oxygen-free phosphorus-doped copper
DGR	Deep Geological Repository
DSR	Dissimilatory Sulphate Reduction
DSSC	Disposal System Safety Case
EBS	Engineered Barrier System
Ecorr	Corrosion Potential
EDX	Energy dispersive X-ray analysis
EDZ	Excavation Disturbed Zone
Eh	Redox Potential
EPFL	École Polytechnique Fédérale de Lausanne
FEBEX	Full-scale Engineered Barriers Experiment
FEP	Features Events and Processes
GDF	Geological Disposal Facility
GDR	Geological Disposal Repository
GR	Green Rust
HE/E	in situ heater test (in PEBS project: Long-term Performance of Engineered Barrier Systems))
HHGW	High Heat Generating Waste
HIC	Hydrogen Induced Cracking
HLW	High Level Waste
HotBENT	High Temperature Effects on Bentonite Buffers
HSR	High-strength Rock
HZDR	Helmholtz-Zentrum Dresden-Rossendorf

IAEA	International Atomic Energy Agency
ICP-OES	Inductively Coupled Plasma Optical Emission Spectroscopy
ILW	Intermediate Level Waste
ITA	In Tunnel Axial
ITD	In Tunnel Deposition
IVD	In Vault Deposition
KIT	Karlsruhe Institute of Technology
LET	Linear Energy Transfer
LHGW	Low Heat Generating Waste
LLW	Low Level Waste
LOT	Long Term Test of Buffer Material
LSSR	Lower Strength Sedimentary Rock
MBM	Mined Borehole Matrix
MIC	Microbiologically Influenced Corrosion
MOX	Mixed Oxide
MPC	Multi-Purpose Container
NRVB	Nirex Reference Vault Backfill
OPC	Ordinary Portland Cement
PA	Performance Assessment
PFA	Pulverised Fly Ash
PVC	Polyvinyl chloride
RAC	Radiation-Assisted Corrosion
RAWRA	Radioactive Waste Repository Authority (Czech Republic)
RH	Relative Humidity
RIC	Radiation-Induced Corrosion
SCC	Stress Corrosion Cracking
SEM	Scanning electron microscope
SGI	Spheroidal Graphite cast Iron
SNF	Spent Nuclear Fuel
SotA	State-of-the-art
SKB	Swedish Nuclear Fuel and Waste Management Company (Svensk Kärnbränslehantering AB)
SRB	Sulphate Reducing Bacteria
TBT	Temperature Buffer Test
THMC	Thermal, Hydraulic, Mechanical, and Chemical
TOC	Total Organic Carbon
UFZ	Helmholtz-Zentrum für Umweltforschung GmbH

UoBe	University of Bern
URL	Underground Research Laboratories
WMO	Waste Management Organisation
XPX	X-ray photoelectron spectroscopy
XRD	X-ray diffraction
XRF	X-ray fluorescence

1. Introduction to the ConCorD project

1.1 Overview of the ConCorD project

The state of the art of the corrosion behaviour of candidate container materials for the disposal of SF and HLW was summarised in a joint IGD-TP activity (Padovani et al., 2017), which also identified areas in which further collaborative R&D may be beneficial. Development of models to predict container failure times and the development of a thorough mechanistic understanding of the corrosion processes involved have progressed significantly over the past 40 years. The understanding of degradation mechanisms and the resulting container durability estimates (as well as other issues like manufacturing, sealing/welding, handling, etc.) is mature and has been demonstrated for existing disposal concepts that envisage the use of copper containers (e.g. Sweden, Finland, Canada) and carbon steel containers (e.g. France, Switzerland, Japan, Czech Republic) in a clay environment. These materials are commonly called “traditional materials” on which “corrosion allowance” designs are based (i.e. they are metals that corrode slowly in a uniform and predictable manner). The second group of materials under consideration for radioactive waste containers are commonly referred to as “novel materials”. Examples of such materials are stainless steels and nickel- and titanium-based alloys, which typically experience very low corrosion rates. Leaching of ceramics is also a form of corrosion that can lead to the degradation of mechanical properties, which is a primary concern for a ceramic container. Such novel materials have the potential to lead to optimisation of container performance and interest in such materials has been expressed by the radwaste community. Nevertheless, several open questions remain, related to, for example, deposition of coatings, sealing of ceramics and their long-term properties.

Despite the significant knowledge base for traditional materials, which is thought to be sufficient to support license applications, several uncertainties linked to coupled processes remain, which can influence performance assessments, namely:

Radiation: In general, it is assumed that one of the specific driving forces for any acceleration of corrosion of radioactive waste containers is likely to be the presence of radiolysis products, either dissolved in solution or in the gas phase. From the point of view of long-term safety, it is important to know to what extent the lifetime of the container and the properties of bentonite will be affected by radiation. To achieve this, experiments need to be conducted that reconstruct repository conditions (i.e. chemistry, presence of buffer, dose rate or total dose) as closely as possible. However, a fundamental open question relating to such experiments is whether dose rate or total dose is the critical irradiation parameter controlling the acceleration of corrosion.

Influence of microbial activity: Microbiologically influenced corrosion (MIC) entails the acceleration of corrosion as a consequence of microbial metabolism. MIC often results from the establishment of microbial communities that utilise electrons from the metal (either directly or via H_2 resulting from the anaerobic corrosion of metals, such as iron) to reduce electron acceptors, such as sulphate. The resulting sulphide production by sulphate reducing bacteria (SRB) can greatly impact the corrosion rate of several metals. One safety function of the bentonite buffer used in many radioactive waste disposal concepts is to minimise microbial activity. There are a few studies that have attempted to establish the dry density threshold that would reliably inhibit microbial activity but it is unclear whether dry density is the key parameter or whether other considerations may also contribute to inhibiting microbial metabolism. However, a complicating factor is that there is mounting evidence for the persistence of O_2 within bentonite buffer material, perhaps as an adsorbed gas. Thus, the fact that O_2 could inhibit SRB, which are strict anaerobes, for extended experimental periods could complicate understanding of the findings.

Corrosion during transients: The evolution of the repository environment in the period after its closure will depend mainly on two factors, namely the nature of the engineered barriers and the composition of the groundwater. After facility closure, the thermal phase of the evolution of the repository is important, for a number of reasons. For example, an important parameter during this phase is the rate of saturation of the bentonite barrier, since saturation leads to swelling of the bentonite and hence the development of mechanical stresses on the container. Such transients can be further influenced by attempts at repository footprint optimisation (e.g., increased container heat production). The corrosion of container materials has usually been studied experimentally under constant environmental conditions and the application of such experimental results to the evolving chemical, mechanical and redox conditions of the early post-closure period need to be

further developed and verified. It is important to be able to confidently evaluate and demonstrate the long-term performance of disposal containers. Based on the knowledge gaps summarised above the main objectives of the ConCorD work package were to:

- Explore the potential for using novel and advanced container materials and processes to optimise container performance within the engineered barrier system.
- Increase/extend the understanding of complex/coupled interfacial processes influencing container performance under repository relevant conditions, with a focus on irradiation-accelerated corrosion, microbial activity and MIC, and the effect of nearfield environmental transients on container degradation.
- Demonstrate advances in mechanistic understanding and develop predictive models, which incorporate system variability and lead to more focused performance assessments that can be applied in safety cases.

The main overall aim of the ConCorD work package was to enable various national programs to evaluate cooperatively the long-term behaviour of container materials to such an extent as to be able to increase confidence in the safe performance of engineered barriers for different regulatory and geological environments, and for typical European SF/HLW disposal concepts. This aspect was viewed as being particularly beneficial for early-stage programmes and those with small inventories, while allowing more advanced programs to consider various options to further optimise their disposal concepts.

The main body of the work conducted in ConCorD was divided into six main tasks, as follows:

- Task 1: Management and coordination.
- Task 2: Novel materials
- Task 3: Corrosion under irradiation
- Task 4: Microbial effects
- Task 5: Corrosion under transients
- Task 6: Modelling and integration into performance assessments.

At the start of the ConCorD project a State-of-the-Art report (SotA, Abdelouas et al., 2022) was prepared within Task 1, to summarise the current scientific understanding in relation to the main topics under consideration in the project. At the end of the project, the SotA was updated to include developments made during the course of the ConCorD project (Abdelouas, 2024).

1.2 Background to synthesis report

The aim of the current synthesis report is to introduce the activities performed within the ConCorD project and to summarise the resulting research outcomes, whilst providing details of the deliverables produced for each of the tasks within the project, where further detailed information about each individual task can be found. The report is divided into separate self-contained sections for each of the main tasks, and each main section is sub-divided as follows (although the exact nomenclature for the headings may be slightly different in each case):

- Introduction to task
- Scope of task
- Progress against task description (i.e. the original task description in the ConCorD proposal)
- Summary of key outputs from task
- Application of task output in performance assessments, where the topic studied in the task was relevant to performance assessments.

The material included in the report was taken from documentation prepared by the individual task leaders and task teams and merged by the report editor. The report gives the key information and a high-level overview about how the experimental work was carried out but details are only given in the main deliverable(s) for each of the tasks. These are referenced from the current report and the reader is referred to those documents for further information. Where several different research groups were working on the same task, the relevant sections of the report are further subdivided, so that the work from each contributor is self-contained but a section for each task is devoted to comparing, contrasting and summarising the overall output from each task.

Section 6 includes a summary of the results of the modelling activities as well as a holistic overview of the output from the ConCorD project and how the new results may be incorporated into performance assessments of geological disposal facilities by the waste producers.

2. Task 2: Novel materials

2.1 Introduction to task

Currently, carbon steel and copper are the main materials proposed for adoption worldwide as nuclear waste disposal canister materials. Prediction of the lifetime of the waste container represents an important input to the safety assessment of the disposal system. This requires a good understanding of the corrosion/leaching behaviour of the canister material over periods of thousands to hundreds of thousands of years. This mechanistic understanding may come from existing information in the literature, from new experimental studies or from numerical models. Advanced material options are of interest due to their potential for optimisation of disposal concepts. For example, they could offer longer canister lifetimes, more accurate and robust long-term prediction of lifetimes, advantages related to a reduced impact on the engineered and geological barriers or related to manufacturing. For example, optimised welding/joining techniques could result in better long-term performance of the welds/joints (e.g. with respect to corrosion/leaching resistance).

The main goal of Task 2 was to explore the potential for using novel materials and processes for the optimisation of long-term container performance. Within the ConCorD project, a number of novel ceramic and metallic materials were considered for containers, both for the production of single material containers or for coated containers. The activities performed in the ConCorD programme included:

- Process optimisation
- Materials characterisation
- Understanding the corrosion/degradation processes of novel ceramic and metallic materials, both for single material container applications and for coating applications.

For containers made of *bulk ceramics*, the key properties for long-term performance are fracture toughness and leaching/alteration, while for thin coatings a primary concern is the presence of porosity or flaws. Alumina-silica-based ceramics and silicon carbide (SiC) are the most promising ceramic solutions considered within Task 2 for single material container applications. With regard to the silicon carbide solution, the addition of chromium seems to improve the corrosion properties of the ceramic. The sintering process of the Cr-doped SiC ceramics was optimised and its long-term corrosion behaviour was studied.

The sealing process is also a technological issue for ceramic canisters. As far as silicon carbide is concerned, the necessary temperature still seems too high for practical applications but this point was not studied within ConCorD. For alumina-silica-based materials, microwave heating is a promising technique, particularly for microwave-responsive sealing materials. This technology is proven on a laboratory scale for sealing glasses. The development of specific larger scale furnaces was not addressed in the current programme as it would need industrial partnership. Within Task 2, the composition of the sealing glasses was optimised using core-shell technology[1], in order to increase the coupling of the material with microwaves and to reinforce the mechanical properties of the seal. The mechanical properties of the assemblies produced were characterised.

For containers made of *bulk metallic materials*, the key properties for long-term performance are good mechanical properties and favourable corrosion behaviour under repository conditions. Copper is considered to be the most promising material in several countries' programs. The work performed within Task 2 focused on testing improved oxygen-free phosphorus-doped copper (Cu-OFP) alloys, especially considering the effect of impurities on their corrosion properties. A number of aspects were considered in the study, such as:

- The uptake and diffusion of hydrogen and its interactions with the copper matrix
- The possibility of micro-galvanic corrosion due to the presence of impurities
- The relationship between hydrogen diffusion into the matrix, creep rate and SCC crack growth in ammonia-containing ground water.

Nickel alloys, titanium alloys and ceramics were also studied within Task 2 as *coatings* for SF/HLW disposal canisters, especially for cases where microbial activity is likely in the near-field, and thus the risk of microbially

[1] This technology is applied in the production of ceramic particles in which the core and the shell materials differ in their ability to couple microwaves. In the ConCorD project, alumina particles homogenously covered with silica nanoparticles were studied.

influenced corrosion (MIC), cannot be excluded. These coating solutions are achieved using physical vapour deposition (PVD) methods. This work is dedicated to the enhancement of the process for obtaining ceramic (TiO_2, CrN) coatings on steel substrates using the PVD method and the preparation of a batch of samples for corrosion tests. Processes for manufacturing metallic (Ti, Cu) coatings on various steel substrates by PVD are also proposed.

In addition to this, *copper/alumina composite coatings* produced by cold spray technology were investigated. The metallic / ceramic composite allows the use of nitrogen as a carrier gas and leads to decreased porosity and improved adhesion. After optimisation of the cold spray technology parameters for the copper/alumina composite coatings, corrosion studies were performed. The results are compared to those of both wrought copper alloys, and electrodeposited and cold spray copper coatings. This work also focused on the synergy between material deformation and the corrosion of the coatings, particularly in the vicinity of porosity defects.

2.2 Scope of task

For the most promising novel materials, experimental studies were designed to contribute to the goal of understanding of corrosion/degradation processes. The work within this task was organised according to the two main types of materials: ceramic and metallic materials. In the case of ceramic materials, the experimental work was focused on studying materials and processes (deposition, sealing) for innovative solutions of ceramic containers and ceramic coatings. For containers made of bulk ceramics, the key properties for long-term performance are fracture toughness and leaching/alteration. For thin coatings, a primary concern is the presence of porosity or flaws. For metallic materials, the main aim of the experimental work was to study and consider the implementation of innovative solutions for metallic anti-corrosion coatings or optimised bulk metallic options. Studies focused on material development (alloy composition, coating technology) and initial corrosion tests to identify the benefit of these new solutions.

2.3 Progress against task description

The details of the experiments undertaken within this task and the full set of results are presented in Gaggiano et al. (2024). The following section summarise the key features of the results obtained.

2.3.1 Subtask 2.1 Ceramic Materials and Coatings

2.3.1.1 Sealing technologies for ceramic containers

IRCER-EMSE worked together on the development of new sealing formulations, for alumina-based (i.e. silico-aluminate materials with a high content of alumina) ceramic canisters and the test of their performance when sealing was performed using microwaves (MW). The major achievement was the unprecedented improvement of the microwave coupling allowing for a fast sintering which, as a result, will allow in real conditions to limit the increase of the temperature during the sealing process in the core of the container containing the nuclear waste “parcel”. The new sealing formulations had also to satisfy the mechanical and leaching resistance specifications.

More specifically, in a first approach, the research was focused on the exploitation of the hetero-aggregation phenomenon in water-based suspensions between an alumina micropowder and a silica nanopowder carrying opposite surface charges. The generation of surface charges was linked to the zeta potential resulting from the acido-basic equilibria arising in water. Following this processing route made it possible to prepare very homogeneous and intimate blends of the two materials at the nanoscale. Knowing that blends were composed of two materials exhibiting different MW coupling efficiencies, the idea was actually to derive benefit locally (i.e. at the powder grain level) of the best-coupling material to get a localised, efficient, homogeneous and fast heating process which is key for the application.

The first MW sealing tests of these hetero-aggregated alumina-silica blends showed an increased MW coupling validating the overall strategy followed. In order to go a step further, silicon carbide was added to the alumina-silica formulations in low quantities (maximum of 2 vol.%). SiC is well-known as one the best ceramics in terms of MW coupling. Contrary to previous studies performed with the addition of SiC micro-powders which showed no improvement, in our case we added nano-SiC (typical size of 20 nm). This SiC was covered with

a native silica layer allowing to implement hetero-aggregation the same way as with nano-silica and in a very homogeneous way. Consequently, we observe a strong boost of the MW coupling as illustrated in the figure below.

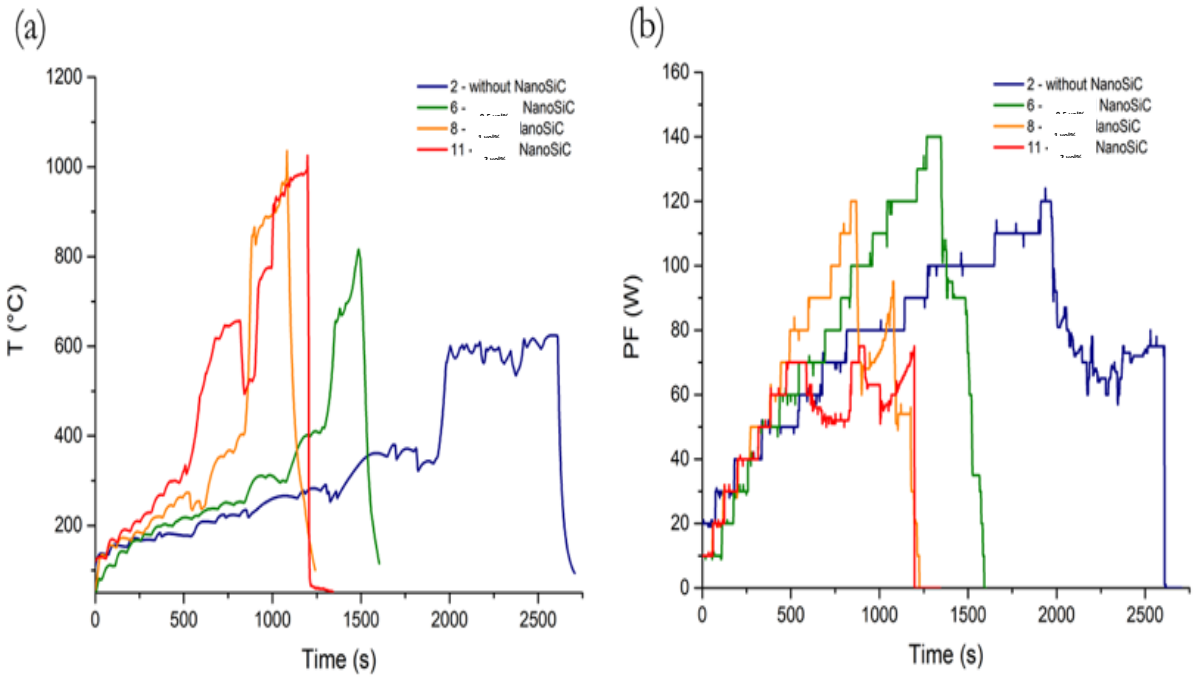

Figure 1. (a) Comparison of microwave coupling for samples containing different amounts of nano-SiC, (b) Corresponding forward power input during the microwave tests necessary to reach 400°C.

Concerning the very positive effect of nano-SiC on MW coupling, we believe that this is not only due to the material itself and to its very homogeneous distribution throughout the volume thanks to the hetero-aggregation. There might also be a “kind of pinning” of the electromagnetic field on nano-SiC. but, at this stage, it remains an assumption that has still to be confirmed. Another issue that has to be studied is the fact that the oxidation of SiC during the sealing produces bubbles that may degrade the mechanical properties (to be studied in the future) and the leaching resistance if bubbles percolate.

Finally, based upon the determination of the permittivity of materials as a function of temperature at the working frequencies, modelling of the MW heating would help to understand MW heating selectivity and the determination of compatible materials (ceramics vs sealing materials) for an efficient and selective heating of the sealing area.

2.3.1.1 Silicon carbide ceramic composite

Research conducted at KIPT was devoted to optimizing the sintering process for the manufacture of composite materials based on SiC doped with Cr. The process of synthesis of SiC-based ceramic composites was performed using hot pressing.

The optimal parameters of the high-pressure sintering process for obtaining the high-density SiC samples were determined (T = 2050 °C; t = 30 min; P = 40 MPa; heating rate of 200 °C/min). SiC ceramic composites with Cr additives (from 0.3 to 0.9 wt%) were prepared and investigated. Structural studies have shown that the obtained SiC(Cr) samples belong to the 6H-SiC polytype with high density. Silicon carbide samples with chromium concentration from 0.3 to 0.5 wt% have higher microhardness (25.5 GPa) and nanohardness (37.8 GPa) than pure SiC (22.8 and 31 GPa, respectively).

Samples of pure SiC and chromium doped (0.3 wt% and 0.5 wt%) SiC were tested for long-term (4,200 hours) corrosion resistance in distilled water at 90°C. The corrosion test results show that pure SiC samples are soluble in water. Chromium alloyed (0.3 wt%) samples dissolve two times slower than pure SiC after 3,500 hours of testing.

2.3.1.1 Chromium nitride and titanium dioxide ceramic coatings

The study of the ceramic coatings performed by KIPT investigated the effect of cathodic arc evaporation (PVD method) parameters (bias potential) on the structure and properties of ceramic coatings CrN and TiO_2.

The CrN coatings of 30 µm thickness have a crystalline structure, the crystallite sizes depend on the bias potential, the smallest crystallite size of 43 nm was obtained at a potential of -150 V. These coatings have high mechanical properties (H=23[2] and E=320 GPa) and high adhesion (HF1[3]) to steel substrate.

TiO_2 coatings with a thickness of 30 µm, deposited at a bias potential of -150V, have an anatase structure and acceptable mechanical properties: hardness of 12 GPa and good adhesion to the steel substrate (HF2).

The CrN coating deposited under bias -150 V with the smallest crystallite size of 43 nm has the best protective properties: after 296 hours of testing at 20°C in 3% NaCl solution, no traces of corrosion were found. Electrochemical studies have shown that in this solution, the potential and corrosion current of the coating (E_{corr} = -187 mV vs Ag/AgCl (3M), I_{corr} = 0.85 µAcm^{-2}) are much lower than those of steel (E_{corr} = -548 mV vs Ag/AgCl (3M) I_{corr} = 29.6 µAcm^{-2}), and no traces of pitting corrosion were found. For the TiO_2 coating on steel substrate the corrosion current is 0.0815 µAcm^{-2} and E_{corr} = -33 mV. After subjecting steel samples with CrN and TiO_2 coatings to near-disposal tests in water at 90°C for 4200 hours, it was observed that the steel corroded intensely with rust formation and dissolution. The TiO_2 coatings showed weight loss and pitting, while the CrN coatings exhibited minimal weight loss and no pitting on the surface, indicating the best corrosion resistance.

2.3.1.2 New copper/alumina ceramic composite coatings

The study of Cu+32vol.%Al_2O_3 composite coatings deposited by the cold spray process was perfromed by EMSE and focused on the microstructure of the deposits, their mechanical properties, corrosion resistance, and creep resistance. Microstructure analysis, for a given set of process parameters (gas temperature of 500°C, nitrogen gas nature, spray distance of 40 mm, gas pressure of 35 bar, deposition line spacing of 4 mm), and two deposition speeds (20 mm s^{-1} and 40 mm s^{-1}) investigated, showed little effect of this speed on porosity. A low porosity is observed within the deposition lines, around 0.37% regardless of the deposition speed, while the overlap zones of the deposition lines exhibit significantly higher porosity, ranging from 1.68% to 2.52%. The EBSD analysis revealed a gradient of plastic deformation within the copper particles between the peripheral zones and the core of the particles. This results from both an increased effect of hammering by the ceramic particles and the phenomenon of recrystallisation of the copper matrix. However, no crystallographic deformation texture is induced by this process.

Mechanical properties evaluated under uniaxial compression show a behaviour similar to that of cold-worked solid copper, with a yield strength close to approximately 300 MPa. Nevertheless, the apparent strain hardening rate is significantly lower, and the maximum strength exhibits dispersion among the different tests conducted. This result arises from the presence of porosities, which tend to close during compression and contribute to reducing the strain hardening rate. Damage to the deposits beyond the ultimate tensile strength results in the fracture of specimens along zones of high porosity density, namely, the overlap of deposition lines. Ultimately, these defects govern the mechanical strength of the deposits beyond a loading exceeding the yield stress.

The electrochemical behaviour characterised at 90°C in a synthetic medium representative of groundwater at the Bure site (France), through dynamic polarisation tests, shows no significant difference between tests on solid copper and composite cold spray deposits. The corrosion rates extracted from the curves using the Tafel method are in the range of 10 to 15 µm yr^{-1}. However, these corrosion rates are relatively high compared to those expected in anoxic environments for copper. The anodic branches of the polarisation curves indicate

[2] The microhardness of the samples was measured by microhardness tester LECO LM700AT at a load of 200 g, with a holding time of 14 s.The pure silicon carbide sample had a microhardness of 22.8 GPa.

[3] The adhesion of CrN coatings was determined using the Daimler−Benz test under 1500 N load. In this test, a six-grade scale (HF1-HF6) indicates the level of adhesion of a coating: HF1–HF4 indicates good adhesion with small cracking or delamination of the coating in the surrounding of the crater, whereas HF5 and HF6 represent a poor adhesion with large coating delamination around the indented zone.

that the materials are in an active state, although there is a pseudo-passivation plateau over a potential range of 200 mV beyond the corrosion potential. Subsequent measurement of the oxygen content in the medium revealed a residual content of about 50 to 100 ppb, contrary to the targeted anoxic test conditions. The results obtained are therefore representative not of the long-term anoxic conditions of underground disposal, but rather of the transitional phase in the first years of disposal.

The corrosion rate measurements by mass loss during immersion tests under these same test conditions for a maximum duration of 6 months show values in the range of 30 to 50 µm yr^{-1}. Examination of the sample surfaces by X-ray diffraction and Raman analysis mainly reveals the predominant presence of copper oxide Cu_2O, along with some islands of carbonates and silica.

The creep tests at 90°C intended for tensile loading could not be conducted due to very low mechanical strength in this mode of loading. Failure occurs rapidly by decohesion along the strings of porosities in the overlap zones of deposition lines. Consequently, these tests were carried out in compression under air at 90°C. The creep behaviour was characterised for three stress levels: 85%, 100%, and 115% of the yield strength. For the two highest loadings, the three phases of primary creep, steady-state creep, followed by final rupture, are observed. The steady-state creep rate is greater with higher stress levels. Creep at 85% of the yield strength shows, after the primary creep phase, a stable level of deformation as long as the deformation does not exceed 4% plastic strain.

2.3.2 Subtask 2.2 Metallic Materials and Coatings

2.3.2.1 Metallic materials

VTT's work aimed to explore the viability of alternative materials for copper canisters, considering factors such as improved availability, corrosion resistance and lower cost. The research focused on investigating the impact of impurities on corrosion properties in the Finnish disposal concept using commercial copper alloys.

VTT evaluated the absorption and diffusion of hydrogen, as well as susceptibility to stress corrosion cracking (SCC), through experiments utilising simulated groundwater with ammonia as an aggressive species. Two copper grades, Cu-OFP and high conductivity phosphorous-doped copper (HCP), were studied in two deformation states (flat and curved) and with different rolling parameters (hot and cold), resulting in a total of six test materials. Immersion tests on U-bend, flat mass loss and electrochemical specimens were conducted in autoclaves, providing sufficient data to (i) calculate uniform corrosion rates, (ii) investigate the microstructure of the samples, (iii) analyse the chemical composition of the samples, and (iv) assess the presence of any SCC.

Immersion tests were performed under conditions that were representative of the fourth phase of repository evolution as defined in a simulation prepared by Nagra (Landolt et al., 2009), and summarised below, in which anoxic conditions prevail. The expected evolution of the environmental conditions can be broken down into the following phases:

- Phase 1: dry air oxidation of the canister, with temperature ranging between 110°C and 140°C for about 0 to 40 years.
- Phase 2: aerobic unsaturated. The surface temperature decreases to about 100°C and lasts for 20 to 30 years.
- Phase 3: aerobic-anaerobic transition, which is expected to last for about 50 years with temperature decreasing to about 90°C.
- Phase 4: long-term saturated, anoxic conditions, which occur after about 100 years of emplacement, and the temperature continually decreases to approximately 40°C after approximately 10,000 years

Two copper grades were studied, namely, Cu-OFP and high conductivity phosphorous-doped copper (HCP), which were obtained in two different deformation states (flat and curved) and with different applied rolling parameters (hot and cold), giving a total of six different test materials.

Based on earlier electrochemical tests, the pH value (approx. 10) and concentration of ammonia hydroxide (100 mg l^{-1}) were chosen to achieve pitting corrosion in an anoxic solution. In order to accelerate SCC, three different potentials were constantly applied to the Cu U-bend specimens (-200, -125 and -50 mV vs SCE) using potentiostats.

The results showed similar electrochemical behaviour for all the alloys after one month of immersion. While Cu-OFP initially exhibited higher corrosion resistance, the average corrosion rates for the 3-month immersion test showed very similar behaviour for HCP. Hydrogen content measurements showed that the copper grain size (ranging from 85 to 152 µm) did not correlate with the hydrogen uptake, and, in fact, hydrogen intake was not detected in this environment unlike expected. Applying different potentials to the U-bends resulted in various oxidation states, with the highest anodic potential (-50 mV vs SCE) leading to the highest oxidation of copper ($Cu(OH)_2$) with a distinctive blueish layer (Figure 2). Although small features suggesting intergranular corrosion were observed, they were either cracks in the oxide film (Figure 1b) or the features were relatively blunt leaving the underlying metal mainly intact (Figure 1c).

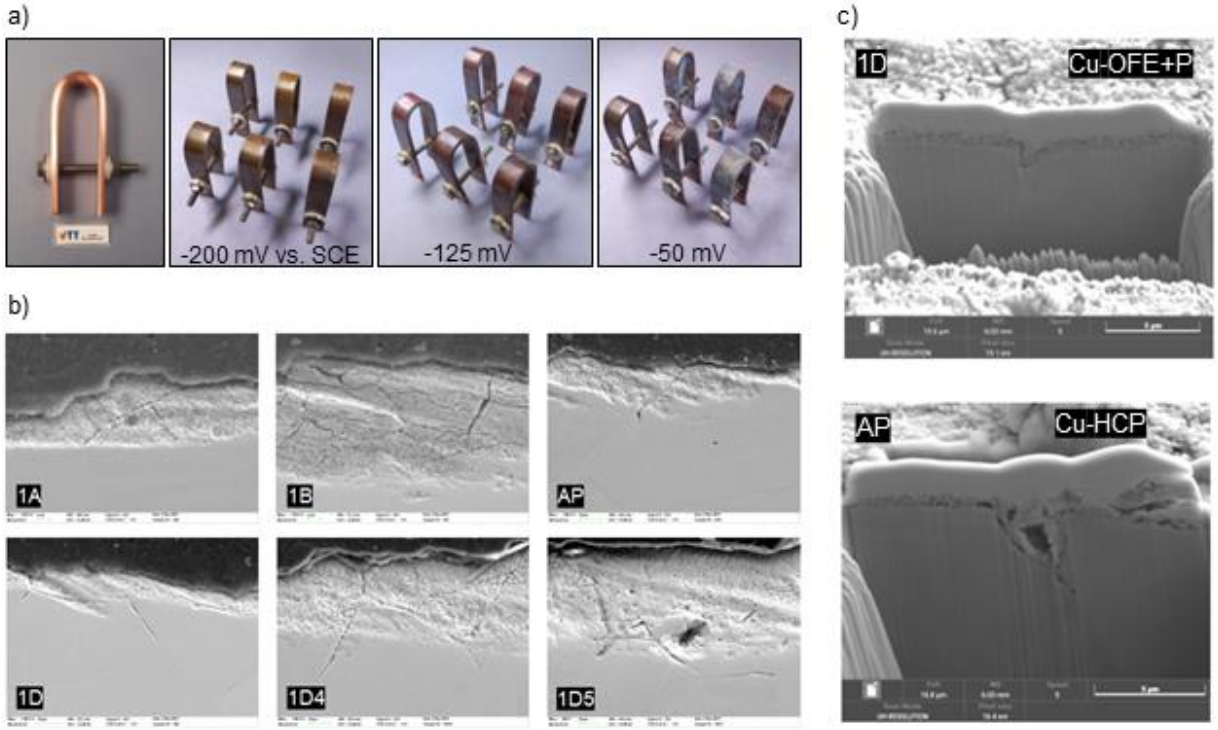

Figure 2. a) Copper U-bend sample before immersion; three sets of six alloys after 3 months immersed in simulated groundwater with 100 mg/l NH_4OH having constant potential applied (-200 mV, -125 mV and -50 mV vs. SCE, respectively); b) Cross-sectional images of Cu U-bends after immersion with application of -50 mV (AP, 1A, 1B: Cu-HCP and 1D, 1D4, 1D5: Cu-OFE+P); c) FIB micro cross sections of both alloys imaged by FEG-SEM.

2.3.2.2 Metallic coatings

The study of the metallic coatings performed by KIPT investigated the effect of bias potential on the structure and properties of copper, titanium, and chromium coatings deposited by cathodic arc evaporation (PVD). The coatings deposited at the optimum bias potential showed good mechanical properties and a high degree of adhesion to the steel substrates. Coatings of Ti, Cu, and Cr with a minimum thickness of 30 µm exhibit exceptional corrosion resistance without pitting when subjected to potentiodynamic testing in a 3% NaCl solution.

Long-term corrosion testing (4,200 hours) of Ti, Cr, and Cu coatings on steel substrates under disposal conditions (water, T = 90°C) showed weight loss and small pits in the Cr coating. The Ti and Cu coatings show

high corrosion resistance as evidenced by their minimal weight change during the test period. However, after 3,000 hours of testing, some pitting and rusting was observed on the surface of the Ti coating.

2.4 Key outputs from Task 2

The ambition of Task 2 of ConCorD was to explore the potential of novel materials and processes for the optimisation of long-term container performance. For the most promising novel materials, the experimental studies were designed to contribute to the understanding of corrosion/degradation processes. The work within this task was organised according to the two main types of materials: ceramic and metallic materials. In the case of ceramic materials, the experimental work was focused on studying materials and processes (deposition, sealing) for innovative solutions of ceramic containers and ceramic coatings. For containers made of bulk ceramics, the key properties for long-term performance are fracture toughness and leaching/alteration. For thin coatings, a primary concern is the presence of porosity or flaws. For metallic materials, the main aim of the experimental work was to study and consider the implementation of innovative solutions for metallic anti-corrosion coatings or optimised bulk metallic options. Studies focused on material development (alloy composition, coating technology) and initial corrosion tests to identify the benefit of these new solutions. The main objectives of Task 2 were fulfilled, and the main project achievements can be summarised as follows:

1. New silico-aluminate materials were developed for the sealing of bulk ceramic (alumina) containers by means of microwave heating. The main result was the unprecedented improvement in microwave coupling, enabling rapid sealing. This will allow limitation of the increase in temperature at the inner side of the container during the sealing process in real conditions. The new sealing formulations also satisfied the required mechanical and leaching resistance specifications.
2. The optimal parameters for the sintering of high-density silicon carbide were determined. Silicon carbide showed good mechanical and corrosion resistance properties for its potential use as bulk ceramic container. In particular, the addition of 0.3% Cr in the material formulation was found to further improve the corrosion resistance of silicon carbide, under the tested conditions.
3. Experiments performed in ammonia-containing simulated groundwater under anaerobic conditions yielded relevant data about the corrosion behaviour of Cu-OFP and high conductivity phosphorous-doped copper (HCP) as bulk materials for containers. The electrochemical behavior of the alloys was elucidated, along with their corrosion rate, hydrogen uptake, and information on the SCC of U-bends at different oxidation states. The results showed similar electrochemical behaviour for all the alloys after one month of immersion. These outcomes of these experiments highlight the fact that HCP copper may be able to safely replace the more traditional oxygen-free copper (Cu-OFP) for use as canister materials, with better availability, lower cost, and sustainable sources, such as recycled materials.
4. Several ceramic (CrN and TiO_2) and metallic (Ti, Cu, and Cr) coatings were produced by means of cathodic arc evaporation with thicknesses up to 30 µm. Among the ceramic coatings, CrN showed the best result in terms of corrosion resistance, with minimal weight loss and no pitting on the surface. Among the metallic coatings, Ti and Cu coatings showed the best corrosion performances under the tested conditions, with minimal weight change throughout the test period, indicating high corrosion resistance, even though some traces of pitting or rusting were observed on the surface of the Ti coating after 3000 hours of testing.
5. The study of novel Cu + 32vol.% Al_2O_3 composite coatings deposited by the cold spray process focused on the microstructure of the deposits, their mechanical properties, corrosion resistance, and creep resistance. Mechanical properties evaluated under uniaxial compression show a behaviour similar to that of cold-worked solid copper. The electrochemical behaviour of this coating, studied at 90°C in a synthetic medium representative of groundwater at the Bure site (France), shows no significant difference between tests on solid copper and composite cold spray deposits. The creep tests at 90°C intended for tensile loading could not be conducted due to very low mechanical strength in this mode of loading (failure occurred rapidly by decohesion of the coating along the strings of porosities in the overlap zones of deposition lines). Consequently, these tests were carried out in compression under air at 90°C. No test in a corrosive environment could be conducted under compression to study the effect of dissolution on the creep rates. For this kind of tests, a specific setup needs to be developed.

3. Task 3: Corrosion under irradiation

3.1 Introduction to task

The main goal of Task 3 was to experimentally assess whether irradiation influences the corrosion of canister materials under disposal conditions, with the aim of acquiring the necessary scientific understanding and relevant experimental data to allow the incorporation of radiation-induced phenomena into performance assessment models (see Section 6.2.2.1). To achieve this goal, it is necessary to identify the critical parameters that determine the extent of any irradiation-induced material degradation. This topic was addressed in Subtask 3.1. As described in the initial State-of-the-Art (SotA) report (Abdelouas et al., 2022), one of the main outstanding questions regarding the effect of radiation on corrosion is whether dose rate or total accumulated dose, or some combination of the two parameters, is the critical factor determining the extent of radiation-assisted corrosion (RAC). At present there is no consensus on whether an additional allowance is required to take account of any possible effects of radiation emitted by the waste package on the corrosion rate. The experiments carried out in Subtask 3.1 were designed to address this question (Subtask 3.1). This approach was combined with another set of irradiated corrosion experiments that were conducted under representative disposal conditions that mimicked different periods during the typical repository evolution (Subtask 3.2). The irradiation studies included bulk copper and carbon steel samples, the most commonly used container materials, but also copper-coated samples and other novel canister material.

The details of the experiments undertaken within Task 3 and the full set of results are presented in Bevas et al. (2024) and Sarrasin et al. (2024).

3.2 Scope of task

3.2.1 Subtask 3.1: Critical irradiation parameter

3.2.1.1 Jacobs experimental set up

In this Subtask, Jacobs set up experiments in simplified model systems covered four orders of magnitude of dose rate, leading to total doses spanning two orders of magnitude. The experiments included unirradiated controls using carbon steel and copper. The testing program in Task 3.1 involved corrosion testing by exposure to a simulated bentonite porewater solution for different durations over a wider range of dose rates, some of which far exceed those anticipated at a container surface in a GDF. The reason for selecting such conditions was to attempt to discern the underlying mechanisms that govern the key corrosion processes that affect container materials under radiation, rather than to try to quantify specific corrosion rates for repository conditions. The key objective was to elicit the overall trends in the data, which are easier to resolve when using a model solution and a very wide range of test conditions, rather than focussing on a precise range of highly representative environments.

A summary of the experimental conditions examined in the whole of Task 3, including Task 3.1, is shown in Table 1 and full details of the experimental set up for Task 3.1 are given in Bevas et al. (2024).

Table 1. High-level summary of the experiments carried out in Task 3 on radiation-assisted corrosion.

Responsible organisation	Task number	Type of experiment	Environment	Material	Durations	Dose rates (Gy hr^{-1})	Total doses (kGy)	Deliverable
Jacobs	3.1	exposure testing	simulated porewater ($NaCl/NaHCO_3$) ambient temperature	copper carbon steel	0 to 10,000 hours	0 to 1,000	0 to 100	D15.7, Bevas et al., (2024)
UJV	3.1	exposure testing	Compacted bentonite (MX-80 bentonite and Bentonite Cerny Vrch, BCV) Various degrees of saturation Room temperature to 150°C. Anoxic conditions.	carbon steel (grade S355J2H)	6, 9, 12 or 18 months	0.4	Not given.	D15.7, Bevas et al., (2024)
Subatech (CNRS)	3.2	exposure testing	Coupons in contact with MX-80 compacted bentonite, or in humid atmosphere only. Anoxic conditions at 25°C.	carbon steel grade P235GH	7 and 39 days	400	Not given.	D15.8, Sarrasin et al., (2024)
CIEMAT	3.2	exposure testing	Compacted bentonite. Dry density 1.4 or 1.6 g cm^{-3}. Saturation level 60% to 100%.	Copper or carbon steel	12 days	14, 66, 697	14 and 140	D15.8, Sarrasin et al., (2024)

The specimens were tested in the form of ribbons measuring 50 × 2 × 1.2 mm. They were fabricated from carbon steel (CS), wrought copper (WC) or cold-sprayed copper (CSC), using electrical discharge machining (EDM). To remove any extraneous surface material, all ribbons were ground using a rotary polisher with silicon carbide papers (P320 and P1200) then ultrasonically cleaned in acetone. The test solution was deaerated 0.1 M NaCl / 0.2 M $NaHCO_3$, with a pH value of 8.0±0.05. The test specimens were mounted in specially designed ampoules fabricated from quartz glass, as shown in Figure 3. Solid state oxygen sensors were placed in two modules to check for any air ingress. An inner carousel was used to hold the prepared metal ribbon samples.

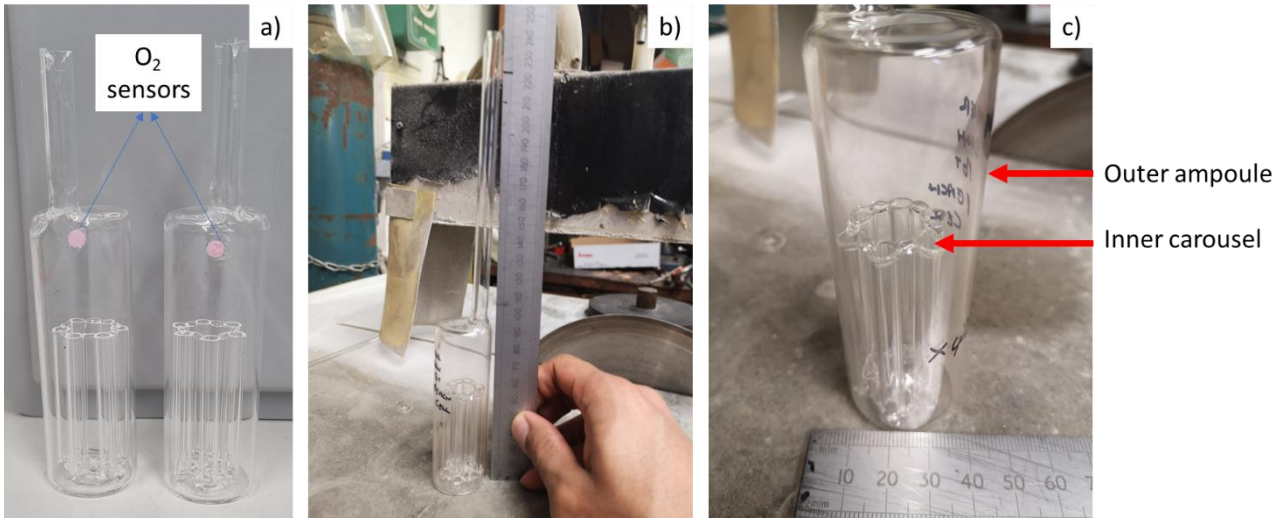

Figure 3. Ampoule Design 1: (a) empty ampoule front view with O_2 sensor spots shown, (b) empty ampoule side view, (c) empty ampoule with inner carousel highlighted.

After the ribbons were placed in the carousel, the buffer solution was added until all the ribbons were submerged. Approximately 45 ml of buffer solution was added to all ampoules of Design 1 and approximately 60 ml to ampoules of Design 2 (not shown). Five ampoules only containing the buffer solution were also prepared and used as blank control samples.

Ampoules were irradiated with γ-radiation from a ^{60}Co source at the Harwell Irradiation Facility, Harwell, Oxfordshire. Dosimetry measurements were taken to identify appropriate separation distances away from the source to give dose rates ranging from 0.1 to 1,000 Gy hr^{-1}. A variety of different dose rates and exposure durations were calculated to achieve total doses of 1 kGy, 10 kGy and 100 kGy. A matrix detailing all dose rates, exposure durations and total doses is given in Table 2.

Table 2. Matrix detailing combination of dose rates and exposure durations for all ampoules. Numbers 0, 1, 10 and 100 in bold denote total radiation dosage received by ampoules containing carbon steel (CS), wrought copper (WC) or cold-sprayed copper (CSC) ribbons. Note. Where cold-sprayed copper (CSC) is listed, cold-sprayed copper ribbons replaced two out of the six wrought copper ribbons in the same ampoule. Ampoules labelled with Ben had samples encased in bentonite instead of the sodium bicarbonate buffer solution.

Exposure Duration (Hrs)	Dose Rate (Gy hr^{-1})								
	0.0	0.1	0.2	1	2	10	20	100	1,000
1	**0** (CS, WC)								**1** (S) **1** (Blank Solution)
10	**0** (CS, WC)							**1** (CS)	**10** (CS)
100	**0** (CS, WC, CSC)					**1** (CS, WC, CSC)		**10** (CS, WC, CSC)	**100** (CS) **100** (Blank Solution)
1,000	**0** (CS, WC, CSC) **0** Ben (CS WC)			**1** (CS, WC, CSC)		**10** (CS, WC, CSC) **10** Ben (CS		**100** (CS, WC)	
5,000	**0** (CS, WC)		**1** (CS, WC, CSC)		**10** (CS)		**100** (CS)		
10,000	**0** (CS, WC) **0** (Blank Solution)	**1** (CS, WC) **1** (Blank Solution)		**10** (CS, WC)		**100** (CS, WC) **100** (Blank Solution)			

3.2.1.2 Disassembly and analysis of Jacobs tests

After the test samples had reached their target immersion durations and/or radiation doses, the test ampoules were transferred to an argon-purged glovebox where they were photographed before being dismantled. The pH of the buffer solution inside was recorded. Once removed from the buffer solution, ribbons were individually rinsed in deionised water and methanol, then dried. The following observations and analyses were subsequently carried out on the metal ribbons:

- Photography and visual inspection
- Mass loss measurements to determine the average anaerobic corrosion rate, in accordance with ASTM G1-03 [ASTM, 2003[i]].
- SEM-EDX of surface of cross-section through corrosion product
- Raman spectroscopy
- X-ray photoelectron spectroscopy (XPS)
- Profilometry

3.2.1.3 UJV experimental set up

The simple bulk solution environments described above, were complemented by irradiation studies carried out by UJV at dose rates of 10 to 100 Gy hr^{-1}, for exposure periods up to 18 months, giving a total absorbed dose of up to 900 kGy. These experiments were conducted in compacted bentonite, with different degrees of saturation, over a temperature range room temperature to 150°C. Carbon steel corrosion coupons were used.

The degree of corrosion was investigated as a function of different dose rates, temperatures and degrees of saturation. The experimental design consisted of carbon steel coupons embedded in two types of bentonite (MX-80 bentonite and Bentonite Cerny Vrch, BCV) that were compacted and saturated under anoxic conditions in stainless steel modules. These were then inserted into sealed chambers using an anoxic glovebox, then irradiated using a ^{60}Co radiation source and heated to a temperature of 90°C or 150 °C for 6, 9, 12 or 18 months.

The applied dose rate (0.4 Gy hr^{-1}) was chosen based on the calculated radiation field to represent the conditions that have been calculated to exist close to the fuel assemblies at the defined temperature (Pospíšková et al., 2017). The modules were sealed to ensure that anoxic conditions were maintained internally. Corresponding unirradiated control tests were set up to determine the influence of radiation on corrosion.

Additional, complementary modules were designed and used to enable an estimation of microbial survivability after exposure under the given conditions.

The test specimens were in the form of discs (10 mm diameter; 1 mm thick) composed of carbon steel, grade S355J2H. They were cut from an outer casing tube of the type used for the Czech canister concept and had a ground finish (46K grit). The initial masses were recorded to a resolution of 0.1 mg.

A synthetic granitic water (SGW3, Table 6) was used as the saturation medium in all experiments conducted by UJV. The chemical composition of the water was calculated as representing waters that are typical of the Rožná mine formation (the Bohemian Massif) layers located at 1,000 m to 1200 m below the surface (Červinka et al., 2018).

Table 6. Chemical composition of synthetic granitic water (Červinka et al. 2018).

Concentration (mg l^{-1})	Na^+	K^+	Ca^{2+}	Mg^{2+}	F^-	Cl^-	NO_3^-	SO_4^{2-}	HCO_3^-
SGW3	89.4	0.7	1.3	0.1	9.9	18.7	-	10.5	163.5

The experimental matrix consisted of 23 cells, each containing compacted bentonite holding embedded steel coupons. In accordance with the DGR concept (Pospiskova et al., 2017), the initial bentonite moisture content was adjusted to 15%, for the cells heated to 150°C, and 20%, for the cells heated to 90°C. The dry density of the compacted bentonite was 1,600 kg m^{-3}. In each corrosion cell, there were 12 carbon steel samples, divided into three layers, each of which contained four steel samples.

The cells were connected to capillaries and saturated under a pressure of 5 MPa for the whole loading period. The synthetic granitic water was deaerated in the glovebox prior to use. All the experimental cells were either loaded in an argon atmosphere in a glovebox or placed in steel vessels then filled with argon prior to their welding. Nine cells were subjected to ^{60}Co irradiation at a surface dose rate of ~0.4 Gy hr^{-1} and nine other cells were heated without irradiation. The nominal test temperatures were 90°C or 150°C. The remaining five unirradiated reference cells were saturated under an argon atmosphere in the glovebox and stored at ambient temperature (~21°C). A summary of the experimental cell conditions for UJV's programme is given in Table 3.

Table 3. Summary of the experimental cells and loading conditions in the UJV experiments.

Cell No.	Bentonite	w initial (%)	w final (%)	Loading period (months)	T (°C)	Radiation (Gy.hr^{-1})
1	BCV	15	21.14	6	150	0.4
2	BCV	15	21.28	6	150	-
3	BCV	15	25.06	9	150	0.4
4	BCV	15	21.96	9	150	-
5	BCV	15	20.54	12	150	0.4
6	BCV	15	9.29	12	150	-
7	BCV	15	22.61	18	150	0.4
8	BCV	15	22.33	18	150	-
9	MX-80	15	16.57	18	150	0.4
10	MX-80	15	20.00	18	150	-
11	MX-80	15	19.58	18	RT	-
12	BCV	20	20.86	9	90	0.4
13	BCV	20	24.55	9	90	-
14	BCV	20	23.24	12	90	0.4
15	BCV	20	23.93	12	90	-
16	BCV	20	18.34	18	90	0.4
17	BCV	20	21.78	18	90	-
18	MX-80	20	20.57	18	90	0.4
19	MX-80	20	20.42	18	90	-
20	BCV	20	22.58	6	RT	-
21	BCV	20	24.54	9	RT	-
22	BCV	20	23.77	12	RT	-
23	BCV	20	23.94	18	RT	-

3.2.1.4 Disassembly and analysis of UJV tests

After the required exposure time of 6, 9, 12 or 18 months, the experiments were disassembled and the test coupons were analysed using the following techniques:

- Photography and visual inspection
- Mass loss measurements to determine the average anaerobic corrosion rate, in accordance with ČSN EN 10210-1.
- SEM-EDX of surface of cross-section through corrosion product
- Raman spectroscopy
- X-ray diffraction (XRD)

- Profilometry

In addition, the bentonite removed from the test cells was analysed using the following techniques:

- X-ray fluorescence (XRF), to obtain the overall chemical composition of the bentonite.
- Spectrophotometric analysis of the total carbon content (C_{tot}) and the total sulphur content (S_{tot}), using a naturally wet sample.
- Analysis of water leachate from bentonite dried at 105°C into pure water by AAS (atomic absorption spectroscopy), capillary zone electrophoresis (CZE) and alkalimetric titration.
- SEM-EDX analysis using a low vacuum system.

3.2.2 Subtask 3.2: Irradiation under repository conditions

3.2.2.1 Subatech experimental set up

A series of irradiation corrosion experiments was set up by Subatech using coupons fabricated from carbon steel grade P235GH, whose composition is given in Table 4. The coupons measuring 10 × 10 × 2 mm were polished to a 3 µm diamond finish. The MX-80 bentonite used for the experiments was pre-equilibrated with water vapour at the required relative humidity (63%, 76% or 99%) in a humidity chamber using standard salt solutions to control the humidity. The dry density for the bentonite was 1.4 g cm^{3} to 1.6 g cm^{-3}. Each steel coupon was placed on top of the pellet with one side in contact with the clay and the other side exposed to the atmosphere using the experimental arrangement shown in Figure 4. Some coupons were tested without contact with the bentonite and were exposed to a humid atmosphere, in which case the coupons were irradiated in the vertical position. The test cells had their head spaces purged for 10 minutes with argon with the aim of producing anoxic conditions and then sealed before they were put inside the irradiator.

The atmosphere in the gamma irradiation facility was purged with argon for a short period before the irradiation started but the test environment was not expected to be fully anoxic. The corrosion tests were exposed to gamma irradiation experiments using a GSM D1 Gamma ^{137}Cs (120 TBq; Eg = 0.66MeV) source located in the Arronax Cyclotron facility (France) at a dose rate[4] of 400 Gy hr^{-1} and at room temperature (25°C).

Table 4. Composition of the P235GH steel (wt%).

Elements									
C	Mn	Si	P	S	Cr	Mo	Ni	Al	Cu
≤0.16	0.60-1.20	≤0.35	≤0.025	≤0.015	≤0.30	≤0.08	0.0	≥0.02	≤0.3
Nb	Ti	V	N						
≤0.02	≤0.03	≤0.02	≤0.012						

[4] This dose rate was chosen to exaggerate the effect of radiolysis on steel corrosion to allow as many experiments to be conducted as possible.

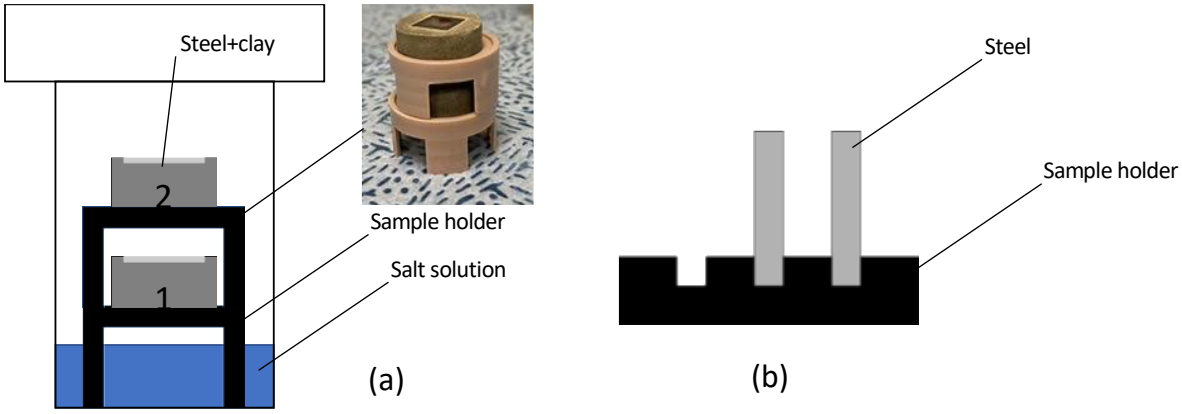

Figure 4 Cell and samples setup (a) steel+clay, (b) steel alone.

3.2.2.2 Disassembly and analysis of Subatech tests

After exposure the samples were transferred to a glovebox for storage prior to analysis using a combination of XRD, mass loss (using 15% HCl inhibited with 5g/L hexamethyltetramine as the descaling agent), visual inspection, SEM-EDX and Raman spectroscopy. The gas composition in the headspace of the test cells was analysed for hydrogen and oxygen using gas chromatography. It was not possible to derive accurate corrosion rates from the measured hydrogen production rates due to the complexity of the system and the possibility of their being other sources of hydrogen than corrosion. The corrosion rate information was therefore derived from the mass loss measurements only.

3.2.2.3 Ciemat experimental set up

The studies conducted by CIEMAT focused on investigating the role of gamma radiation at the canister /bentonite barrier. Two main sets of laboratory experiments were carried out:

1. Experiments to simulate the expected conditions at the canister / bentonite interface at the early stage of a DGR (Phase 2 – see Section 2.2 for definition).
2. Experiments to analyse the evolution and impact of radiation on corrosion products previously released at this interface.

In the first type of experiment, a natural bentonite was used to prepare compacted samples at different dry densities (1.4 g cm^{-3} and 1.6 g cm^{-3}), which were then pre-hydrated with porewater to give saturation levels of 60% or 100%. To analyse the impact of accumulated γ-dose on container corrosion at the bentonite barrier, custom-built sealed cells were prepared containing thin copper or carbon steel coupons placed on a surface of compacted bentonite.

The second type of experiment simulated the canister / bentonite surface where pre-existing oxides on the steel or copper were placed in contact with the bentonite. Selected samples of bulk corrosion products for copper and iron were irradiated and analysed to investigate the effect of radiation on them. Compacted bentonite samples covered with a thin layer of magnetite were also irradiated under the same conditions to analyse their behaviour.

Samples were prepared in triplicate to enable comparison of unirradiated conditions with γ-radiation at accumulated doses of 14 kGy and 140 kGy. These values were chosen as for the current NAGRA repository design, 14 kGy of accumulated dose is within the range of γ-radiation expected at the canister/bentonite interface in the early stage of the repository. The accumulated dose of 140 kGy is above the anticipated dose, but it was selected to give a factor of $\times$10 higher radiation level, for comparison purposes. After irradiation, the test samples were characterised to evaluate metal corrosion rates, the identity of corrosion products and to characterise any changes induced in the bentonite.

The material for fabricating the carbon steel coupons used for the experiments was provided by Jacobs; it was cut from a prototype canister prepared for Nagra (Patel, 2012). The carbon steel discs were 1.9 cm in diameter with an average thickness of 1.5 mm. Copper samples were obtained from SKB in the form of round bars of Cu-OFP, with the composition given in Table 5. Following manufacture, the samples were cleaned and dried. The surfaces were used in their 'as-machined' condition (i.e. not polished).

Table 5. Composition of Cu-OFP sample reference provided by SKB.

	Trace elements (ppm)										
Cu	**Ag**	**Al**	**As**	**Bi**	**Cd**	**Co**	**Cr**	**Fe**	**H**	**Mn**	**Ni**
99.99 %	15.075	0.095	0.39	0.72	<0.35	0.325	0.28	0.405	0.47	<0.11	0.58
	O	**P**	**Pb**	**S**	**Sb**	**Se**	**Si**	**Sn**	**Te**	**Zn**	**Zr**
	1.9	58.3	1.665	4.655	1.27	<0.65	1.26	0.87	<2.7	<1.1	<0.090

The bulk corrosion products selected for testing, as being representative of the corrosion products that will be formed on steel and copper, were as follows:

- CuO: Copper (II) oxide nanopowder < 50 nm
- Cu_2O: Copper (I) oxide >99.99 % trace metal basis
- Fe_2O_3: Fe(III) oxide nanopowder <50 nm particle size
- Fe_3O_4: Fe(II, III) oxide nanopowder 50-100 nm particle size (SEM), 97% trace metals basis
- α-Fe(III)OOH: Goethite, laboratory prepared as described in (Missana et al. 2009).

The materials, which were obtained as commercial nano-powder oxide, were fully characterised before and after irradiation to analyse their main characteristics, mainly oxide phase, particle size and surface properties.

The bentonite used in the experiments was FEBEX bentonite from the Cortijo de Archidona deposit (Almería) (Huertas et al., 2000), which has a montmorillonite content greater than 90%, with quartz, plagioclase, potassic feldspar, calcite and trydimite as accessory minerals and a cation exchange capacity of 100 meq $100g^{-1}$ (42% Ca, 33% Mg, 23% Na and 2% K). Prior to compaction, the FEBEX clay was ground and sieved to a fraction <0.5 mm. Raw FEBEX clay was used in these experiments without any additional treatment or purification. Complete mineralogical, physical, chemical and microbial characterisation of this clay was carried out before and after experiments.

The waters used to saturate the compacted bentonite samples were the respective FEBEX porewaters, corresponding to each compaction density (1.4 and 1.6 g cm^{-3}). These synthetic waters were prepared following the recipes proposed by Fernandez & Rivas, 2005 (see Table 6).

Table 6. Chemical composition (M) of synthetic porewaters respectively prepared for FEBEX bentonite samples compacted at 1.4 (PW-1.4) and 1.6 g cm^{-3} (PW-1.6). Recipes from (Fernandez & Rivas, 2005).

Reference Density	KCl (M)	$CaCl_2 \cdot 2H_2O$ (M)	$MgCl_2 \cdot 6H_2O$ (M)	Na_2SO_4 (M)	NaCl (M)	$NaHCO_3$ (M)	pH
PW-1.4	$1.01 \cdot 10^{-3}$	$1.36 \cdot 10^{-2}$	$1.48 \cdot 10^{-2}$	$4.87 \cdot 10^{-2}$	$5.79 \cdot 10^{-3}$	$1.10 \cdot 10^{-3}$	7.56
PW-1.6	$1.09 \cdot 10^{-3}$	$1.50 \cdot 10^{-2}$	$1.66 \cdot 10^{-2}$	$4.59 \cdot 10^{-2}$	2.1610^{-2}	1.0110^{-3}	7.55

Reference powder samples of FEBEX bentonite and selected iron and copper oxides were separately placed in high-density polyethylene (HDPE) tubes, without any additional preparation, to be subjected to γ-irradiation under the same conditions applied for samples simulating the canister / bentonite interface. Copper and carbon steel discs were separately placed in polypropylene isotactic tubes with 5 ml of the required porewater simulant. Table 7 lists the 18 metal samples and their respective test conditions.

Table 7. List of metal samples immersed in waters for irradiation. In these experiments there was no bentonite, the conditions were oxic, the temperature was ambient and the samples were immersed in 5 ml of water and a polypropylene reaction vessel.

Radiation level	Test details		
	Reference	**Metal**	**Water type**
Unirradiated	T3-19*	Cu-OFP	PW-1.4
	T3-20*	Cu-OFP	PW-1.6
	T3-21*	carbon steel	PW-1.4
	T3-22*	carbon steel	PW-1.6
	T3-23*	Cu-OFP	DW
	T3-24*	Cu-OFP	DW
Gamma Irradiated 14 kGy total dose (dose rate 66 Gy hr^{-1})	T3-19	Cu-OFP	PW-1.4
	T3-20	Cu-OFP	PW-1.6
	T3-21	carbon steel	PW-1.4
	T3-22	carbon steel	PW-1.6
	T3-23	Cu-OFP	DW
	T3-24	Cu-OFP	DW
Gamma Irradiated 140 kGy total dose (dose rate 697 Gy hr^{-1})	T3-33	Cu-OFP	PW-1.4
	T3-34	Cu-OFP	PW-1.6
	T3-35	carbon steel	PW-1.4
	T3-36	carbon steel	PW-1.6
	T3-37	Cu-OFP	DW
	T3-38	Cu-OFP	DW

* unirradiated

The pieces, materials and installation procedure of the closed cells designed for samples simulating metal canister / bentonite interface at different experimental conditions are shown in Figure 5 and the

details of the test conditions are summarised in Table 8. Porewater corresponding to the chosen density of the bentonite was added to each compacted sample. In summary, a total of 16 separate samples was set up with bentonite at two compaction densities (1.4 g cm^{-3} or 1.6 g cm^{-3}), two degrees of saturation (60% and 100%), with four experiments each with no metal (i.e. irradiated clay only), copper coupons, carbon steel coupons and magnetite. Three gamma irradiation conditions were used: (1) unirradiated (Table 9) (2) gamma-irradiated at 14 kGy with a dose of 66 Gy hr^{-1} (Table 10) and (3) gamma- irradiated at 140 kGy with a dose of 697 Gy hr^{-1} (Table 11). Not all samples were irradiated at higher doses. The metal samples were all irradiated in air. The samples were irradiated by sealing them in a watertight metal container then placed in an irradiation pool facility containing ^{60}Co sources. After irradiation, samples were put into a jar that was purged with nitrogen then transferred to the appropriate analytical laboratory.

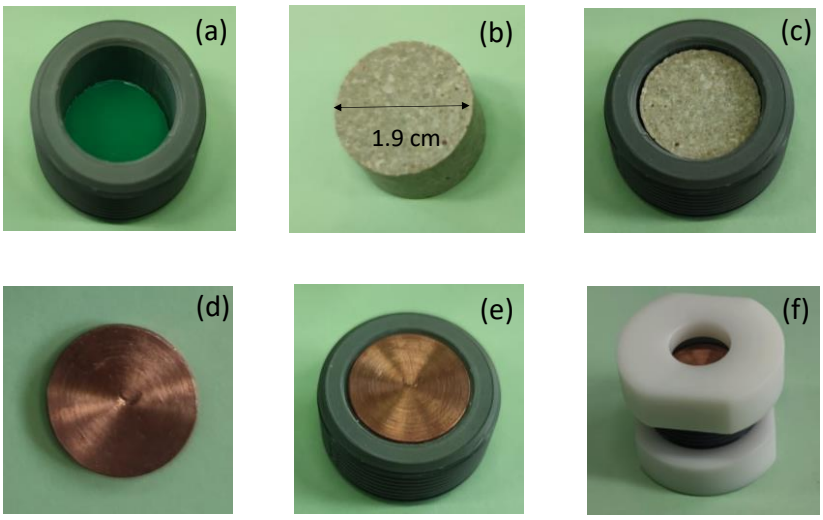

Figure 5. Closed cell designed for samples simulating metal canister/bentonite interface: (a) PVC open cylinder, (b) compacted bentonite sample. (c) bentonite inserted in the PVC ring, (d) copper metal disc (e) copper disc placed on the surface of the clay tablet, (f) closed cell.

Table 8. Dimensions and characteristics of compacted bentonite samples prepared at different compaction densities, with different water saturation degree (w.c. in %).

Compacted bentonite samples	1.4 g/cm^3 w.c. 60 %	1.4 g/cm^3 w.c. 100 %	1.6 g/cm^3 w.c. 60 %	1.6 g/cm^3 w.c. 100 %
Radius (cm)	0.95	0.95	0.95	0.95
Thickness (cm)	1	1	1	1
Compaction density (g cm^{-3})	**1.4**	**1.4**	**1.6**	**1.6**
Clay initial humidity (%)	13	13	13	13
Weighed clay (g)	4.5	4.5	5.1	5.1
Clay specific weight (g/cm^{-3})	2.7	2.7	2.7	2.7
Desired saturation degree (%)	**60**	**100**	**60**	**100**
Necessary water for saturation (ml)	0.8	1.4	0.7	1.2
Initial water (humidity) (ml)	0.5	0.5	0.6	0.6
Added Porewater (ml)	0.3	0.9	0.1	0.6

Table 9. Metal / FEBEX bentonite samples tested unirradiated under aerobic conditions at ambient temperature in a closed cell, showing the sample reference, the type of metal coupon or oxide included, the compaction dry density, the type of added water, the degree of saturation and the water volume added.

Reference	Metal or oxide	Density (g cm^{-3})	Hydration water	Water saturation conditions	Water Volume (ml)
T3-01*	none	1.4	PW-1.4	60%	0.8
T3-02*	none	1.4	PW-1.4	100%	1.4
T3-03*	none	1.6	PW-1.6	60%	0.7
T3-04*	none	1.6	PW-1.6	100%	1.2
T3-05*	Cu	1.4	PW-1.4	60%	0.8
T3-06*	Cu	1.4	PW-1.4	100%	1.4
T3-07*	Cu	1.6	PW-1.6	60%	0.7
T3-08*	Cu	1.6	PW-1.6	100%	1.2
T3-09*	carbon steel	1.4	PW-1.4	60%	0.8
T3-10*	carbon steel	1.4	PW-1.4	100%	1.4
T3-11*	carbon steel	1.6	PW-1.6	60%	0.7
T3-12*	carbon steel	1.6	PW-1.6	100%	1.2
T3-13*	magnetite	1.4	PW-1.4	60%	0.8
T3-14*	magnetite	1.4	PW-1.4	100%	1.4
T315*	magnetite	1.6	PW-1.6	60%	0.7
T3-16*	magnetite	1.4	PW-1.6	100%	1.2

Table 10. Metal / FEBEX bentonite samples prepared for gamma irradiation at 14 kGy at a dose rate of 66 Gy hr-1 under aerobic conditions at ambient temperature in a closed cell, showing the sample reference, the type of metal coupon or oxide included, the compaction dry density, the type of added water, the degree of saturation and the water volume added.

Reference	Metal or oxide	Density (g cm^{-3})	Hydration water	Water saturation conditions	Water Volume (ml)
T3-01	none	1.4	PW-1.4	60%	0.8
T3-02	none	1.4	PW-1.4	100%	1.4
T3-03	none	1.6	PW-1.6	60%	0.7
T3-04	none	1.6	PW-1.6	100%	1.2
T3-05	Cu-OFP	1.4	PW-1.4	60%	0.8
T3-06	Cu-OFP	1.4	PW-1.4	100%	1.4
T3-07	Cu-OFP	1.6	PW-1.6	60%	0.7
T3-08	Cu-OFP	1.6	PW-1.6	100%	1.2
T3-09	carbon steel	1.4	PW-1.4	60%	0.8
T3-10	carbon steel	1.4	PW-1.4	100%	1.4
T3-11	carbon steel	1.6	PW-1.6	60%	0.7
T3-12	carbon steel	1.6	PW-1.6	100%	1.2
T3-13	magnetite	1.4	PW-1.4	60%	0.8
T3-14	magnetite	1.4	PW-1.4	100%	1.4
T315	magnetite	1.6	PW-1.6	60%	0.7
T3-16	magnetite	1.4	PW-1.6	100%	1.2

Table 11. Metal / FEBEX bentonite samples prepared for gamma irradiation at 140 kGy at a dose rate of 697 Gy h--1 under aerobic conditions at ambient temperature in a closed cell, showing the sample reference, the type of metal coupon or oxide included, the compaction dry density, the type of added water, the degree of saturation and the water volume added.

Reference	Metal /oxide	Density (g cm^{-3})	Hydration water	Water saturation conditions	Water Volume (ml)
T3-25	Cu-OFP	1.4	PW-1.4	60%	0.8
T3-26	Cu-OFP	1.4	PW-1.4	100%	1.4
T3-27	Cu-OFP	1.6	PW-1.6	60%	0.7
T3-28	Cu-OFP	1.6	PW-1.6	100%	1.2
T3-29	carbon steel	1.4	PW-1.4	60%	0.8
T3-30	carbon steel	1.4	PW-1.4	100%	1.4
T3-31	carbon steel	1.6	PW-1.6	60%	0.7
T3-32	carbon steel	1.6	PW-1.6	100%	1.2

3.2.2.4 Disassembly and analysis of Ciemat tests

Powder materials were analysed before and after irradiation to a total dose of 14 kGy or 140 kGy to determine whether phase changes had occurred as a result of irradiation. For metals that were immersed in selected waters the post-irradiation analysis concentrated on assessing the corrosion and quantifying the concentration of dissolved copper or iron in the aqueous phase. For samples simulating the canister / bentonite interface the analyses were focused on determining the corrosion rates by mass loss, identifying the main corrosion products and characterising the neighbouring bentonite. The techniques applied included to the metal samples and the bentonite:

- Corrosion rate from mass loss measurements
- Water analysis to determine the concentrations of iron and copper using ICO-OES
- X-ray diffraction (XRD)
- Fourier transform IR spectroscopy (FT-IR)
- SEM-EDX
- Raman spectroscopy
- Zeta potential measurements to analyse the impact of γ-radiation on surface characteristics of oxide and bentonite particles
- Point of zero charge, pH_{PZC} by electrolyte titration
- Potentiometric acid-base titration.

3.3 Progress against task description

The full set of results from this Subtask are given in Bevas et al. (2024). This section contains a summary of the key results from the work performed in this task by Jacobs and UJV.

3.3.1 Subtask 3.1: Critical irradiation parameter

3.3.1.1 Results of Jacobs' test programme

An outline of the spectroscopic analyses carried out on carbon steel and wrought copper samples is detailed in Table 12 and Table 13, respectively. Note that only visual inspections were carried out on cold-sprayed copper samples. Mass loss measurements were carried out on all carbon steel samples and all wrought copper samples exposed for 10,000 hr.

Table 12. Outline of the spectroscopic analysis carried out on carbon steel specimens presented in Bevas et al. (2024). The total dose received in each condition is highlighted in bold. Note, X-SEM = cross-section SEM analysis.

Exposure Duration (hr)	Dose Rate (Gy hr^{-1})								
	0.0	0.1	0.2	1	2	10	20	100	1,000
1									**1 kGy** X-SEM
14								**1 kGy** X-SEM	**10 kGy** X-SEM
100	**0 kGy** X-SEM					**1 kGy** X-SEM SEM Raman XPS		**10 kGy** X-SEM SEM Raman XPS	**100 kGy** X-SEM SEM Raman XPS
1,000									
5,000	**0 kGy** X-SEM		**1 kGy** X-SEM SEM Raman		**10 kGy** X-SEM SEM Raman		**100 kGy** X-SEM		
10,000									

Table 13. Outline of the spectroscopic analysis carried out on wrought copper specimens presented in Bevas et al., 2024. The total dose received in each condition is highlighted in bold. Note, X-SEM = cross-section SEM analysis.

Exposure Duration (hr)	**Dose Rate (Gy hr^{-1})**								
	0.0	0.1	0.2	1	2	10	20	100	1,000
1									
10									
100	**0 kGy** X-SEM					**1 kGy** X-SEM SEM Raman XPS			
1,000									
5,000	**0 kGy** X-SEM		**1 kGy** X-SEM SEM Raman						
10,000									

Copper corrosion rate measurements

The results of the corrosion rate measurements for copper derived from mass loss measurements are shown in Figure 6. The corrosion rates for copper were determined from tests that were operated for 10,000 hours, from triplicate specimens (the results for the unirradiated control test were acquired from quadruplet specimens).

Average corrosion rates are listed in Table 14. In unirradiated conditions the average corrosion rate was just 0.02 µm yr^{-1}, which is consistent with the expectation that copper is largely immune to corrosion in unirradiated, anoxic solution at slightly alkaline pH.

The average corrosion rate of irradiated samples exhibited a strong dose rate/total dose dependence from 0.1 to 10 Gy hr^{-1} (1-100 kGy) as shown in Figure 6. Since the corrosion rates were only determined from tests conducted for 10,000 hours, there is no indication of the trend in corrosion rate as a function of time. From Figure 6, although the average corrosion rate exhibits a strong dose rate/total dose dependence increasing from ~0.05 to 1.2 µm yr^{-1} from 0.1 to 10 Gy hr^{-1}, this effect is sub-linear and decreases at the higher dose rates/total doses.

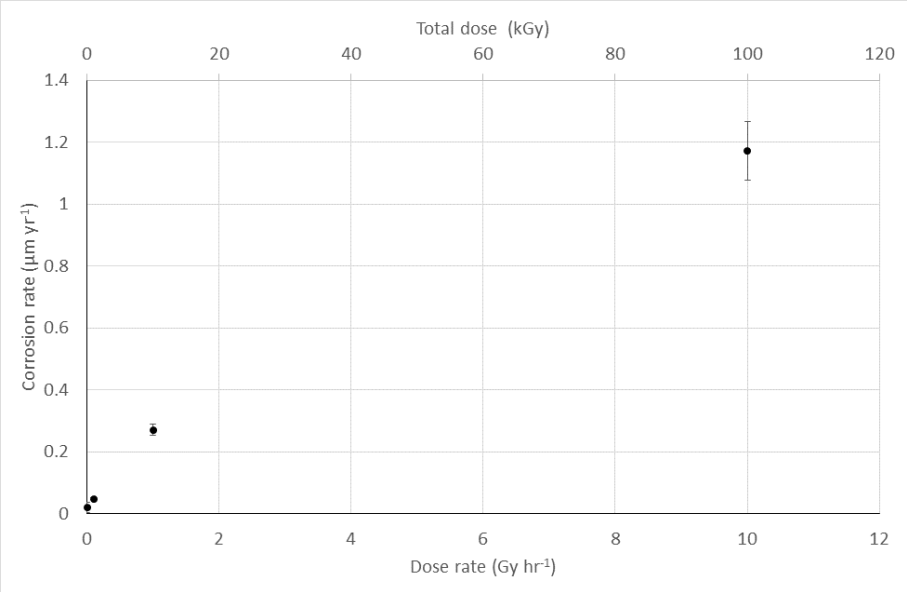

Figure 6. Copper average corrosion rate versus dose rate/total dose for tests operated for a duration of 10,000 hours. Error bars indicate the standard deviation between different specimens within the same test.

Table 14. Average corrosion rate of wrought copper exposed for 10,000 hr. Standard deviation of repeat measurements in brackets.

Dose rate (Gy hr^{-1})	Average corrosion rate (µm yr^{-1})
0	0.02 (0.02)
0.1	0.05 (<0.01)
1.0	0.27 (0.02)
10	1.17 (0.09)

Carbon steel corrosion rate measurements

Carbon steel corrosion rates were determined from triplicate specimens except for the results from the unirradiated control test that was operated for 1 hour, and the test performed at a dose rate of 100 Gy hr^{-1} that was operated for 14 hours, which had duplicate specimens. In unirradiated conditions, the magnitude of the thickness loss due to corrosion increased with time up to 5,000 hours, after which no increase in thickness loss was observed (see dark red bars in Figure 7). From Figure 7, it can be seen that a smaller average thickness loss was observed on unirradiated specimens (dark red bar) after 10,000 hours of exposure compared with 5,000 hours. In practice, this is probably due to experimental error as there is no feasible way that the thickness loss could be lower after a longer duration. This perspective is supported by the large error on the measurements made at 10,000 hours that indicate a maximum thickness loss comparable to that observed after 5,000 hours. In most likelihood, these results indicate a high attenuation in instantaneous corrosion rate with time that reduces to below the uncertainty of measurement after 5,000 hours of exposure.

Thickness loss due to corrosion was converted into average corrosion rate as shown on a log scale in Figure 9. In the absence of radiation, the corrosion rate decreases substantially with time, from an initial average corrosion rate of ~180 µm yr^{-1} in the first hour to less than 2 µm yr^{-1} after 10,000 hours. The attenuation in corrosion rate approximately exhibits a power law decay but a good fit of the data could not be obtained for a simple decay equation of the form At^{-B} where t is time and A and B are constants. A rapid attenuation in corrosion rate was also observed in tests exposed to gamma radiation, except for results obtained at 1,000 Gy hr^{-1} between 14 and 100 hours of exposure, which indicated a possible increase in corrosion rate. For durations of exposure between 1,000 and 10,000 hours, the relative rate of attenuation in corrosion rate was similar between unirradiated samples and those irradiated at 1 and 10 Gy hr^{-1}, with slightly lower rates of attenuation observed with increasing dose rates. Nevertheless, at 0, 1 and 10 Gy hr^{-1} the increase in corrosion loss between 1,000 and 10,000 hours was less than 1 µm (Figure 7) indicating an average corrosion rate in this period of < 1 mm yr^{-1}.

For tests performed for durations of 5,000 hours and longer, gamma radiation at dose rates greater than or equal to 10 Gy hr^{-1} significantly increased the amount of corrosion that took place. Whilst it appears that the average corrosion loss exhibits a monotonic dose rate dependence in the 10,000 hour tests, this apparent trend is most likely attributable to random variation in the data. This is more evident when comparing the data from the tests performed for 5,000 and 10,000 hours. Whilst the mean corrosion loss at 1 Gy hr^{-1} is greater than at 0 and 0.1 Gy hr^{-1} after 10,000 hours of exposure, the corrosion loss at 0 Gy hr^{-1} measured after 5,000 hours exposure is greater than all the losses measured at 10,000 hours with the exception of the test at 10 Gy hr^{-1}. For tests performed for a duration of 1,000 hour, the corrosion loss was significantly greater at a dose rate of 100 Gy hr^{-1}; at 10 Gy hr^{-1} the mean corrosion loss was greater than in the absence of radiation, but the difference was within the repeatability of the measurements. Following 100 hours of exposure, a significant increase in corrosion

rate was observed at 100 and 1,000 Gy hr^{-1} compared to the unirradiated control test. Whereas, at shorter durations there is no clear trend in the data, which could be partly due to the very low corrosion losses observed at short durations. Hence, we have placed a greater importance in the trends of the mass loss data obtained from the longer duration tests. The average corrosion rate is plotted versus dose rate as shown in Figure 10 for the full range of test conditions. The same data are shown over the range of dose rates anticipated at the external surface of canisters in a GDF, see Figure 10.

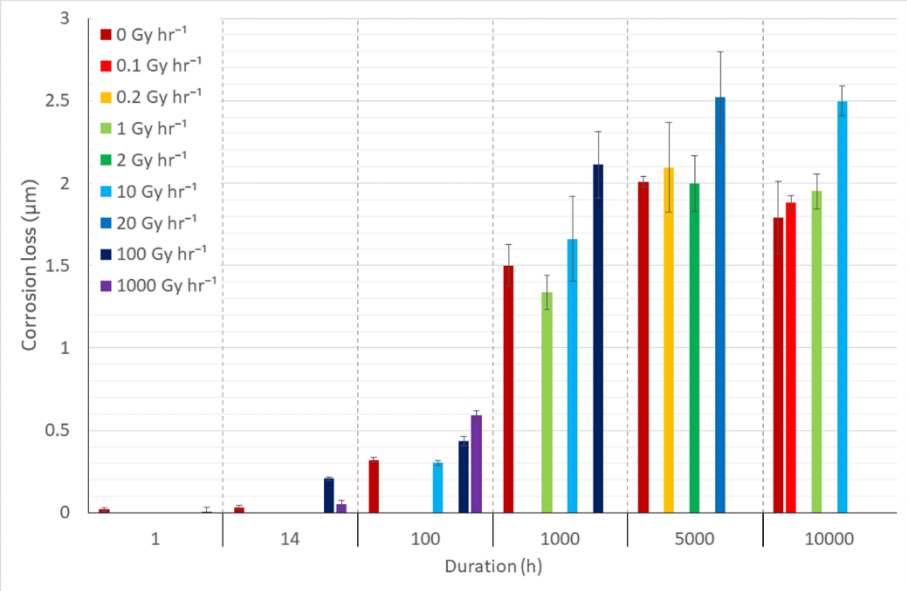

Figure 7. Thickness loss of carbon steel due to corrosion shown for each test duration (from 1 hour to 10,000 hours) with dose rate increasing from left to right between 0 and 1,000 Gy hr^{-1}. Error bars indicate the standard deviation between different specimens within the same test.

One can also compare the increases in corrosion relative to unirradiated controls as a function of total dose, as shown in Figure 8. Doing so for total dosages of 100 kGy showed dose rates of 10 Gy hr^{-1} and above lead to a significant increase in corrosion loss compared to corresponding 0 Gy hr^{-1} control samples. This corrosion loss threshold increased to a dose rate of 100 Gy hr^{-1} when exposed to a total dose of 10 kGy. The difference in corrosion loss between controls and irradiated samples of the same dose rate increases with increasing total dose/exposure duration. The figure implies that the impact of radiation is greater for higher total doses. However, it must be noted that this impact could be related to the increased test duration, particularly since the corrosion rate is observed to show rapid attenuation over time.

Compared with the amount of corrosion that takes place in unirradiated conditions the increase in corrosion due to radiation was fairly modest, with the exception of the results measured at 100 Gy hr^{-1} for 14 hours. Even at a comparatively high dose rate of 10 Gy hr^{-1} the average corrosion rate after 10,000 hours was only 2.2 µm yr^{-1}, compared with an unirradiated rate over the same time period of 1.5 mm yr^{-1}. Furthermore, the results indicate that the corrosion rate is expected to decrease further over longer durations of exposure. In some tests a lower corrosion rate was observed in the presence of radiation than in the corresponding control test. However, where this was observed the difference between the corrosion losses from irradiated tests and the unirradiated control test were within the range of repeatability of the measurement. The largest reduction in corrosion rate compared to the unirradiated control was observed at 1 Gy hr^{-1} after 1,000 hour duration of exposure, but at the same dose rate and a longer duration of 10,000 hours this apparent inhibiting effect was not observed, indicating it was possibly due to random variation.

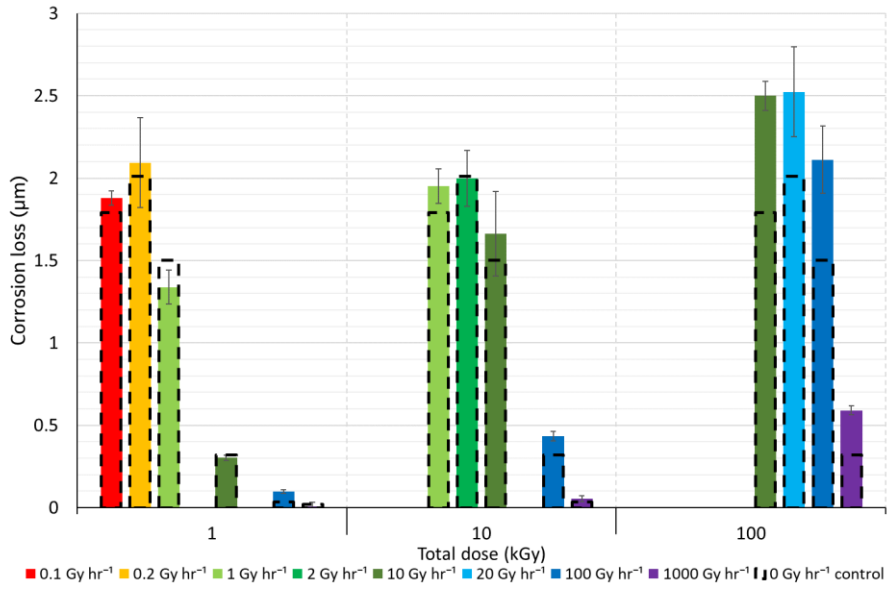

Figure 8. Thickness loss of carbon steel due to corrosion shown for each total dose (from 1 kGy to 100 kGy) with dose rate increasing from left to right between 0 and 1,000 Gy hr^{-1}. Error bars indicate the standard deviation of irradiated samples between different specimens within the same test condition. Dotted columns indicate corrosion loss of corresponding control sample (0 Gy hr^{-1}) at the same duration. Note, these results are from tests operated for durations between 1 and 10,000 hours.

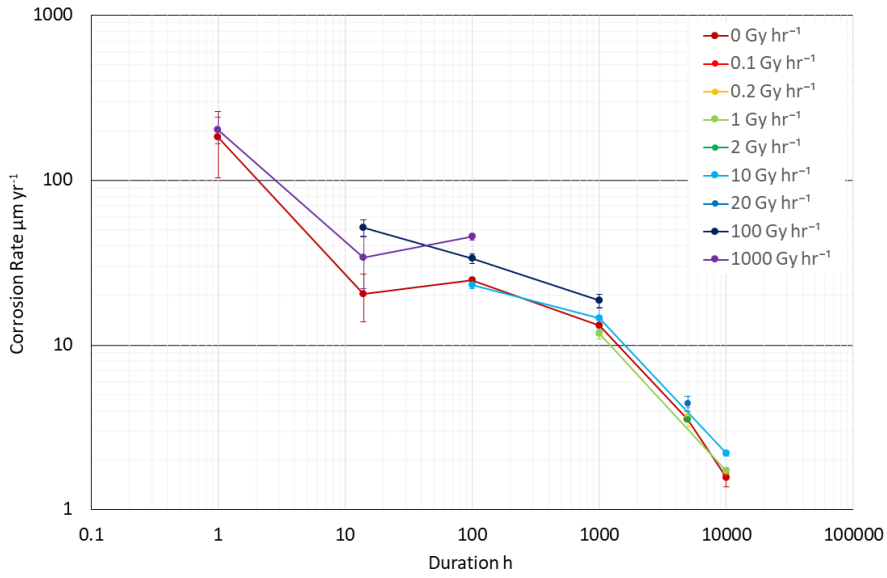

Figure 9. Carbon steel average corrosion rate versus time for dose rates between 0 to 1,000 Gy hr^{-1} expressed on a log scale. Error bars indicate the standard deviation between different specimens within the same test.

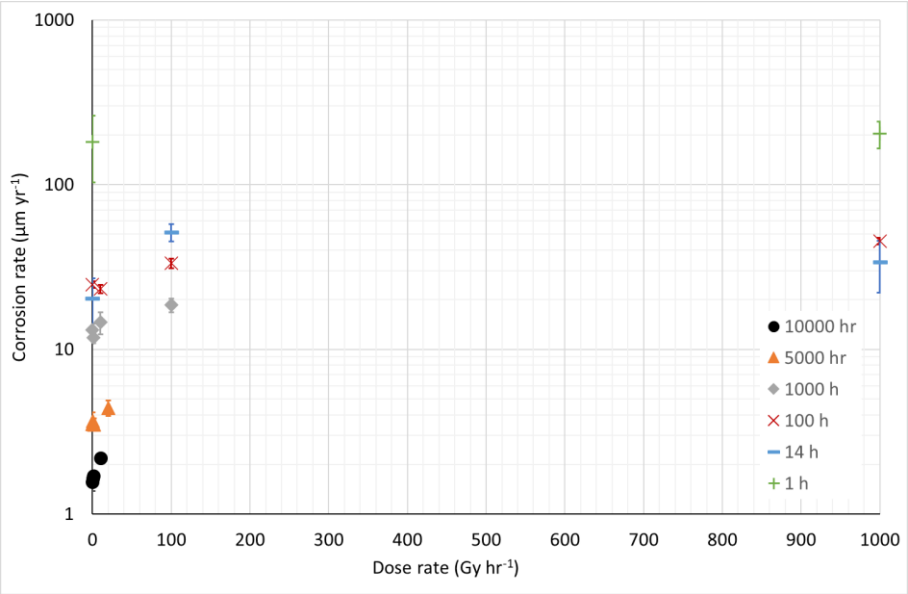

Figure 10. Carbon steel average corrosion rate expressed on a log scale versus dose rate for tests operated for durations of 1 to 10,000 hours. Error bars indicate the standard deviation between different specimens within the same test.

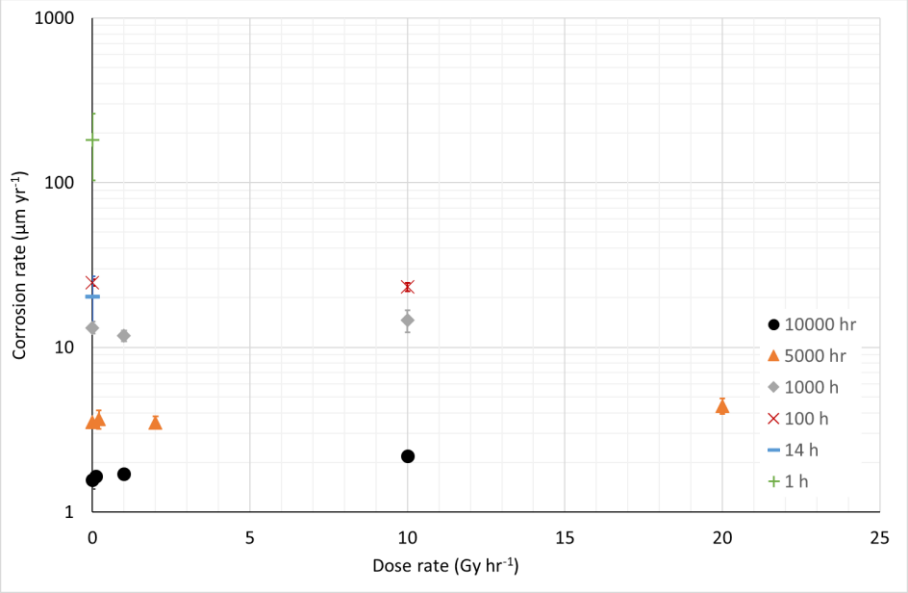

Figure 11. Carbon steel average corrosion rate expressed on a log scale versus dose rate for tests operated for durations of 1 to 10,000 hours. Data is repeated from Figure 10 but with the x-axis limited to 25 Gy hr^{-1} to better display the trend at lower dose rates. Error bars indicate the standard deviation between different specimens within the same test.

Post test analysis

A summary of the post-test visual appearance of the copper test coupons is given in Table 15 and example photographs of the test specimens are given in Bevas et al. (2024). In unirradiated conditions the coupons remained largely pristine for all test durations with only two exceptions. The first exception was specimen WC4-1#2, tested for 1,000 hours, which had one dark spot on the edge of the coupon

approximately 0.5 mm in diameter. The second exception was specimen WC6-1#5, which exhibited patches of black corrosion product on the surface after 10,000 hours. In both cases, the duplicate specimens that were also present in the test did not exhibit any visible corrosion products. Visual assessment of the extent of corrosion product on the surface of irradiated specimens indicated that it broadly correlated with the total dose received (i.e. it increased with both dose rate and duration of exposure to a similar extent). However, individual repeat specimens within a single test tended to show a wide variation in the extent of corrosion product present on the surface. Wrought and cold-sprayed copper generally exhibited a similar amount of corrosion, with the only exception being the results observed after 100 hours of testing at a dose rate of 10 Gy hr^{-1}, which showed the presence of black patchy corrosion product on the two cold-sprayed copper coupons but not on the four wrought copper coupons.

In general, the presence of radiation did not have a big impact on the visual appearance of the carbon steel specimens. The appearance of corrosion product on the surface of the specimens appeared to be dominated by the test duration, with all specimens exhibiting a complete coverage of black corrosion product at durations exceeding 1,000 hours irrespective of the degree of radiation exposure. At shorter durations the corrosion presented as either discontinuous patches of corrosion product or light tarnishing. Additionally, the extent of corrosion appeared to increase with increasing dose rate/total dose, but the effect was minimal.

Table 15. Overview of the visual observation of copper specimens exposed to radiation dose rates between 0.1 and 100 Gy hr^{-1} for total doses of 1, 10 and 100 kGy.

Dose Rate (Gy hr^{-1})	Total dose (kGy)		
	1	**10**	**100**
0.1	Majority of specimen surface appears pristine, some small black/brown corrosion product on some specimens		
0.2	Majority of specimen surface appears pristine, some small black/brown corrosion product on some specimens		
1	Majority of specimen surface appears pristine, some small black/brown corrosion product on some specimens	Specimens covered in a significant fraction of black/brown corrosion product	
10	CSC coupons exhibiting small amount of black/brown corrosion, WC coupons appear pristine	Specimens covered in a significant fraction of black/brown corrosion product	Specimens covered in brown/black corrosion product with small green sections on ends of samples
100		Specimens covered in a significant fraction of black corrosion product	Specimens covered in green corrosion product with some areas covered in brown/black corrosion product

Surface SEM-EDX showed that none of the copper samples exhibited any evidence of corrosion products in cross-section. A summary of observations made for carbon steel is shown in Table 16.

Table 16. Summary of results from cross-section SEM/EDX analysis spectroscopy analysis of carbon steel samples analysed. The total dose received in each condition is highlighted in bold.

Exposure Duration (hr)	Dose Rate (Gy hr^{-1})								
	0	0.1	0.2	1	2	10	20	100	1,000
1									**1 kGy** No oxide
14								**1 kGy** No oxide.	**10 kGy** One oxide particle observed on one analysis area.
100	**0 kGy** ~ 1 µm thick patchy oxide. Carbon found in corrosion layer.					**1 kGy** ~ 2 µm thick patchy oxide. Carbon found in corrosion layer.		**10 kGy** ~ 2 µm thick patchy oxide. Carbon found in corrosion layer.	**100 kGy** No oxide
1,000									
5,000	**0 kGy** ~ 6 µm thick continuous oxide layer.		**1 kGy** ~ 6 µm thick continuous oxide layer.		**10 kGy** ~ 6 µm thick continuous oxide layer.		**100 kGy** ~ 6 µm thick continuous oxide layer.		
10,000									

Raman spectroscopy was conducted on two wrought copper samples, one exposed for 100 hr at a dose rate of 10 Gy hr^{-1} and another for 5,000 hr at 0.2 Gy hr^{-1}. Both samples were exposed to a total dose of 1 kGy and Raman spectra of the 5,000 hr sample can be found in Bevas et al. (2024). The only identifiable peaks on wrought copper corresponded to cuprite, Cu_2O.

For carbon steel Raman spectra were obtained for samples exposed for 100h to a dose rate of 10, 100, and 1,000 Gy hr^{-1} (total doses of 1 kGy, 10 kGy, and 100 kGy respectively) in addition to 5,000h exposure samples exposed to 0.2 and 2 Gy hr^{-1} (1 kGy and 10 kGy respectively). It was found that siderite and goethite were present on all the samples analysed by Raman spectroscopy, but maghemite was also observed on the sample tested at 1,000 Gy hr^{-1} for 100 hr.

The XPS analysis was focused on wrought copper and carbon steel samples exposed for 100 hr. Wrought copper was only exposed to a dose rate of 10 Gy hr^{-1} at this duration and a mixture of copper metal and Cu_2O were identified on the surface indicating a thin copper (I) oxide film on the surface in the region of nanometres thick. A mixture of Fe(II) and Fe(III) oxidation state species were identified on all carbon steel samples. Fe_3O_4 was identified as the likely source of Fe(II) species however it could not be determined whether Fe_2O_3 or Fe(O)OH was the main source of Fe(III) species. Comparison of the Fe(III):Fe(II) ratios found Fe(III) species increased in proportion to Fe(II) species at higher dose rates.

For copper, XPS analysis of wrought copper exposed for 100 hr at a dose rate of 10 Gy hr^{-1} (WC3-6) was performed before and after depth profiling (DP). From analysis of the Cu XPS and peak shapes, it was concluded that there was a thin layer of Cu_2O on the copper substrate, only a few nm thick, which may have been pre-existing. There was also a small component of sulphide on the surface.

Carbon steel samples exposed for 100 hr at 10 (CS3-6), 100 (CS3-8) and 1,000 (CS3-9) Gy hr^{-1} were analysed with XPS including depth profiling. Table 17 shows the elemental composition of the samples' surface before and after depth profiling. A mixture of Fe_3O_4 and either Fe_2O_3 or Fe(O)OH were the dominant components in the Fe2p spectra of samples exposed to 10 Gy hr^{-1} (CS3-6#5B) and 1,000 Gy hr^{-1} (CS3-9#4B). The Fe(III):Fe(II) ratios of 10 Gy hr^{-1} and 1,000 Gy hr^{-1} samples were 1.4 and 3.3 respectively, indicating proportionately more Fe(III) species were formed at 1,000 Gy hr^{-1} compared to 10 Gy hr^{-1}.

Table 17. Surface composition for carbon steel specimens CS3-6#5B (100 hr exposure, 10 Gy hr^{-1} dose rate), CS3-8#4B (100 hr exposure, 100 Gy hr^{-1} dose rate), and CS3-9#4B (100 hr exposure, 1,000 Gy hr^{-1} dose rate), pre- and post-depth profile (DP).

Sample		Concentration at.%										
		C	O	Fe	Cu	N	Cl	Mn	Na	S	Ca	Ni
CS3-6#5B	Pre-DP	70.3	23.1	3.2	1.2	1.6	0.3	0.1	0.1	0.1	0.1	-
	Post-DP	19.2	47.0	31.6	0.3	0.1	-	0.6	0.7	0.1	0.3	0.1
CS3-8#4B	Pre-DP	49.9	41.2	6.3	1.3	0.1	0.1	0.1	0.2	0.4	0.3	-
	Post-DP	8.3	54.0	35.4	0.7	-	-	0.2	0.8	-	0.6	-
CS3-9#4B	Pre-DP	56.0	32.1	5.6	3.6	1.1	-	0.3	-	1.0	0.1	0.1
	Post-DP	13.9	34.6	49.8	1.2	-	-	0.4	-	-	0.1	-

General overview

For copper, which is typically immune (or very close to immunity) to corrosion under anoxic conditions due to its thermodynamic stability, the corrosion rate was significantly enhanced by gamma radiation even at low dose rates. When comparing the corrosion rate under radiation to the values obtained in unirradiated control tests (after 10,000 hr), gamma radiation led to an increase in corrosion rate from around 2 to 60 times when the dose rate was increased from 0.1 to 10 Gy hr^{-1}. Considering the range of dose rates anticipated for copper canisters of 0.2 to 0.8 Gy hr^{-1} in a GDF, the present data showed that corrosion rate depends on dose rate$^{0.94}$ in this range. However, it is anticipated that this dependence could differ significantly when the buffer material is present and for different geometries (e.g. that of a canister in a repository). When converted into an absolute rate, the increase in corrosion rate due to radiation was approximately 0.03 to 1.15 µm yr^{-1} for dose rates of 0.1 to 10 Gy hr^{-1}. Based on the relationship between dose rate and corrosion rate, if the corrosion rate in the presence of radiation does not attenuate appreciably with time, then it is expected that for a given total dose, a greater amount of RIC will occur if the dose is applied at a lower dose rate, within the range of dose rates investigated.

For carbon steel, an increase in the corrosion rate due to radiation could only be observed above a dose rate of 10 Gy hr^{-1} in the current test configuration. There may be an effect at lower dose rates that can't be resolved from the present data, owing to the higher corrosion rates and larger relative uncertainty of the carbon steel corrosion rates compared to copper. At a dose rate of 10 Gy hr^{-1} and an equivalent exposure duration, the increase in corrosion rate of carbon steel due to radiation was similar to that observed for copper, 0.90 µm yr^{-1} compared to 1.15 µm yr^{-1}, respectively. However, since carbon steel exhibits a considerably higher corrosion rate in unirradiated conditions compared to copper, the relative increase in corrosion rate due to radiation is much smaller, hence the lower enhancement factor observed for carbon steel. A further consideration is that the corrosion rate of carbon steel exhibits a high rate of attenuation that did not appear to occur for copper. The impact of longer exposure durations (leading to substantially lower average corrosion rates) is that it severely hinders the ability to directly compare the effect of applying the same dose at different dose rates on the corrosion rate.

Implications for accelerated testing

Testing the corrosion resistance of candidate canister materials in simulated repository environments is a complex issue. Due to the inherently long design life of the various canister designs, testing either has to be performed under realistic conditions for a duration that comprises a very small fraction of the design life, or under accelerated conditions in an attempt to capture the impact of processes that act over a longer timescale. A key facet of this is the impact of radiation on corrosion processes, namely the impact of radiation dose and dose rate. A strategy to attempt to simulate the influence of radiation-induced corrosion is to irradiate test specimens to a total dose that is close to the dose that would be received by a canister over its design life, but delivered at a greatly increased dose rate to enable the total dose to be delivered over a practical timeline. This approach invites a number of critical questions that must be answered in order to make use of these data when making corrosion assessments for canister materials in a GDF, namely:

- Will altering the dose rate at which a total dose is delivered alter the amount of radiation-induced corrosion that takes place, and if so in what way?
- Will altering the dose rate at which a total dose is delivered have an influence on other corrosion processes (e.g. oxide formation, water reduction)?

Based on the experimental results obtained in the present study, it is clear that the influence of dose rate on the magnitude of both the corrosion rate and the magnitude of the increase in corrosion rate that occurs in the presence of radiation is sub-linear over the range of conditions investigated. A minimum value of the dose rate at which an increase in corrosion rate was observed was 0.1 Gy hr^{-1} for copper and 10 Gy hr^{-1} for steel, respectively. If we consider a system where the corrosion rate is at a steady state, then there are several direct implications of this. Firstly, if the dose rate of interest is one

in which no effect of radiation on corrosion is observed, or there is an inhibiting effect, then performing a test at a higher dose rate that accelerates corrosion will produce an exaggeration in the extent of radiation-induced corrosion, even if the dose rates are applied to the same total dose. Secondly, if the dose rate of interest is at a level where an increase in corrosion is observed, then performing a test at a higher dose rate will diminish the increase in corrosion than is observed under radiation for a fixed dose. However, it should be noted that at dose rates higher than those studied here (i.e. 10 Gy hr^{-1} for copper), this trend may not hold due to other effects not considered (i.e. the influence of short-lived highly oxidising radicals at the metal surface). For a system that is not at steady state, such as for carbon steel, the situation is more complex and the influence of radiation on the rate of attenuation of corrosion must also be considered. If radiation does not influence the rate of attenuation in corrosion, then the above statements are also true for an unsteady system. However, if the presence of radiation increases or decreases the rate of attenuation in corrosion rate, then it is impossible to determine what the effect of accelerating the dose rate would be without detailed knowledge of how that influences the subsequent change in corrosion rate and or the chemistry of the system. From the surface analysis presented here, and elsewhere, there is evidence that the dose rate influences the chemistry of the corrosion product, particularly for carbon steel. If the latter was true, since in this system the corrosion resistance is partly derived by formation of a protective or semi-protective film, varying the dose rate will impact the corrosion rate in a complex way.

3.3.1.2 Results of the UJV test programme

Corrosion rate measurements

The corrosion rates derived from mass loss measurements indicated small variations in corrosion rate in the steel samples embedded in BCV (Bentonite Cerny Vrch) bentonite heated to 150°C and irradiated for 6, 9, 12 and 18 months (10.1±2.0 to 12.3±2.1 µm yr^{-1}) (Table 18). Unirradiated samples exhibited the highest corrosion rate after 6 months of thermal loading (24.3±2.2 µm yr^{-1}) and the corrosion rate decreased with loading time (13.3±1.6 to 18.0±1.9 µm yr-1). The samples embedded in BCV bentonite heated to 90 °C (both irradiated and unirradiated) exhibited the highest corrosion rates after 6 months' exposure (14.9±1.7 to 17.4±4.1 µm yr-1 (Figure 12). The lowest corrosion rates were observed in samples stored at laboratory temperature without any irradiation (Figure 12).

Table 18. Corrosion rates of steel samples. AVG – average, ± L – confidence interval of the Student's distribution at the significance level α = 0.05.

Cell no.	Bentonite	AVG	± L	Cell no.	Bentonite	AVG	± L
1	BCV	12.0	1.5	15	BCV	13.1	2.1
3	BCV	11.1	1.9	17	BCV	12.9	2.3
5	BCV	12.3	2.1	20	BCV	6.0	0.8
7	BCV	10.1	2.0	21	BCV	4.7	0.2
2	BCV	24.3	3.2	22	BCV	3.6	0.6
4	BCV	18.0	1.9	23	BCV	2.6	0.1
6	BCV	13.3	1.6	9	MX-80	17.2	0.3
8	BCV	17.5	1.1	10	MX-80	18.9	0.3
12	BCV	14.9	1.7	11	MX-80	2.2	0.1
14	BCV	11.7	1.8	18	MX-80	4.7	0.1
16	BCV	9.3	1.4	19	MX-80	4.5	0.7
13	BCV	17.4	4.1				

Different corrosion rates were observed when steel samples were embedded in MX-80 bentonite (Figure 13). The highest corrosion rates were observed when steel samples were embedded in MX-80 bentonite and heated to 150°C for 18 months (17.2±0.3 µm yr^{-1} and 18.9±0.3 µm yr^{-1} for irradiated and unirradiated samples, respectively). The steel samples embedded at MX-80 bentonite heated to 90°C for 18 months had lower corrosion rates (4.7±0.1 µm yr^{-1} and 2.2±0.1 µmyr^{-1} for irradiated and unirradiated cells, respectively), which are comparable to those of unheated samples (4.5 ± 0.7 µm yr^{-1}) (Figure 13).

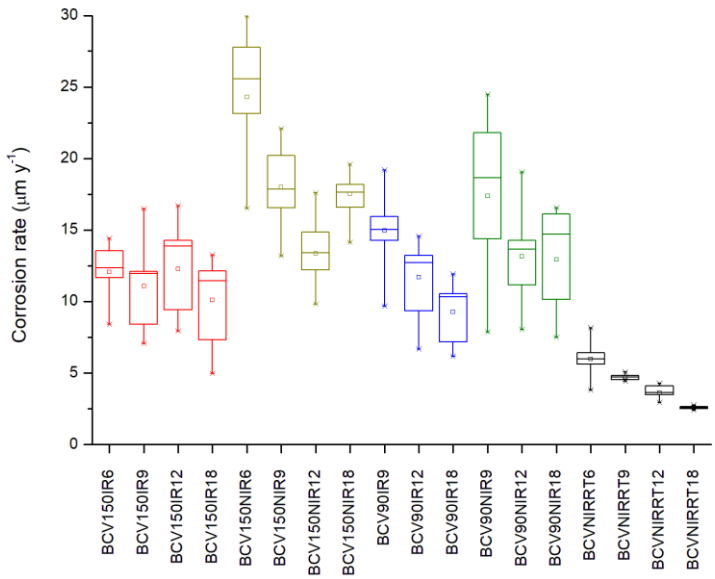

Figure 12. Corrosion rate of steel samples heated in BCV bentonite at 150°C (red – irradiated, dark yellow – unirradiated), 90°C (blue – irradiated, green – unirradiated) and at laboratory temperature (black). The exposure period is indicated by last 1-2 digits in the title of the samples (6, 9, 12 or 18).

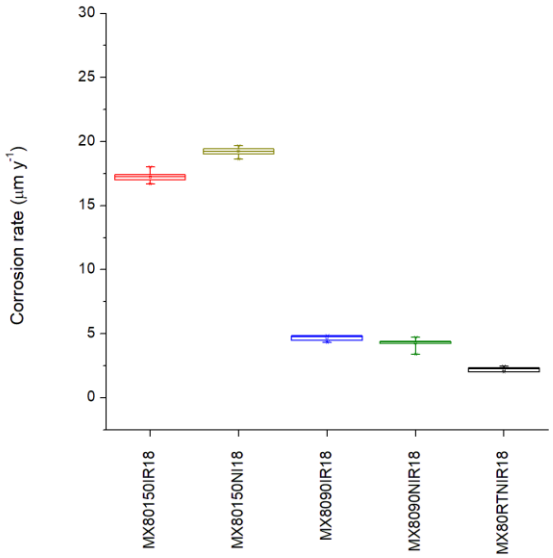

Figure 13. Corrosion rate of steel samples embedded in MX-80 bentonite heated to 150°C (red – irradiated, dark yellow – unirradiated), 90°C (blue – irradiated, green – unirradiated) and at laboratory temperature (black). The exposure period was 18 months.

The steel samples were embedded in bentonite in three layers in each cell and homogeneous saturation was targeted. Fully saturated cells exhibited very low confidence intervals (e.g. 0.1 μm yr^{-1}) but some cells (e.g. 2,3,15 and 17) exhibited higher corrosion rates in the two layers closest to the source of water and the samples located in the third outermost layer experienced the lowest corrosion rates and the largest confidence intervals. This behaviour is probably a reflection of the inhomogeneity of saturation.

Post test analysis

Light optical microscopy (LOM) analysis revealed the presence of surface depressions, which were approximately 25 to 30 μm deep and filled with corrosion products. The thickness of the corrosion layer varied from 10 to 45 μm and it was directly correlated with the exposure period. Irradiation and heating at 150°C led to the formation of thinner corrosion layers, typically ranging from 10 to 20 μm. A corrosion layer of a similar thickness (5 to 20 μm) was found in the unirradiated steel samples. More extensive corrosion layers (20 to 45 μm thick) were observed in the steel samples heated to 90°C and were unaffected by irradiation.

SEM-EDX analysis showed different compositions of corrosion products depending on the experimental temperature. At 90°C layers of Fe-oxide (Fe-oxy-hydroxide) and carbonates mixed with minerals originating in the bentonite were observed. On the other hand, the steel samples heated to 150°C contained: a layer composed of Fe-Si-O(OH) and a layer of carbonates mixed with minerals coming from bentonite. The formation of an Fe-Si-O(OH) layer was more obvious in samples heated to 150°C and irradiated.

Profilometry confirmed the occurrence of surface corrosion of the steel samples embedded in the BCV bentonite, based on the mean value and variation relative to the reference plane (Table 19). The mean value of the BLANK sample (Table 19) reflects the roughness of the surface related to the steel preparation and grinding prior to the experiment. Lower mean values of some steel samples (e.g., cells no. 1 to 5) compared to the BLANK steel sample reflect limitations of the profilometry analysis as well as surface smoothing due to corrosion (Table 19).

Table 19. Deviation from the reference mean value and variance from reference point based on profilometry.

Cell no.	Side A			Side B		
	Mean value (µm)	Standard mean deviation (µm)	Variation (µm²)	Mean value (µm)	Standard mean deviation (µm)	Variation (µm²)
1	0.00	3.35	11.24	n.a.	n.a.	n.a.
3	0.00	3.72	13.85	-0.02	4.21	17.74
5	0.16	4.95	24.46	0.18	4.54	20.61
2	0.02	3.29	10.85	n.a.	n.a.	n.a.
4	-0.03	4.43	19.59	0.08	4.21	17.71
6	0.36	4.76	22.63	0.03	5.51	30.33
12	0.28	5.54	30.66	1.15	8.64	74.65
14	-2.00	9.71	94.3	-0.64	6.73	45.25
13	-1.35	11.08	122.72	-0.46	8.13	66.07
15	-2.39	10.59	112.23	-1.11	9.31	86.67
22	0.24	4.01	16.05	0.49	3.98	15.82
BLANK	0.27	3.76	14.15	0.04	2.19	4.8

Corrosion of the steel sample embedded in BCV bentonite at laboratory temperature exhibited minor corrosion propagating along the initial surface inhomogeneities. Continuous corrosion was observed for all steel samples heated to 150°C and 90°C. After 12 months corrosion completely affected the steel surfaces. The most extensive corrosion occurred near the edges of the steel samples.

XRD analysis identified Magnetite and Fe-rich carbonates as the main corrosion products on steel samples embedded in BCV bentonite that were heated to 90°C and 150°C. Chukanovite and siderite were identified in all samples, confirming that anoxic conditions existed in the experiments. In all analyses, iron and minerals coming from the bentonite (i.e. montmorillonite, illite, quartz and calcite) were detected.

Bentonite characterisation

Analysis of BCV bentonite (Table 20) indicated an increased Fe_2O_3 content in all the samples and an increased content of MnO in heated samples. The main source of both species is believed to be the steel samples. The CaO content decreased rapidly after 6 months in all heated samples and returned to its original values after 12 months of heating up at 150°C. A continuous decrease of CaO content was observed in bentonite heated to 90°C. The MgO content decreased in all heated samples for the whole exposure period. An increase in K_2O content indicated possible smectite illitisation.

The chemical composition of water leachates of BCV_input bentonite and bentonite heated to 90°C and 150°C indicates prevailing Na-HCO_3 type (Table 21). The concentration is dependent on the solid-to-liquid (s:l) ratio. A significant effect of both temperature and irradiation on the concentration of water leachable species was observed.

Thermal loading at 150°C decreased the concentration of water leachable Na^+, K^+ and Mg^{2+} and slightly increased the concentration of Ca^{2+} and Cl^-. Only a minor effect was observed for SO_4^{2-} in unirradiated BCV bentonite. Thermal loading at 90°C decreased the concentration of water leachable Na^+ and Mg^{2+} and slightly increased the concentration of K^+, Ca^{2+}, Cl^- and SO_4^{2-}. Only a minor effect was observed on Mg^{2+} and the concentration of HCO_3^- decreased in all heated samples. Irradiation was found to

decrease the concentration of water leachable Na^+, Ca^{2+}, Cl^- and SO_4^{2-}. No effect of irradiation was observed on K^+, Mg^{2+} and HCO_3^-.

Table 20. Chemical composition of BCV bentonite heated to 150°C (150), 90°C (90) and at ambient temperature (RT), irradiated (IR) or unirradiated (NIR) (in wt%). The data were recalculated to give 0.00 wt% of loss of ignition.

Bentonite no.	BCV_IN	BCV-150-IR-6	BCV-150-IR-9	BCV-150-IR-12	BCV-150-NIR-6	BCV-150-NIR-9	BCV-150-NIR-12	BCV-90-IR-9	BCV-90-IR-12	BCV-90-NIR-9	BCV-90-NIR-12	BCV-RT-NIR-6	BCV-RT-NIR-9	BCV-RT-NIR-12
Na_2O	0.35	0.42	0.40	0.35	0.42	0.39	0.42	0.33	0.33	0.35	0.33	0.32	0.31	0.28
MgO	3.34	3.24	3.27	3.02	3.32	3.20	3.13	3.27	3.22	3.29	3.23	3.30	3.28	3.25
Al_2O_3	20.31	19.47	19.00	18.80	19.05	19.08	18.73	19.10	18.92	19.18	18.93	19.31	19.38	19.01
SiO_2	54.44	55.13	54.99	54.34	54.64	54.54	54.19	54.22	54.42	54.09	54.47	54.60	54.91	54.82
P_2O_5	0.56	0.58	0.56	0.62	0.57	0.58	0.60	0.54	0.58	0.55	0.57	0.54	0.54	0.59
SO_3	0.04	0.07	0.06	0.08	0.06	0.06	0.12	0.07	0.09	0.08	0.10	0.07	0.07	0.08
K_2O	1.04	1.12	1.18	1.18	1.14	1.20	1.17	1.15	1.15	1.14	1.15	1.19	1.18	1.17
CaO	3.29	3.15	3.18	3.28	3.16	3.20	3.32	3.17	3.09	3.12	3.09	3.17	3.14	3.18
TiO_2	2.92	2.64	2.71	3.02	2.61	2.86	3.00	2.96	3.03	3.07	2.94	2.93	2.83	3.05
V_2O_5	0.05	0.04	0.00	0.00	0.03	0.00	0.00	0.00	0.00	0.00	0.00	0.00	0.00	0.00
Cr_2O_3	0.07	0.08	0.08	0.09	0.09	0.08	0.08	0.08	0.08	0.08	0.08	0.08	0.08	0.08
MnO	0.21	0.23	0.22	0.24	0.24	0.25	0.26	0.23	0.23	0.22	0.23	0.20	0.20	0.26
Fe_2O_3	13.19	13.46	13.97	14.78	14.16	14.41	14.83	14.42	14.71	14.48	14.72	14.14	13.91	14.04
Co_2O_3	0.01	0.01	0.01	0.01	0.01	0.01	0.01	0.01	0.01	0.01	0.01	0.01	0.01	0.01
NiO	0.02	0.03	0.03	0.03	0.03	0.03	0.03	0.03	0.03	0.03	0.03	0.03	0.03	0.03
BaO	0.08	0.23	0.24	0.05	0.31	0.00	0.00	0.13	0.00	0.19	0.00	0.00	0.00	0.04
Others	0.08	0.10	0.12	0.11	0.16	0.12	0.11	0.30	0.11	0.12	0.12	0.12	0.12	0.12

Bentonite no.	BCV_IN	BCV-150-IR-6	BCV-150-IR-9	BCV-150-IR-12	BCV-150-NIR-6	BCV-150-NIR-9	BCV-150-NIR-12	BCV-90-IR-9	BCV-90-IR-12	BCV-90-NIR-9	BCV-90-NIR-12	BCV-RT-NIR-6	BCV-RT-NIR-9	BCV-RT-NIR-12
Total	100	100.	100	100	100	100	100	100	100	100	100	100	100	100
LOI	15.95	23.50	20.70	8.02	20.20	18.70	10.30	19.20	9.37	19.20	9.66	18.70	19.50	9.51

Table 21. Concentration of water leachates in BCV_input and BCV heated to 150°C (150), 90°C (90), ambient temperature (RT), irradiated (IR) and unirradiated (NIR).

Sample no.	s:l (g/L)	Na^+	K^-	Ca^{2+}	Mg^{2+}	Fe^{x+}	Cl^-	SO_4^{2-}	NO_3^-	F^-	HCO_3^-
BCV_input	25.18	1.41	0.13	0.06	0.11	bdl	0.01	0.06	bdl	0.03	1.73
	114.03	3.80	0.26	0.10	0.23	bdl	0.03	0.25	bdl	0.09	4.19
	201.94	4.95	0.33	0.13	0.29	bdl	0.05	0.44	bdl	0.10	5.17
BCV150 IR6	23.82	1.51	0.12	0.04	0.03	bdl	0.04	0.09	bdl	bdl	1.54
	115.97	3.14	0.16	0.06	0.04	bdl	0.10	0.29	bdl	bdl	2.81
	209.18	4.09	0.20	0.10	0.05	bdl	0.16	0.45	bdl	bdl	3.52
BCV150 NIR6	23.55	1.56	0.12	0.05	0.02	bdl	0.04	0.11	bdl	bdl	1.57
	113.39	3.36	0.18	0.08	0.03	bdl	0.12	0.28	bdl	bdl	3.06
	203.69	4.47	0.22	0.12	0.03	bdl	0.20	0.43	bdl	bdl	3.93
BCV150 IR9	118.10	2.73	0.22	0.06	0.04	bdl	0.06	0.28	bdl	bdl	2.56
BCV150 NIR9	22.67	1.31	0.14	0.04	0.02	bdl	0.05	0.10	bdl	bdl	1.32
	113.22	2.64	0.19	0.07	0.02	bdl	0.11	0.27	bdl	bdl	2.36
	203.12	3.50	0.22	0.11	0.02	bdl	0.13	0.38	bdl	bdl	3.09
BCV150 IR12	21.82	1.17	0.15	0.07	0.03	bdl	0.01	0.08	bdl	bdl	1.36
	109.75	2.76	0.22	0.11	0.04	bdl	0.03	0.21	bdl	bdl	2.82
	196.70	3.41	0.23	0.13	0.04	bdl	0.06	0.30	bdl	bdl	3.31
BCV150 NIR12	21.93	1.50	0.14	0.07	0.02	bdl	0.08	0.11	0.04	bdl	1.48
	109.47	3.46	0.21	0.10	0.03	bdl	0.07	0.28	bdl	bdl	3.28
	196.60	4.64	0.25	0.16	0.04	bdl	0.16	0.42	bdl	bdl	4.30
BCV90IR9	117.54	3.20	0.29	0.11	0.21	bdl	0.11	0.31	bdl	bdl	3.39
BCV90NIR9	119.87	3.19	0.26	0.11	0.19	bdl	0.14	0.42	bdl	bdl	3.06
BCV90IR12	22.81	1.29	0.20	0.08	0.13	bdl	0.02	0.09	bdl	bdl	1.72
	107.29	3.16	0.25	0.11	0.19	bdl	0.13	0.29	bdl	bdl	3.29
	194.58	4.05	0.38	0.15	0.27	bdl	0.19	0.45	bdl	bdl	4.16
BCV90NIR12	22.89	1.18	0.20	0.08	0.14	bdl	0.07	0.12	bdl	bdl	1.53
	108.48	3.04	0.33	0.11	0.21	bdl	0.18	0.33	bdl	bdl	3.18
	194.33	4.30	0.40	0.17	0.29	bdl	0.30	0.52	bdl	bdl	4.27
BCVRTNIR6	116.32	2.91	0.39	0.11	0.27	bdl	0.05	0.26	bdl	bdl	3.49
BCVRTNIR9	22.77	1.19	0.25	0.10	0.22	bdl	0.04	0.11	bdl	bdl	1.83
	112.12	2.86	0.39	0.11	0.29	bdl	0.05	0.26	bdl	bdl	3.51
BCVRTNIR12	22.03	1.11	0.28	0.12	0.24	bdl	0.02	0.10	bdl	bdl	1.88
	107.87	3.03	0.49	0.16	0.37	bdl	0.01	0.19	bdl	bdl	4.18
	194.91	4.26	0.53	0.20	0.50	bdl	0.02	0.28	bdl	bdl	5.64

General Overview

Irradiation was found to decrease the corrosion rate of steel samples in BCV bentonite at both test temperatures (150°C and 90°C), based on both mass loss measurements and profilometry analysis. A similar trend was observed in MX-80 bentonite heated to 150°C. A very minor effect of irradiation on steel corrosion was observed in MX-80 bentonite heated to 90°C.

Fe-oxy-hydroxide and Fe-carbonates were identified on steel-BCV bentonite surfaces heated to 90°C. An Fe-Si-O(OH) layer was found on samples heated to 150°C. Minimal effect of radiation on the composition of corrosion products was found.

The thickness of the corrosion layer correlated well with the duration of the exposure period. More extensive and thicker layers were identified on steel samples heated to 90°C and this cab attributed to the higher degree of saturation and the higher water content of the bentonite, which can facilitate formation of corrosion products. With regard to the BCV bentonite parameters, irradiation decreased the content of CaO and MgO, and the concentration of water leachable Na^+, Ca^{2+}, Cl^- and SO_4^{2-}. No effect of irradiation was observed on water leachable K^+, Mg^{2+} and HCO_3^-.

Summary and conclusions of UJV testing

The steel samples embedded in the BCV bentonite heated to 150°C suffered a lower corrosion rate when irradiated, compared to unirradiated. The thickness of the surface corrosion products identified on irradiated samples heated to 150°C indicated an almost constant corrosion rate for the whole testing period. Unirradiated samples heated to 150°C showed the highest corrosion rate after 6 months with a decreasing corrosion rate after 18 months' exposure. The decreasing corrosion rate observed in both irradiated and unirradiated steel samples heated to 90°C correlated with an increasing exposure period. Particularly low corrosion rates were found on steel samples embedded in water-saturated BCV bentonite stored at laboratory temperature without irradiation. An inhibiting effect of irradiation on steel corrosion was observed when the steel samples were embedded in MX-80 bentonite heated to 150°C. Almost no effect was observed when the MX-80 bentonite was heated to 90°C.

Longer exposure periods led to the formation of a larger amount of corrosion products, which facilitated their identification. Haematite and Fe-rich carbonates (chukanovite, $Fe_2(CO_3)(OH)_2$ and siderite, $FeCO_3$) were identified in the corrosion layers on the steel surface. The thickness of the corrosion layer varied, ranging from 10 to 45 µm, and was directly correlated with the exposure period. Unirradiated steel samples heated to 90°C developed corrosion product layers up to 45 µm thick after 12 months. In contrast, irradiation and heating at 150°C led to the formation of thinner corrosion layers, typically ranging from 10 to 20 µm thick. A corrosion layer composed of amorphous or poorly crystalline Fe-Si-O was identified on the surface of steel heated at 150 °C. The origin of the Fe-Si-rich layers needs to be confirmed by future research.

3.3.2 Subtask 3.2: Irradiation under repository conditions

3.3.2.1 Results of the Subatech test programme

Corrosion rate measurements and surface analysis

The detailed results from this task are presented in Sarrasin et al. (2024). Although measurements were made of the amount of hydrogen generated in the test cells it was not possible to derive reliable corrosion rate data form these experiments. However, corrosion rates were derived from mass loss measurements and the results are summarised in Table 22 for the experiments with steel only and no bentonite. The results from the reference sample experiments (i.e. without irradiation) are shown in Table 23. The results of the steel corrosion experiments (i.e. without bentonite) under irradiation are plotted in Figure 14.

The results of steel corrosion in contact with bentonite as a function of RH and time (and hence total dose) are given in Table 24. The experiments were conducted between 7 and 39 days at room temperature. The total dose was between 50 and 400 kGy. As with the experiments using steel alone, it is noticeable that the highest corrosion rate was encountered for experiments at the lowest RH of 63%. Also, the corrosion rate decreased with increasing time for all the experiments (Figure 15 and Figure 16). Figure 16 clearly shows that, as with the experiments using the steel alone, the corrosion

rate at the lowest RH value of 63% was very high compared to experiments at the highest RH value (i.e. 100%).

SEM analysis found a thick layer of corrosion product. For the experiments conducted at ambient atmosphere without RH control, XRD analysis identified the major corrosion products as being magnetite (Fe_3O_4), siderite ($FeCO_3$), goethite (FeOOH) and akaganeite (beta β-$Fe^{3+}O(OH,Cl)$), and to a lesser extent chukanovite ($Fe_2(CO_3)(OH)_2$), under near saturation conditions (99%) together with haematite. The XRD results for steel coupons in atmospheric conditions, and for steel In contact with bentonite, are summarised in Table 25 and Table 26 respectively.

Table 22. Corrosion experiments of steel coupons without bentonite under different experimental conditions (RH, time, and dose).

Sample		Relative Humidity (%)	Total Dose (kGy)	Irradiation time (days)	Corrosion rate (µm yr^{-1})	Error of Corrosion Rate (µm yr^{-1})	Error in Percentage
L	19	Ambient	50	7	24.2	2.3	10%
F	46		100	10	23.2	2.3	10%
F	33	63	50	7	426.9	2.4	1%
F	40		100	10	290.9	4.0	1%
F	18		200	21	247.3	1.8	1%
F	23		400	39	232.5	0.5	0%
F	37	76	50	7	32.2	3.8	12%
F	42		100	10	35.0	3.8	11%
F	20		200	21	33.7	1.1	3%
F	72		400	39	16.2	0.6	4%
F	38	99	50	7	170.3	2.3	1%
F	45		100	10	14.1	2.3	16%
F	21		200	21	1.5	1.7	119%
F	74		400	36	10.6	0.7	6%

Table 23. Reference corrosion experiments of steel.

Sample		Temperature (°C)	Relative Humidity (%)	Irradiation time equivalent (days)	Corrosion rate (µm/year)	Error of Corrosion Rate (µm/year)	Error in Percentage
F	90	25	63	26	0	-	-
F	92	25	99	26	1.02	0.90	88%

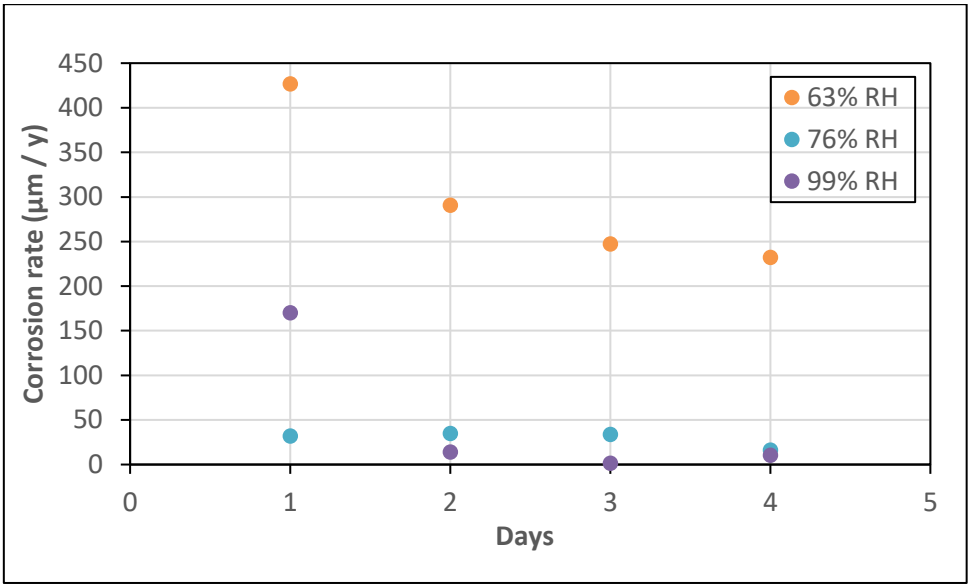

Figure 14. Corrosion rate of steel coupons, in the absence of bentonite and hydrated at 25°C and different RH values as a function of time. In the presence of radiation at a dose rate of 400 Gy hr^{-1}.

Table 24. Corrosion experiments of steel coupons in contact with bentonite under different experimental conditions (RH, time, and dose).

Sample		Relative Humidity (%)	Total Dose (kGy)	Irradiation time (days)	Corrosion rate (µm/year)	Error of Corrosion Rate (µm/year)	Error in Percentage
F	10	63	50	7	107.3	5.1	5%
F	1		100	12	129.0	3.1	2%
F	48		200	21.5	52.3	1.7	3%
F	31		400	39	29.5	0.9	3%
F	12	76	50	7	21.0	5.5	26%
F	58		100	14	59.0	2.7	5%
F	50		200	21.5	18.2	1.7	9%
F	27		400	39	6.4	0.9	8%
F	15	99	50	7	39.4	5.5	14%
F	60		100	14	58.0	2.7	11%
F	54		200	21.5	10.1	1.8	18%
F	29		400	39	28.0	1.0	2%
F	76	H_2O (~100%)	200	21	2.6	1.7	67%

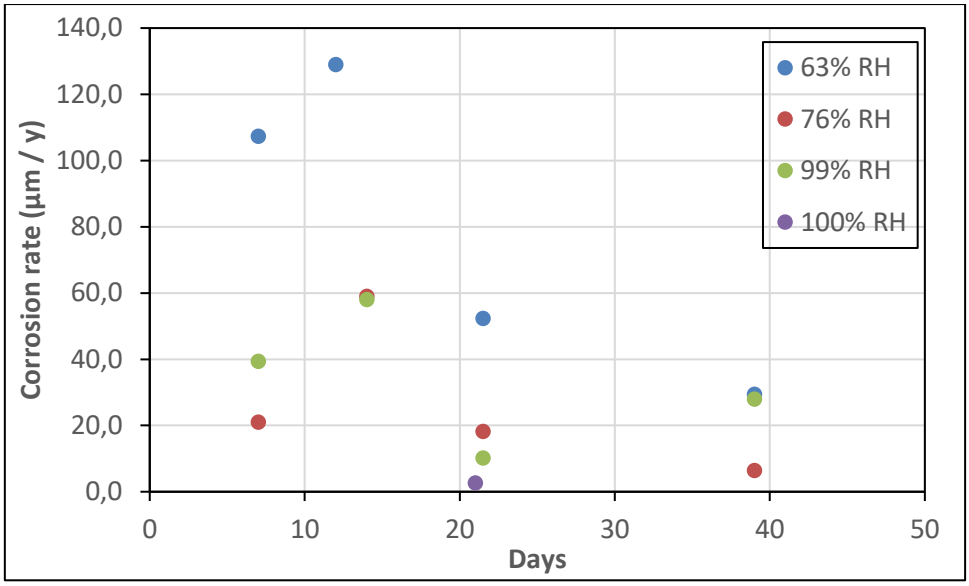

Figure 15. Corrosion rate of steel coupons in contact with bentonite hydrated at 25°C and different RH as a function of time.

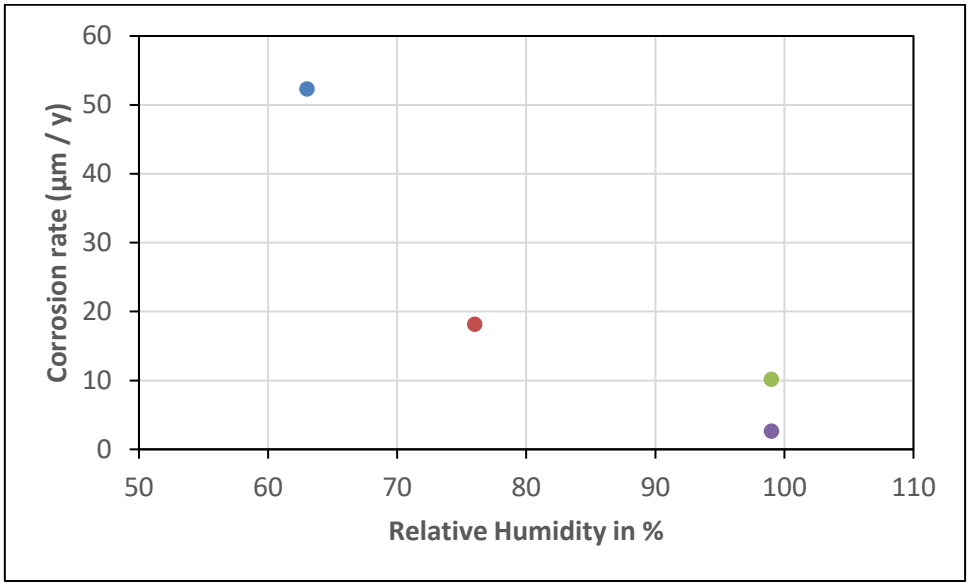

Figure 16. Corrosion rate of steel coupons in contact with bentonite hydrated at 25°C for 21 days and different RH.

Table 25. Corrosion products formed in experiments with steel coupons under different experimental conditions (RH, time, and dose).

Sample		Relative Humidity (%)	Total Dose (kGy)	**Phases** **M:** Major phase (> 5%) **m:** minor phase (< 5%) **tr:** trace (<1%)
L	19	Ambient	50	Undetected
F	46	Ambient	100	Undetected
F	33	63	50	Siderite 12.9% (M), Goethite: 7.1% (M), Magnetite: 8.4% (M), Iron: 71.6% (M)
F	40	63	100	Akaganeite: 13.1% (M), Goethite: 19.1% (M), Fougerite: 10.8 (M), Magnetite: 12.9% (M), Siderite: 6.7% (M), Ferrihydrite: 24.8% (M), Fe0.8Mn0.2 4.6% (m), Iron: 8.1% (M)
F	18	63	200	Goethite: 12.6% (M), Siderite: 15.5% (M), CSi: 49.3% (M), Ferohyxyte: 16.2% (M), Iron: 6.4% (M)
F	23	63	400	Goethite: 14.1% (M), Siderite: 16.6% (M), Magnetite: 8.4% (M), CSi: 54% (M), Fe0.8Mn0.2: 5.2% (M), Iron: 1.7% (m)
F	37	76	50	Akaganeite: 5.7% (M), Goethite: 2.4% (m), Magnetite: 1.3% (m), Iron: 90.6% (M)
F	42	76	100	Goethite: 4.7% (m), Magnetite: 6.8% (M), Siderite: 8.1% (M), Iron: 80.3% (M)
F	20	76	200	Akaganeite: 17.4% (M), Calcite: 3.7 (m), Iron: 78.9% (M)
F	72	76	400	Goethite: 16.9% (M), Magnetite: 3.1% (m), Iron: 79.9% (M)
F	38	99	50	Not detected any phases
F	45	99	100	Akaganeite: 1.5% (m), Siderite: 1.1% (m), Iron: 97.4%
F	21	99	200	Goethite: 1.6% (m), Hematite: 0.4 (tr), Iron: 97.9% (M)
F	74	99	400	Chukanovite: 6.8% (M), Magnetite: 1.3% (m), Siderite: 0.9% (tr), Goethite: 2.1% (m), Iron: 88.9% (M)

Table 26. Corrosion products formed in experiments with steel coupons in contact with bentonite under different experimental conditions (RH, time, and dose).

Sample		Relative Humidity (%)	Total Dose (kGy)	**Phases** **M:** Major phase (> 5%) **m:** minor phase (< 5%) **tr:** trace (<1%) **Atm**: atmospheric side **Clay**: side in contact with bentonite
F	10	63	50	**Atm**: Magnetite: 4.8% (m), Siderite: 3.0% (m), Calcite: 23.1% (M), Xifengite?: 2.2% (m), Iron: 66.9% (M) **Clay**: Magnetite: 0.5% (tr), Calcite: 0.4% (tr), Montmorillonite: 1.3% (m), Iron: 97.7% (M)
F	1	63	100	**Atm**: Goethite: 12.3% (M), Siderite: 11% (M), Magnetite: 7.2% (M) **Clay**: Goethite: 1.2% (m), Magnetite: 0.4% (tr), Calcite: 0.6% (tr), Montmorillonite: 1.8% (m), knife: 29.2% (M), Iron: 66.9% (M)
F	56	63	100	**Atm**: Siderite: 5.8% (M), Magnetite: 5.4% (M), Xifengite?: 5.6% (M), Lepidocrocite: 5.1% (M), CSi: 34.3% (M), Ringwoodite?: 6.2% (M), Iron: 37.5% (M) **Clay**: Magnetite: 1.1% (m), Montmorillonite: 2.7% (m), Magnesium Calcite: 31% (M), Iron: 65.2% (M)
F	48	63	200	**Atm**: Magnetite: 1.4% (m), Iron: 98.6% (M) **Clay**: Magnetite: 1.2% (m), Magnesium Calcite: 6.2% (M), Montmorillonite: 2.2% (m), Fe0.5Mg1.5O5: 2.3% (m), Iron: 88.1% (M)
F	31	63	400	**Atm**: Calcite: 7.2% (M), Goethite: 16% (M), Siderite: 34.8% (M), Akaganeite: 13.7% (M), Xifengite?: 4.5% (m), Iron: 23.8% (M) **Clay**: Calcite: 2.4% (m), Iron: 97.6%
F	12	76	50	**Atm**: Magnetite: 0.7% (tr), Akaganeite: 2.3% (m), Magnesium Calcite: 4.7% (m), Iron: 92.3% (M) **Clay**: Almost nothing detected, Magnetite: 0.4% (tr), Iron: 99.6% (M)
F	4	76	100	**Clay**: Magnetite: 0.5% (tr), Calcite: 1.9% (m), Iron: 97.6% (M)
F	58	76	100	**Atm**: Siderite: 8.6% (M), Magnesium Calcite: 30.2% (M), Akaganeite: 8.7% (M), Montmorillonite: 1.4% (m), Iron: 51.1% (M) **Clay**: Akaganeite: 6.8% (M), Calcite: 1.5% (m), Magnetite: 1.4% (m), Akermanite: 9.2% (M), Pigeonite: 3.6% (m), Siderite: 2.8% (m), Iron:74.8% (M)
F	50	76	200	**Atm**: Goethite: 3.3% (m), Calcite: 11.1% (M), Akaganeite: 6.2% (M), Magnetite: 1.5% (m), Siderite: 0.8% (tr), Cronstedtite: 3.2% (m) Iron: 73.9% (M) **Clay**: Siderite: 3.7% (m), Akaganeite: 6.7% (M), Calcite: 0.9% (tr), Montmorillonite: 2.1% (m), Iron: 86.5% (M)

Sample		Relative Humidity (%)	Total Dose (kGy)	**Phases** **M:** Major phase (> 5%) **m:** minor phase (< 5%) **tr:** trace (<1%) **Atm**: atmospheric side **Clay**: side in contact with bentonite
F	27	76	400	**Atm**: Goethite: 5.4%, Calcite: 1.4% (m), Iron: 93.2% (M) **Clay**: Siderite: 2.2% (m), Goethite: 0.8% (tr), Akaganeite: 2% (m), Magnesium Calcite: 3.2% (m), Montmorillonite: 2% (m), Iron: 89.8% (M)
F	28	76	400	**Atm**: Goethite: 6.6% (M), Iron: 93.4% **Clay**: Nothing detected, unidentified peak at 31.518 (very small)
F	15	99	50	**Atm**: Goethite: 2% (m), Iron: 98% (M) **Clay**: Goethite: 1.1% (m), Calcite: 1.6% (m), Montmorillonite: 1.1% (m), Iron: 95.1% (M)
F	8	99	100	**Clay**: Goethite: 3.2% (m), Calcite: 1.3% (m), Montmorillonite: 1.4% (m), Iron: 94.1%
F	9	99	100	**Clay**: Goethite: 7.6% (M), Calcite: 2.1% (m), Montmorillonite: 1.7% (m), Iron: 88.7% (M)
F	60	99	100	**Atm**: Goethite: 1.3% (m), Akaganeite: 3.1% (m), Lepidocrocite: 0.6% (tr), Montmorillonite: 3.1% (m), Calcite: 1.7% (m), Linzhiite?: 0.9% (tr), Chukanovite: 3.6% (m), Iron: 85.8% (M) **Clay**: Siderite: 5.2% (M), Akaganeite: 3.7% (m), Goethite: 1.1% (m), Magnesium Calcite: 1.6% (m), Lepidocrocite: 1% (tr), Chukanovite: 3.6% (m), Linzhiite?: 0.8% (tr), Iron: 78.2% (M)
F	54	99	200	**Atm**: Siderite: 1.6% (m), Hematite: 0.5% (tr), Ulvospinel: 0.8% (tr), Linzhiite: 0.5% (tr), Iron: 96.7% (M) **Clay**: Magnesium Calcite: 3.4% (m), Siderite: 11.4% (M), Lepidocrocite: 0.6% (tr), Goethite: 0.8% (tr), Chukanovite: 3.6% (m), Linzhiite?: 1% (m), Iron: 72.1% (M)
F	52	99	400	**Atm**: Goethite: 1.1%, Siderite: 6.5% (M), Lepidocrocite: 1.4% (m), Chukanovite: 8.6% (M), Magnetite: 0.5% (tr), Magnesium Calcite: 2.1% (m), Iron: 79.8% (M) **Clay**: Siderite: 14.5% (M), Linzhiite: 1.2% (m), Calcite: 5.3% (M), Magnetite: 1.0% (tr), Lepidocrocite: 1.5% (m), Akaganeite: 3.3% (m), Iron: 73.2% (M)
F	30	99	400	**Atm**: Siderite: 10.7% (M), Goethite: 5.0% (M), Lepidocrocite: 2% (m), Magnetite: 2.8% (m), Iron: 79.4% **Clay**: Siderite: 11.1% (M), Goethite: 4.5% (m), Calcite: 4.3% (m), Iron: 80.1% (M)
F	29	99	400	**Atm**: Goethite: 1.5% (m), Calcite: 5.8% (M), Iron: 92.7% **Clay**: Magnetite: 1.1% (m), Calcite: 6.2% (M), Siderite: 6.5% (M), Montmorillonite: 2.8% (m), Quartz: 2.2% (m), Iron: 81.2 % (M)

Sample		Relative Humidity (%)	Total Dose (kGy)	Phases **M:** Major phase (> 5%) **m:** minor phase (< 5%) **tr:** trace (<1%) **Atm**: atmospheric side **Clay**: side in contact with bentonite
F	76	H2O (~100%)	200	**Atm**: Siderite: 2.4% (m), Montmorillonite: 1.4% (m), Ferrihydrite: 1.1% (m), Linzhiite: 0.8% (tr), Birnessite: 0.8% (tr), Iron: 93.4% (M) **Clay**: Calcite: 3% (m), Siderite: 1.4% (m), Goethite: 0.6% (tr), C6Co0.7Fe0.3KN6Ni: 1.0% (tr), Montmorillonite: 2% (m), Iron: 92.1% (M)

Discussions and conclusions from Subatech test programme

Radiolysis of water leads to the formation of a number of oxidising species, such as $OH^{\bullet}$ radicals or H_2O_2 molecules, which can lead to iron oxidation to Fe^{2+} and further to Fe^{3+}. Hence, even under deaerated conditions Fe^{3+}-based corrosion products (e.g. goethite) were frequently identified on the steel corroded at 63%, 76% and 99% RH. An important result to highlight is that the highest corrosion rate was obtained at the lowest RH value of 63%. This can be explained by the enhanced release of H_2 from the very thin layer of water at the steel (solid) interface, about 2-3 layers of H_2O as indicated by Ebert et al. (1991). Hydrogen fast release inhibits the reaction of its recombination with $OH^{\bullet}$ radicals as shown in the following equation:

$$2\,H_2 + 2OH^{\bullet} + O_2 \rightarrow 2\,H_2O + H_2O_2$$

The inhibition of the reaction consuming $OH^{\bullet}$ radicals ensures that they remain available for interaction with the steel surface and the formation of magnetite Fe_3O_4 (containing Fe^{2+}), and ultimately goethite FeOOH (containing Fe^{3+}). This hypothesis is supported by the results of the H_2 production measurements as a function of RH. In fact, the highest production rate of H_2 was observed in the experiments with the lowest humidity 63%, and decreased with increasing RH from 63% to 76% and then to 99%.

3.3.2.2 Results from Ciemat Test programme

Irradiated powder materials

The XRD patterns measured on unirradiated samples confirmed the phase of all selected oxides: CuO, Cu_2O, Fe_2O_3, Fe_3O_4 and α-FeOOH. After irradiation at 66 Gy hr^{-1} to give a cumulative dose of 14 kGy, the oxide structure of all analysed Cu(I), Cu(II), Fe(II) and Fe(III) materials was unaltered by radiation. This result was also confirmed by FT-IR and Raman spectroscopies.

Measurements of zeta potential, the point of zero charge and potentiometric titrations found some differences in the zeta potentials on the oxides irradiated to 14 kGy at 66 Gy hr^{-1} and to 140 kGy at 697 Gy hr^{-1}), which may affect the ability of irradiated oxides to retain different radionuclides, but this aspect requires further research.

As for the irradiated powder oxides, XRD analysis, FTIR analysis and zeta potential measurements of irradiated bentonite did not detect any change in the bentonite mineralogy. This indicates that the FEBEX bentonite is very stable at the γ-radiation doses applied.

Metal corrosion in different bentonite porewaters

Table 27 shows the results of corrosion rates determined from mass loss measurements after cleaning the specimens, after 12 days of experiment. The corrosion rates were much higher for the carbon steel than the Cu-OFP. Cu-OFP experienced greater alteration when irradiated compared to unirradiated, but the difference between samples irradiated to 14 kGy and 140 kGy were small, despite the 10× higher dose, suggesting an inhibiting effect at higher radiation dose. After cleaning most of the copper discs regained their initial appearance, indicating little corrosion damage.

In the absence of radiation, the corrosion rate of Cu-OFP was around ~3 µm yr^{-1}, but after γ-irradiation exposure to 14 kGy and 140 kGy, the corrosion rates were ~49 and 25 µm yr^{-1}, respectively. This substantial increase in corrosion rate in the presence of radiation is consistent with the general observations reported in the tests performed by Jacobs (Bevas et al, 2024, Section 3.3.1).

Most of the carbon steel discs were covered by an orange layer, which is attributed to a mixture of Fe(III) oxides, mainly haematite. After cleaning, the surface of the carbon steel discs was still damaged by corrosion. The corrosion rates of carbon steel immersed in porewater were higher in the PW-1.6, which had a higher NaCl content (Table 17). Unirradiated sample corrosion rates were lower than irradiated, but similar corrosion rates were measured for carbon steel immersed in porewaters after gamma-irradiation exposure to 14 and 140 kGy.

Table 27. Corrosion rate determined for Cu-OFP and carbon steel discs, immersed in 5 ml of various bentonite porewaters and deionised water. Samples were unirradiated, or irradiated to a dose of 14 kGy or 140 kGy. Corrosion rates were derived from mass loss measurements after 12 days' exposure.

γ-irradiation	Sample	Material	Water type	Mass loss (g)	Loss (μm)	Corrosion rate (μm yr^{-1})
Unirradiated	T3-19*	Cu-OFP	PW1.4	0.0003 ± 0.0003	0.109	3.3
	T3-20*	Cu-OFP	PW1.6	0.0003 ± 0.0003	0.103	3.1
	T3-23*	Cu-OFP	DW	0.0005 ± 0.0001	0.174	5.3
	T3-21*	carbon steel	PW1.4	0.0112 ± 0.0001	4.858	147.8
	T3-22*	carbon steel	PW1.6	0.0247 ± 0.0002	10.714	325.9
	T3-24*	C-Steel	DW	0.0137 ± 0.0002	5.943	180.8
14 kGy (dose rate 66 Gy hr^{-1}	T3-19	Cu-OFP	PW1.4	0.0040 ± 0.0013	1.52	46.2
	T3-20	Cu-OFP	PW1.6	0.0045 ± 0.0003	1.71	51.9
	T3-23	Cu-OFP	DW	0.0000 ± 0.0002	0.00	0.0
	T3-21	carbon steel	PW1.4	0.0176 ± 0.0005	7.63	232.2
	T3-22	carbon steel	PW1.6	0.0262 ± 0.0004	11.36	345.7
	T3-24	C-Steel	DW	0.0137 ± 0.0003	5.94	180.8
140 kGy (dose rate 697 Gy hr^{-1})	T3-33	Cu-OFP	PW1.4	0.0017 ± 0.0005	0.64	19.6
	T3-34	Cu-OFP	PW1.6	0.0026 ± 0.0006	0.99	30.0
	T3-37	Cu-OFP	DW	0.0006 ± 0.0003	0.23	6.9
	T3-35	carbon steel	PW1.4	0.0237 ± 0.0001	10.81	328.7
	T3-36	carbon steel	PW1.6	0.0224 ± 0.0004	9.72	295.5
	T3-38	C-Steel	DW	0.0203 ± 0.0003	8.81	267.8

The copper and iron concentrations measured in solution (unfiltered) after the different irradiation experiments are shown in Figure 17. The concentration of copper in solution was low in all cases and lower than that of iron, in agreement with the higher corrosion rates measured for carbon steel. In both cases, higher iron and copper values were measured in solutions exposed to higher radiation doses, but measured concentration values in solution were lower than the values expected on the basis of mass loss measurements, which indicates that most of the oxidised copper or iron was precipitated. It is also noteworthy that the iron and copper concentrations measured in solution after filtering the samples with a 0.2 µm filter were very low (>30 ppm in the case of Fe), which indicates that most of the Fe present in solution was in particulate form.

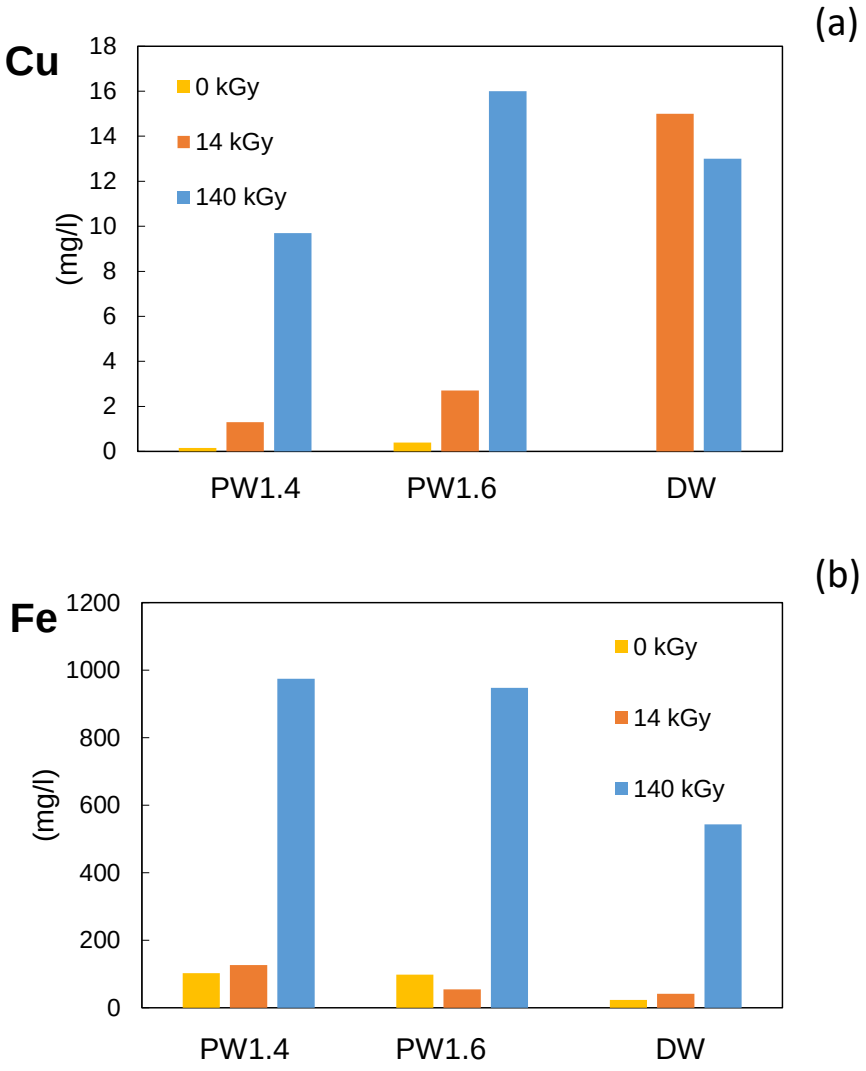

Figure 17. Metal concentrations measured in unfiltered solution after metal disc immersion in 5 ml of different bentonite porewaters PW1.4 and PW1.6 and in deionised water (DW) irradiated at different conditions (0, 14 kGy and 140 kGy). (a) Cu in solution in mg/l (Cu-OFP experiments) and (b) Fe in solution in mg l^{-1} (carbon steel experiments).

Magnetite / bentonite samples

XRD analysis of the closed cells containing a thin surface layer (1-2 mm) of magnetite (Fe_3O_4) over compacted bentonite showed that irradiation did not cause any appreciable differences in the unirradiated magnetite (Mag) or the magnetite / bentonite interface.

Metal canister /bentonite samples

The corrosion rates obtained by mass loss measurements are collected in Table 28. Once again, the corrosion of Cu-OFP specimens was very limited compared to that of carbon steel samples. The highest corrosion rates were measured for carbon steel discs in contact with bentonite at lower compaction density (1.4 g cm^{-3}) and with the highest degree of water saturation. This indicates that the high salinity of the porewater is the main corrosive agent in the system. In fact, higher corrosion rates were even measured on the samples directly immersed in the porewater (Table 24). Higher corrosion rates were measured on irradiated carbon steel samples, compared to unirradiated ones, but no differences were measured between the two irradiation doses investigated (14 kGy and 140 kGy).

SEM, FTIR and Raman spectroscopy studies were carried out on both metal samples (uncleaned) and on the bentonite contact surface to identify the alteration products. It was found that very little corrosion product had developed on the Cu-OFP disc surfaces, but the main corrosion products were identified as Cu(II) oxides.

SEM examination of a carbon steel disc (T3-10), which corresponds to a sample contacted by compacted bentonite at 1.4 g cm^{-3} and 100% water content, irradiated at 14 kGy showed a mixture of Fe-rich phases and bentonite minerals, as well as precipitated salts. EDX analyses indicated the presence of Fe-Cl phases, Ca-Fe phases, as well as Fe oxides, mixed with residual bentonite particles (suggested by the presence of Si, Al, Mg and Ca).

The nature of alteration products was very similar on all carbon steel coupons in contact with compacted bentonite under different conditions. The main Fe-rich phases identified by Raman spectroscopy where haematite, goethite and ferrihydrite.

Table 28. Corrosion rates determined for Cu-OFP and carbon steel discs in contact with compacted bentonite at two different compaction densities with two degrees of saturation (w.c. %). Triplicate samples were unirradiated, irradiated at 14 kGy and irradiated at 140 kGy. Corrosion rates were based on mass loss measurements after 12 days' exposure.

	Sample	Material	Compaction (g cm^{-3})	% water content	Mass loss (g)	Loss (µm)	Corrosion rate (µm yr^{-1})
Unirradiated	T3-05*	Cu-OFP	1.4	60%	0.0019 ± 0.0003	0.721	21.9
	T3-06*	Cu-OFP	1.4	100 %	0.0006 ± 0.0001	0.228	6.9
	T3-07*	Cu-OFP	1.6	60%	0.0001 ± 0.0002	0.038	1.2
	T3-08*	Cu-OFP	1.6	100 %	0.0000 ± 0.0004	0.000	0.0
	T3-09*	carbon steel	1.4	60%	0.0071 ± 0.0003	3.080	93.7
	T3-10*	carbon steel	1.4	100 %	0.0132 ± 0.0004	5.726	174.2
	T3-11*	carbon steel	1.6	60%	0.0061 ± 0.0005	2.646	80.5
	T3-12*	carbon steel	1.6	100 %	0.0111 ± 0.0006	4.815	146.4
γ-irradiated dose: 14 kGy dose rate: 66 Gy hr^{-1}	T3-05	Cu-OFP	1.4	60%	0.0004 ± 0.0007	0.15	4.4
	T3-06	Cu-OFP	1.4	100 %	0.0004 ± 0.0002	0.14	4.4

	Sample	Material	Compaction (g cm^{-3})	% water content	Mass loss (g)	Loss (µm)	Corrosion rate (µm yr^{-1})
	T3-07	Cu-OFP	1.6	60%	0.0004 ± 0.0001	0.15	4.5
	T3-08	Cu-OFP	1.6	100 %	0.0004 ± 0.0004	0.14	4.1
	T3-09.1	carbon steel	1.4	60%	0.0078 ± 0.0006	3.38	102.9
	T3-10.1	carbon steel	1.4	100 %	0.0145 ± 0.0002	6.29	191.3
	T3-11.1	carbon steel	1.6	60%	0.0094 ± 0.0003	4.08	124.0
	T3-12.1	carbon steel	1.6	100 %	0.0145 ± 0.0001	6.29	191.3
γ-irradiated dose: 140 kGy dose rate: 697 Gy hr^{-1}	T3-25	Cu-OFP	1.4	60%	0.0000 ± 0.0003	0.00	0.0
	T3-26	Cu-OFP	1.4	100 %	0.0002 ± 0.0006	0.08	2.3
	T3-27	Cu-OFP	1.6	60%	0.0000 ± 0.0006	0.00	0.0
	T3-28	Cu-OFP	1.6	100 %	0.0000 ± 0.0007	0.00	0.0
	T3-29	carbon steel	1.4	60%	0.0084 ± 0.0005	3.64	110.8

	Sample	Material	Compaction (g cm^{-3})	% water content	Mass loss (g)	Loss (µm)	Corrosion rate (µm yr^{-1})
	T3-30	carbon steel	1.4	100 %	0.0151 ± 0.0002	6.55	199.2
	T3-31	carbon steel	1.6	60%	0.0077 ± 0.0007	3.34	101.6
	T3-32	carbon steel	1.6	100 %	0.0116 ± 0.0005	5.03	153.0

Irradiated compacted bentonite samples (no metal)

Finally, the state of the compacted bentonite samples without metal present after γ-irradiation (14 kGy or 140 kGy total dose was analysed by XRD and FTIR. No changes in bentonite mineralogy or structure were detected.

Summary and conclusions of the CIEMAT test programme

The experiments carried out by CIEMAT were designed to simulate the conditions at the canister / bentonite interface during the early stage of repository evolution in which the bentonite is not fully water saturated, the γ-irradiation accumulated dose is ~14 kGy and conditions are still oxic (i.e. Phase 2: Aerobic unsaturated phase). The experiments were short-term (~12 days) and considered two main cases:

(I) Copper and carbon steel coupons immersed in synthetic representative bentonite porewaters, and

(2) Copper and carbon steel coupons in compacted bentonite at two densities (1.4 g cm^{-3} and 1.6 g cm^{-3}), hydrated with the corresponding synthetic porewater at two water saturation levels (w.c. 60% or 100 %), for comparison.

With respect to the γ-irradiation levels, the samples were tested (i) unirradiated, (ii) to an accumulated dose of 14 kGy, or (iii) to an accumulated dose of 140 kGy.

In addition, compacted bentonite samples with a thin surface layer of iron oxide (Fe_3O_4) were analysed to investigate the impact of radiation on the release of corrosion products into the bentonite. In parallel, reference samples of iron and copper powder oxides (simulating the relevant corrosion products), and powdered bentonite, irradiated to determine whether there was any effect on them.

CIEMAT results corroborated the limited corrosion of copper specimens compared to that of carbon steel ones. In general, higher corrosion rates were measured on gamma-irradiated carbon steel samples contacting bentonite at lower compaction density where higher volume of porewater is available. Higher corrosion rates were measured in irradiated than in unirradiated samples but no significant changes in corrosion rates were detected for irradiated samples achieving 14 or 140 kGy of accumulated dose, suggesting an inhibiting effect at higher doses.

3.4 Overview of radiation-assisted corrosion studies within ConCorD

Direct comparison of the UJV and Jacobs results is difficult owing to a large number of different variables between the tests, however some inferences can be made by comparing the two data sets. The only direct comparison that can be made is between the tests operated at ambient temperature in the absence of radiation, which gives an indication of the inherent difference in corrosion rate caused by the two test configurations. From the UJV tests in BCV bentonite, the corrosion rate in ambient conditions varied from 6 µm yr^{-1} to 2.6 µm yr^{-1} after being exposed for ~4,400 to ~13,000 hours, respectively. In comparison, in the unirradiated Jacobs tests, the corrosion rate varied from 3.5 µm yr^{-1} to 1.5 µm yr^{-1} after being exposed for 5,000 to 10,000 hours. This shows that despite the very different test configurations, the magnitude of the corrosion rate due to water reduction and the rate of attenuation is similar in UJV test and Jacobs tests.

UJV tests that were subjected to radiation, at 90°C and 150°C, received total doses between 1.8 and 5.3 kGy, which were applied at a dose rate of 0.4 Gy hr^{-1}. The closest conditions to these from the Jacobs testing program were tests run at dose rates of between 0.1 and 1 Gy hr^{-1}, which received total doses of between 1 and 10 kGy, but were performed at ambient temperature. In the UJV tests, under all conditions tested, radiation either conferred an inhibiting effect or had no significant influence on corrosion rate. The magnitude of the inhibiting effect was greater at higher temperature, and from the tests in BCV bentonite the effect appeared to be broadly greater at shorter durations. Comparing these results with those of the Jacobs testing under the aforementioned exposure conditions shows that in the Jacobs tests no inhibiting effect was observed; there was a slight increase in corrosion rate when radiation was present but at 0.1 to 1 Gy hr^{-1} for total doses between 1 to 10 kGy the effect was not significant. However, when the total dose of 1 to 10 kGy was applied at higher dose rates between 10 to 1000 Gy hr^{-1}, a significant increase in corrosion rate compared to unirradiated conditions was observed for several of the tests. These results invite the question as to whether the inhibiting effect that is observed in the UJV tests at high temperature would give way to a corrosion rate enhancement at dose rates higher than the 0.4 Gy hr^{-1} that was tested, as observed in the Jacobs tests, or whether the inhibiting effect is solely related to the presence of bentonite and/or elevated temperature? Conversely, if the Jacobs tests were performed at higher temperature would an inhibiting effect have been observed at lower dose rates?

A key observation from the UJV tests was the substantial influence of temperature on corrosion rate, both in the presence and absence of radiation. At 150°C, in the absence of radiation the corrosion rate in BCV bentonite varied between 24 µm yr^{-1} and 13 µm yr^{-1} with an experimental repeatability of roughly 10 to 25 µm yr^{-1} based on the ranges of corrosion rates reported. In the Jacobs tests, the increase in corrosion rate due to the presence of radiation was less than 1 µm yr^{-1} at a dose rate of 10 Gy hr^{-1} following exposure durations of between 5,000 and 10,000 hours. Hence, the same 1 µm yr^{-1} enhancement would probably not be detectable if the unirradiated corrosion rate was as high as was observed in the UJV tests performed at 150°C, as it is considerably lower than the repeatability. Furthermore, where the unirradiated corrosion rate was higher (e.g. 24 µm yr^{-1}) the increase in corrosion rate associated with radiolytically generated oxidants could be offset by other effects such as a change in the chemistry of the oxide.

The results of the tests performed in bentonite by Subatech (Sarrasin et al., 2024), indicated an increase in corrosion rate due to radiation at lower RH (63% and 76%), with ranges of corrosion rates overlapping those reported by Jacobs and UJV. However, at higher levels of saturation no significant influence of radiation was observed at 25°C, which is consistent with the results of the UJV tests performed at 90 °C in MX-80 bentonite. In the absence of clay, a similar increase in corrosion rate was observed in the presence of radiation for tests performed at 76% RH. However, for tests performed at 63% RH, the

corrosion rate in the presence of radiation was extremely high even after nearly 1000 hours of testing (~230 µm yr^{-1}) and was greater than the corrosion rate observed in the Jacobs tests performed in porewater simulant for durations between 100 and 1,000 hours at dose rates between 100 Gy hr^{-1} and 1000 Gy hr^{-1}, which are the closest comparable irradiation conditions.

A second set of tests, performed by CIEMAT (Sarrasin et al., 2024), comprised exposure tests on copper and carbon steel in FEBEX bentonite at either full saturation or 60% water content, or in FEBEX porewater with no bentonite present. The exposure conditions were irradiation at ambient temperature at 66 Gy hr^{-1} and 697 Gy hr^{-1} to give total doses of 14 kGy and 140 kGy, respectively. Unirradiated control tests were run under comparable conditions. For carbon steel tests performed in the presence of bentonite, the average corrosion loss was greater under radiation than in unirradiated conditions, but the differences were small compared to the variations associated with repeatability. Furthermore, there was no significant difference in the measured corrosion rates between the two dose rates (and resulting total doses – same test durations were used). For tests performed in porewater in the absence of bentonite, there was an increase in average corrosion loss under radiation and the corrosion loss increased with increasing dose/dose rate. As with the tests performed in bentonite, the difference in corrosion rate under different radiation exposures (i.e. 0, 14 and 140 kGy) was smaller than the differences observed between nominally identical repeat tests. For tests performed on copper in the presence of bentonite, the corrosion rates were all below 10 µm yr^{-1}, but there appeared to be an inhibiting influence of radiation on corrosion with lower average corrosion rates observed at increasing dose rates. Interestingly, for the copper tests that were performed in porewater without bentonite, there was a substantial increase in corrosion rate in the presence of radiation compared to the unirradiated control tests, broadly consistent with the general observations reported in the tests performed by Jacobs. In the absence of radiation the corrosion rate was ~3 µm yr^{-1}, but following irradiation exposure to 14 and 140 kGy, the corrosion rates were ~49 and 25 µm yr^{-1}, respectively.

From the CIEMAT results, the increase in corrosion rate of steel during exposure to bentonite contrasts the results of the test performed by UJV, which were also performed in bentonite. The key differences between the two test configurations are the dose rate, temperature and type of bentonite. Of these parameters, the higher dose rate in the CIEMAT tests would be expected to result in an increased corrosion rate, owing to the greater rate of formation of radiolytically generated oxidants. However, there may also be an impact of bentonite type and temperature given that they appeared to have an influence on the UJV results. The results for carbon steel performed in porewater without bentonite are broadly similar to the results observed in the Jacobs tests; namely, there does appear to be an enhancement of corrosion rate by radiation, however it is difficult to resolve above the noise of the measurement for short duration tests.

The results of the tests on copper in porewater are in fair agreement with the Jacobs tests, showing an increase in corrosion rate due to radiation. However, unlike in the Jacobs tests, which were performed over the dose rate range 0.1 to 10 Gy hr^{-1}, the CIEMAT tests showed that the corrosion loss with radiation did not increase with increasing dose rate between 66 Gy hr^{-1} and 697 Gy hr^{-1}. This is an important observation as it demonstrates that, whilst there is a dose rate effect at very low dose rates, this influence cannot be accelerated linearly by increasing the dose rate up to very high dose rates (697 Gy hr^{-1}). A further key observation was that the increase in corrosion rate due to radiation that was observed in porewater did not occur in bentonite. In fact, in the latter, an inhibiting effect was possibly observed. The reason for the difference in results between porewater tests and those performed in bentonite is not yet certain, but it is anticipated that the reduced transport of oxidants in bentonite compared to porewater, the reduced water density in bentonite, and the ability of bentonite to react with radiolytically generated oxidants could all be contributing factors. These parameters may also explain the inhibiting influence of radiation on the corrosion rate of carbon steel that was observed in the UJV tests. Consequently, a key aspect for future work would be to assess the impact of bentonite on mitigating RIC under a wider range of conditions e.g., different bentonites, temperatures, and saturation levels. Additionally, it might be important to consider any effect of gamma radiation on the properties of

the bentonite that may influence its ability to self-seal (e.g. a possible reduction in swelling pressure if there is a shift from monovalent to divalent cations in the smectite interlayers of the montmorillonite).

4. Task 4: Microbial effects

4.1 Introduction to task

Within this task, remaining uncertainties associated with the impact of microbial activity in buffer materials on corrosion are addressed. Microbially influenced corrosion (MIC) can accelerate anaerobic corrosion as a consequence of microbial metabolism. MIC can also play a role in the HLW and SF repository environment, even if biofilm formation on the surface of canisters is not expected (owing to the high initial thermal load and radiation field), nor yet observed in relevant experiments. However, it is well established that H_2 will be produced via anaerobic corrosion of some container materials (i.e. steel). In thatcase, the H_2 produced could drive microbial processes such as sulphate reduction and methanogenesis. The associated sulphide production in the former could greatly affect the corrosion rate, particularly for copper but also for steel containers.

It has already been demonstrated that sulphate-reducing bacteria (SRB) are present in the host rock at most repository locations considered (Bagnoud et al., 2016; Bell et al., 2020) as well as in potential backfill materials (e.g. in bentonite as shown in Matschiavelli et al., 2019; Martinez-Moreno et al., 2023; Povedano-Priego et al., 2023). Thus, the question is not whether sulphate reduction can occur in the repository, but whether it can be inhibited or controlled in a way that minimises the impact on the corrosion rate of the container materials in the repository. The bentonite buffer is expected to play an important role in precluding microbial activity for the purpose of limiting any negative microbial impact on corrosion rates. Thus, it is critical to optimally select and design the bentonite buffer to inhibit or control microbial activity.

The early phase of the repository will be characterised by elevated temperatures, peak radiation levels and a low water saturation state. Therefore, in the multi-barrier concept, it is important to understand the effect of radiation on the mineralogy and performance of the barrier material (i.e. bentonite). Furthermore, the effect of radiation as well as elevated temperatures during the initial hot phase of the DGR on microbial survivability and potential for future growth should be evaluated. As such conditions are expected to create unfavourable physicochemical conditions for microorganisms, the evolution of a zone of no microbial activity around the canister was predicted (Stroes-Gascoyne and West, 1997). However, long-term experiments under realistic repository conditions are needed to provide experimental evidence of this phenomenon. As part of the EU-project Microbiology in Nuclear waste Disposal (MIND), deliverable D2.15, (Černá et al., 2019) reported on the effect of gamma radiation and pressure on the bentonite indigenous microbial community (type BaM, Keramost, Czech Republic) in a granitic porewater (VITA from the Josef Underground Research Center, Czech Republic). The latter was a natural source of sulphate-reducing bacteria. It was found that the microorganisms that grew in the bentonite-porewater slurry were subjected to inhibition by gamma irradiation. Indeed, the exposure to 19,656 Gy at a constant dose rate of 13 Gy hr^{-1} resulted in a decrease in total microbial biomass, but not species richness, and in small changes in the microbial community structure (Černá et al., 2019). However, it did not eliminate bacteria from the bentonite suspension. These results suggest that some of the bacteria that are naturally present in bentonite are radiation resistant. Furthermore, past long-term experiments suggested that bentonite microorganisms can survive long-term extreme heat treatment (Kašpar et al., 2021) and the associated desiccation.

Therefore, Subtask 4.1 of ConCorD aimed to investigate the evolution of microbial communities in bentonite under simulated repository conditions. It focused on studying the effect of irradiation, temperature, water saturation, and bentonite compaction. Such experiments aim to increase our knowledge about the microbial response to the condition expected during the hot repository phase.

In the past, a few studies have attempted to determine the dry density threshold that would reliably inhibit microbial activity (e.g. Bengston and Pedersen et al., 2017; Stroes-Gascoyne, 2010). In the study of Povedano-Priego et al. (2021), the bacterial community did not differ for two compaction dry densities (1.5 and 1.7 g cm^{-3}). However, it is still unclear whether dry density is the key parameter or whether

other considerations may contribute to inhibiting microbial metabolism. Microbial activity need not rely solely on the presence of organic carbon, since autotrophic growth, with H_2 as the electron donor, sulphate as the electron acceptor and CO_2 as the carbon source, is also conceivable. In fact, such a potential exists in specific host rocks, such as Opalinus Clay, and in the backfill material bentonite (Matschiavelli et al., 2019). An in-situ experiment that was conducted in the Mont Terri underground laboratory in Switzerland showed that SRB growth was stimulated by the addition of H_2. These organisms served as primary producers and they were the origin of a microbial food web that developed in the borehole (Bagnoud et al., 2016). However, the absence of bentonite was a major limitation in this experiment, and it would be more relevant to measure H_2 consumption in bentonite as a function of dry density and swelling pressure.

Therefore, **Subtask 4.2** examined the fundamental variables influencing the bentonite dry density threshold at which microbial activity is inhibited for two different types of bentonite (MX-80 and Calcigel).

It is known that SRB are present in bentonite, but their number does not contribute significantly to the total number of anaerobic microorganisms in the clay, as found in an experiment at Mont Terri (Burzan et al., 2022) and in previous studies on Spanish clay (Martinez-Moreno et al., 2023; Povedano-Priego et al., 2023). A complicating matter is that there is increasing evidence for the persistence of O_2 (perhaps as an adsorbed gas) in bentonite.

Therefore, in **Subtask 4.3**, the hypothesis that O_2 bound in bentonite may inhibit SRB (which are strictly anaerobic microorganisms) is evaluated. The impact of O_2 would be relevant over relatively short-term periods during which the clay has not fully swelled and there may be potential for microbial growth. While O_2 may be depleted during the longer periods relevant to the repository, allowing SRB to grow if conditions permit, the short-term effect was tested in a new in situ experiment at Mont Terri.

The details of the experiments undertaken within this task and the full set of results are presented in Morales Hidalgo et al. (2024).

4.2 Scope of task

4.2.1 Comparison of DNA extraction protocols

In Task 4, we wanted to enable proper comparison of the results obtained across various experiments. However, a known challenge of clay-rich samples is that they hamper the efficiency of several standard cultivation-independent methods. Clay particles are known to tightly adsorb organic and inorganic phosphorous compounds (Cai et al., 2007). A few DNA extraction methods have been published for clay; however, they have either been validated by spiking a single strain or not validated at all (Chi Fru and Athar, 2008, Engel et al. 2019a, Povedano-Priego et al., 2021). Validation using a mock community is essential, as applying various DNA extraction methods to clay samples has resulted in significant variation in the outcomes of 16S rRNA gene amplicon sequencing (Mijnendonckx, et al., 2021). Thus, a more standardised research methodology is needed to study microbial communities in low biomass, clay-rich environments. This is especially important if cross-comparison of the results obtained through 16S rRNA gene amplicon sequencing is needed. Therefore, within the ConCorD project, we compared two distinct DNA extraction methods (Engel, et al. 2019; Povedano-Priego et al., 2021) that have shown suitability for clay samples (Mijnendonckx et al. 2021).

We used two commercial microbial community standards consisting of DNA or intact cells of three Gram-negative bacteria, five Gram-positive bacteria and two yeast species of varying size and cell wall stability (ZymoBIOMICS Mock Community standards, Zymo Research Corporation, Irvine, USA) (Figure 18). Mock 1 contained a total cell concentration of ca. 1.4×10^{10} cells ml^{-1} and a linear distribution of the strains, while Mock 2 contains ca. 1.5×10^{9}cells ml^{-1} with a logarithmic distribution of the strains. Two grams of sterile MX-80 bentonite (sterilised by gamma irradiation with a total dose of 50 kGy) were supplemented with 12.5 ml phosphate-buffered saline (PBS), and either 75 µl of Mock 1 or Mock 2, or nothing (control). All experiments were performed in triplicate. Samples were thoroughly mixed by

vortexing and incubated for 3 days at 4°C to enable water absorption into, and cell interaction with, bentonite. After the incubation step, samples were centrifuged at 11,000 rpm for 10 min. The supernatant was discarded and the pellet used for DNA extraction. To elucidate the possible bias introduced by the presence of bentonite on DNA recovery, extractions were also performed directly on both mock communities.

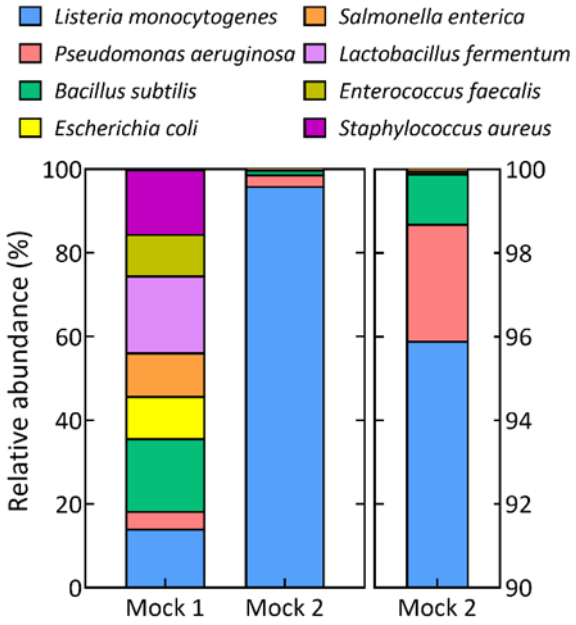

Figure 18: Overview of the theoretical composition of both mock communities used in this study. The right plot represents a focus on the 90-100% abundance from the middle plot.

A detailed description of all experimental procedures is available in Mijnendonckx et al. (2024).

4.2.2 Subtask 4.1: Impact of irradiation on microbial viability

The aim of this subtask was to investigate the effect of gamma radiation on the survival of microbial populations, including SRB, in compacted bentonite. This aim was investigated in two ways: the first was to add a known microbial community to compacted, saturated bentonite (designated 'amended') and to assess its survival post-irradiation. The second was to vary the compaction state, the temperature, and the saturation level of the bentonite in addition to the radiation exposure and to characterise the microbial community before and after treatment. Both approaches were closely connected to experiments conducted in Task 3 as they represent the analysis of the microbial community from samples generated by the experiments described within that task.

Impact of radiation on the amended community: FEBEX bentonite was compacted into blocks with a density of 1.6 g cm^{-3}. A custom consortium of SRB was assembled, which included the genera *Desulfovibrio, Desulfotomaculum, Desulfuromonas,* and *Desulfosporosinus* along with a metal-reducing bacterium from the genus *Geobacter*. Sodium acetate (1.5 mM) was added as an energy and carbon source for the microorganisms. The consortium and sodium acetate solution were added prior to compaction. In addition, unamended controls were also prepared. All the samples were saturated with bentonite porewater ($1.50 \cdot 10^{-2}$ M $CaCl_2$, $1.66 \cdot 10^{-2}$ M $MgCl_2$, $1.09 \cdot 10^{-3}$ M KCl, $4.59 \cdot 10^{-2}$ M Na_2SO_4, $2.16 \cdot 10^{-2}$ M NaCl, $1.01 \cdot 10^{-3}$ M $NaHCO_3$, pH=7.5) to achieve 100% saturation post-compaction. Small copper coupons (diameter 10 mm, thickness 4 mm) simulating metal canisters used for confining nuclear waste in deep geological repositories were included in the middle of each block to quantify their corrosion under controlled conditions. One set of samples was irradiated at the beginning of the experiment (total dose of 14 kGy), another only after 6 months (14 kGy), and a third both at the beginning

and after 6 months of incubation (28 kGy). In all cases, the dose rate was 66 Gy hr^{-1} and the duration 8.8 days. All samples (whether irradiated or not) were incubated for up to one year at 28°C under anoxic conditions.

Impact of environmental conditions on the native community: Four distinct experimental setups were prepared using Czech bentonite BCV and reference bentonite MX-80. All experiments were conducted under anoxic conditions. The first two sets consisted of bentonite compacted to a dry density of 1.6 g cm^{-3} embedded with carbon steel coupons, and partially pre-saturated (relative humidity 15% for samples heated to 150°C and 20% for those heated to 90°C). The prepared samples were connected to the pressure saturation system (full saturation with synthetic granitic porewater) and continuously exposed to heat (either at 90°C or 150°C) or heat and irradiation (≈0.4 Gy hr^{-1}) for 6, 9, 12 or 18 months (for BCV) or for 18 months (for MX-80) (Figure 19). The third set consisted of pre-saturated (relative humidity 15% representing 60% saturation level) compacted bentonite (BCV or MX-80) with a dry density of 1.6 g.cm^{-3} but, in contrast to above, lacking metal coupons and not connected to a porewater reservoir. As above, the samples were continuously exposed to heat (90°C or 150°C) or heat and irradiation (≈ 0.4 Gy.hr^{-1}) for 12 months. A subset of samples was re-saturated with sterile deionised water for 6 months post-treatment to simulate rewetting after the hot repository phase. The last set of bentonite samples (BCV or MX-80) consisted of bentonite in the naturally dry state or suspended in sterile deionised water at a bentonite to water ratio of 1:3 w/w (BCV) or 1:6 w/w (MX-80). The samples were continuously exposed to heat (90°C or 150°C) or heat and irradiation (≈0.4 Gy hr^{-1}) for 12 months. For all sets of experimental conditions, corresponding unheated and unirradiated controls were also prepared.

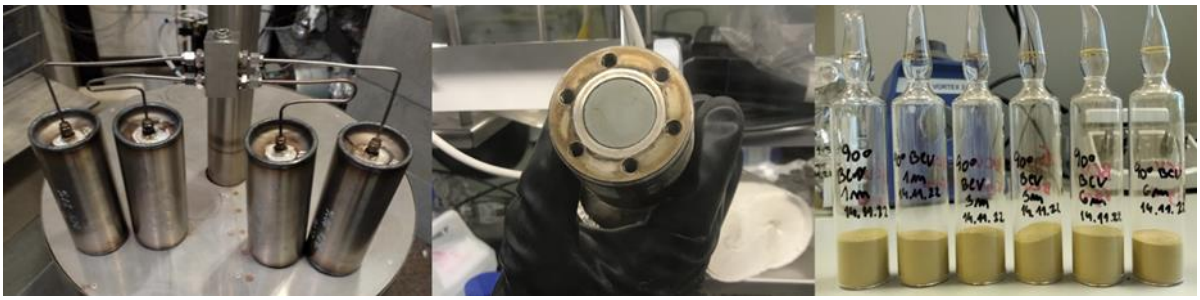

Figure 19: Steel vessels containing steel cells connected by metal capillaries with saturation medium situated in the irradiation area, steel cell with compacted bentonite and glass ampoules with bentonite powder.

At the end of each experiment, the microbial community was characterised in bentonite sub-samples through a combination of cultivation approaches (enrichment media, plate counts or natural incubations in water suspended form without added nutrients), microscopy, and molecular methods (quantitative PCR (qPCR) and 16S rRNA gene amplicon sequencing) to identify changes in the community and to estimate microbial survival after the exposure to extreme conditions.

4.2.3 Subtask 4.2: Impact of bentonite dry density and particle size on microbial activity

It is well established that dry density inversely correlates with microbial activity in bentonite but the underlying mechanism constraining microbial activity in high density bentonite remains elusive. To address this knowledge gap, a diffusion cell reactor that was adapted for working under sterile conditions and high pressures was developed to conduct experiments that systematically varied dry density. A new system is needed because investigating growth of microorganisms in bentonite is fraught with potential bias and rarely includes sufficient statistical power in the form of experimental replicates.

Therefore, replicate (up to 12) small (10 cm high and 6 cm in diameter) diffusion reactors were designed based on opposing diffusion gradients of electron donor and acceptor. The diffusion reactor design from Luc Van Loon (Van Loon et al., 2003) was used and adapted to microbial applications (Figure 20).

Reactors with inflow and outflow lines at the top and bottom respectively were manufactured at EPFL and HZDR. Bentonite (MX-80 or Calcigel) was compacted under oxic conditions to reach selected dry densities (e.g. 1.2, 1.4, or 1.6 g cm^{-3}). Titanium filter plates (1 µm pore size) were placed at both ends of the cells to allow diffusive flow. To prevent microbial growth on the filters (a common experimental artifact), a reservoir of artificial Opalinus clay porewater containing 14 mM of sulphate as the electron acceptor, in equilibrium with a N_2/CO_2:80/20 (v/v) gas phase, was injected from the bottom of the cell, thus allowing continuous flow past the filter and diffusive transport into the bentonite. Simultaneously, another reservoir of sulphate-free artificial Opalinus clay porewater equilibrated with H_2 gas (as the electron donor) was injected from the top of the cell. To maintain a fixed concentration of dissolved H_2 (~5.5 mM) in the porewater, the H_2/CO_2: 80/20 (v/v) gas phase pressure in the reservoir was maintained at 1.5 bars. This set-up was designed to stimulate indigenous microbial growth in the middle part of the compacted bentonite, where the solutions of electron acceptor and donor meet. The porewater flow rate at each end of the cell was set at 0.1 ml min^{-1} using a peristaltic pump.

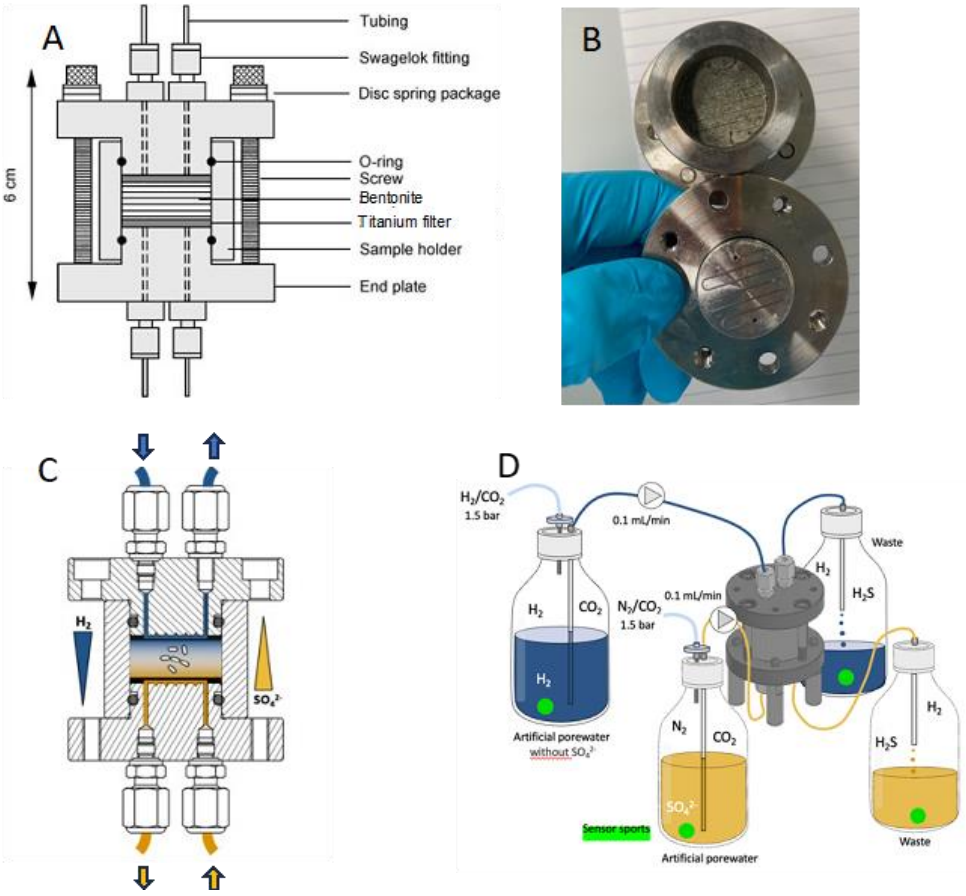

Figure 20. A. Diagram showing the reactor (modified from Van Loon et al., 2003). B. image of the reactor showing the groove in the end plate with fingers for scale. C. Illustration of the gradient of electron donor and acceptor. D. Solutions and waste vessel when connected to a reactor. The optode system sensor is shown with a green dot.

However, because of the presence of gypsum ($CaSO_4.2H_2O$) in the MX-80 bentonite, the first phase of the experiment involved the diffusion-controlled dissolution of gypsum. It entailed pumping a sulphate- and bromide-free anoxic (equilibrated with 1.5 bar N_2/CO_2) APW past the bentonite on both sides of the reactor and measuring the sulphate concentration in the effluent (Figure 20). Thus, the clay was saturated through the recirculating flow of anoxic APW (sulphate-free) at both ends of the reactor while the effluent went to a waste beaker.

To identify the microorganisms that grow under each condition and to what extent, DNA was extracted from the bentonite from the entire reactor, qPCR was applied to measure growth (16S rRNA gene copies), and the diversity assessed using 16S rRNA gene amplicon sequencing. Because there were many replicate reactors, duplicates were sacrificed at each time point and used to reconstruct the temporal dependence of the community growth.

The extent to which microbial activity can affect corrosion in high-density bentonite remains unclear. Therefore, an oedometer-based experimental setup developed at SCK CEN was used to study microbial corrosion of carbon steel at a bentonite dry density of 1.6 g cm^{-3}.

All preparations were performed in an anoxic glove box with a manually controlled atmosphere of 99% argon and 1% hydrogen. Bentonite powder (MX-80) was added to the oedometers and four carbon steel coupons (on average 17.9 mm and 0.35 mm thick) were placed in MX-80 such that all coupons were completely covered with bentonite. Subsequently, the oedometers were closed and percolation was initiated with sterile synthetic Opalinus Clay water with or without 1.5 bar of a H_2:CO_2 (80:20 v/v) mixture. Full saturation of the first three oedometers that were setup was reached after 5 months. The water continues to be collected to monitor the composition of the percolate over time. An additional three oedometers were setup in which the bentonite was sterilised via irradiation with ca. 57 kGy (6.4 kGy hr^{-1}). At the end of the project, the cells were dismantled, and corrosion of the carbon steel plates studied by measuring weight loss and compared with SEM/EDX. Water activity of the bentonite was measured, and bentonite mineralogy and microbial presence was visualised with SEM/EDX. Moreover, the bentonite microbial community was investigated in detail by a combination of cultivation independent (ATP, flow cytometry, 16S rRNA amplicon sequencing) and cultivation-dependent techniques.

In total, five conditions of anaerobic microcosms consisting of serum bottles containing 30 ml of anoxic artificial porewater (APW) (composition from Matschiavelli et al., 2019) were prepared in the glovebox. In general, 15 g of as-received Calcigel bentonite (Cal) were added to each autoclaved serum bottle. Two cast iron coupons (cast iron GGG40 measuring 1 × 1 × 0.5 cm, polished using fine-grit sandpaper, one sputtered with gold and one without, all cleaned in an ultrasonic bath using acetone) were placed into each bottle. The gas phase was defined by purging with a mixture of N_2:CO_2:H_2/80:10:10 at 0.5 bar. The condition of this microcosm was denoted HCalC (Hydrogen+Calcigel+Coupons). For microcosms with the same component but without hydrogen gas, the gas phase was defined with a mixture of N_2:CO_2/90:10 at 0.5 bar and this condition was denoted CalC (Calcigel+Coupons). On the other hand, microcosms containing hydrogen gas and Calcigel bentonite but no metal coupons were denoted HCal (Hydrogen+Calcigel). Two conditions of microcosms with sterilised Calcigel bentonite were also set up, these conditions were denoted SC (Sterilised Calcigel+Coupons) and HSC (Hydrogen+Sterilised Calcigel+Coupons). The sterilisation of the bentonites was achieved by autoclaving bentonite in serum bottles with APW twice prior to the addition of metal coupons or hydrogen gas. All the conditions of microcosms were performed in triplicates at 37°C in the dark for one day, 3, 6 and 9 months.

The geochemistry of APW after incubation was analysed for sulphate, total inorganic carbon and cations (e.g. total Fe, Ca^{2+}, Mg^{2+}, Na^{+} and K^{+}). The H_2 gas concentration in the headspace of each microcosm was also measured. The metal coupon surfaces were characterised by SEM before and after the incubation. To determine the corrosion rates, the cleaned coupons before incubation were weighed using a precision balance. DNA was extracted from as-received Calcigel bentonite, CalC microcosms at 3 months, and 9 months, HCalC microcosms at 3 months, 6 months and 9 months using PowerMax Soil Kit (QIAGEN, Germany) as previously described (Engel et al., 2019). Only slight modifications of the protocol were used as described in EURAD Deliverable 15.9. (Morales Hidalgo et al., 2024).

4.2.4 Subtask 4.3: Impact of bentonite-associated oxygen on microbial activity and viability

It has been observed that bentonite deployed into an anoxic environment exhibits microbial growth, but the microbial community is dominated by aerobes. Therefore, an in situ experiment was designed to test the hypothesis that O_2 adsorbed onto bentonite inhibited the growth of anaerobes. Mini reactors (53 mm high and 38 mm in diameter) filled with bentonite and containing embedded copper and steel coupons were placed in larger modules and lowered into an anoxic, Opalinus clay borehole in Mont Terri, Switzerland. Some of the mini reactors contained untreated bentonite while others contained sterile bentonite (sterilisation by gamma irradiation). Additionally, prior to deployment, the bentonite was either exposed to an atmosphere of 100% O_2, 100% N_2, or the ambient atmosphere (21% O_2) for 12 months, allowing a direct evaluation of the impact of O_2 on the microbial community that will develop within the bentonite and the associated extent of corrosion. Each condition included six replicate reactors that included coupons of carbon steel and copper, embedded in the bentonite. After 20 months, duplicate reactors were retrieved, and the community and extent of corrosion analysed. Later time points will be evaluated, such as 36 months and 60 months.

4.3 Progress against task description

4.3.1 Comparison of DNA extraction protocols

The most important differences between the methods and the labs were the quantity of the total DNA that could be extracted from the samples and the purity of the DNA, which either facilitated or hindered PCR amplification.

4.3.1.1 Total DNA

Each laboratory successfully obtained quantifiable DNA concentrations from all samples spiked with a mock community, except for Lab 1 when analysing bentonite samples spiked with Mock 2. However, results show that, even in the absence of bentonite, DNA yields were lower than half of the expected amount. In the presence of bentonite, this discrepancy increased at least sevenfold (Figure 21). On the one hand, large differences were observed between the two laboratories that employed the kit-based extraction method for both conditions, with and without bentonite. Lab 3 obtained ten times more DNA from Mock 1, and in the presence of bentonite, and for all samples spiked with Mock 2, an 80-fold difference was observed in DNA extracted. The slight differences in the DNA extraction procedure could result in the observed variability. On the other hand, these differences were not observed when using the phenol-chloroform based method for mock-only sample extractions, but similarly high differences were observed in spiked bentonite samples where Lab 3 achieved a notably higher total DNA yield than Lab 2 (*ca*. 18 and 5 times more for samples spiked with Mock 1 and Mock 2, respectively). Notably, in Lab 3, the presence of bentonite did not adversely affect the efficiency of DNA extraction when using the phenol-chloroform extraction method, but large differences were observed among the replicates (Figure 21). It is worth mentioning that the kit-based extraction method failed to yield any measurable amount of DNA from the sterile unspiked bentonite samples, while the phenol-chloroform-based method successfully extracted DNA from five out of six replicates those samples.

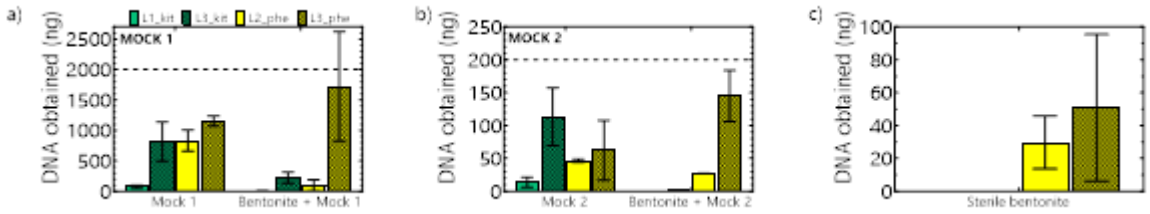

Figure 21: Total amount of DNA obtained for samples with a) Mock 1 or bentonite spiked with Mock 1 and b) Mock 2 or bentonite spiked with Mock 2 and c) sterile unspiked samples. The theoretical DNA

yield expected in all samples following the procedure recommended by the manufacturer is given by a dotted line. Samples represent the average of three replicates except for L1_kit where two replicates were tested and L3_kit which includes four replicates. Kit based methods are shown in green, while phenol-chloroform based are shown in yellow.

4.3.1.2 *16S rRNA gene amplicon sequencing*

In total, we extracted DNA from 62 samples, including 48 samples spiked with a mock community, 12 sterile unspiked samples and two negative kit controls. Successful PCR was achieved for a total of 41 out of 48 samples spiked with a mock community, 6 of the 12 sterile bentonite samples and the 2 negative kit controls. However, for numerous samples, additional purifications were needed to obtain a successful PCR product. All the samples were sent for 16S rRNA gene amplicon sequencing along with PCR reactions performed on three replicates of the Mock1 community, and several controls.

As a first step, possible contaminants were identified and removed from the dataset. After eliminating the ten Amplicon Species Variants (ASVs) that were identified as true contaminants, most samples spiked with a mock community consisted of only the eight genera present in the mock. In the unspiked sterile bentonite samples, contaminants constituted more than 96% of the total reads, reaching over 99% in four out of six samples. We confirmed that minimal PCR bias and only minor variation across the different replicates was introduced by amplifying and sequencing DNA mock community standards composed of DNA instead of intact cells.

In the analysis of samples spiked with Mock 1, both DNA extraction methods successfully captured all species, with minimal variation among replicates (Figure 22). However, higher variability was observed in samples extracted with the phenol-chloroform method (Figure 22). Notably, the variation in Lab 2 (L2)-processed samples without bentonite decreased after applying an additional phenol chloroform extraction according to the method from Lab 3 (Figure 22). The presence of bentonite did not adversely affect the correlation with the theoretical composition. The samples spiked with Mock 2 also showed minor variations among the replicates and Spearman's correlation values above 0.6 (Figure 22). However, higher contaminant ASV abundance, especially in the presence of bentonite was observed. It is important to note that diluting the samples to mitigate the impact of PCR inhibitors could lead to a significant increase in the presence of contaminants (Figure 23).

Nonmetric multidimensional scaling confirmed limited variability among replicates, with better grouping in samples without bentonite. PERMANOVA analysis indicated a significant effect of the DNA extraction method on both mock communities, but pairwise comparisons revealed no significant differences in microbial composition. The only distinction was between the DNA mock and phenol-chloroform-extracted samples spiked with Mock 1 and Mock 2. Bentonite had a significant effect on extraction methods, but pairwise comparisons mostly showed insignificant differences, except for Mock 1 kit- based extraction and Mock 2 phenol-chloroform extraction (Figure 23).

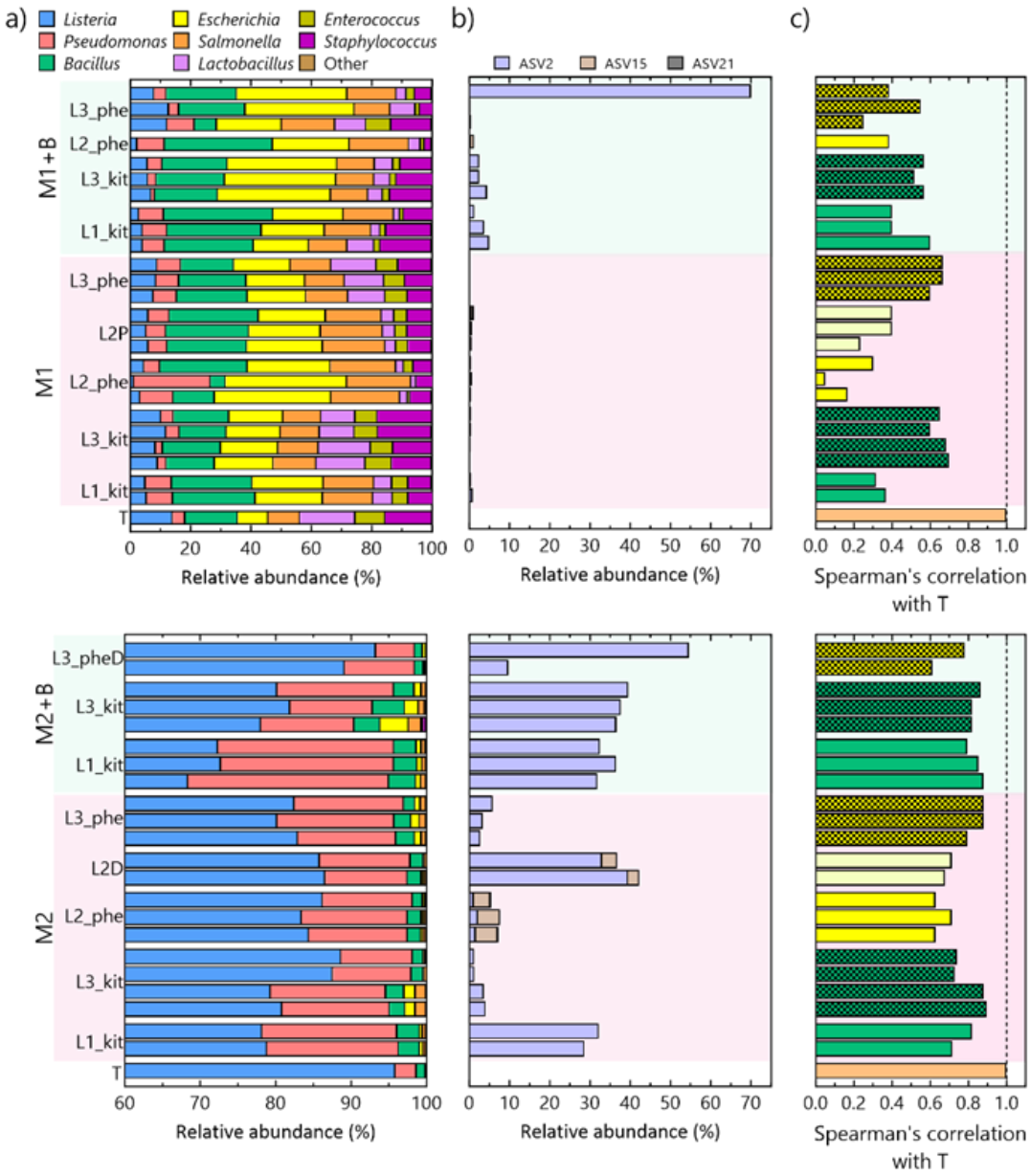

Figure 22. a) Bar plot showing the relative abundance of the genera present in samples spiked with Mock 1 or Mock 2 after removal of the contaminants; b) relative abundance of ASVs identified as contaminants in samples with Mock 1 and Mock 2. Only ASVs with a relative abundance >0.1% are shown; c) Spearman's correlation coefficients compared to the theoretical distribution (T); L1 and L3a represent results of the kit-based extraction and are shown in green and dotted green; L2 and L3b are results from the phenol-chloroform extraction and are presented in yellow and dotted yellow. L2P represent samples after an additional phenol chloroform extraction according to the method of Lab 3 and samples that are 40-times diluted as PCR template are designated with L2D. Samples diluted before a successful PCR reaction was obtained are indicated with L3_PheD. Samples without bentonite are shown in pink and samples with bentonite are coloured light green.

Overall, we conducted a comprehensive inter-laboratory comparison of two DNA extraction methods on bentonite clay. We showed that minor modifications to the extraction method could improve the extraction efficiency. Importantly, our findings indicate that the choice between the two methods is not critical, and each has advantages. The phenol-chloroform based method appears to be the optimal choice for bentonite samples, as it yields a higher amount of DNA. However, this method is more time-consuming and may be more susceptible to impurities in the final DNA sample and technical variations.

On the other hand, if highly pure DNA is required, the kit-based method is recommended. However, pooling many samples might be necessary to obtain sufficient DNA using this method. Lastly, our findings emphasise the importance of including appropriate controls when working with challenging samples, particularly those with low biomass.

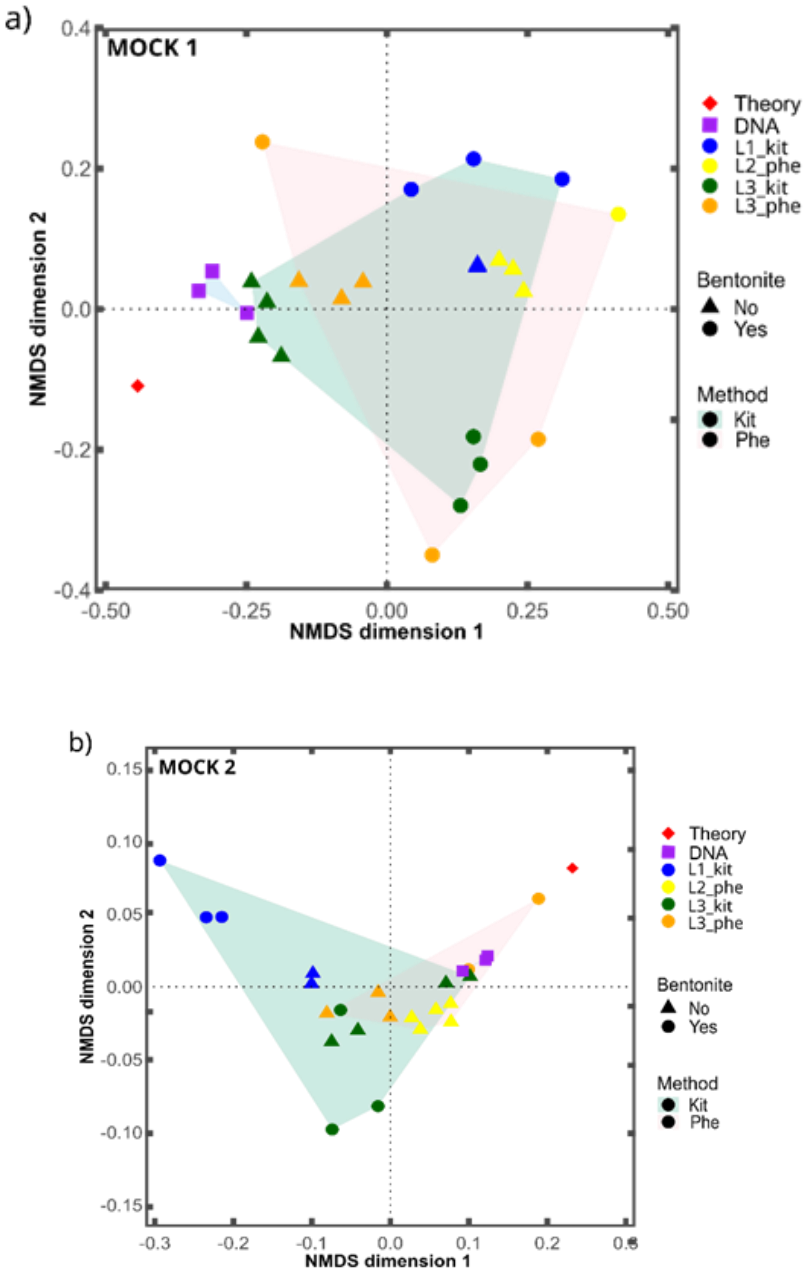

Figure 23: NMDS of ASV-based bacterial community composition in samples spiked with a) Mock 1 and b) Mock 2, using Bray-Curtis distances (stress = 0.13 and 0.02). Kit-based approaches performed by Lab 1 are shown in blue, while those performed by Lab 3 are shown in green, with a green convex hull encompassing the group. Phenol-Chloroform based methods carried out by Lab 2 are depicted in yellow, and those performed by Lab 3 are shown in orange, grouped with a pink convex hull. Samples without bentonite are represented as triangles, while samples with bentonite are shown as circles. The DNA mock is depicted as purple squares, and the expected composition is represented by a red diamond.

4.3.2 Subtask 4.1 Impact of irradiation on microbial viability

Two independent experiments were performed within this subtask. In the first experiment, we investigated the effect of gamma radiation on the microbiology of FEBEX bentonite. In the second, some of the samples were amended with an SRB consortium to analyse the persistence of this bacterial group.

In the original FEBEX bentonite powder, no difference in microbial diversity was found between irradiated and unirradiated bentonite powder, but viability (by colony-forming units (CFUs) of aerobes and Most-Probable Number (MPN) of SRB) was found to be zero in the irradiated bentonite powder sample.

In the prepared compacted bentonite samples, the microbial diversity analysis revealed that unirradiated samples and those irradiated with 14 kGy halfway through the incubation period showed similar microbial communities after one year of incubation. However, the double-irradiated treatments (radiation exposure at time zero and 6 months) exhibited a different microbial distribution with certain resilient genera such as *Massilia*, *Acinetobacter*, *Pseudomonas* that could have persisted through mechanisms like sporulation, which offers higher radiation tolerance (Laskowska and Kuczyńska-Wiśnik, 2020; van Gerwen et al., 1999).

In general, the most abundant genera in the samples (both with and without irradiation) at time zero and after one year of incubation are bacteria known for their resistance to harsh conditions such as *Saccharopolyspora*, *Pseudomonas*, *Streptomyces*, *Acinetobacter*, and *Bacillus*. Biomass abundance (quantified by qPCR with the 16S rRNA gene) in samples irradiated at 6 months (14 kGy) was similar to that for unirradiated samples, but lower for samples irradiated twice (cumulative dose 28 kGy). However, no microbial growth was observed, neither at time 0 nor at 6 months of incubation, for treatments initially irradiated with 14 kGy. In contrast, viable cells were detected in the year-long treatment irradiated at the same dose but after 6 months of incubation, indicating that the impact of radiation differs depending on the growth stage of the bacterial community. Pitonzo et al., (2019) observed a similar trend (total dose of 9.34 kGy) where irradiated bacteria could be reactivated to a cultivable stage over time when environmental conditions become favourable again. This corroborated previous diversity results and it shows that when the total dose is reduced to 14 kGy and is preceded by a 6-month incubation period, microbial survival was observed. Thus, 1-year incubation results suggested possible recovery of bacterial communities from irradiation.

No major differences were observed in the microbial composition (based on 16S rRNA gene amplicon sequencing) of unamended and SRB-amended samples. Additionally, quantification of the abundance of SRB (using marker genes *apsA* and *dsrA*) after 1 year of incubation (regardless of irradiation treatment) revealed a very low or non-detectable signal in all unamended samples. In contrast, in the treatments amended with an SRB consortium and irradiated, some resilience was observed. Unfortunately, DNA-based tools such as this one, do not allow the probing of whether or not cells are alive. However, the abundance of cultivable bacteria can be quantified by the assessing the Most Probable Number, using specific media. In the SRB-amended treatments, the cultivable sulphate-reducing cells were detected in unirradiated samples at two time points: 6 months and 1 year. In contrast, irradiated treatments (both at 14 kGy and 28 kGy) showed no viable cells, except for a small signal in the irradiated SRB-consortium sample at 6 months, which identified *Desulfosporosinus* and *Bacillus* as survivors of irradiation. Both genera are spore-formers and hence have the capability to resist irradiation and desiccation. In general, it can be concluded that gamma irradiation (i.e. for cumulative doses of 14 kGy and 28 kGy) negatively affects SRB viability.

Copper discs within the bentonite blocks were analysed after 6 months by microscopy and spectroscopy (ESEM, XPS, and micro-FTIR; the latter two are pending). The results (Figure 24) show signs of corrosion in unirradiated samples, especially in those samples amended with the SRB consortium, revealing copper oxide, sulphur compounds, and chloride-containing precipitates (which may be related to the presence of porewater). Moreover, irradiated samples (14 kGy) showed less corrosion, with localised copper chloride precipitates. Only treatments with the SRB consortium showed signs of possible copper sulphide precipitates. This finding could indicate the impact of microorganisms on copper corrosion.

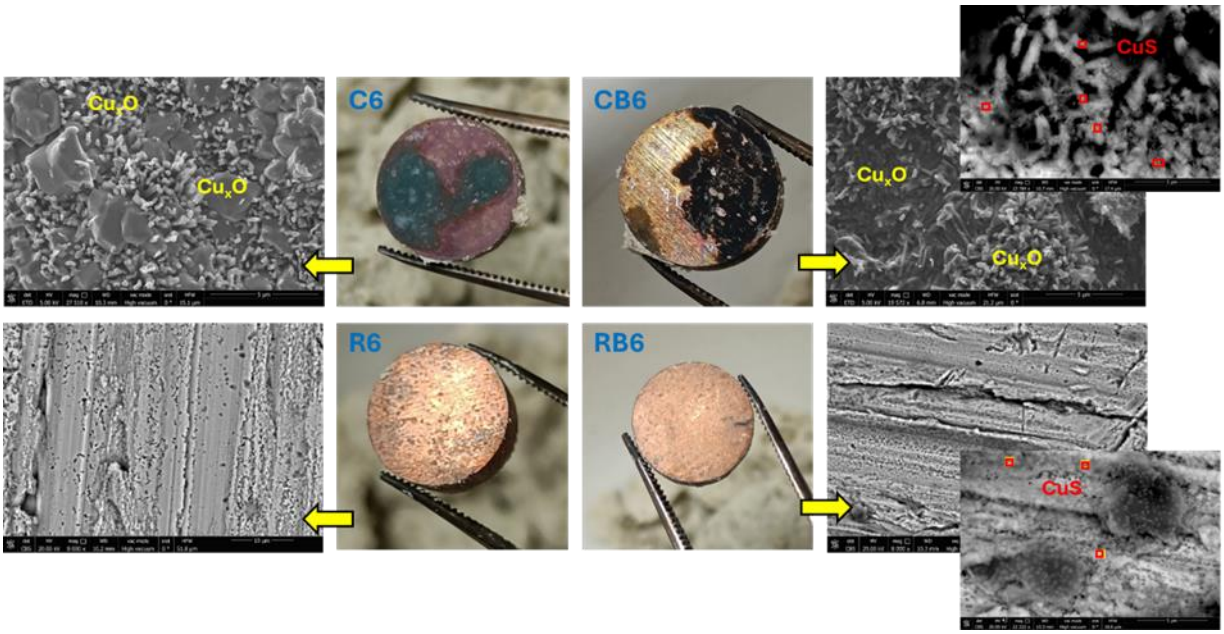

Figure 24: Copper discs from different treatments (C6, CB6, R6, RB6) after 6 months of anoxic incubation. Electron images from scanning electron microscopy of the surface of the Cu discs with yellow marks in the areas of copper oxide precipitates and red marks in the areas of S signal (possible copper sulphide).

From a mineralogical point of view, no significant changes were observed in the bentonite samples after irradiation (14 or 28 kGy) after 6 and 12 months of incubation and/or with the addition of bacteria. The bentonite samples maintained the main character of a dioctahedral two-layer hydrated Ca-Mg-montmorillonite, with typical vibrational bands, and their expansibility or swelling behaviour, with no signs of illitisation (Figure 25). In addition, no modifications were observed in the cation exchange properties and ion inventories of the analysed samples with respect to the untreated FEBEX bentonite.

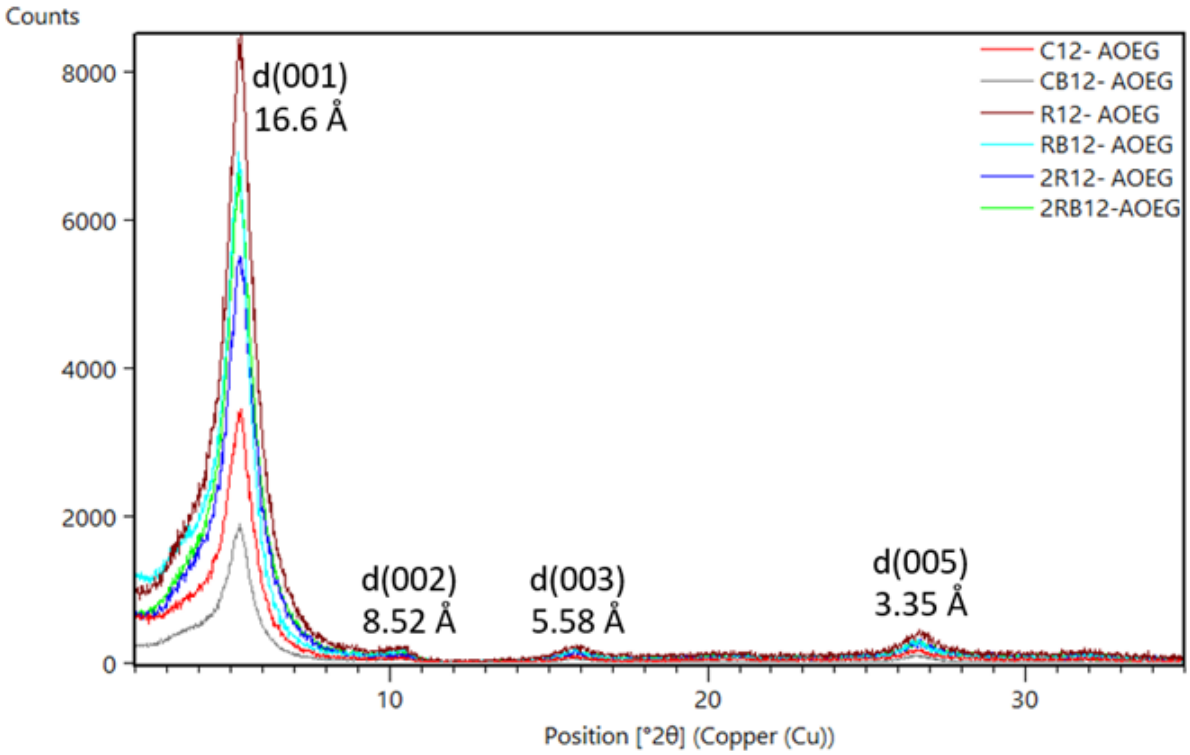

Figure 25: XRD patterns of oriented aggregate samples after ethylene glycol treatment of the bentonite samples after 1 year of anaerobic incubation (C: non-irradiated controls; B: SRB consortium; R: one-time irradiated treatments in the middle of the incubation time (14 kGy); 2R: two-times irradiated treatments (28 kGy)).

In the second experiment, we focused on examining the impact of four repository-relevant stressors (temperature, radiation, water saturation, and compaction) on the viability of indigenous microorganisms in bentonite. The cultivation results for heat/IR treated BCV and MX-80 samples showed microbial proliferation in only a few culture samples across all three cultivation conditions, regardless of the temperature (150°C or 90°C) or the presence of radiation (Table 29). The positive BCV cultures were mostly dominated by single dominant genera such as *Kocuria*, *Enhydrobacter* or *Nocardioides*. The spore-forming genus *Kocuria* was reported in soils contaminated with toxic metals or exposed to high levels of ionising radiation (Timkina et al., 2022). Additionally, quantification of microorganisms (by qPCR) in treated BCV and MX-80 bentonite samples did not reveal noticeable growth in any of the samples and no microbial proliferation was detected, even in treated compacted bentonite incubated for 6 months after the heat treatment. The same result was obtained from all the incubations of all treated samples in suspended form after the treatment (Table 29). Thus, our data thus demonstrated a strong effect of long-term exposure at both temperatures tested (90°C and 150°C), leading to a dramatic loss of viability and cultivability of indigenous bentonite microorganisms, with similar effects observed in both BCV and MX-80 bentonite. The effect of temperature alone was sufficient to observe no viable organisms; therefore, the effect of irradiation, bentonite state, or water availability could not be assessed since they were combined with the heat treatment.

An additional experiment with heated BCV powder enabled us to unravel the effect of the duration of heat exposure. Microbial proliferation was detected in several samples exposed to 90°C for 1 to 6 months (but much less after 12 months as explained above). On the other hand, the cultivability dramatically decreased in samples exposed to 150°C for similar periods of time. These results contradict the data previously obtained on BCV powder heated at 150°C for 6 and 12 months within the Eurad WP HITEC project (Kašpar et al., 2021). Here, microbial proliferation was detected after 6 months' exposure and possibly also after 12 months' exposure, but only heated bentonite in suspended form was

considered and no enrichment culture or microscopic analysis was included to independently confirm these findings. Additionally, the microbiological analyses were performed on samples provided to the team but they were not obtained by trained microbiologists; therefore we cannot exclude the possibility of false positives but we can exclude false negatives.

Table 29. Summary result table of the main experiment. 30D - 30 days natural incubations, CorrP - bentonite corrosion layer, Water - saturation water, R2A AE/ANA/PGM - media cultivations, LD/qPCR - result of microscopic/qPCR analysis (+ positive/- negative).

Sample name	Experiment	Metal coupons	Continuous saturation	Dry density (kg/m3)	Start w	Final w	Exposure (m)	Temperature (°C)	Radiation dose (Gy/h)	Fresh Gen1 (qPCR)	Fresh Gen2 (qPCR)	30D (LD)	30D (qPCR)	CorrP (qPCR)	Water (qPCR)	R2A AE1 (LD)	R2A AE1 (qPCR)	R2A AE2 (LD)	R2A AE2 (qPCR)	R2A ANA1 (LD)	R2A ANA1 (qPCR)	R2A ANA2 (LD)	R2A ANA2 (qPCR)	PGM1 (LD)	PGM1 (qPCR)	PGM2 (LD)	PGM2 (qPCR)
cBCV_C20_6m_con	A+B	yes	yes	1600	0.200	0.226	6	RT	0	-	-	-	+	+	+	+	+	+	+	+	+	+	+	+	+	+	+
cBCV_C21_9m_con	A+B	yes	yes	1600	0.200	0.245	9	RT	0	-	NA	+	+	-	+	+	+	+	+	+	+	+	+	+	+	+	+
cBCV_C22_12m_con	A+B	yes	yes	1600	0.200	0.238	12	RT	0	+	-	+	+	NA	+	+	+	+	+	+	+	+	+	+	+	+	+
cBCV_C23_18m_con	A+B	yes	yes	1600	0.200	0.239	18	RT	0	+	NA	+	+	+	NA	+	+	+	+	+	+	+	+	+	+	+	+
cBCV_C12_9m_T90_IR	B	yes	yes	1600	0.200	0.209	9	90	0.4	-	NA	-	-	-	NA	-	-	-	+	-	-	-	-	-	+	+	+
cBCV_C14_12m_T90_IR	B	yes	yes	1600	0.200	0.232	12	90	0.4	-	-	-	-	NA	NA	-	-	-	-	-	-	-	-	-	-	-	-
cBCV_C16_18m_T90_IR	B	yes	yes	1600	0.200	0.183	18	90	0.4	-	NA	-	-	-	NA	-	-	+	+	-	+	-	-	-	-	-	-
cBCV_C13_9m_T90	B	yes	yes	1600	0.200	0.246	9	90	0	-	-	-	-	-	NA	-	-	-	-	-	-	-	-	-	-	-	-
cBCV_C15_12m_T90	B	yes	yes	1600	0.200	0.239	12	90	0	-	-	-	-	NA	NA	-	-	-	-	-	-	-	-	-	-	-	-
cBCV_C17_18m_T90	B	yes	yes	1600	0.200	0.218	18	90	0	-	NA	-	-	-	NA	-	-	-	-	-	-	-	-	-	-	-	-
cBCV_C1_6m_T150_IR	A	yes	yes	1600	0.150	0.211	6	150	0.4	-	-	-	-	-	NA	-	-	-	-	-	-	-	-	-	-	-	-
cBCV_C3_9m_T150_IR	A	yes	yes	1600	0.150	0.251	9	150	0.4	-	NA	-	-	-	NA	-	-	-	-	+	+	-	-	-	-	-	-
cBCV_C5_12m_T150_IR	A	yes	yes	1600	0.150	0.205	12	150	0.4	-	-	-	-	NA	NA	-	-	-	-	-	-	-	-	-	-	-	-
cBCV_C7_18m_T150_IR	A	yes	yes	1600	0.150	0.226	18	150	0.4	-	NA	-	-	-	NA	-	-	-	-	-	-	-	-	-	-	-	-
cBCV_C2_6m_T150	A	yes	yes	1600	0.150	0.213	6	150	0	-	NA	-	-	-	NA	-	-	-	-	-	-	-	-	-	-	-	-
cBCV_C4_9m_T150	A	yes	yes	1600	0.150	0.220	9	150	0	-	NA	-	-	-	NA	+	+	-	-	-	-	-	-	+	+	-	-
cBCV_C6_12m_T150	A	yes	yes	1600	0.150	0.093	12	150	0	-	-	-	-	NA	NA	-	-	-	-	-	-	+	+	+	+	-	-
cBCV_C8_18m_T150	A	yes	yes	1600	0.150	0.223	18	150	0	-	NA	-	-	-	NA	-	-	-	-	-	-	-	-	-	-	-	-
cMX80_C11_18m_con	A	yes	yes	1600	0.150	0.196	18	RT	0	-	NA	-	-	+	NA	+	+	+	+	+	+	+	+	+	+	+	+
cMX80_C18_18m_T90_IR	A	yes	yes	1600	0.200	0.206	18	90	0.4	-	NA	-	-	-	NA	-	-	-	-	-	-	-	-	-	+	-	-
cMX80_C19_18m_T90	A	yes	yes	1600	0.200	0.204	18	90	0	-	NA	-	-	-	NA	-	-	-	-	-	-	-	-	-	-	-	-
cMX80_C9_18m_T150_IR	A	yes	yes	1600	0.150	0.166	18	150	0.4	-	NA	-	-	-	NA	-	-	-	-	-	-	-	-	-	-	-	-
cMX80_C10_18m_T150	A	yes	yes	1600	0.150	0.200	18	150	0	-	NA	-	-	-	NA	-	-	-	-	-	-	-	-	-	-	-	-
cBCV_C33_12m_con	C	no	no	1600	0.150	0.118	12	RT	0	+	-	+	+	NA	NA	+	+	+	+	+	+	+	+	+	+	+	+
cBCV_C32_12m+6_con	C	no	no+R	1600	0.150	0.243	12+6	RT	0	-	-	+	+	NA	+	+	+	+	+	+	+	+	+	+	+	+	+
cBCV_C29_12m_T90_IR	C	no	no	1600	0.150	0.125	12	90	0.4	-	-	-	-	NA	NA	-	-	-	-	-	-	-	-	-	-	-	-
cBCV_C28_12+6m_T90_IR	C	no	no+R	1600	0.150	0.243	12+6	90	0.4	-	-	-	-	NA	-	-	-	-	-	-	+	-	-	-	-	-	-
cBCV_C31_12m_T90	C	no	no	1600	0.150	0.141	12	90	0	-	-	-	-	NA	NA	-	-	-	-	-	-	-	-	-	-	-	-
cBCV_C30_12m+6_T90	C	no	no+R	1600	0.150	0.242	12+6	90	0	-	-	-	-	NA	-	-	-	-	-	-	-	-	-	-	-	-	-
cBCV_C25_12m_T150_IR	C	no	no	1600	0.150	0.101	12	150	0.4	-	-	-	-	NA	NA	-	-	-	-	-	-	-	-	-	-	-	-
cBCV_C24_12m+6_T150_IR	C	no	no+R	1600	0.150	0.237	12+6	150	0.4	-	-	-	-	NA	-	-	-	-	-	-	-	-	-	-	-	-	-
cBCV_C27_12m_T150	C	no	no	1600	0.150	0.099	12	150	0	-	-	-	-	NA	NA	-	-	-	-	-	-	-	-	-	-	-	-
cBCV_C26_12m+6_T150	C	no	no+R	1600	0.150	0.232	12+6	150	0	-	-	-	-	NA	-	-	-	-	-	-	-	-	-	-	-	-	-
cMX80_C36_12m_con	C	no	no	1600	0.150	0.132	12	RT	0	-	-	+	+	NA	NA	+	+	+	+	+	+	+	+	+	+	+	+
cMX80_C34_12m_T90_IR	C	no	no	1600	0.150	0.125	12	90	0.4	-	-	-	-	NA	NA	-	-	-	-	-	-	-	-	-	-	-	-
cMX80_C35_12m_T90	C	no	no	1600	0.150	0.125	12	90	0	-	-	-	-	NA	NA	-	-	-	-	-	-	-	-	-	-	-	-
sBCV_C45_12m_con	D	no	NA	suspension 1:3		NA	12	RT	0	+	NA	NA	NA	NA	NA	+	+	+	+	+	+	+	+	+	+	+	+
sBCV_C39_12m_T90_IR	D	no	NA	suspension 1:3		NA	12	90	0.4	-	NA	-	-	NA	NA	-	-	-	-	-	-	-	-	-	-	-	-
sBCV_C40_12m_T90	D	no	NA	suspension 1:3		NA	12	90	0	-	NA	-	-	NA	NA	-	-	-	-	-	-	-	-	-	-	-	-
sBCV_C37_1m_T150_IR	D	no	NA	suspension 1:3		NA	1	150	0.4	-	NA	-	-	NA	NA	-	-	-	-	-	-	-	-	-	-	-	-
sBCV_C38_1m_T150	D	no	NA	suspension 1:3		NA	1	150	0	-	NA	-	-	NA	NA	-	-	-	-	-	-	-	-	-	-	-	-
pBCV_C46_12m_con	D	no	NA	powder	0.114	NA	12	RT	0	-	NA	+	+	NA	NA	+	+	+	+	+	+	+	+	+	-	+	+
pBCV_C43_12m_T90_IR	D	no	NA	powder	0.114	NA	12	90	0.4	-	NA	-	-	NA	NA	-	-	-	-	-	-	-	-	-	-	-	-
pBCV_C44_12m_T90	D	no	NA	powder	0.114	NA	12	90	0	-	NA	-	-	NA	NA	-	-	-	-	-	-	-	-	-	-	-	-
pBCV_C41_12m_T150_IR	D	no	NA	powder	0.114	NA	12	150	0.4	-	NA	-	-	NA	NA	-	-	-	-	-	-	-	-	-	-	-	-
pBCV_C42_12m_T150	D	no	NA	powder	0.114	NA	12	150	0	-	NA	-	-	NA	NA	-	-	+	+	-	-	-	-	-	-	-	-
sMX80_C55_12m_con	D	no	NA	suspension 1:6		NA	12	RT	0	+	NA	NA	NA	NA	NA	+	+	-	-	+	+	+	+	+	+	+	+
sMX80_C49_12m_T90_IR	D	no	NA	suspension 1:6		NA	12	90	0.4	-	NA	-	-	NA	NA	-	-	-	-	-	-	-	-	-	-	-	-
sMX80_C50_12m_T90	D	no	NA	suspension 1:6		NA	12	90	0	-	NA	-	-	NA	NA	-	-	-	-	-	-	-	-	-	-	-	-
sMX80_C47_1m_T150_IR	D	no	NA	suspension 1:6		NA	1	150	0.4	-	NA	-	-	NA	NA	-	-	-	-	-	-	-	-	-	-	-	-
sMX80_C48_1m_T150	D	no	NA	suspension 1:6		NA	1	150	0	-	NA	-	-	NA	NA	-	-	-	-	-	-	-	-	-	-	-	-
pMX80_C56_12m_con	D	no	NA	powder	0.074	NA	12	RT	0	-	NA	+	+	NA	NA	+	+	+	+	+	+	+	+	+	+	+	+
pMX80_C53_12m_T90_IR	D	no	NA	powder	0.074	NA	12	90	0.4	-	NA	-	-	NA	NA	-	-	-	-	-	-	-	-	-	-	-	-
pMX80_C54_12m_T90	D	no	NA	powder	0.074	NA	12	90	0	-	NA	-	-	NA	NA	-	-	-	-	-	-	-	NA	-	-	-	-
pMX80_C51_12m_T150_IR	D	no	NA	powder	0.074	NA	12	150	0.4	-	NA	-	-	NA	NA	-	-	-	-	-	-	-	-	-	-	-	-
pMX80_C52_12m_T150	D	no	NA	powder	0.074	NA	12	150	0	-	NA	-	-	NA	NA	-	-	-	-	-	-	-	-	-	-	-	-

Our study has shown that both bentonite types (BCV and MX-80) host a diverse indigenous microbial community, in which many taxa are known to be resistant to harsh environments and to be able to form spores that can germinate to a metabolically active state when the conditions become favourable again. Almost all the BCV and MX-80 control samples resulted in positive culture results (Table 29) with a

diverse microbial composition. In BCV samples, in the R2A (aerobic and anaerobic) medium, we observed the growth of common bentonite genera belonging to the families Bacillaceae and Clostridiaceae, and the genus *Pelosinus*. In PGM medium, genera such as *Pelosinus* and *Sporacetigenium* were most abundant, followed by genus *Desulfosporosinus*, *Bacillus*, a range of *Clostridium* spp. along with rarer genera, for example *Sporomusa* and *Anaerosporomusa,* all of which are spore formers. In control MX-80 samples, the overall diversity was much lower and the samples cultivated in R2A (aerobic and anaerobic) primarily included genera belonging to the order Bacillales, particularly the genus *Paenibacillus* and, to a lesser extent, the genera *Clostridium* or *Lysinibacillus*. All of these taxa are spore formers. For PGM medium, genera such as *Sporacetigenium*, *Desulfosporosinus*, *Anaerospora, Sedimentibacter* and *Pelosinus,* or members of the order Bacillales, dominated the culture samples. Our results demonstrate that the viability of the bentonite microbial community remained unaffected even after 18 months in the bentonite samples compacted to a dry density of 1600 kg m^{-3}.

Previous work predicted that the initial hot phase of deep geological repository (DGR) evolution, when temperature and irradiation reach their peak, would cause a dramatic loss in microbial survivability, resulting in the potential creation of zones free of biological activity around the canister (Aoki et al., 2010; Stroes-Gascoyne and West, 1997). The results obtained from the treated bentonite samples are in good accordance with this hypothesis and we showed that microbial activity (including spore-forming microorganisms) in bentonite and, therefore, the risk of MIC, might be strongly suppressed in the areas where the bentonite will be exposed to a temperature of 90°C or higher for the long term, presumably near the canister surface. However, the formation and spatial distribution of this presumed biology-free zone will depend upon the overall temperature within the DGR. The presence of highly resistant bentonite microorganisms capable of germination to a metabolically active state when the conditions become favourable again was clearly demonstrated in the heated samples (up to 6 months' exposure at 90°C), where some bacteria still showed cultivability post-exposure. Long-term experiments testing the microbial response to temperatures below 90°C are needed to determine the possible effect of temperature gradients on microbial survivability in the bentonite sealing layer. Another unresolved question is the rate of microbial recolonisation of the abiotic zone from the surrounding environment. Combining microbial survivability data with mathematical modelling of the evolution of environmental conditions in the DGR during its lifetime has excellent potential for increasing the accuracy of long-term predictions of microbial effects in the DGR.

4.3.3 Subtask 4.2 Impact of bentonite dry density on microbial activity

A knowledge gap was identified regarding the impact of dry density on microbial activity. This should be studied for a variety of bentonite types (here: MX-80 and Calcigel). Extensive optimisation of the reactor design was performed: (a) to avoid tubing failure, various types of tubing were tested and the best was found to be thick Norprene tubing (ID 1.6 mm and OD 4.8 mm); (b) to avoid filter corrosion, titanium filters were selected, as stainless filters rapidly corroded; (c) to prevent leakage from the plastic to stainless steel tubing joints, the stainless steel tubing was wrapped in Teflon tape, the Norprene tubing slid on top and a zip tie added to hold the plastic tubing in place. With this setup, the microorganisms can only grow where the electron donor and acceptor gradients meet, that is, within the bentonite (Figure 20C). It is also possible to adjust the flow rate of one or other of the solutions, as H_2 is expected to diffuse faster than sulphate. Finally, bromide (Br^-) is added to the sulphate-containing solution to serve as a conservative diffusion tracer. To ensure that oxygen does not enter the system and fuel microbial growth, dissolved oxygen (DO) in the APW and the waste bottles are monitored continuously via an optical sensor (optode) system (Figure 20D). The solution that is flowed into the bentonite is artificial Opalinus Clay porewater.

The saturation of the Wyoming bentonite and gypsum dissolution was tested in the 1st experimental phase at EPFL. This was done via the diffusion-controlled dissolution of gypsum by pumping a sulphate- and bromide-free anoxic APW (equilibrated with 1.5 bar N_2/CO_2) past the bentonite on both sides of the

reactor and measuring the sulphate concentration in the effluent. This was performed with bentonite placed in the diffusive reactor at 1.2 g cm^{-3} dry density. Approximately 100 mg of sulphate were released from the bentonite through the slow dissolution of gypsum and it took approximately 95 days to reach a plateau in sulphate release from bentonite.

In the second experimental phase, H_2 and sulphate were added to the reactor. Twelve reactors were packed with bentonite MX-80 and one end of each of the reactors was connected to a reservoir of APW that included sulphate and bromide (under 1.5 bar of N_2/CO_2), while the other end received APW in equilibrium with 1.5 bar of H_2 (

Figure 26).

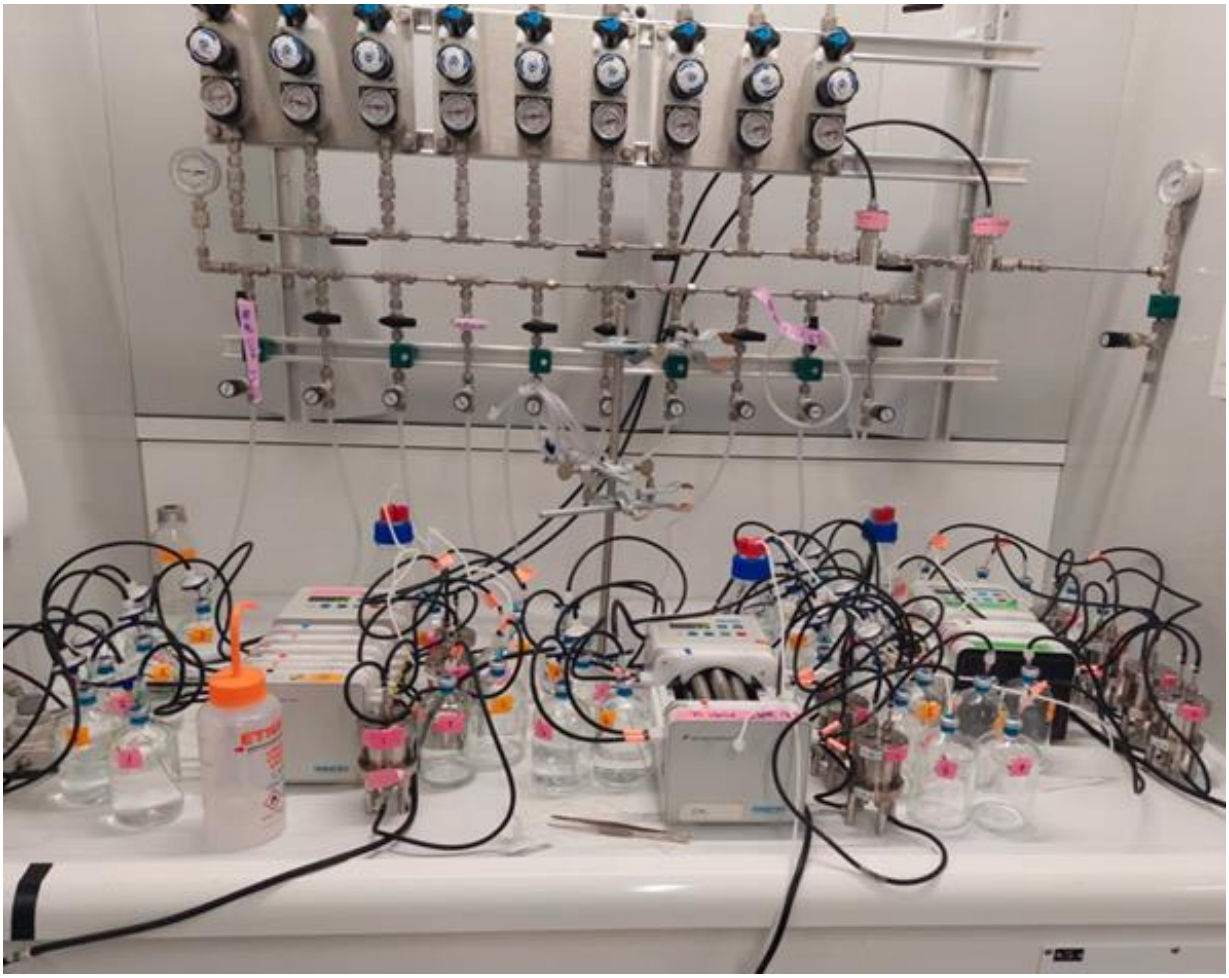

Figure 26. Experimental set-up showing the 12 reactors and the APW reservoirs during the experimental phase 2. Each reactor included two APW reservoirs (used for either end) and two waste bottles.

The difficulty associated with this experiment is that the reservoir APW cannot be recirculated. This entails producing large volumes of anoxic APW to continuously run the experiment. Daily reservoir change is needed to keep the experiment running. The experiment was performed for 3 weeks, and three reactors were destructively sampled at time zero and after each week. Unfortunately, neither sulphate nor bromide was detected in the effluent for the 3 weeks of the experiment.

From the collected bentonite, DNA was extracted and 16S rRNA gene fragments were amplified via qPCR. In contrast to the original bentonite, at time zero, corresponding to the bentonite at the beginning of the H_2 and sulphate amendment (in opposite directions), there was a large range of 16S rRNA copy

number per gram of dry bentonite, with values ranging from 5.0E+04 to 4.3E+05 (Figure 27). Most intriguingly, the values are order of magnitudes larger than those obtained for the original bentonite. Therefore, it was concluded that growth occurred during the first phase (gypsum dissolution phase) as no H_2 was being supplied at that time. Another source of electrons, for example organic carbon contained in the bentonite must have been present. The microbial community analysis is ongoing and will provide more insight into the specific microorganisms able to grow under these conditions.

The other surprise was the observation that subsequent time points did not show evidence of an increase in biomass but rather no statistically significant change between 0, 7, 14 and 21 days, despite the addition of H_2 as an electron donor starting at time zero. The most likely interpretation for this observation is that sulphate and H_2 had not diffused sufficiently to meet each other and the biomass no longer had an electron acceptor, therefore, there was no additional growth relative to time zero. The conclusion from this result is that a much longer time is needed for biomass growth under diffusion limited conditions.

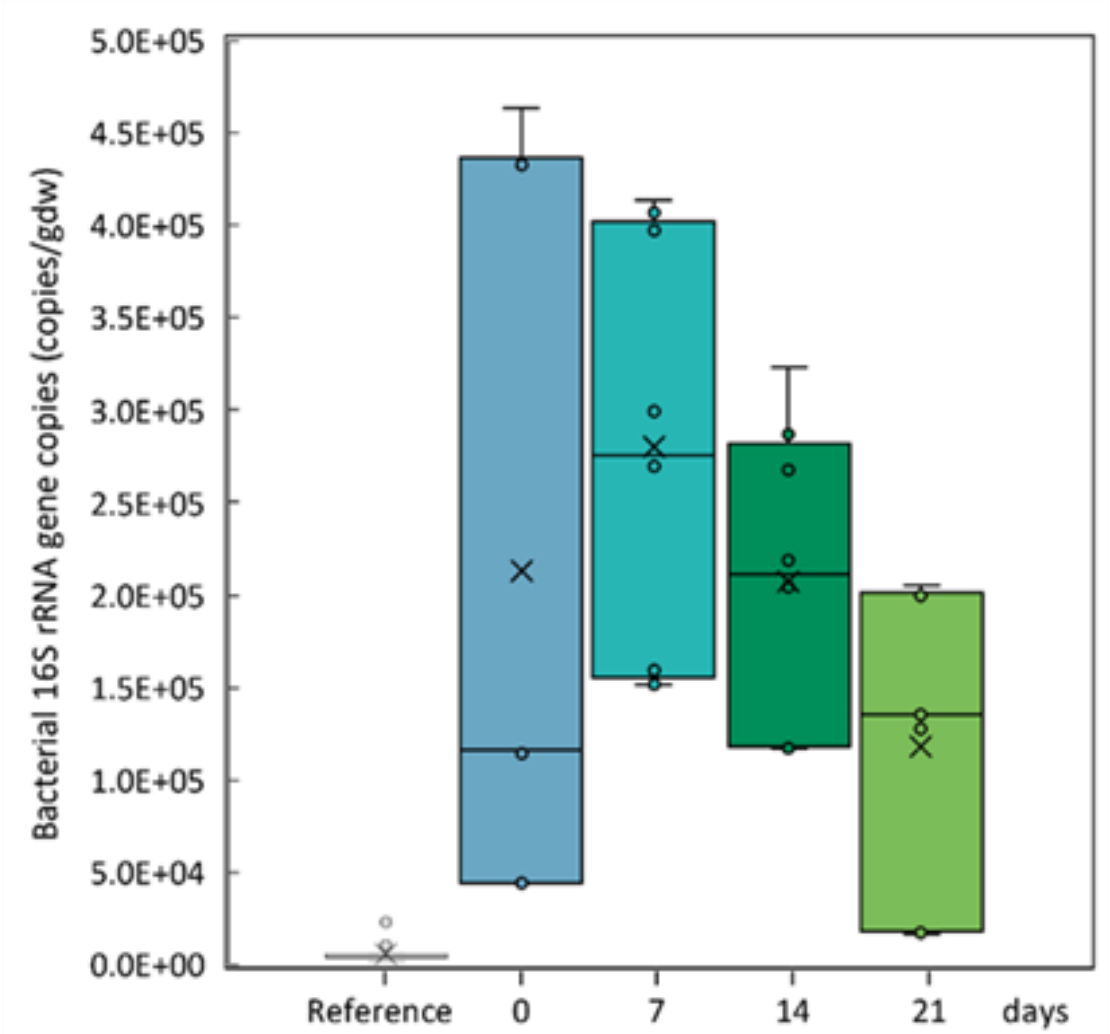

Figure 27. Bacterial abundance expressed as 16S rRNA gene copy numbers per gram of bentonite (dry weight) for the reference bentonite (as received) and the bentonite after treatment for dissolution (0 days) and subsequently after 7, 14 and 21 days. Data are presented in a box and whisker plot in which the median is indicated with a cross, the mean with a line and each data point with a dot. The box shows the 25th to 75th percentile and the whiskers show the maximum and minimum values of the data.

At HZDR, the same diffusion reactor as at EPFL was set up with some small differences (Figure 28). Due to several difficulties in setting up this system (e.g. material procurement, corrosion of filters) the team only managed to develop and establish a diffusion reactor setup during the project. The first

experimental phase with the saturation of the Calcigel bentonite and its gypsum dissolution was also performed. The Calcigel bentonite has a water content of 4.96±0.28% and at least 0.056 mg of sulphate per gram of bentonite. Therefore, it is expected that the time needed for saturation and dissolution of sulphate for Calcigel would be faster than MX-80 bentonite due to the lower content of sulphate. After 48 hours, we observed that Calcigel bentonite appeared to be saturated.

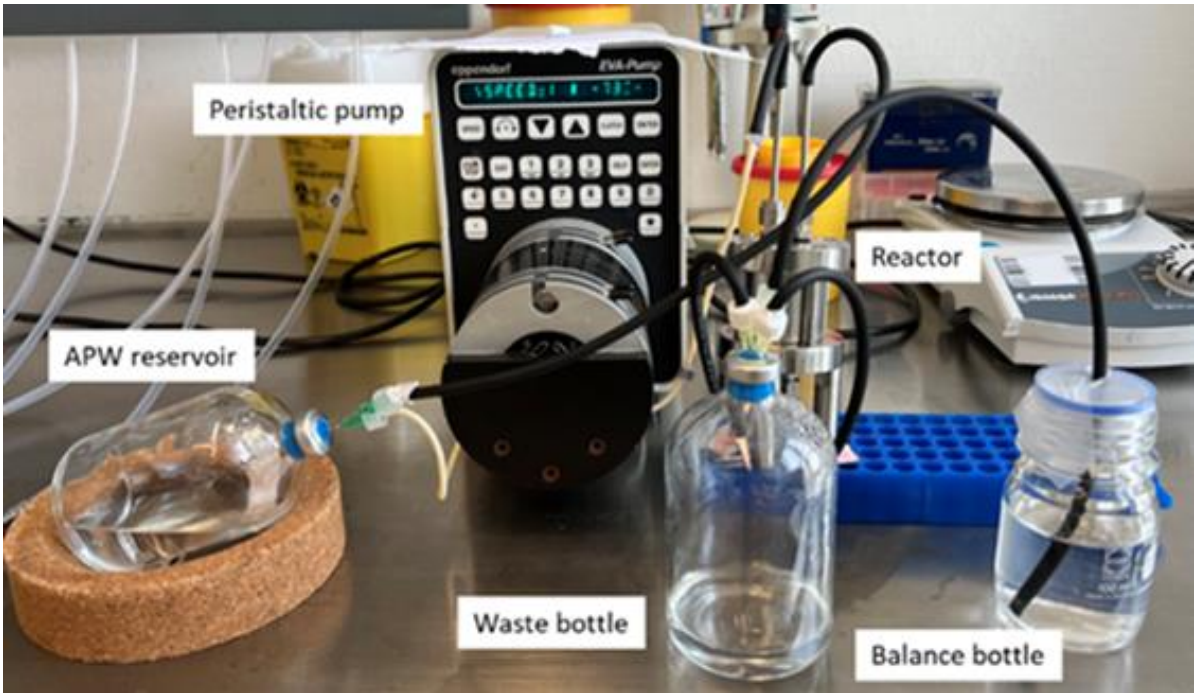

Figure 28. The final reactor setup for the trial saturation and equilibration phase. The anoxic artificial Opalinus Clay porewater (APW) reservoir was pressurised with N_2 gas at 1.5 bar and the waste bottle was flushed with N_2 gas before closure.

During the development of the diffusion reactor setup, batch microcosms with Calcigel bentonite incubated under different conditions and different incubation times were prepared. The results showed that in the microcosms containing hydrogen in the atmosphere, Calcigel bentonite and metal coupons (HCalC), sulphate concentration decreased the most (Figure 29). In addition, the hydrogen content in the atmosphere of these microcosms was also lower than that in those with sterile bentonite. This leads to the conclusion that hydrogen as a potential electron donor and sulphate as an electron acceptor were consumed in these microcosms by the microorganisms present.

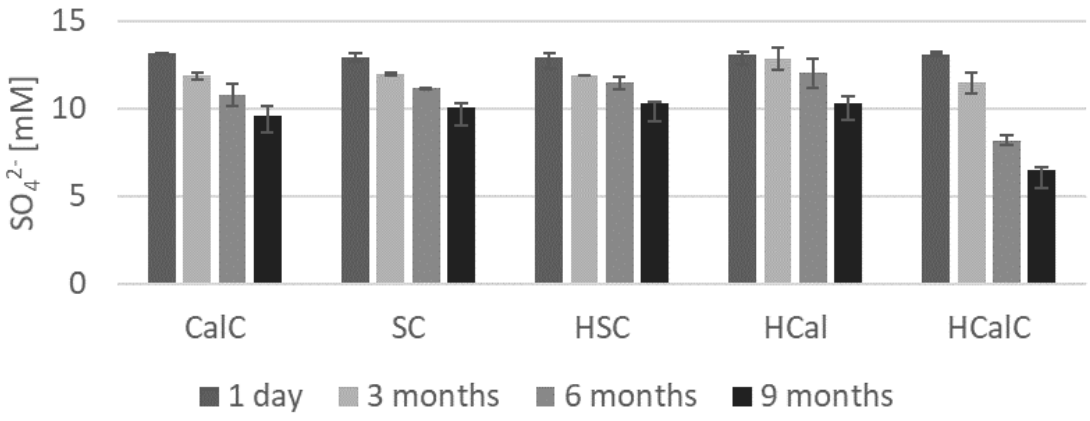

Figure 29. The changes of sulphate concentration in microcosms under five different conditions. CalC: Calcigel bentonite + metal coupons; SC: sterilised Calcigel bentonite + metal coupons; HSC: hydrogen gas + sterilised Calcigel bentonite + metal coupons; HCal: hydrogen gas + Calcigel bentonite; HCalC: hydrogen gas + Calcigel bentonite + cast iron coupons.

Microbial diversity analysis also showed that sulphate-reducing bacteria from the genus *Desulfotomaculum* were enriched in these samples, indicating that Calcigel bentonite harbours sulphate-reducing bacteria that are active under the applied conditions. The analysis of the surface of the coupons from these microcosms showed that the alteration of the surface of the coupons was more intense at lower incubation times because a layer of Ca- containing minerals was later formed that seemed to protect the surface of the coupons. In addition, sulphide minerals were found on the surface, which indicate again the activity of sulphate-reducing bacteria. A high corrosion rate was also observed in these microcosms. A similar high corrosion rate was only observed in microcosms with hydrogen in the atmosphere and sterilised Calcigel bentonite (HSC) (Figure 30). These microcosms also contained the highest hydrogen content in the atmosphere, which indicates the occurrence of abiotic corrosion.

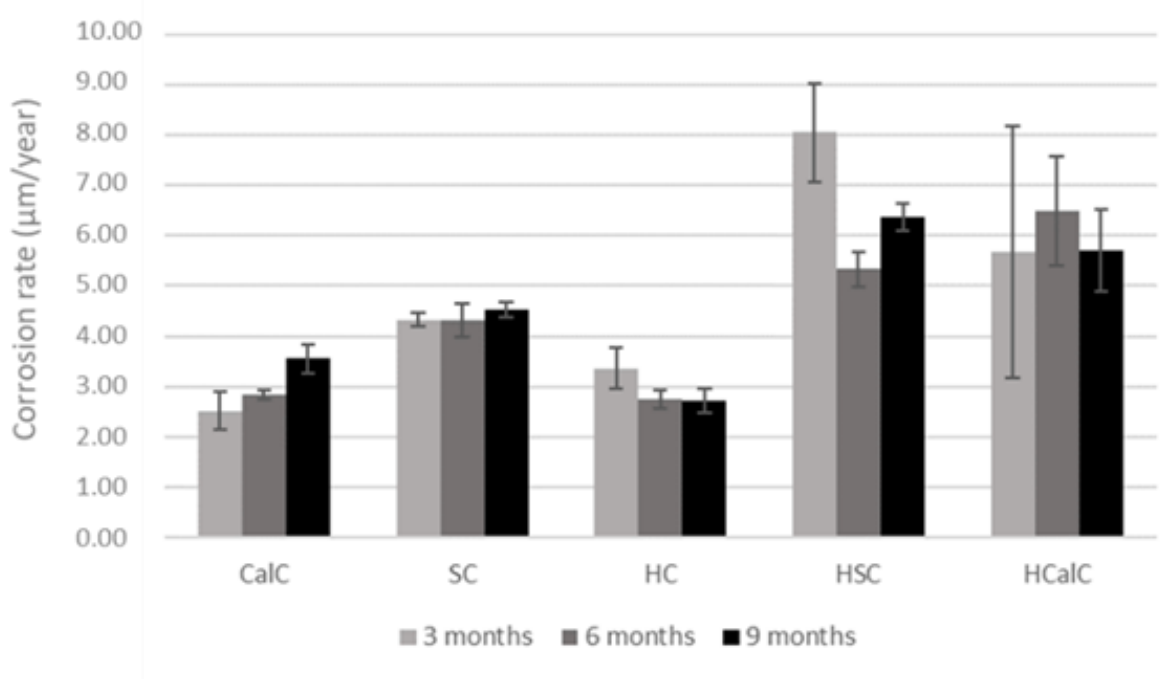

Figure 30. Corrosion rates of coupons incubated in microcosms under five different conditions. CalC: Calcigel bentonite + cast iron coupons; SC: sterilised Calcigel bentonite + cast iron coupons; HC: hydrogen gas + cast iron coupons, HSC: hydrogen gas + sterilised Calcigel bentonite + cast iron coupons; HCalC: hydrogen gas + Calcigel bentonite + cast iron coupons.

Overall, the results show that the Calcigel bentonite is a good candidate for studying the impact of dry density on microbial activity and corrosion because this bentonite has a low sulphate content and it contains naturally occurring sulphate-reducing bacteria that can under suitable conditions contribute to corrosion, through the production of sulphide, or prevent corrosion, through the consumption of generated hydrogen.

At SCK-CEN, three oedometer cells developed in-house were dismantled after 244 days of percolation (419 days in total). So far, only hydrogen measurements in the headspace of the percolate bottles are available and these indicate an increase of hydrogen in the first three consolidation cells (sterile bentonite without additional hydrogen) (Figure 31). This increase was slower towards the end of the percolation, suggesting faster corrosion at the beginning of the experiment, which evolves towards a slower process. There are only two data points available for the biotic conditions (Cell 5 and Cell 6), but hydrogen levels are ca. 5 times lower. It appears that bacteria are still active in the consolidation cells and are consuming the hydrogen. It is only possible to identify microbial presence and activity after dismantling of the consolidation cells and these investigations are still ongoing.

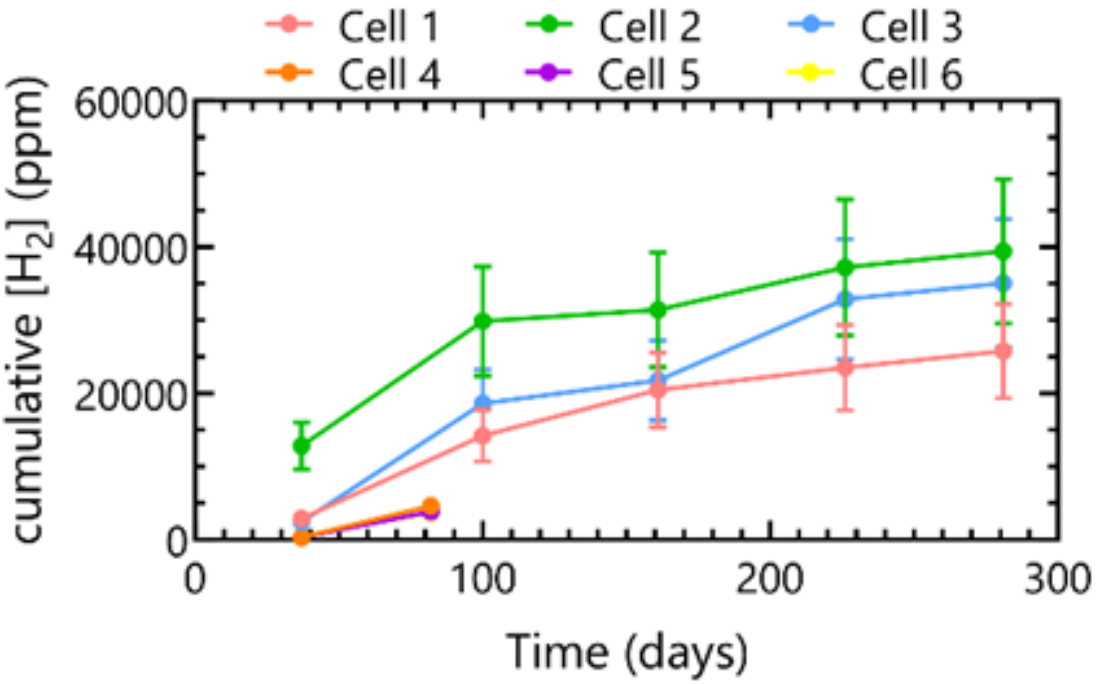

Figure 31. Cumulative hydrogen concentrations in the headspace of the percolate samples collected every two months. Values represent the result and measurement uncertainty. The measurement uncertainty is relatively high as it also includes the fact that septum bottles were not completely leak tight for hydrogen.

4.3.4 Subtask 4.3 Impact of bentonite-associated oxygen on microbial activity and viability

Retrieval of six mini modules after 20 months enabled direct comparison of the impact of the initial O_2 concentration in the atmosphere in equilibrium with bentonite prior to deployment, and bentonite sterility, on the microbial community, mineralogical changes and corrosion rate. Differences in the thickness of the dark rim on the outside of the bentonite slice is readily observable (Figure 32). Indeed, bentonite initially equilibrated in the absence of O_2 exhibited the thickest rim on the outer perimeter of the bentonite cylinder. In contrast, the 100% O_2 condition, exhibited the thinnest. Intermediate O_2 concentrations exhibited an intermediate thickness. In addition, the difference between sterile and non-sterile bentonite exposed to 21% O_2 is evident with the non-sterile case exhibiting more dark spots in the inner part of the bentonite slice.

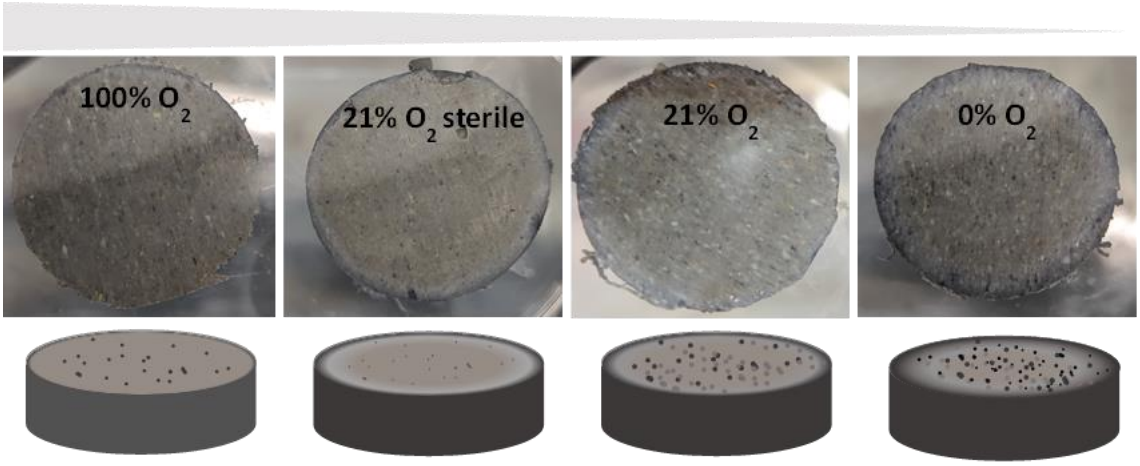

Figure 32. images of slices of bentonite from the mini modules deployed within an Opalinus Clay borehole for 20 months. The condition is indicated for each case. The bottom part of the figure is a schematic rendition of the observations.

The qualitative observations are borne out in the in-depth analyses. First, micro-XRF analysis showed the pattern of sulphur distribution in cross-section rims for each condition. In the absence of O_2, the S-containing layer was thickest (Figure 33), while it was not detectable in the bentonite originally exposed to 100% O_2. Furthermore, the sterile bentonite exposed to 21% O_2 shows a clearly delimited enrichment, while the non-sterile condition exhibits more diffuse S. These results suggest active sulphate reduction in the 0% O_2 experiment resulted in the precipitation of iron sulphide phases but not in the 100% O_2 condition. Furthermore, in the sterile bentonite, SRB originated from the borehole water while in the non-sterile case, they originated from both the bentonite and the borehole water, explaining the difference in S distribution.

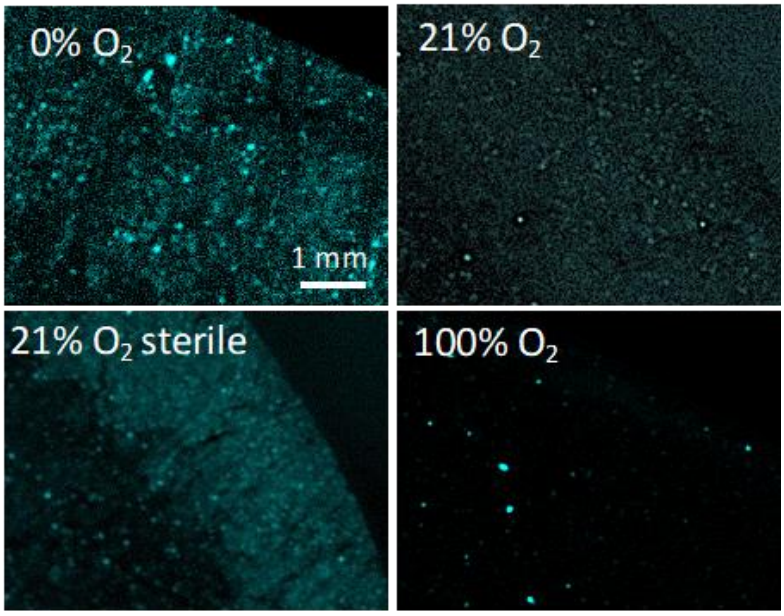

Figure 33. MicroXRF maps of bentonite cross-sections from bentonite prepared in four ways prior to deployment: (a) exposed to 0% O2 atmosphere for 12 months; (b) sterile and exposed to 21% O2 atmosphere for 12 months; (c) exposed to 21% O2 atmosphere for 12 months. (d) exposed to 100% O2 atmosphere for 12 months.

Furthermore, microbial growth varies substantially between different conditions (Figure 34). Quantification of microbial biomass using the 16S rRNA gene and qPCR evidences an increase in

biomass in the outer layer and to a lesser extent in the inner part of the bentonite. The greatest increase in biomass is observed in the 100% O_2 case, suggesting proliferation of aerobic microorganisms, both in the outer rim and the inner part of the bentonite. In addition, more growth is observed in the 21% O_2, non-sterile bentonite case than the sterile case. Moreover, the sterile bentonite (21% O_2) exhibits very limited increase in biomass in the inner part, supporting the S microXRF data in suggesting that the borehole microorganisms colonised the outer rim of the bentonite. Finally, the condition corresponding to 0% O_2 exhibits the least growth, supporting the hypothesis that the growth of aerobes is the major contributor to biomass accumulation in this system. DNA sequencing is underway to evaluate whether it is also supported by the microbial community composition.

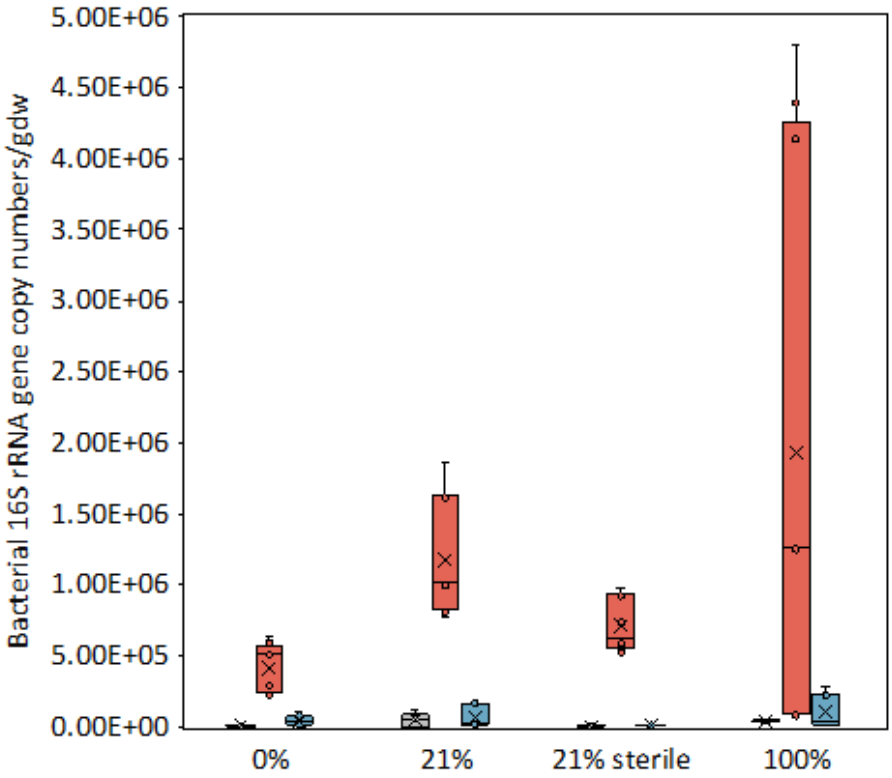

Figure 34. Biomass abundance (measured as 16S rRNA gene copy number normalised to mass) for the four conditions (0% O_2, 21% O_2, 21% O_2 sterile and 100% O_2).

The corrosion of steel coupons placed within the bentonite was evaluated. The thickness of the dense product layer (DPL) in direct contact with the steel and resulting from the precipitation of corrosion products varied with the treatment. The thickest layer was observed at 21% O_2, followed by 100% O_2, suggesting O_2-dependent corrosion. Interestingly, by comparing the sterile to the nonsterile 21% O_2 condition, we observe that the non-sterile condition exhibits a much thicker DPL than the sterile condition, suggesting a role of aerobic bacteria in stimulating corrosion. Copper coupons exhibited no evidence of corrosion in all conditions.

Overall, the data obtained here demonstrate a key role for O_2 in stimulating the growth of (presumably aerobic) microorganisms in bentonite and inhibiting sulphate reducing ones.

4.4 Summary of key outputs from Task 4

The results obtained in Task 4 demonstrate that the high initial temperatures and gamma radiation during the saturation phase have the potential to create a biology-free (i.e. abiotic) bentonite zone, where temperatures of at least 90°C are maintained for the long-term. The suppression of microbial activity in

the vicinity of the canister implies that biofilm formation need not be considered on the canister surface. ConCorD developed novel experimental strategies to systematically investigate the threshold dry density that results in the inhibition of microbial growth, for all types of bentonite. Additionally, it was shown that the Calcigel bentonite is a good candidate for studying the impact of dry density on microbial activity and corrosion because it has a low sulphate content and contains naturally occurring sulphate-reducing bacteria that can under suitable conditions contribute to corrosion (through the production of sulphides).

Based on previous work, it is expected that the only form of microbially-influenced corrosion that should be considered is that due to the diffusion of aggressive metabolic by-products (typically sulphide) to the canister surface from locations where microbial activity is possible. In accordance with this assumption, the compacted bentonite samples from UGR that were supplemented with SRB and iron-reducing bacteria showed the highest alteration of the metal surface (in 1.6 mg m^{-3} dry density FEBEX bentonite). This suggests that sulphide production may affect the corrosion rate even in bentonite compacted at a high dry density (1.6 g cm^{-3}). Unirradiated compacted bentonite samples, without additional bacteria, showed that the metal surface was covered with copper oxides (TEM-EDX, Cu + O) and the coupons exhibited a low corrosion rate.

The influence of O_2 adsorbed on bentonite on corrosion and on sulphate reduction was investigated. First, the DPL was thickest for bentonite pre-exposed to O_2, suggesting the impact of bentonite-associated O_2 on (aerobic) corrosion. Second, the most microbial growth was detected for the bentonite pre-exposed to 100% O_2, while the bentonite pre-exposed to anoxic conditions showed the least growth. Finally, the distribution of sulphur in bentonite suggested an accumulation of sulphur in bentonite inversely proportional to the gas phase concentration of O_2 with which the bentonite was pre-equilibrated. This task also systematically investigated DNA extraction from bentonite and identified the strengths and weaknesses of the two existing DNA extraction protocols. This is important to ensure that distinct methods are validated for the community of microbiologists studying the clay microbiome.

Overall, this task was rich in tool development and validation, and provided conclusive results on the impact of heat and irradiation on microbial survival and growth in bentonite, as well as the impact of clay associated O_2 on microbial growth.

5. Task 5: Corrosion under transients

5.1 Introduction to task

The ConCorD WP was devoted to those less defined processes impacting container durability in deep geological repositories (DGRs) for high-level radioactive waste and, specifically, Task 5 was proposed to analyse in detail the effect of coupled near-field transitory environmental conditions on container corrosion.

Metal corrosion mechanisms are well known and corrosion of container materials has been extensively studied under constant or steady-state conditions (Abdelouas et al., 2022 and references therein; Frankl et al., 2023) that commonly reflect the repository environment in the long-term. However, uncertainties still exist about the role that evolving conditions, which are imposed during the early post-closure period by the different barriers in the near-field, may have on container durability.

At the container / engineered barrier interface, metal corrosion behaviour will depend on the metal's characteristics and it will be controlled by the physico-chemical and specific environmental conditions established by the radioactive waste itself, by the other engineered barriers and by the surrounding groundwater (King and Padovani, 2011). After facility closure, saturation of the bentonite barrier with water from the repository host rock will lead to clay swelling and the development of mechanical loads on, and stresses in, the container. All these factors together will promote transitory conditions in the near-field mainly due to the following aspects: (i) temperature, (ii) radiation levels, (iii) porewater chemical composition, (iv) water activity, (v) redox conditions / oxygen consumption rate, (vi) extent of microbial activity, (vii) processes involving gas generation and (vii) mechanical stresses.

Given the nature of the radioactive waste and the materials that are being considered as barriers today, the above-mentioned transitory conditions are expected, but their temporal evolution, time span and impact on repository security are not known. In addition, other less well defined external perturbations may also impact the durability of waste containers. An understanding of the evolution of the environment surrounding the canister in the repository over long periods of time is essential for a reliable analysis of the corrosion of canister materials.

Task 5 was set up with the objective of experimentally analysing the impact of selected transitory environmental conditions on the corrosion of metal and alloys, considering different candidate container materials for radioactive waste. From the outset, it was mainly proposed to experimentally analyse the effect of coupled thermal, chemical and hydraulic conditions on the corrosion of container materials in the presence of the engineered bentonite barrier. Some experiments considered radiation transients as well, but the microbial and mechanical processes were not specifically addressed in this task.

Four research teams participated in the task, namely CIEMAT (ES), GRS (DE), KIT-INE (DE) and UJV-SURAO (CZ). For the definition of laboratory experiments, particular physico-chemical scenarios established at the container/bentonite interface and specific transient or coupled processes were taken into account for each individual partner.

UJV-SURAO studied the effect of increased temperature (up to 150°C) and gamma-radiation on accelerated corrosion of the reference Czech carbon steel reference canister in contact with Ca-Mg BCV Czech bentonite.

CIEMAT studied the impact of hydraulic (i.e. water saturation) transients, redox transients and thermal transients (going from ambient temperature to 80°C), together with gas evolution, on carbon steel and copper corrosion to relate the induced corrosion with gas/hydraulic and temperature conditions. Carbon steel- and Cu-based canisters were considered. Samples from in situ experiments carried out in Äspö underground research laboratories (described in Svensson et al, 2011) were also analysed and published in Fernandez et al. (2022).

GRS, in cooperation with KIT-INE, analysed the temporal evolution of the rate and propagation of corrosion of spheroidal graphite cast iron GGG40 (SGI) and copper-nickel alloy C71500 (CuNi) in contact with bentonite slurry or suspension, saturated with selected waters at typical near-field temperatures (30, 50 and 80°C). The influence of oxidising/reducing conditions on the growth and long-term chemical and mechanical stability of the protective oxide films (e.g. haematite) was emphasised. The redox topic was complemented by studies at increased temperature and pressures of 5, 50 and 100 bar, using both accelerated and conventional corrosion techniques.

All corrosion experiments included bentonite buffer to address existing uncertainties. The near-field conditions analysed included hydraulic, thermal, redox and radiation transients, where at least one parameter was changed with time. Specific set-ups were developed and many analyses were carried out, which were focused on identifying the physico-chemical effects of the different transients on container material corrosion, and experiments and analyses were designed and planned to (i) provide metal corrosion rates, (ii) identify the main corrosion products released and (iii) to evaluate the engineered barrier alteration. Experiments were designed to provide relevant experimental data that will be helpful in evaluating the long-term behaviour of container materials and the contacting bentonite engineered barrier in performance assessments. Relevant information was periodically provided to support the work carried out in Task 6.

5.2 Scope of task

The scope of the experimental studies proposed in Task 5 was focused on the interface between the metal container and the engineered barrier, made up of compacted bentonite, in accordance with the repository concepts being considered in Canada, Czech Republic, Finland, Japan, Spain, Switzerland and Sweden.

Each research group selected specific container materials for investigating container corrosion and took account of specific near-field transient conditions and characteristic engineered barrier conditions. Table 30 summarises the main materials and conditions analysed experimentally by the different research groups. All experimental details are described in ConCorD Deliverable 15.12 (Fernandez et al, 2024). The experiments are grouped by materials and type of experiment. Seven different types of laboratory experiments were carried out to analyse the effect of coupled thermal, redox, hydration and γ-radiation transients, as summarised in Table 30. The main characteristics of each type of experiment are described below.

Table 30. Summary of transient experiments carried out in Task 5 to analyse container degradation under different conditions. Experiments are grouped by type of experiment (I to VII), indicating the materials and transients analysed by the different research teams.

Metal	Bentonite	Water hydration	Temperature (°C)	Transient	Team	Type
Carbon steel **(Czech and Nagra reference)**	Compacted Ca-Mg BCV Na-MX-80	Granitic water	90°, 150	Thermal, γ-radiation	UJV	Type I
	Compacted Ca-Mg FEBEX	Granitic water	80	Coupled hydration, thermal and redox	CIEMAT	Type II
	Compacted FEBEX	Granitic water	80	Coupled hydration, and thermal	CIEMAT	Type III
		Clay porewater				
	Compacted SWy-3	Granitic water				
		Clay porewater				
	Compacted BCV	Granitic water				
		Clay porewater				
Cu-OFP **(Swedish, SKB)**	Compacted FEBEX	Granitic water	80	Coupled, hydration, redox and thermal	CIEMAT	
		Clay porewater				
	Compacted SWy-3	Granitic water				
		Clay porewater				
	Compacted Ca-Mg BCV	Granitic water				

Metal	Bentonite	Water hydration	Temperature (°C)	Transient	Team	Type
		Clay porewater				
SGI cast iron (SKB)	Wyoming slurry	OPA porewater	30, 50	Thermal, γ-hydraulic	GRS	Type IV
	Wyoming slurry	OPA porewater	30, 50	Thermal, γ-irradiation	GRS	Type V
	Wyoming suspension (experiments with or without haematite)	Grimsel granitic water	25, 50	Static and dynamic thermal and redox transients	KIT	Type VI (static) & Type VII (dynamic)
CuNi alloy	Wyoming suspension (experiments with or without sulphide)	Grimsel granitic water	25, 50	Static and dynamic thermal and redox transients	KIT	

5.2.1 Materials tested

The corrosion behaviour of four types of metal materials was analysed at laboratory scale:

- **Carbon steel (Nagra carbon steel and Czech carbon steel)** samples used in UJV and CIEMAT experiments are representative of the Swiss Nuclear Waste Management Agency (Nagra) reference canister (Figure 35a, b and c) and the Czech reference canister (Figure 35d and e). The Nagra carbon steel sample was provided by Jacobs (UK) and consisted of a circular section of around 2 kg of carbon steel ASTM A694-08 F65 (Patel et al, 2012). The Czech carbon steel S355J2H was supplied by Škoda and obtained by cutting a tube, which serves as the outer casing in the Czech canister concept (Pospíšková et al. 2017, Matulová et al. 2023).
- **Spheroidal graphite cast iron (SGI)** EN-GJS-400-15 was selected by KIT (Figure 36a) and GRS (Figure 36b). This material is being considered for the construction of canisters for a KBS-3V Swedish repository (Jonsson et al., 2018) and it is also a component of the POLLUX® containers developed for the direct final storage of heat-generating nuclear waste. Owing to its high carbon content, using SGI as the outer cask reduces the external gamma and neutron dose rate.
- **Oxygen-free phosphorus-doped copper (Cu-OFP)**, which is representative of the Swedish repository concept, was used by CIEMAT. Cu-OFP samples were provided by the Swedish Nuclear Fuel and Waste Management Company (SKB, Sweden). Figure 37 shows the rod used, reference T77 +750 40º, to obtain discs of 27.5 mm diameter and average thickness 1.5 mm. Cu-OFP is composed of 99.99 wt.% Cu with small traces of other elements. More details can be found in Fernández et al. (2024).

- **Copper nickel alloy (CuNi)** samples were also selected by KIT for their experiments (Figure 38). It was CuNi grade CW354H / UNS C71500 (or DIN 2.0882), which mainly consists of Cu with about 30 wt.% of admixed Ni (Fernandez et al., 2024). Countries such as Sweden, Finland and Canada envisage the use of copper in the construction of waste containers and understanding of the degradation mechanisms of this material is quite advanced. Copper can be alloyed with nickel, and some alloys, such as UNS C71500, find application in the construction of evaporators and heat exchange tubes, with excellent corrosion behaviour in sea water.

From the point of view of maturity with respect to knowledge about the corrosion behaviour of candidate container materials, carbon steel and Cu-OFP are considered to be those for which there is the broadest knowledge, while the corrosion behaviour of GGG40 cast iron and CuNi alloys is less well known.

- **Bentonites:** Metal contact with bentonite was included in all experiments, but each research team selected a specific near-field scenario. Corrosion studies with carbon steel and Cu-OFP samples were performed in contact with compacted bentonites, Na SWy-3 bentonites, Czech BCV (Laufek et al., 2021) and Spanish FEBEX bentonites (Huertas et al. 2006; Fernandez et al., 2004) and were tested under different conditions. Studies with SGI and CuNi alloy were carried out in contact with Na-MX-80 bentonite slurry or Na-MX-80 suspensions in dilute conditions; more details can be found in Fernandez et al. (2024). SWy-3 and MX-80 are equivalent bentonites from Wyoming (USA).
- **Waters:** In carbon steel corrosion studies, bentonite was hydrated with waters of different salinity, specifically granitic groundwaters SGW3 (Červinka et al, 2018), low saline granitic water (Fernandez et al., 2024) or bentonite porewater (Fernandez et al, 2005), at different degrees of saturation.

SGI degradation studies were carried out with groundwater representative of two rock host concepts: granite (Grimsel groundwater, Switzerland), sedimentary clay rock (Opalinus water representative of Callovo Oxfordian formations (France) or bentonite porewater. The compositions and characteristics of all selected waters are described in Fernández et al. (2024).

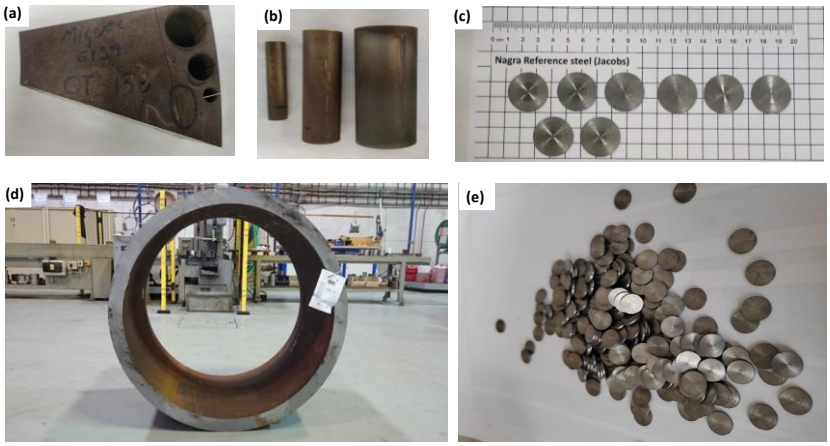

Figure 35. Carbon steel samples used by CIEMAT and UJV: (a) Nagra carbon steel ASTM A694-08 F65 (Patel et al, 2012); (b) Cylindrical test rods; (c) Nagra carbon steel coupons; (d) Czech carbon steel S355J2H (Pospíšková et al. 2017, Matulová et al. 2023) and (e) Czech carbon steel coupons.

Figure 36. Spheroidal graphite cast iron GGG40 (SGI) coupons used by (a) KIT and (B) GRS, for their laboratory experiments.

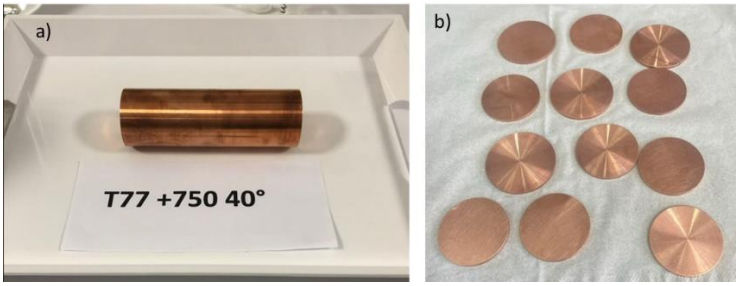

Figure 37. Cu-OFP samples: (a) Cylindrical test tube reference T77 +750 40° of Cu-OFP, representative material of SKB design, (b) Cu-OFP discs of 27.5 mm diameter and 1.5 mm thickness.

Figure 38. Copper nickel alloy samples (CuNi) CW354H / UNS C71500 (or DIN 2.0882) selected by KIT for laboratory experiments.

5.2.2 Summary of laboratory experiments and set-up developed in Task 5

Type I: carbon steel in compacted bentonite subjected to radiation and thermal transients (UJV)

The experiments carried out by UJV with Czech carbon steel consisted of 23 modules, each containing compacted BCV bentonite with embedded Czech carbon steel coupons, mounted in an anoxic box (Figure 39). Samples were γ-irradiated (^{60}Co source) and constantly heated at 150°C for 6, 9, 12 or 18 months. The dose rate (0.4 Gy hr^{-1}) was calculated by simulating conditions close to the fuel assembly at the defined temperature (Pospíšková et al. 2017).

According to the DGR concept (Pospíšková et al., 2017) the initial bentonite moisture content was adjusted to 15% (modules heated up at 150°C) and 20% (modules heated up at 90°C). The dry density of compacted bentonite was 1600 kg m^{-3}. In each corrosion module, there were 12 Czech carbon steel samples that were divided into three layers, with each layer containing four steel samples. The experimental design consisted of bentonite with embedded carbon steel samples compacted and saturated in modules, then inserted into sealed chambers (mounted in an anoxic box).

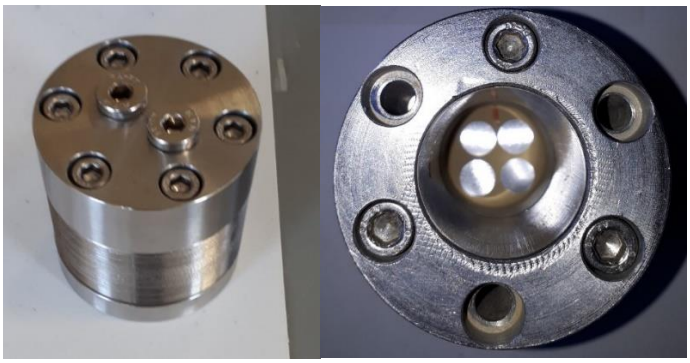

Figure 39. UJV experimental set-up: (left) corrosion module; (right) Czech carbon steel samples with BCV bentonite inside the corrosion module, to analyse the effect of thermal and irradiation transients.

Type II: carbon steel in compacted bentonite subjected to coupled redox and thermal transients (CIEMAT)

Figure 40 shows the set-up designed by CIEMAT to analyse transient states, from the initial unsaturated compacted bentonite under oxic conditions to fully saturated anoxic conditions, hydrated with enough water to allow compacted bentonite / granitic water / carbon steel interactions at a high temperature (80°C). Samples consisted of compacted FEBEX bentonite at two dry densities: 1.4 and 1.6 g cm^{-3}, with the initial degree of saturation being 41.3% and 55.6%, respectively. Two coupons of Nagra carbon steel were placed in the middle of the compacted sample.

Samples were introduced into a PARR reactor (Model 4600) where 120 ml of low saline granitic water were added to hydrate the bentonite during the experiment, with the temperature set at 80°C to achieve 100 % saturation. At the end of the test, and prior to opening the reactor, gas and water samples were collected (Figure 40, lower) and afterwards the cell was dismantled and the compacted bentonite block was transferred to an anoxic glove box for sampling both the coupons and the bentonite. The duration of the tests was up to 1 year.

Figure 40. Setup used by CIEMAT for studying coupled redox and thermal transients at 80°C with Nagra-carbon steel / bentonite samples (upper); collection of gas and water samples at the end of the experiment (lower).

Type III: carbon steel and Cu-OFP in compacted bentonites subjected to convective water vapour thermal fluxes under dynamic conditions (CIEMAT)

Figure 41 shows the water adsorption tests designed by CIEMAT to simulate convective water-vapour thermal fluxes at the metal/bentonite interface. Table 31 presents a summary of all the experiments carried out with three bentonites (FEBEX, SWy-3 and Czech bentonite BCV) compacted at 1.4 or 1.6 g cm^{-3}. A different metal coupon was introduced into the middle of each compacted bentonite: Czech and Nagra carbon steel, and Cu-OFP. At the top and bottom of the sample, a dialysis sheet was placed to allow infiltration of water. Each cell was placed inside a desiccator with a deionised water solution and a vacuum applied (10^{-3} mm Hg vacuum). The dialysis sheet and the perforated covers allowed for exchange of water in the vapour phase between the clay and the atmosphere inside the desiccators (95-100% RH). The tests were performed at a temperature of 80°C, inside an oven that was thermostatically controlled at 353.15K. The duration of the tests was up to 1 year.

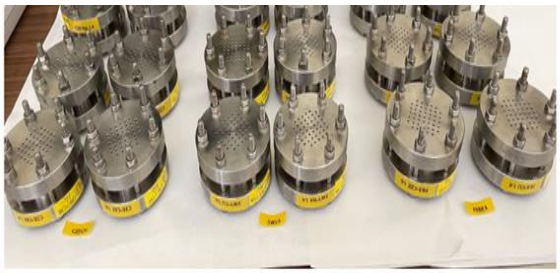

Figure 41. Set-up for convective water vapour thermal flux experiments carried out by CIEMAT under oxic conditions and at 80°C with three bentonites compacted at a dry density of 1.4 and 1.6 g cm^{-3} with Czech and Nagra carbon steel coupons and Cu-OFP coupons.

Table 31. Initial conditions of the dynamic experiments at 80°C.

Oxic Conditions / Degree of Saturation = 55.6% and 41.3% for ρ_d=1.60 and 1.40 g cm^{-3}, respectively / Temperature = 80°C / RH= 95 to 100%					
Type of Cell	*Bentonite*	*Metal*	*Type of water*	*Dry Density (g cm^{-3})*	*Cell*
	FEBEX	Nagra carbon steel	Water vapour 95-100% RH	1.4	1
				1.6	2
		Cu-OFP		1.4	3
				1.6	4
		Czech Steel		1.4	5
				1.6	6
	SWy3	Nagra carbon steel		1.4	7
				1.6	8
		Cu-OFP		1.4	9
				1.6	10
		Czech carbon steel		1.4	11
				1.6	12
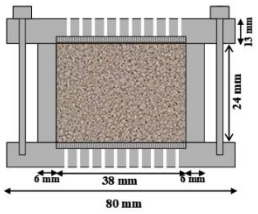	Czech BCV bentonite	Nagra Steel		1.4 1.6	13 14
		Cu-OFP		1.4	15
				1.6	16
		Czech Steel		1.4	17
				1.6	18

Type IV: Spheroidal graphite cast iron (SGI) in bentonite suspension subjected to thermal and hydraulic transients (GRS)

GRS' experiments were designed for monitoring the corrosion of spheroidal graphite cast iron (SGI) in contact with a slurry of Wyoming bentonite (Kaufhold et al., 2008, 2015), hydrated with Opalinus Clay water for a period 90 days. Naturally air-saturated synthetic porewater was used for the preparation of the slurry. Thus, these conditions are thought to reproduce the very initial corrosion processes upon intrusion of water into the steel-bentonite interface in the cooling phase after repository closure. Dissolved oxygen in the disposal was provided by air trapped in voids of the closure filling materials. The experiments were performed in a so-called 'bentonite-cell' (Figure 42). The slurry and the supernatant liquid, with their original contents of dissolved oxygen, were separated from each other by a perforated plate, which maintained a constant slurry porosity and avoided turbulence. Incoming oxygen from the surroundings was avoided by purging the upper part of the cells with argon connected to water traps.

The corrosion process was monitored by measuring:

(i) the corrosion potential or open circuit potential (OCP)

(ii) impedance spectra in the frequency region 10^5 to 10^{-3} Hz at the OCP and

(iii) polarisation curves at 0.166 mV s^{-1} from -0.1 V vs OCP until reaching an anodic current of 15 µA.

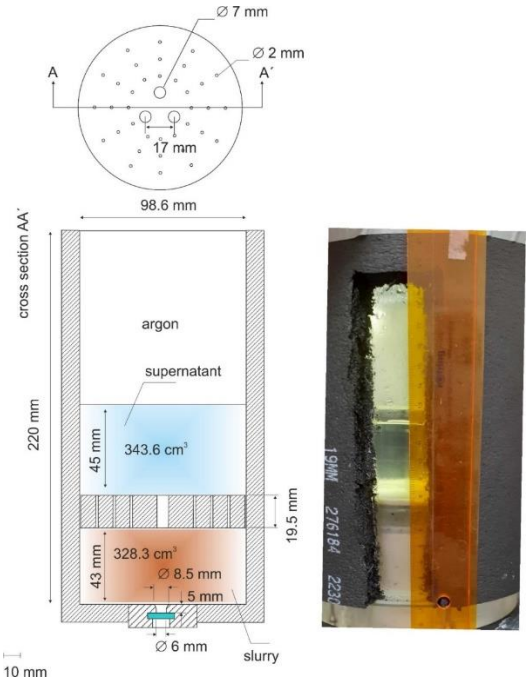

Figure 42. (left) Schematic diagram of the 'bentonite-cell' showing geometrical dimensions used by GRS to analyse SGI corrosion in a bentonite slurry; (right) picture of the cell.

Type V: Spheroidal graphite cast iron (SGI) in bentonite suspension subjected to thermal and γ-radiation transients (GRS)

This experiment, which was linked to Task 3 activities, consisted of analysing the corrosion of SGI in a slurry, with a Wyoming bentonite to Opalinus Clay water ratio of 1:10. Four samples were put inside a liner manufactured from PEEK in a stainless-steel reactor (Figure 43), which was closed tightly and γ-irradiated for 220 days in the Panoza-facility of UJV-Rez (Prague) at a dose rate of 130 kGy hr^{-1}. The temperature was set to 50°C using an electric oven.

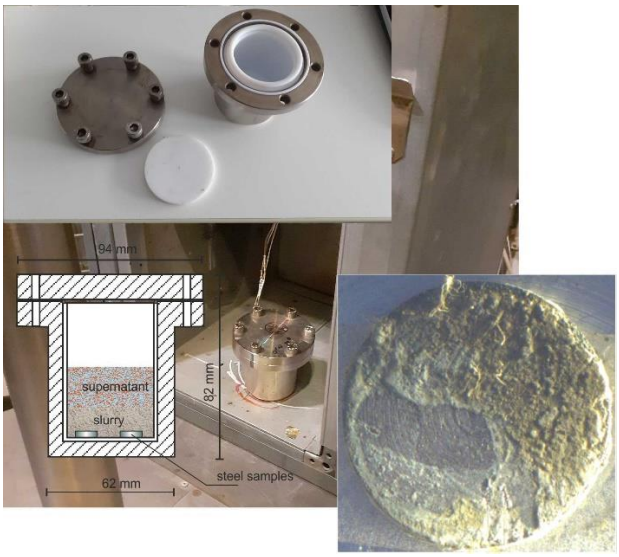

Figure 43. Picture describing the experimental set-up used by GRS for gamma-radiation and thermal transients on SGI/bentonite slurry. Picture at the right-bottom corner shows the optical appearance of the sample after finalisation of the experiment.

Type VI: Spheroidal graphite cast iron (SGI) and CuNi alloy in bentonite slurry subjected to static thermal and redox transients (KIT)

KIT performed two type of corrosion experiments with spheroidal graphite cast iron (SGI) (Figure 36 Left) and CuNi coupons (Figure 38), including a 100 g L^{-1} bentonite suspension. Experiments were performed under anoxic conditions using an Ar-filled or N_2-filled glove box, or airtight holders when needed. Preparation details are described in Fernández et al. (2024) and Finck et al. (2023). Table 32 summarises the experimental conditions of static and dynamic experiments carried out with SGI and Table 33 presents the experiments carried out with CuNi alloy.

In static experiments, coupons placed in contact with the bentonite suspension (50 ml) in a closed vessel and left to react (inner volume 90 ml) (Finck et al., 2023). Each vessel contained two polished coupons (4 mm × 20 mm × 8 mm) placed on a PTFE (polytetrafluoroethylene) stand, which was conditioned prior to use to avoid fluorine leaching.

The first series of experiments was performed at room temperature (25°C) by simply leaving vessels in the glovebox following closure. A second series of experiments was performed at 50°C by using heating plates in order to identify any possible effect of temperature on corrosion processes. At both temperatures, contact times were 3 months and 6 months.

In some SGI corrosion experiments, haematite (commercial iron(III) oxide, Alfa Aesar) was added as 0.5 wt.%. Some CuNi corrosion experiments included sulphide (commercial 1 mg ml^{-1} IC certified standard solution (disodium sulphide nonahydrate in water, Sigma-Aldrich). In experiments under static conditions, the sulphide content could not be changed over time so that a defined starting concentration of 3 µM was used.

Type VII: Spheroidal graphite cast iron (SGI) and CuNi alloy in bentonite slurry subjected to dynamic thermal and redox transients (KIT)

Dynamic experiments were performed with the same materials as described above for the static experiments, using reactors with one inlet and one outlet and comprising a stainless steel body and a PTFE inner liner. They were equipped with inlet and outlet metallic filters made of 316L stainless steel (Tridelta Siperm GmbH, Germany) with a mean pore size of ~7 µm.

Each reactor contained one coupon (4 mm × 8 mm × 8 mm) and ~3.1 ml of 100 g L^{-1} suspension. At the inlet and outlet, the reactors were connected to tubing made of PEEK (polyether ether ketone) and a

defined low water flow (2.5 ± 0.4 µL min^{-1}) was imposed using a peristaltic pump (Minipuls 3, Gilson) and calibrated tubing made of PVC with an inner diameter of 0.25 mm.

The water was collected at specific time intervals at the outlet and weighed to determine the precise flow rate. pH and Eh were measured in the water, which was then ultracentrifuged before being analysed by ICP-OES and IC. Only one series, with a reaction time of 3 months, could be performed and sampling times were 4, 5, 6, 8, 10 and 12 weeks.

In the CuNi static experiments, the porewater initially contained no sulphide until week 6, then 1 µmol L^{-1} until week 8, then subsequently 2 µmol L^{-1} until week 10 and finally 3 µmol L^{-1} until week 12. In SGI corrosion experiments, haematite was added as 0.5 wt.%.

Table 32. List of corrosion experiments performed by KIT using spheroidal graphite cast iron (SGI), along with recorded pH (±0.10) and Eh (±50 mV) (values recorded at 25°C) and the corrosion rate (C.R., ±15%) determined by weight loss (ASTM, 2011) (n.d. = not determined).

Condition	Applied transient	T (°C)	Duration (months)	pH	E_h (mV vs S.H.E.)	C. R. (µm yr^{-1})
Static	/	25	3	8.17	-441.	4.8
Static	0.5 wt.% α-Fe_2O_3	25	3	8.13	87	5.1
Static	/	50	3	8.13	-254	10.0
Static	0.5 wt.% α-Fe_2O_3	50	3	7.91	-149	10.6
Static	/	25	6	7.87	-47	2.6
Static	0.5 wt.% α-Fe_2O_3	25	6	7.74	-310	3.7
Static	/	50	6	7.73	-430	4.0
Static	0.5 wt.% α-Fe_2O_3	50	6	7.80	-420	6.9
Dynamic	/	25	3	9.2 to 9.7	-171 to -181	n.d.
Dynamic	0.5 wt.% α-Fe_2O_3	25	3	9.0 to 9.7	-167 to -179	n.d.
Dynamic	0.5 wt.% α-Fe_2O_3	50	3	9.0 to 9.7	-177 to -207	n.d.

Table 33. List of corrosion experiments performed by KIT using the cupronickel alloy (CuNi), along with recorded pH (±0.10) and Eh (±50 mV) (values recorded at 25°C) and the determined corrosion rate (C.R., ± 15%) by weight loss (ASTM, 2011) (n.d. = not determined).

Condition	Applied transient	T (°C)	Duration (months)	pH	E_h (mV *vs* S.H.E.)	C. R. (µm yr^{-1})
Static	/	25	3	8.17	225	1.2
Static	3 µM sulphide	25	3	8.09	271	1.1
Static	/	50	3	8.04	283	2.7
Static	3 µM sulphide	50	3	7.58	167	1.6
Static	/	25	6	8.09	287	0.1
Static	3 µM sulphide	25	6	7.94	245	0.1
Static	/	50	6	8.34	297	1.3
Static	3 µM sulphide	50	6	8.09	263	1.9
Dynamic	/	25	3	8.9 to 9.7	-166 to -179	n.d.
Dynamic	0-1-2-3 µM sulphide	25	3	9.4 to 9.5	-179 to -189	n.d.
Dynamic	/	50	3	8.9 to 9.5	-169 to -185	n.d.
Dynamic	0-1-2-3 µM sulphide	50	3	8.4 to 9.1	-171 to -183	n.d.

5.2.3 Post-mortem analyses: characterisation and corrosion rates

In all experiments, complete post-mortem analyses were carried out by many analytical and characterisation techniques on metal coupons and bentonite samples as extensively described in Fernandez et al. (2024). Corrosion rates were determined in all cases by metal weight mass loss, following ASTM standards (ASTM, 2011).

5.2.4 Summary of in situ laboratory samples analysed subjected to near-field transients

Task 5 studies were not restricted to the laboratory and in situ experiments were also considered.

KIT selected for their laboratory experiments equivalent conditions to those being analysed in the Material Corrosion Test (MaCoTe) in situ corrosion experiment at the Grimsel Test Site in Switzerland (Reddy et al., 2020), where selected candidate canister materials embedded within bentonite were exposed to natural borehole granitic water.

CIEMAT analysed bentonite samples from ABM5 and LOT experiments (Svensson et al., 2011), provided by SKB (Sweden). Table 34 presents a summary of materials and conditions analysed from the Äspö experiment. From LOT Experiments a Na-bentonite (MX-80 bentonite) and metal samples

from a copper tube slice (SS 5015-04 grade) were analysed. From the ABM 45:5 experiments, two types of bentonite samples (MX-80 (USA) and Ahsa NW BFL-L (India)) and two metal samples from the heater (carbon steel P235TR1) and from thermocouples (type K, chromel-alumel) were analysed (Fernandez et al., 2022).

The results of CIEMAT analyses of in situ experiments carried out within ConCorD were published in Fernandez et al. (2022).

Table 34. Characteristics of ABM and LOT in situ samples (Äspö URL, Sweden) analysed by CIEMAT in Task 5 (Fernandez et al, 2022).

Experiment	Transient parameters	Metal samples	Clay sample	Physico-chemical conditions
In situ test: **LOT Experiment (S2 parcel)**	Temperature Redox Bentonite Saturation Chemical evolution	Heater: Copper tube SS 5015-04 grade Cu-coupons (tube 80x80 mm)	MX-80 (block 31)	Artificial Groundwater: Äspö granitic groundwater Temperature: 90°C Duration: 20 years
In situ test: **ABM 45:5 Experiment**	Temperature Redox Bentonite Saturation Groundwater Type Chemical evolution	Heater: Carbon Steel P235TR1 (block 30) Thermocouples: type K (chromel-alumel) (block 3E)	MX-80 (Block 15, 30) Asha 505 (Block 3) bentonites at contact with thermocouples and titanium coupons	Natural Groundwater: Äspö granitic groundwater Temperature: 50°C (3.5 years) up to 250°C (last 6 months) Duration: 5 years

5.3 Progress against task description

All the proposed studies experimentally analysed metal corrosion under relevant repository transitory conditions expected at the canister/bentonite interface. A detailed description of the results obtained is available in ConCorD Deliverable 15.12 (Fernandez et al., 2024).

5.3.1 Carbon steel in compacted bentonite subjected to radiation and thermal transients under anaerobic conditions (UJV)

The UJV-SURAO experiments evaluated (Type I experiment in Section 5.2.2) the effect of increased temperature and gamma irradiation on the corrosion of Czech carbon steel in compacted BCV Ca-Mg bentonite. MX-80 bentonite was also included in a limited number of tests.

Figure 44 (left) shows the corrosion rates measured for Czech carbon steel samples loaded in BCV bentonite at 90°C or 150°C, γ-irradiated or unirradiated. Figure 44 (right) shows the corrosion rates measured for Czech carbon steel in MX-80 Wyoming bentonite.

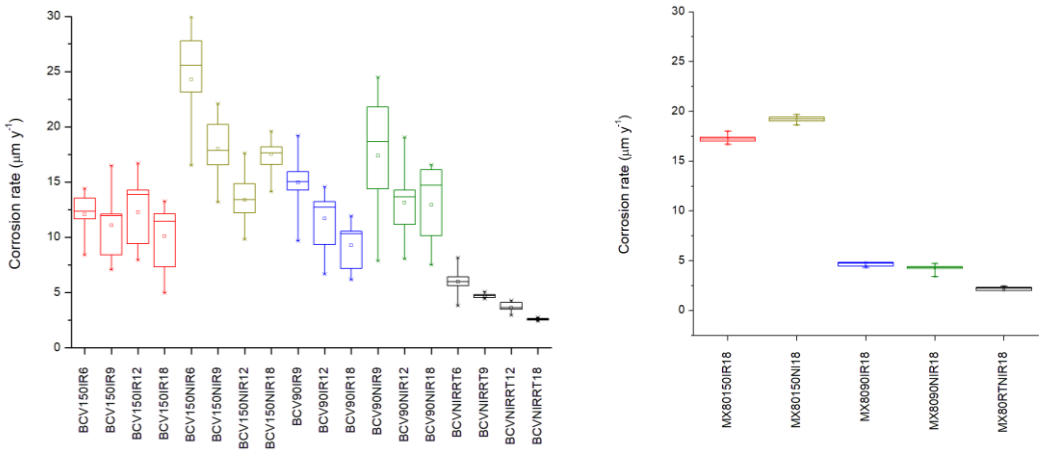

Figure 44. Corrosion rate of (left) carbon steel samples with BCV bentonite at 150°C (red – irradiated, dark yellow – unirradiated), 90°C (blue – irradiated, green – unirradiated) and at laboratory temperature (black). The loading period is indicated by last 1–2 digits in the title of the samples (i.e. 6, 9, 12 or 18 months) and (right) carbon steel samples embedded in MX-80 bentonite heated at 150°C (red – irradiated, dark yellow – unirradiated), 90°C (blue – irradiated, green – unirradiated) and at laboratory temperature (black). The loading period was 18 months.

The results showed that the carbon steel samples inside the BCV compacted bentonite and heated at 90°C showed lower corrosion rates than those heated at 150°C. Lower corrosion rates were measured on irradiated compared to unirradiated samples. Experiments at 150°C in the BCV bentonite gave lower corrosion rates, around 2 µm yr^{-1}, and the highest corrosion rate, 24.3 µm yr^{-1} was measured combining 150°C and irradiation. Unirradiated samples heated to 150°C showed the highest corrosion rate after 6 months, with decreasing tendency to corrode when the loading period was extended to 18 months. Longer loading periods minimised the difference in the corrosion rate of irradiated and unirradiated steel samples. The minimum corrosion rate was found in steel samples embedded in water-saturated BCV bentonite stored at laboratory temperature without irradiation.

No effect, or a very minor effect, of irradiation on corrosion rate was observed when the steel samples were heated in the MX-80 bentonite.

A longer loading period led to the formation of a higher amount of corrosion products, thus facilitating their identification. Haematite and Fe-rich carbonates (chukanovite, siderite) were confirmed to have formed corrosion layers on the steel surface. The thickness of the corrosion layer varied, ranging from 10 to 45 µm, and it was directly correlated with the duration of exposure.

Carbon steel samples that remained unirradiated and were heated at 90°C exhibited corrosion layers up to 45 µm thick after 12 months of loading. In contrast, irradiation, and thermal loading at 150°C, led to the formation of thinner corrosion layers, typically ranging from 10 to 20 µm. A corrosion layer composed of Fe-Si-O was identified on the surface of steel subjected to thermal loading at 150°C, indicating an amorphous or poorly crystalline structure. The origin of Fe-Si-rich corrosion products needs to be confirmed by future research.

The combination of high temperature and saturation of SGW3 water led to the partial transformation of Na-smectite into Ca/Mg-smectite in the MX-80 bentonite. This transformation was indicated by the proportions of exchangeable cations and by splitting of the montmorillonite basal diffraction line. The heated BCV bentonite indicated partial cation exchange of Ca^{2+}/Mg^{2+} by Na^{+} coming from the saturation medium and enrichment in Fe^{x+} and Mn^{2+} coming from the carbon steel.

5.3.2 Carbon steel in compacted bentonite subjected to coupled redox and thermal transients (CIEMAT)

The experiment with Nagra carbon steel in compacted FEBEX bentonite sample (1.4 g cm^{-3}) hydrated with granitic water (200 ml) at 80°C corresponds to the Type II experiment in Section 5.2.2. The starting conditions were oxic but they became anoxic.

At the end of the test (after 135 days), and prior to opening the reactor, gas and water samples were collected after several cycles of Ar flushing and applying vacuum inside the sampling lines. The following gases were observed: H_2, CO_2, methane and a range of other hydrocarbons (C_2 to C_4). Oxygen and nitrogen were also detected, although there was a decrease in the oxygen and nitrogen concentrations compared to reference atmospheric values (i.e. 78.08 vol% N_2, 20.95 vol% O_2 and 0.93 vol.% Ar). This suggests that there was contamination during sampling or that there were different local redox conditions inside the cell: (a) oxic, with oxygen being consumed over time, and (b) reduced, at the bentonite / coupon interface where H_2 is generated. The presence of hydrogen indicates that metal coupon corrosion occurred under anoxic conditions and that the oxygen detected was probably due to air contamination during sampling. Argon gas was used for flushing the gas lines.

After gas analysis, the cell was dismantled and the compacted block bentonite was placed in an anoxic glove box for sampling both the carbon steel coupon and the bentonite (Figure 45). The corroded coupons were analysed and the corrosion rate for Nagra carbon steel was determined to be 53.2 µm yr^{-1}. The coupons exhibited a uniform generalised corrosion and the corrosion products were identified as magnetite, siderite, calcite, aragonite, pyrrhotite, anhydrite, gypsum and a carbonate green rust.

The bentonite samples in contact with the coupons were also analysed. The bentonite showed a change of colour from slight brownish to greenish, indicating a redox change from the middle to both ends of the compacted bentonite, that is, a diffusion profile of Fe(II) though the compacted bentonite. However, apart from the visually observed Fe(II) front, the analyses of bentonite smectite indicated that the clay particles remained unaltered.

Figure 45. Detail of sampling of FEBEX bentonite at 1.4 g cm^{-3} and Nagra carbon steel coupon at the end of the static experiment in the reactor at 80°C.

5.3.3 Carbon steel in compacted bentonites subjected to convective water vapour thermal fluxes under dynamic conditions (CIEMAT)

Experiments with metal coupons and compacted bentonites (subjected to convective water fluxes at 80°C) lasted for around 286 days (# and Type III experiment in Section 5.2.2).

In all experiments with carbon steel, bentonite samples were completely saturated (either Nagra or Czech carbon steel) and the metal coupons exhibited a degree of corrosion. The corrosion rates determined in each experiment are presented in Table 35. The highest degree of corrosion was observed for the Nagra carbon steel interacting with FEBEX bentonite compacted at 1.4 g cm^{-3} (Figure 46), probably due to the high salinity of the FEBEX porewater, which is higher with respect to the other bentonites.

The main corrosion product observed on the coupons was magnetite, although there were other Fe oxy-hydroxides, such as haematite, goethite, lepidocrocite and akaganeite. The carbonates, calcite ($CaCO_3$,

trigonal) aragonite ($CaCO_3$, rhombic) and dolomite ($CaMgCO_3$) were observed by XRD analyses. Siderite was only observed by SEM and gypsum and anhydrite were also detected.

Sulphur species were only detected in SWy-3 and Czech BCV bentonites. In some samples, iron calcium silicates (e.g. hedenbergite, $CaFeSi_2O_6$) were observed. This finding suggests that dissolved silica must have been available in the system (Kaufhold et al., 2020), which is certainly favoured by the elevated temperature.

At first sight, the FEBEX and Czech bentonites seemed more altered, showing the presence of magnetite and goethite, as well as aragonite. In any case, the extent of alteration inside the bentonite was <2 mm in all bentonite samples, showing an increase of iron content, emanating from the metal-bentonite interface. Distal bentonite samples remained unaltered.

Figure 46. Dismantling of the FEBEX bentonite compacted at 1.4 g cm^{-3} with Nagra carbon steel coupon: altered bentonite and corroded carbon steel is shown.

Table 35. Corrosion rates determined in the metal carbon steel coupons in compacted bentonites by mass loss weight (Nagra: carbon steel; Czech: Czech carbon steel).

Sample	Carbon steel	Dry density (g/cm^3)	Thickness (mm)	Diameter (mm)	Coupon density (cm^3)	Loss (µm)	Contact time (days)	Corrosion rate (µm/year)
FEBEX	Nagra	1.4	1.5	30.0	8.2	323.92	286	413
FEBEX	Nagra	1.6	1.5	30.0	8.2	43.99	286	56
SWy3	Nagra	1.4	1.5	30.0	8.2	62.09	286	79
SWy3	Nagra	1.6	1.5	30.0	8.2	21.82	286	28
SWy3	Czech	1.4	0.9	10.0	8.2	36.02	286	46
Czech	carbon steel	1.4	1.5	30.0	8.2	196.70	286	251

5.3.4 Cu-OFP in compacted bentonites subjected to convective water vapour thermal fluxes under dynamic conditions (CIEMAT)

The Cu-OFP coupons embedded in compacted bentonite samples subjected to convective water thermal fluxes (Type III experiments in Section 5.2.2) showed a significant degree of corrosion. Figure 46 shows an example of dismantling a cell with SWy-3 compacted bentonite at 1.4 g cm^{-3} with a Cu-OFP coupon. After 326 days duration, all bentonite samples were completely saturated.

The corrosion rates determined by mass loss measurements are presented in Table 36. The highest degree of corrosion appeared to be for the Cu coupon interacting with the Czech bentonite, with a corrosion rate of 8 to 9 µm yr^{-1}; the corrosion rate depended more on the type of bentonite than on the dry density. The extent of bentonite alteration at the bentonite / coupon interface was <0.5 to 1 mm in all the samples, which was much lower than that observed from carbon steel coupons. The presence of both cuprite (red, Cu_2O, Cu(I)) and tenorite (black, CuO, Cu(II)) was indicated.

Figure 47. Dismantling the SWy-3 bentonite compacted at 1.4 g cm^{-3} with an SKB Cu-OFP coupon.

Table 36. Corrosion rates determined for Cu-OFP metal coupons (diameter 27.5 mm, thickness 1.5 mm, density 9.2 g cm^{-3}) in contact with compacted bentonite for 326 days.

Sample	Dry density (g cm^{-3})	Initial weight (g)	Metal loss (µm)	Corrosion rate (µm yr^{-1})
FEBEX	1.4	7.6489	3.623	4
FEBEX	1.6	7.8243	2.800	3
SWy3	1.4	6.8022	5.691	6
SWy3	1.6	7.5552	5.508	6
Czech	1.4	8.4522	7.887	9
Czech	1.6	7.3394	6.789	8

5.3.4.1 Spheroidal graphite cast iron (SGI) in bentonite suspension subjected to thermal and hydraulic transients (GRS)

The GRS experiments analysed the corrosion of spheroidal graphite cast iron (SGI) in contact with a slurry of Wyoming bentonite hydrated with Opalinus Clay water over a period 90 days under anoxic conditions (Type IV experiment in Section 5.2.2). The corrosion process was monitored by measuring the corrosion potential, the polarisation resistance and polarisation curves at regular intervals.

The mean current values and the peak diffusion-controlled corrosion limit were extracted from the measured polarisation curve. The corrosion potential and the corrosion current were measured by extrapolating the cathodic and anodic branches to the zero-current point, for temperatures of 30°C and 50°C. From the corrosion currents calculated from the mean values of the polarisation curves, assuming a dissolution reaction $Fe \rightarrow Fe(II) + 2\ e^-$, it is possible to calculate the corrosion rates, as described in Fernandez et al. (2024).

The measured SGI corrosion rates were 6±1 µm yr^{-1} and 13±1 µm yr^{-1} at 30°C and 50°C respectively. These values are in line with those obtained by mass loss measurements for coupon experiments

carried out by KIT-INE (see Table 32). To interpret the results it was assumed that the diffusion-controlled reaction is oxygen reduction (see Figure 48).

$$O_2(aq) + 4\ e^- + 2\ H_2O \rightarrow 4\ OH^-$$ Equation 1

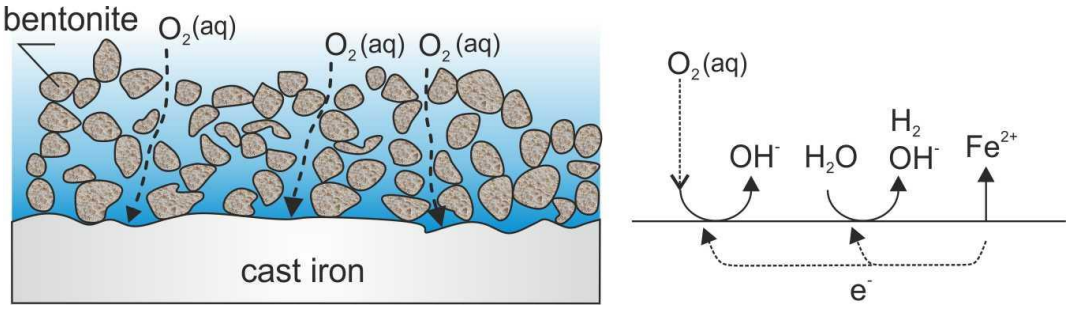

Figure 48. Model of the cast iron-bentonite interface used for the interpretation of results from the electrochemical experiments.

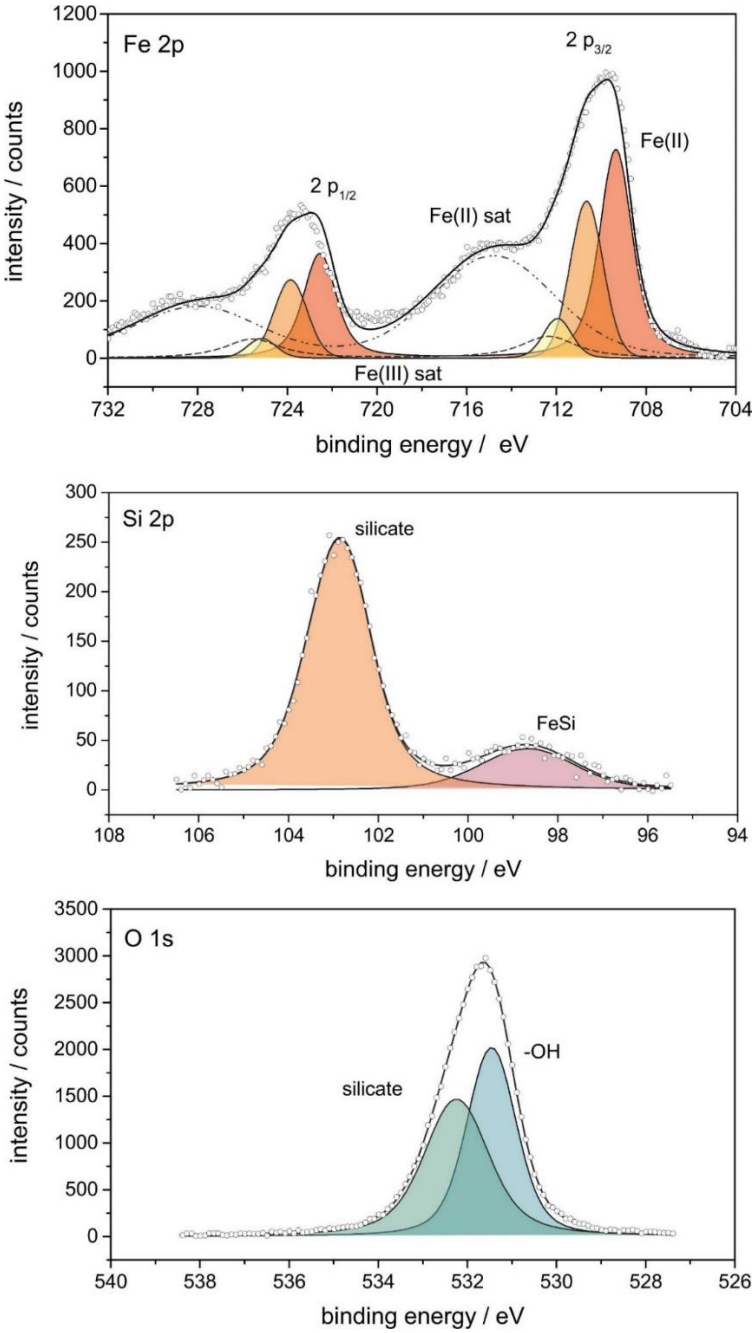

Figure 49. XPS core level Fe2p, O1s and S2p performed on the corroded cast iron surface free of bentonite.

5.3.5 Spheroidal graphite cast iron (SGI) in bentonite suspension subjected to thermal and γ-radiation transients (GRS)

The corrosion experiments for SGI cast iron in a saturated Wyoming bentonite slurry using Opalinus Clay water (w/s ratio 1:10, Type V experiment in Section 5.2.2) were carried out under the same conditions described above (Section 5.3.4.1) but they were γ-irradiated for 220 days in the Panoza-facility of UJV-Rez (Prague). The temperature was set to 50°C using an electric oven. The dose rate, measured with a dosimeter inside the reactor, was 130 kGy hr^{-1}. In this case a corrosion rate of 52 µm yr^{-1} was calculated considering a homogeneous degradation of the whole pellet. This value is ca. five times larger than that determined electrochemically without radiation.

The oxygen content measured in the supernatant solution was 0.03 mg l^{-1}, indicating the development of an anaerobic atmosphere (fully saturated water has ~8 mg l^{-1} oxygen). Chemical analysis of a filtrate of the supernatant liquid indicated the formation of NO_3^- and NO_2^- at concentrations of 6.45 10^{-6} mol L^{-1} and 1.52 10^{-5} mol L^{-1} respectively and 3.6 10^{-3} mol L^{-1} of a sulphur compound different from SO_4^{2-} (probably HS^-). Analysis of the SGI bentonite-free surface indicated the formation of fundamentally $Fe(OH)_2$ and silicates.

5.3.6 Spheroidal graphite cast iron (SGI) subjected to static or dynamic thermal and redox transients (KIT)

The corrosion experiments performed with spheroidal graphite cast iron *(*SGI) included a 100 g L^{-1} Wyoming bentonite suspension test environment. These experiments were performed under anoxic conditions at room temperature (25°C) and at 50°C with contact times of 3 months and 6 months, under static (Type VI experiments in Section 5.2.2) and dynamic conditions (Type VII experiments in Section 5.2.2).

Under static conditions, metallic corrosion affected the redox potential and, overall, reducing conditions developed as a consequence of steel corrosion, suggesting the formation of Fe(II)-bearing compounds, except at 25°C when haematite was present. Lower Eh values were recorded after 6 months, except in the experiment at 25°C in the absence of α-Fe_2O_3.

In some static experiments, the SGI / suspension interface exhibited a slight blue-green colour indicating that some reaction had occurred. Colour is among the properties of smectites that is greatly affected by redox reactions, especially for Fe-rich smectites (Stucki, 2011). The observed change of colour may either have been due to reduction of structural iron within the smectite component of the bentonite, or the formation of corrosion products (e.g. green rust compounds).

The corrosion rate of SGI was calculated based on mass loss for static experiments, but no corrosion rates could be estimated for dynamic conditions. Under static conditions, after 3 months at 25°C in contact with the bentonite suspension, the corrosion rate of 4.8 µm yr^{-1} (Table 32) was higher than that reported (~2 µm yr^{-1}) for carbon steel embedded in compacted MX-80 and exposed to natural granitic porewater for 394 days in the MaCoTe experiment (Reddy et al., 2020). Both the difference in reaction time (90 days vs 394 days) and the difference in temperature (25°C vs rock temperature) can account for the different observed rates. In addition, the use of a suspension instead of compacted bentonite also plays a role because of the greater availability of water in the former.

Increasing the temperature to 50°C significantly increased the corrosion rate, in agreement with other reported findings (Hesketh et al., 2023). Corrosion rates decreased systematically with increasing reaction time, for instance at 25°C from 4.8 µm yr^{-1} after 3 months to 2.6 µm yr^{-1} after 6 months.

The same trends were observed in experiments performed in the presence of haematite, though the rates were slightly higher compared to experiments in the absence of added ferric compounds. Under static conditions, the presence of haematite affected the in situ redox potential and the corrosion rate. The formation of iron silicates could be detected in some samples, especially at 50°C, suggesting that dissolved silica must have been available in the system (Kaufhold et al., 2020), favoured by the slightly elevated temperature and the prevailing pH / Eh conditions. Interestingly, data also indicated that neoformed iron silicates contained some aluminium, meaning that the availability of dissolved silica alone cannot account for the observed secondary phases. Consequently, the reaction pathway may not simply consist of precipitation from dissolved species but may be more complex and possibly involve some kind of dissolution-reprecipitation mechanism.

After 6 months of reaction under static conditions, the surface was more damaged compared to 3 months, even at 25°C (Figure 50). The surface was particularly damaged within a small circular area surrounding graphite inclusions, suggesting preferential dissolution of iron without affecting the graphite. This observation may suggest the development of different electrochemical potentials at the surface of

the conducting coupon between the inclusion and its immediately surrounding metal, whereby graphite would act as cathodic site. This spatial separation of anodic and cathodic sites results in the development of a galvanic cell (Schlegel et al., 2018), which is favourable to increasing the extent of metallic corrosion. Interestingly, the presence of layered compounds can also be seen after 6 months at 25°C, suggesting the presence of $Fe(OH)_2$ but not green rust type compounds. This finding supports the view that conditions were clearly reducing at the coupon / suspension interface.

XPS analyses provided complementary chemical information as well as speciation information. For all analyses the findings were comparable. The spectrum recorded at the metal surface (Figure 51) identified the presence of metallic Fe, suggesting that no Fe-bearing secondary phase was attached to the surface. Low concentrations of sulphide were also detected at the coupon surface, most probably as iron sulphide (e.g. due to pyrite naturally present in the bentonite adhering to the surface).

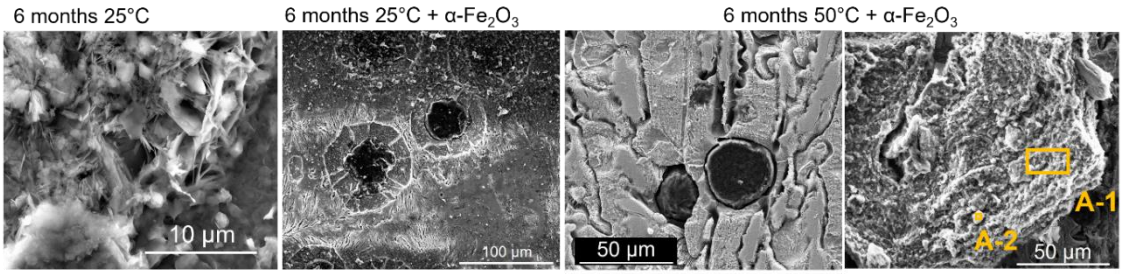

Figure 50. Scanning electron micrographs (in SE mode) of SGI coupons corroded for 6 months under static conditions (exact conditions are indicated above the micrographs). Areas marked in orange were selected for EDX analysis.

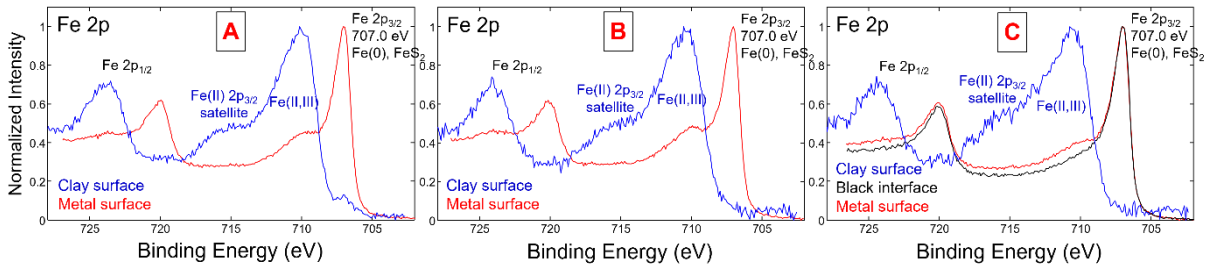

Figure 51. X-ray photoelectron spectra recorded on the SGI corroded for 3 months at 25°C in absence of α-Fe_2O_3 (A), SGI corroded for 3 months at 50°C in the presence of α-Fe_2O_3 (B) and SGI corroded for 6 months at 25°C in the presence of α-Fe_2O_3 (C).

At the clay surface, Fe 2p spectra show shake-up satellites characteristic of Fe(II). Shake-up satellites of Fe(III) were weak or not present. Interestingly, the binding energy of Fe 2p3/2 lines were at about 710 eV, which is characteristic for iron oxides containing Fe(III), but also for Fe(II) in silicates. This finding would agree with the visual observation of a blue-green coloration at the coupon / suspension interface, suggesting a possible reduction of structural Fe(III) within the smectite. In addition, this finding would also agree with the presence of a mixed Fe(II)/Fe(III)-bearing secondary phase such as odinite or berthierine ($(Fe^{II},Fe^{III},Al,Mg)_3(Si,Al)_2O_5(OH)_4$) suggested from SEM-EDX analysis. XPS data suggest that Fe prevails in the divalent and trivalent oxidation states at the coupon / bentonite interface in all experiments, and no significant impact due to the presence of haematite could be detected.

Under dynamic conditions, after 3 months exposure to a bentonite suspension at 25°C (Figure 52), the coupon surface appeared non-uniformly corroded, with some areas having exposed cementite lamellas, which were comparable to the coupon corroded under static conditions at 25°C (Figure 50). In the presence of added haematite, the morphology seems comparable although with Fe removal going deeper at grain boundaries. At 50°C, in the presence of added haematite, the iron removal from the surface seems larger: observations suggest that elevated temperature and the presence of haematite

both promote the surface degradation / corrosion. At the surface exposed to the suspension for 3 months at 25°C with added haematite present, iron was present in the divalent and trivalent oxidation states (Figure 53). In the parallel experiment at 50°C, the Fe 2p spectrum agrees with the presence of metallic Fe, suggesting that no Fe-bearing secondary phase was attached to the surface. The steel degradation mechanisms under dynamic conditions seem very similar to those under static conditions, but the surface damage appeared greater.

At the clay surface, Fe was present as a mixture of Fe(II) and Fe(III), comparable to the observations from experiments under static conditions (Figure 53). This finding suggests that Fe(II) formed during steel corrosion reacted with the contacting bentonite, resulting either in the (partial) reduction of structural Fe(III) in the bentonite or the formation of a mixed Fe(II)/Fe(III) compound. However, no neoformed Fe-bearing phase could be detected at the coupon / bentonite interface, suggesting a partial reduction of structural Fe in the bentonite.

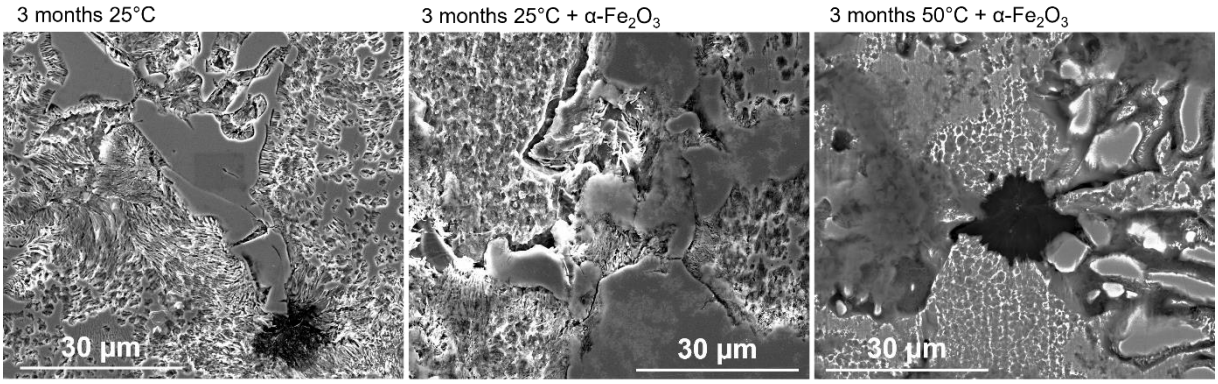

Figure 52. Scanning electron micrographs (in SE mode (centre and left) or BSE mode (right)) of SGI coupons corroded for 3 months under dynamic conditions (exact conditions are indicated above the micrographs).

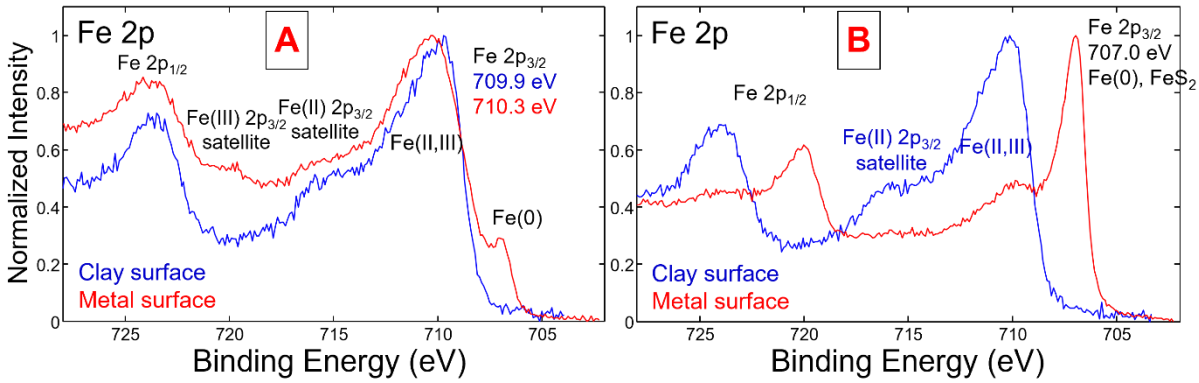

Figure 53. X-ray photoelectron spectra recorded on SGI corroded under dynamic conditions for 3 months at 25°C in the presence of α-Fe_2O_3 (A) and SGI corroded for 3 months at 50°C in the presence of α-Fe_2O_3 (B).

5.3.7 CuNi alloy experiments subjected to static or dynamic thermal and redox transients (KIT)

Experiments carried out with CuNi alloy and bentonite suspension, subjected to thermal and redox transients for 3 months under static conditions showed that pH and Eh did not evolve much from the values for the starting pre-equilibrated bentonite suspension, except for the experiment at 50°C with 3 µM of added sulphide. After 6 months, no significant difference was observed for the measured pH

or Eh, suggesting that neither the presence of sulphide nor increased temperature had any significant effect on the evolution of pH and Eh. It is interesting to note that Eh values are clearly positive, in contrast to experiments with the cast iron, and conditions did not become reducing even in the presence of added sulphide.

Upon removal of the coupons from the suspension, the interface was brownish in some experiments performed at 50°C and observations suggest the formation of secondary copper and/or nickel compounds accumulating at the coupon surface.

No presence of corrosion products could be detected by XRD analysis of the corroded specimens. Findings suggest that either secondary phases formed in insufficient amounts to be detected or that they may have been removed when cleaning off the excess suspension, because electron microscopy showed the presence of particles at the coupon / suspension interface. Scanning electron microscopy was subsequently applied to analyse the corroded coupons.

EDX analyses of the particles indicate the presence of Cu-rich oxide particles in all samples, sometimes with low amounts of associated sulphur. The Cu-rich particles had small sizes and were present at the surface of a substrate predominantly made of Cu, rendering the exact determination of the elemental composition complicated because of a high contribution from the underlying substrate. However, EDX spectra recorded on well separated particles confirmed the presence of Cu only. No Fe or Ni could be found associated with the particles. Sulphur was only detected in some samples, ruling out the formation of Cu sulphide as a corrosion product.

SEM-EDX results (Figure 54) revealed a Cu:O atomic ratio of 2:1, thus suggesting the presence of Cu_2O (cuprite) particles. Complementary XPS measurements after 3 months at 25°C, showed the presence of Cu_2O, together with Ni(0), while Cu(0) and $Ni(OH)_2$ were detected in the parallel experiment at 50°C. The Cu speciation did not evolve between 3 and 6 months, with the presence of Cu_2O at 25°C and Cu(0) at 50°C, but no Ni could be detected in samples after 6 months exposure. These findings may suggest that at 25°C Cu is oxidised to Cu(I) but Ni is not oxidised, whereas at 50°C Ni is oxidised to Ni(II) but Cu is not oxidised.

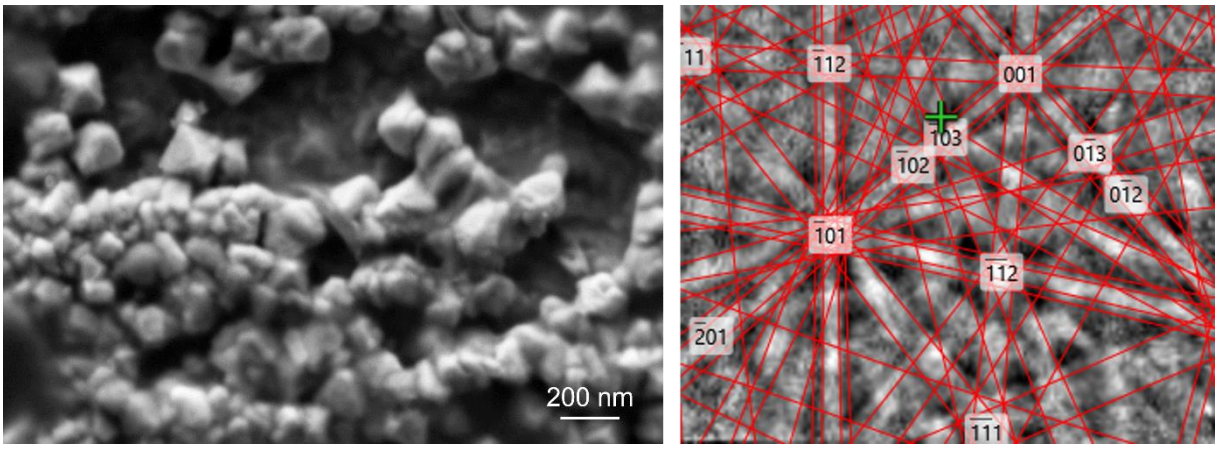

Figure 54. Scanning electron micrograph recorded at 2.5 kV acceleration voltage (left), and Kikuchi pattern and indexing with Cu_2O (red, right).

The presence of added sulphide had no significant impact on the Cu and Ni speciation at both temperatures and both exposure times. Sulphides could be detected at the surface of all coupons, with larger amounts detected in experiments at 50°C. Almost no Cu or Ni could be found associated with the clay surface, meaning that CuNi corrosion resulted in the formation of low solubility secondary phases at the coupon / suspension interface where the alloy was exposed. Similarly, no Si, Fe or Al, which are the main elemental components of bentonite, could be found associated with the corrosion products. This latter finding agrees with the reported existence of different reaction mechanisms at the Fe / bentonite interface compared to the Cu / bentonite interface (Kaufhold et al., 2017).

The alloy used in the present study contained ~30 wt.% Ni with lower proportions (<1 wt.%) of Fe and Mn, but analyses revealed the dominant presence of Cu-bearing secondary phases, thus suggesting that the degradation mechanism may involve copper. Since metallic Cu does not corrode in pure water (Hedin et al., 2018; Senior et al., 2019) not many possibilities may explain the observed findings. Considering that only marginal amounts of S were found associated with secondary phases the only oxidant present was residual oxygen, which would agree with the findings of Kaufhold et al. (2017) because the MX-80 bentonite used contained only low amounts of pyrite (0.6 wt.%, Karnland, 2010). Since cuprite was clearly detected at the surface of the coupons, but not Cu sulphide, residual oxygen must have been present in large excess compared to sulphide. Indeed, considering the starting sulphide concentration and the volume of suspension, only very low amounts of Cu sulphide would be expected to form. In addition, under the prevailing conditions, (i.e. excess of residual oxygen, as suggested from the observation of neoformed Cu_2O compared to added sulphide), the oxidation of sulphide to thiosulphide or other S species may also have occurred. These considerations would also be in line with observed corrosion rates being hardly affected by the presence or absence of sulphide.

Corrosion experiments with CuNi under dynamic conditions were performed in parallel. Compared to experiments under static conditions, measured pH values were significantly higher under dynamic conditions. Measured Eh values were all very comparable and clearly negative, ranging from -166 mV to -189 mV, and did not exhibit any significant variation with time, temperature or sulphide presence. These outcomes suggest the development of reducing conditions, which contrasts with results from experiments under static conditions.

Interestingly, the observed pH and Eh values and their evolution with time compare well with those obtained in experiments under dynamic conditions with SGI. Though pH variations can be interpreted as dilution of the suspension by the inlet water, this may hardly explain the observed Eh evolution because the redox potential of the inlet water was positive (115 mV), suggesting that either the protocol used to measure Eh (i.e. in water at outlet) or the setup used may have an effect on these values.

The sample corroded for 3 months at 25°C appeared to be covered by a thin layer of fine-grained material, suggesting significant contribution from the underlying substrate. At 50°C, secondary phases exhibited a thin layered morphology, up to several µm across, suggesting that temperature played a role in the development of the morphology of the secondary phases formed. The measured elemental composition of the particles is consistent with a Cu oxide but without Ni present.

Overall, the results for experiments conducted under dynamic conditions were very comparable to those obtained under static conditions, with the predominant formation of Cu oxide particles. With the formation of these secondary phases, a Ni-rich layer formed above the underlying coupon and Ni is not associated with the Cu oxides. Nickel was only found as hydroxide at the surface of some coupons. Finally, only limited amounts of S were found at the coupon surface. Based on the comparable secondary phases detected in experiments under static conditions, positive Eh values would be expected and not the negative values measured in the outlet water. One possible explanation could thus be the absence of bentonite and/or secondary phases acting as a redox buffer of the system during Eh measurements.

5.3.8 Results from samples from in situ Äspö laboratory experiments subjected to near-field transients

Results from in situ laboratory experiments from the Äspö underground laboratory were published in Fernandez et al. (2022). In the large scale in situ ABM5 experiment, all bentonites preserved their hydro-geochemical properties after being subjected to saline groundwater infiltration, heating and interaction with corroding metals during the 4.4 years of the experiment. The main change observed in all bentonites was the modification of exchangeable cation composition, which is explained on the basis of equilibration with Äspö saline groundwater that is enriched with Ca and Na salts. The initial bentonite porewater was modified in all the bentonite blocks after their interaction with the saline Na-Ca-Cl

groundwater. Porewaters changed from mainly an initial Na-Cl or Na-SO_4 water type towards a Na-Ca-Cl porewater in all the bentonite blocks analysed, except for MX-80 block 1, which changed from Na-SO_4 to Na-Cl water-type. Water-vapour fluxes probably increased the salinity of the porewaters at the top part of the package.

Fe increased as a function of the distance towards contact with the heater. Heater corrosion resulted in the increase of iron in the bentonite and goethite, haematite and siderite were found as corrosion products. No magnetite was detected. Although the ratio of ferrous to ferric iron increased in the close vicinity of the carbon steel heater, the majority of the Fe content was present as Fe(III).

5.4 Overview of key outputs from Task 5

5.4.1 Influence of temperature and degree of saturation of bentonite on carbon steel corrosion

Temperature and the degree of saturation of the bentonite are the main factors affecting corrosion rates of carbon steel samples embedded in bentonite. Higher corrosion rates were measured at 150°C than at 90°C (Figure 44). Non-uniform corrosion, connected to heterogeneous saturation, was observed previously in various clay / bentonite environments (e.g. King 2008; Zuna et al. 2023). Corrosion rates in model environments range from units to tens of µm yr^{-1} for most authors (e.g. Neff et al. 2010; Smart et al. 2012). These rates correlate well with the corrosion rates measured in the heated Czech BCV and MX-80 bentonites.

There was no verified effect of initial humidity on the steel corrosion rate, but increasing the initial humidity of bentonite seems to have had an inhibiting effect on the steel corrosion rate (Figure 55). The parallel influences of temperature, irradiation and humidity make it impossible to distinguish which parameter dominated. A possible explanation may be that there was insufficient pressure used in the saturation of irradiated cells, which caused corrosion in water vapour rather than in pore solution. Corrosion products originating in vapour conditions are conventionally more compact and thinner than those formed in bulk aqueous solution.

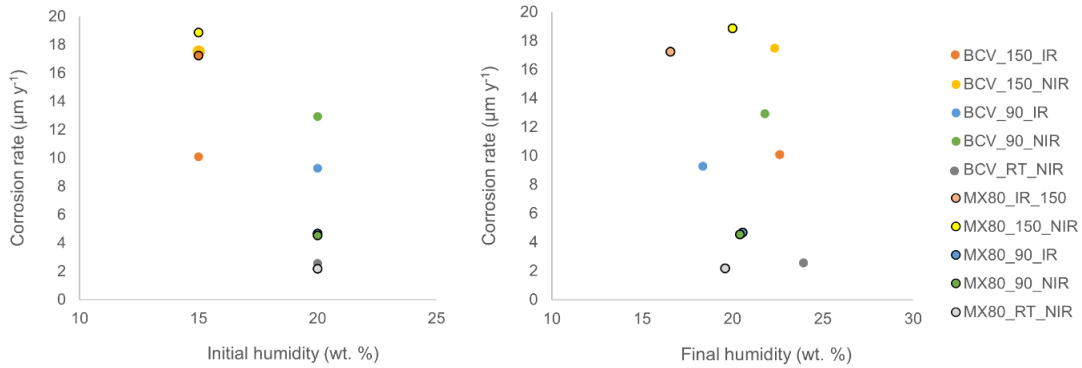

Figure 55. Correlation of Czech carbon steel corrosion rate with (left) initial and (right) final humidity of BCV bentonite.

The thickness of the corrosion layer correlated well with the heating temperature and length of exposure period. A more extensive and thicker layer was identified on steel samples heated at 90°C. This feature is explained by the higher saturation of bentonite and higher water content, which can facilitate formation of corrosion products. Formation of Fe-Si-rich corrosion layers was found to depend on the heating temperature up to 150°C. The source of silica is believed to be the amorphous phases of the bentonite (e.g. Kaufhold et al., 2013) and/or smectite alteration (Madejová et al., 2009). Theoretical models of corrosion product formation predict the formation of magnetite as the main corrosion product, as well as siderite and chukanovite as minor corrosion products in the early stages of environmental development ((e.g. Bildstein et al., 2006, Wilson et al., 2017. Greenalite ($(Fe^{2+},Fe^{3+})^{2-}{}_3Si_2O_5(OH)_4$), chamosite ($(Fe^{2+})_5Al(Si,Al)_4O_{10}(OH,O)_8$) and Fe-illite ($(K,H_3O)(Al,Fe)_2(Si, Al)_4O_{10}[(OH)_2,(H_2O)]$), should be present in the system according to the long-term models. Mainly magnetite, but also chukanovite and siderite were confirmed in some experiments. This is in accordance with the expected model. Absence of silicate-based corrosion products is explained by the short duration of the experiments (e.g. King et al., 2008; Stoulil et al., 2013, 2022).

A thermal effect (150°C) on the proportions of Ca^{2+} and Mg^{2+} as exchangeable cations is clearly visible. High temperature caused an increase in the Ca^{2+} content and a decrease in the Mg^{2+} content. Bentonite heated at 90°C exhibited comparable values to those of unheated bentonite.

Thermal loading at 150°C induced an increase in Ca^{2+} and a decrease in Mg^{2+} levels in the BCV bentonite, similar to those observed in the MX-80 bentonite. An increase of Na^+ in the exchangeable cation position was observed in the BCV bentonite heated to 150°C. There is expected to be a combined effect of heating and Na^+ input from SGW3.

Enrichment of bentonite by Fe^{x+} was confirmed by XRF. Charpentier et al. (2006) documented the transformation of montmorillonite by interaction of MX-80 bentonite with Fe-powder in the presence of alkaline solutions and elevated temperatures. Montmorillonite was still the dominant clay phase at 80°C and 150°C but enriched in Fe and depleted in Si. Fe-vermiculite predominated at 300°C and was associated with zeolite and saponite. The montmorillonite transformation led to significant modification of the material properties as exhibited by decreasing swelling due to the presence of less swelling vermiculite and non-swelling zeolite. On the other hand, zeolite (mordenite) exhibited high cation exchange capacity and high adsorption capacity, which was comparable to the initial bentonite.

Formation of magnetite was documented by XRD for all carbon steel samples. The presence of iron sulphide was detected as a result of the SRB (sulphate-reducing bacteria) activity. These bacteria use lactate added to the Opalinus water representative of Callovo Oxfordian (France) formation and hydrogen formed by steel corrosion as an energy source for sulphate reduction. However, 70% of the steel surface was still covered by magnetite and the corrosion products contained less than 3% of sulphide compounds. Siderite, chukanovite and β-$Fe_2(OH)_3Cl$ were detected after 6 months. In the

current experiments the influence of sulphate-reducing bacteria (SRB) was minimal due to the high temperature. The main conclusions connected to the microbiological analyses of BCV and MX-80 bentonites sampled in the current experiments were reported in Concord Task 4 (Hidalgo et al., (2024).

5.4.2 Influence of bentonite type and degree of saturation on carbon steel corrosion

Overall, carbon steel corrosion rates increase with temperature and the degree of salinity of the porewater, and decrease with increasing dry density (Table 35). The corrosion rates obtained in these transient experiments with carbon steel coupons ranged from 28 to 413 µm yr^{-1}, depending on the salinity of the porewater and the dry density of the bentonite. Higher corrosion rates were observed for high salinity porewaters and lower dry densities, as observed for FEBEX bentonite compared to SWy-3 and Czech bentonites. In any case, the extent of alteration inside the bentonite was <2 mm in all bentonite samples, with smectite clay particles being preserved. The main corrosion product detected in all the laboratory experiments performed with carbon steel was magnetite, which is transformed into other Fe(III) mineral phases as a function of the oxygen content of the environment.

The lower corrosion rate of Fe-pellets embedded in the Na-bentonites compared to those embedded in Ca-bentonites was observed by Kaufhold et al. (2015b). The initial expectation was that Na-bentonites would be more corrosive due to the formation of voluminous water-rich gels, which hence leave more water at the interface. However, experiments showed less corrosion in Na-bentonites. Fe-rich bentonites were also not more corrosive than others. The lower corrosion rate in Na-bentonite compared to Ca-bentonites was explained by a possible effect of different pH values.

5.4.3 Influence of thermal and radiation transients on carbon steel corrosion

No effect at all, or a very minor effect, of irradiation on corrosion rate was observed when the steel samples were heated in the MX-80 bentonite. This can be explained by the low dose rates used in the experiment. On the other hand, the measured corrosion rates indicated less corrosion of carbon steel when it was embedded in the BCV bentonite and unirradiated at 150°C compared to samples subjected to irradiation. This phenomenon is more attributed to the degree of saturation than the influence of radiation (Figure 44).

5.4.4 Influence of thermal and hydration transients on Cu-OFP corrosion

The corrosion rates of Cu-OFP samples subjected to the same coupled thermo-hydraulic gradients were significantly lower than those for carbon steel under the same conditions (ranging from 3 to 9 µm yr^{-1}, Table 36). The degree of corrosion depended more on the type of bentonite than on its dry density. The extent of bentonite alteration at the bentonite / coupon interface was <0.5 to 1 mm for all samples, which was much lower than that observed for carbon steel coupons. The presence of both cuprite (red, Cu_2O, Cu(I)) and tenorite (black, CuO, Cu(II)) corrosion products was indicated.

5.4.5 Effect of thermal, redox and radiation transients on corrosion of spheroidal graphite cast iron (SGI) corrosion

In all experiments, SGI corroded upon exposure to the bentonite suspension. The pH hardly changed, but the redox potential decreased in all experiments, suggesting the formation of Fe(II)-bearing secondary phases. Increasing the temperature to 50°C significantly increased the corrosion rate in the present study, in agreement with other reported findings (Hesketh et al., 2023). Corrosion rates increase with temperature because of a decreased activation barrier, for example for chemical and electrochemical reactions.

Corrosion rates decreased systematically with increasing reaction time, for instance at 25°C from 4.8 µm yr^{-1} after 3 months to 2.6 µm yr^{-1} after 6 months. This result also agrees with reported corrosion rate evolution in general and hint at the formation of a protective passivation layer at the coupon surface.

The corrosion of SGI subjected to a γ-radiation dose rate of 130 kGy hr^{-1} was five times larger than that determined under the same conditions without radiation.

5.4.6 Effect of haematite presence on spheroidal graphite cast iron (SGI) corrosion

The presence of haematite did not significantly alter the SGI degradation mechanism, but served as a sink for Fe(II), which possibly retarded the formation of a protective layer of Fe(II)-bearing compounds and very probably caused an increase of the corrosion rate. For this steel, graphite inclusions very probably serve as cathodic sites where water is reduced and the coupled anodic reaction corresponds to preferential ferrite oxidation.

In the context of HLW, the formation of haematite at the container surface during the initial oxic period can result in a corrosion rate that is initially higher than it would be in the absence of α-Fe_2O_3. The outcomes of the study did not provide evidence for an alteration of the degradation mechanism, only its rate. Over time and with metallic corrosion further proceeding, haematite is very likely to be converted into mixed Fe(II)/Fe(III) compound(s).

5.4.7 Effect of thermal and redox transients on corrosion of CuNi alloy: role of sulphide presence

Copper oxides were the most abundant secondary phases observed in the CuNi corrosion experiments under all applied conditions. The presence of added sulphide had no significant effect and only minor amounts of sulphide species were detected, which were partly also attributable to the presence of pyrite that is naturally present within the bentonite. Interestingly, these findings parallel the outcomes from in situ corrosion experiments. Indeed, most of the Cu corrosion products detected in the MaCoTe experiment are oxides and only minor amounts of sulphide compounds were detected (Reddy et al., 2020). It may thus be possible that longer exposure times, or higher sulphide concentrations, would be needed to observe unambiguously the formation of Cu sulphide species in substantial amounts.

Copper does corrode in the presence of sulphide, but not in pure water. In the present study, the only additional oxidant present was residual oxygen. Interestingly, under the prevailing pH and Eh conditions, the nature of the detected corrosion products agree with the reported Pourbaix diagrams (Puigdomenech and Taxen, 2000). These reported data further indicate that sulphide compounds would only be stable under more reducing conditions. It is also interesting to note that Ni, although present in substantial amounts in the alloy, did certainly not play any significant role in the degradation mechanism because no Ni was found associated with the corrosion products.

In the context of HLW, the outcomes of the present study do not allow conclusions to be drawn on any negative effect of a progressive increase or constant supply of sulphide on CuNi corrosion behaviour. No effect of Ni in the alloy on the corrosion behaviour could be identified either. During the long-term evolution under repository conditions, it can be hypothesised that CuNi would degrade and result in the formation of Cu sulphides (as a product of copper oxide reacting with dissolved sulphides (Hollmark et al., 2012)) and the formation of a separate Ni hydroxide, through the conversion of this latter compound into sulphide cannot be excluded.

6. Task 6: Modelling and integration for performance assessment

6.1 Scope of the task

6.1.1 Sub-task 6.1: Develop modelling tools and integrate experimental data from other Tasks

6.1.1.1 Reactive transport modelling of steel corrosion in bentonite (Amphos 21)

Background

The corrosion of canisters in geological disposal facilities (GDFs) can be considered from several points of view: the material of the canister, the corrosive nature of the environment, for instance the porewater composition in the engineered barrier, the temperature and degree of liquid saturation, and the intensity of irradiation from the spent fuel (King and Padovani, 2011).

When focusing on carbon steel, the phenomenon of corrosion and the possible migration of radioisotopes due to corrosion processes can also be approached from several perspectives, such as the possibility of hydrogen gas generation leading to significant pressure build-up and mechanical failure of the canister, the degradation of the engineered barriers due to chemical alteration (caused by pH variation and transport of corrosion products), or the nature of the oxide phases formed on the surface, which will determine the extent of corrosion in the long term. Water radiolysis products may also increase the corrosion potential and the formation of less stable corrosion products under low dose rates, preventing the formation of a stable passive film.

Motivation

The main goal of Task 6.1 was to develop a robust numerical tool for general use in the simulation of uniform corrosion under transient conditions that replicate possible scenarios of GDF at a laboratory scale. The work focused on the behaviour of carbon steel embedded in compacted bentonite and slurries, and the impact of relevant environmental factors, such as temperature, irradiation or porewater composition, on the rate of corrosion (see Section 3) The model is intended to describe all the physical features presented in 1.1 above except the mechanical degradation of the canister.

Special attention was paid to the impact of water radiolysis and chloride radiolysis on corrosion processes. Although water radiolysis does not seem to increase the corrosion rate in the long term according to experiments, radiolysis of chloride might catalyse the production of oxygen and significantly increase oxic corrosion. In this sense, 8-day irradiation of carbon steel samples embedded in compacted FEBEX bentonite (0.16 mM of Cl^- in porewater) at a dose rate of 66 Gy hr^{-1} has led to an unexpected extent of corrosion (Fernandez et al., 2024). The numerical model developed in Task 6.1 aimed to reproduce this phenomenon and assess whether a stable protective film is likely to reduce the corrosion rate in the long term.

6.1.1.2 Adding microbial activity to geochemical models (UFZ)

Corrosion of containers under disposal conditions is a crucial factor in assessing the performance and safety of all repository types, irrespective of the specific host rock location. Thus, it is vital to grasp the essential aspects of all relevant processes (such as thermo-hydro-mechanical, geochemical and microbiological) to construct a safety case. Figure 56 demonstrates UFZ's focus across the process chain at different scales, examining microbiological processes in detail regarding corrosion under disposal conditions. It also models near- and far-field processes. The link to the near-field simulations is gas production by chemical and microbiological processes, which is part of the WP ACED project. For detailed information, please refer to Vehling et al. 2024. When examining the transport of radionuclides in the far-field, diffusion processes in the host rock, as well as transport and dilution in the adjacent aquifer system, are significant contributors (Selzer et al. 2024). The primary focus of UFZ's work in the

ConCorD project was the experimental study of microbiological processes regarding corrosion, along with constructing models for near-field processes.

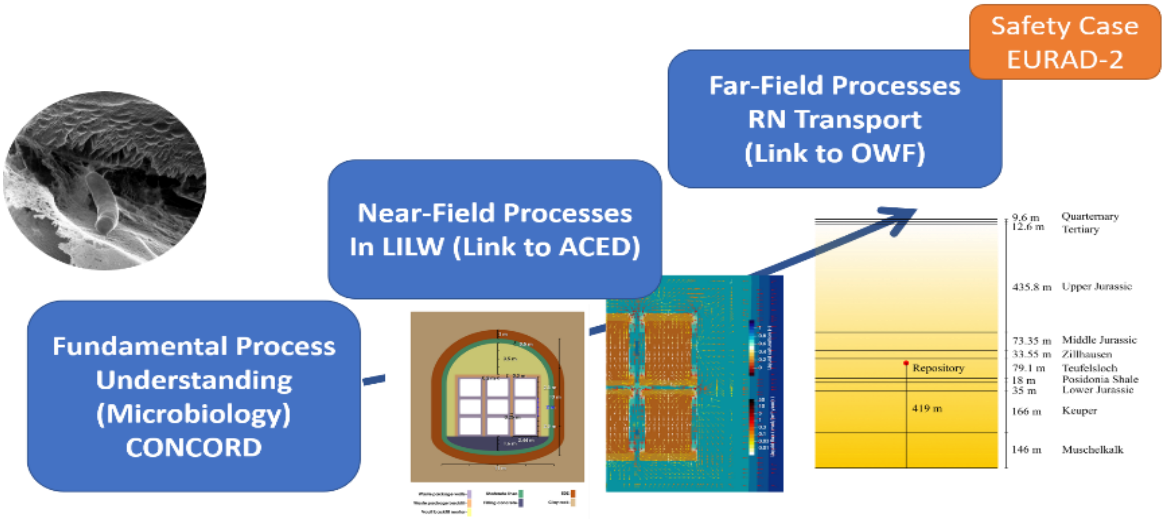

Figure 56: From fundamental process understanding towards safety case – the role of microbiological processes regarding corrosion under disposal conditions and subsequent modelling of near- and far-field processes.

6.1.1.3 Repository scale modelling of sulphide (UoBe)

The main objective of the study of University of Bern in EURAD ConCorD (Task 6) was to model the sulphide system in the near-field of the Swiss deep geological repository (DGR) using an improved biogeochemical model, and to estimate sulphide corrosion for both copper and steel canisters under various conditions. To accomplish this task, new features were implemented into the biogeochemical conceptual model and the model geometry, and sensitivity calculations were performed.

6.1.2 Subtask 6.2: Integration for performance assessment

Apart from work on developing models for corrosion behaviour in a repository, as discussed in the previous section, a main goal of Task 6 was the synthesis of new knowledge acquired during the course of ConCorD into a form applicable for container performance assessment, considering the specific needs of the safety cases developed by implementers. This is the aim of the current section, taking account of both experimental and modelling activities carried out within ConCorD. It should be noted that the sections dealing with Tasks 3, 4 and 5, include discussion of the ramifications of the specific results obtained to performance assessments. The aim of the current section is to highlight further high-level implications deriving from each of these tasks.

In preparing a performance assessment for a disposal concept, many different aspects of corrosion need to be considered. An example of this approach is SKB's recent PSAR Fuel and Canister Process Report (SKB, 2022). The main aspects of corrosion that need to be considered in a full corrosion assessment, for both copper and carbon steel, include the following:

- Atmospheric corrosion in encapsulation plant and during possible interim storage
- General corrosion due to initially trapped O_2
- General corrosion due to O_2 in glacial meltwater penetrating to repository depth
- Effect of radiation under both saturated and unsaturated conditions
- Corrosion by sulphide for both intact and eroded buffer
- Corrosion by water
- Localised corrosion under aerobic conditions
- Localised corrosion under anaerobic conditions

- SCC of copper
- SCC of steel
- Microbially influenced corrosion
- Earth currents

As is clear from the information presented above, the main focus of the experimental work conducted in ConCorD that is relevant to performance assessments was on (i) the effects of radiation on corrosion and (ii) the role of microbial activity. Both these tasks produced valuable results that should be taken into account in future performance assessments. These two aspects are considered below. The results from Task 2 were mainly related to developing novel materials and new technologies and, although valuable, they are of less direct relevance to current performance assessments. Therefore, the results of Task 2 have been considered with regard to potential future performance assessments.

6.2 Progress against task description

6.2.1 Subtask 6.1 Develop modelling tools to integrate experimental data from other Tasks

6.2.1.1 Reactive transport modelling of steel corrosion processes in bentonite (Amphos21)

Numerical model

The development of the numerical model was carried out in three different stages:

Firstly, a 1D reactive transport model was developed of the experimental cell with the geochemistry of compacted bentonite and the slurry, considering a constant anoxic corrosion rate in the COMSOL – PhreeqC coupling tool iCP (Nardi et al., 2014).

Then, secondly, the radiolysis of water and chloride was incorporated into the coupling scheme depicted in Figure 57, along with a large number of radiolytic species that were not coupled with the geochemical database. The radiolytic species were used as input to the electrochemical corrosion model in COMSOL (Comsol Multiphysics, 2021), and the corrosion rate and the pH were coupled to the homologous variables in PhreeqC (Parkhurst and Appelo, 2013). Finally, the anodic currents of all reducing species and those of the corresponding oxidised products (see Section 2.3) were used as a Neumann flux in the transport equations. Also, the most relevant charged species are transported with the Nernst-Planck equation after calculating the electric potential.

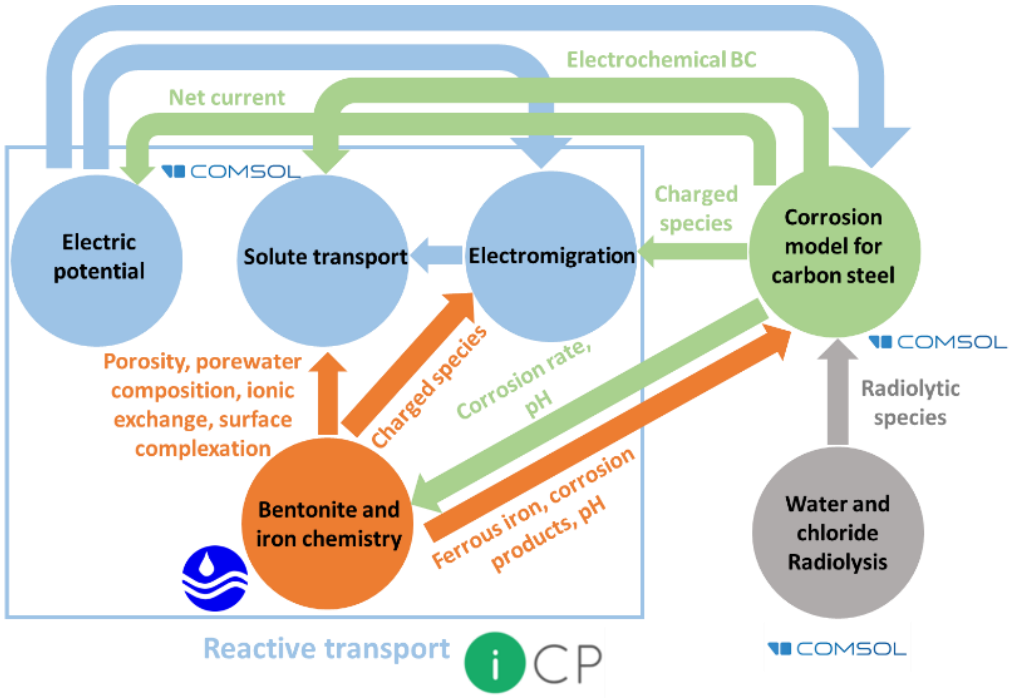

Figure 57. Electrochemical numerical model. Coupling scheme between reactive transport, corrosion of carbon steel and radiolysis of water and chloride.

Reactive transport

The development of the numerical model was carried out on the iCP computational platform (Nardi et al., 2014), which couples transport equations in COMSOL with geochemical calculations in PhreeqC. This tool has been largely tested in GDF reactive transport simulation of engineered barriers such as compacted bentonite (Idiart and Coene; 2019; Idiart et al., 2019).

In the present case, the geochemical model was dedicated to compacted FEBEX bentonite or MX-80 slurries. The modeling of the former was based on the initial mineralogical composition and the porewater presented by Fernandez et al. (2000), whereas the latter was modeled as a dilution of the compacted MX-80 analysed by Bradbury and Baeyens (2003). From these data, together with inputs from the transport, corrosion and radiolysis models, PhreeqC was used to update the chemical composition of the water and the bentonite (including its porosity), using the database Thermochimie v10d (Giffaut et al., 2014), which accounts for chemical equilibrium, kinetics and more specific aspects, such as cation exchange or surface complexation.

Water and chloride radiolysis

Radiation-induced corrosion of steel canisters used to contain the spent fuel (SF) is a process of potential importance for the long-term safety of a deep geological repository (DGR). Under normal conditions, the outer surface of the canister will be exposed to gamma radiation. The ionising gamma radiation will produce both molecular and radical oxidants (radical OH, O_2 and H_2O_2) and reductants (e^-, H·and H_2) through radiolysis, with O_2 and H_2O_2 being key species for the radiation-induced corrosion of the canister. Moreover, the radiolysis of chloride-containing solutions has an impact on the concentration of the species produced by gamma radiation and, therefore, it is an important aspect to consider in the assessment of waste container integrity (Morco, 2020).

The model integrates the generation of water radiolysis species (Kelm and Bohnert, 2004; Pastina and LaVerne, 2001; Riba et al., 2021) and chloride radiolysis species by gamma radiation, by considering a

complete radiolysis system for both water and chloride. The model was implemented in COMSOL (Figure 57).

Electrochemical corrosion model for carbon steel

The corrosion model was restricted to carbon steel and spheroidal graphite iron (see Part 3 below). The formulation is based on mixed potential theory (King and Kolar, 2012) for the four reactions listed in Equations 2a-d, which account for both oxic and anoxic corrosion; both forms of corrosion are considered to be uniformly distributed over the working electrode surface.

$$\mathrm{Fe} \leftrightarrow \mathrm{Fe}^{2+} + 2\mathrm{e}^- \qquad \text{Equation 2-a}$$

$$\mathrm{O_2} + 2\mathrm{H_2O} + 4\mathrm{e}^- \leftrightarrow 4\mathrm{OH}^- \qquad \text{Equation 2-b}$$

$$2\mathrm{H}^+ + 2\mathrm{e}^- \leftrightarrow \mathrm{H_2} \qquad \text{Equation 2-c}$$

$$2\mathrm{H_2O} + 2\mathrm{e}^- \leftrightarrow \mathrm{H_2} + 2\mathrm{OH}^- \qquad \text{Equation 2-d}$$

The parametrisation of the model (Table 37) is mostly based on the work by Chen et al. (2018) for mild steel in water with 1 wt.% chloride and dissolved oxygen, both of which are expected to play a key role in radiolysis due to γ-radiation. The model was adapted to carbon steel by adopting a lower value for the reference exchange current density ($j_{0,\mathrm{Fe}}^{\mathrm{ref}}$), taken from Garcia et al. (2021), and a correlation between the iron reversible potential ($E_{\mathrm{rev,\,Fe}}$) and the concentration of Fe^{2+} on the metal surface (Soliz and Cáceres, 2015).

	Standard potentials (vs SHE) for Fe, O_2, H^+ and H_2O				Reference exchange current density for Fe, O_2, H^+ and H_2O				
Symbol	$E^0_{\mathrm{rev,Fe}}$	$E^0_{\mathrm{rev,O_2}}$	$E^0_{\mathrm{rev,H^+}}$	$E^0_{\mathrm{rev,H_2O}}$	$j^{\mathrm{ref}}_{0,\mathrm{Fe}}$	$j^{\mathrm{ref}}_{0,\mathrm{O_2}}$	$j^{\mathrm{ref}}_{0,\mathrm{H^+}}$	$j^{\mathrm{ref}}_{0,\mathrm{H_2O}}$	
Value	-0.447	0.401	0	-0.828	0.169	$7.0{\cdot}10^{-4}$	0.03	$1.4{\cdot}10^{-5}$	
Unit	V	V	V	V	A m^{-2}	A m^{-2}	A m^{-2}	A m^{-2}	
	Active enthalpy for exchange for Fe, O_2, H^+ and H_2O				Refence temperature				
Symbol	ΔH_{Fe}	$\Delta H_{\mathrm{O_2}}$	$\Delta H_{\mathrm{H^+}}$	$\Delta H_{\mathrm{H_2O}}$	$T^{\mathrm{ref}}_{\mathrm{Fe}}$	$T^{\mathrm{ref}}_{\mathrm{O_2}}$	$T^{\mathrm{ref}}_{\mathrm{H^+}}$	$T^{\mathrm{ref}}_{\mathrm{H_2O}}$	$C^{\mathrm{ref}}_{\mathrm{H^+}}$
Value	37,500	23,200	30,000	30,000	298.15	303.15	298.15	293.15	0.1
Unit	J mol^{-1}	J mol^{-1}	J mol^{-1}	J mol^{-1}	K	K	K	K	mol m^{-3}

Table 37. Electrochemical parameters used in the corrosion model for Equations 2-a to 2-d.

The anodic currents (Equation 3) were restricted by the mass transport limiting current $j_{\mathrm{lim},i}$ (Equation 4) except for water reduction, due to the high liquid saturation in all considered cases. This limitation will be more pronounced in scenarios with compacted bentonite or film formation due to reduced diffusivity. Then, the corrosion rate is calculated straightforwardly in Equation 5.

Poisson's equation for the electric potential, φ (V), is calculated considering electroneutrality (Equation 6a), zero potential on the cell outer wall Γ_o (Equation 6b) and the corrosion potential E_{corr} on the metal surface Γ_m (Equation 6c).

As shown in Equations 7 and 8, the model is coupled to the temperature T (K) and the pH of the bulk solution, which is driven by the corrosion rate, the precipitation of corrosion products and the geochemistry of bentonite (Figure 57).

$$j_{\mathrm{ct},i} = j_{0,i} \times e^{\frac{-(\varphi - E_{\mathrm{rev},i})}{b}};\ b = \frac{RT}{nF} \qquad \text{Equation 3}$$

$$\frac{1}{j_i} = \frac{1}{j_{\mathrm{ct},i}} + \frac{1}{j_{\mathrm{lim},i}} \qquad \text{Equation 4}$$

$$j_{\mathrm{corr}} = j_{\mathrm{Fe}} = j_{\mathrm{O_2}} + j_{\mathrm{H^+}} + j_{\mathrm{H_2O}} \text{ at } \varphi = E_{\mathrm{corr}} \qquad \text{Equation 5}$$

$$\nabla^2\varphi = 0 \quad \text{Equation 6a}$$

$$\varphi = 0 \text{ on } \Gamma_o \quad \text{Equation 6b}$$

$$\varphi = E_{\text{corr}} \text{ on } \Gamma_m \quad \text{Equation 6c}$$

$$E_{\text{rev,O}_2} = E^0_{\text{rev,O}_2} - 2b(\text{pH} - \text{pK}_\text{w}) \quad \text{Equation 7a}$$

$$E_{\text{rev,H}^+} = E^0_{\text{rev,H}^+} - 2b\ \text{pH} \quad \text{Equation 7b}$$

$$E_{\text{rev,H}_2\text{O}} = E^0_{\text{rev,H}_2\text{O}} - 2b(\text{pH} - \text{pK}_\text{w}) \quad \text{Equation 7c}$$

$$j_{0,\text{O}_2} = j^{\text{ref}}_{0,\text{O}_2}\left(\frac{c^{\text{b}}_{\text{H}^+}}{c^{\text{ref}}_{\text{H}^+}}\right)^{-0.001678T} e^{-\frac{\Delta H_{\text{O}_2}}{R}\left(\frac{1}{T}-\frac{1}{T^{\text{ref}}_{\text{O}_2}}\right)} \quad \text{Equation 8a}$$

$$j_{0,\text{H}^+} = j^{\text{ref}}_{0,\text{H}^+}\left(\frac{c^{\text{b}}_{\text{H}^+}}{c^{\text{ref}}_{\text{H}^+}}\right)^{0.5} e^{-\frac{\Delta H_{\text{H}^+}}{R}\left(\frac{1}{T}-\frac{1}{T^{\text{ref}}_{\text{H}^+}}\right)} \quad \text{Equation 8b}$$

$$j_{0,\text{H}_2\text{O}} = j^{\text{ref}}_{0,\text{H}_2\text{O}}\left(\frac{c^{\text{b}}_{\text{H}^+}}{c^{\text{ref}}_{\text{H}^+}}\right)^{0.5} e^{-\frac{\Delta H_{\text{H}_2\text{O}}}{R}\left(\frac{1}{T}-\frac{1}{T^{\text{ref}}_{\text{H}_2\text{O}}}\right)} \quad \text{Equation 8c}$$

where $j_{\text{ct},i}$ and $j_{\text{lim},i}$ (A m^{-2}) are the charge transfer and limiting mass transfer current densities, respectively, $E_{\text{rev},i}$ (V) are the reversible potentials of each reduction reaction (Equations 2b-1d), n is assumed to be 2 and refers to the number of the electrons emitted by the iron oxidation reaction (Equation 2-a), whereas F (C mol^{-1}) corresponds to the Faraday constant and R to the universal gas constant (J K^{-1} mol^{-1}). The iron reversible potential $E_{\text{rev, Fe}}$ (V) is calculated as a function of the ferrous iron concentration (Equation 9) and, together with the iron reference exchange current density $j_{0,\text{Fe}}$ (A m^{-2}) in Equation 10, the anodic current can be derived (Equation 11) and used to calculate the corrosion potential imposing Equation 5. Then, the corrosion rate calculated from the corrosion current density j_{corr} (A m^{-2}) is transferred to PhreeqC together with the pH provided by COMSOL in order to account for the generation of ferrous iron and the consequent precipitation of corrosion products and porewater composition changes.

$$E_{\text{rev, Fe}} = E^0_{\text{rev,Fe}} + b\log(c_{\text{Fe}^{2+}}) \quad \text{Equation 9}$$

$$j_{0,\text{Fe}} = j^{\text{ref}}_{0,\text{Fe}} \times e^{\frac{-\Delta H_{\text{Fe}}}{R}\left(\frac{1}{T}-\frac{1}{T^{\text{ref}}_{\text{Fe}}}\right)} \quad \text{Equation 10}$$

$$j_{\text{ct,Fe}} = j_{0,\text{Fe}} \times e^{\frac{(\varphi - E_{\text{rev},i})}{b}} \quad \text{Equation 11}$$

Finally, the anodic currents of the reduced species (O_2, H^+) and those corresponding to the oxidised species (OH^-, H_2) are used as Neumann boundary conditions on the metal surface for the Nernst-Planck transport equations (Equations 12a and 12c), where c_j (mol m^{-3}) are the concentrations of aqueous species, R_j (mol m^{-2}·s) are the sink/source terms due to radiolytic reactions, z (-) is the charge and D_{eff} (m^2 s^{-1}) is the effective diffusion coefficient. The outer boundary (cell wall) is considered to be closed (Equation 12b). The porosity field ε is updated by the evolution of the mineralogy provided by the geochemistry and it is then transferred to COMSOL in order to account for the effect of film formation and precipitation of minerals in the bentonite buffer on the transport of aqueous species.

$$\frac{\partial(\varepsilon c_j)}{\partial t} - D_{\text{eff}}\nabla^2 c_j - zFD_{\text{eff}}c_j\nabla\varphi = R_j \quad \text{Equation 12a}$$

$$\left(\nabla\varphi + zFD_{\text{eff}}c_j\varphi\right)\cdot\mathbf{n} = 0 \text{ on } \Gamma_o \quad \text{Equation 12b}$$

$$\left(\nabla\varphi + zFD_{\text{eff}}c_j\varphi\right)\cdot\mathbf{n} = j_j \text{ on } \Gamma_m \quad \text{Equation 12c}$$

Simulation of laboratory corrosion experiments under transient conditions

Validation of the model presented in Section 2 was carried out by simulating some laboratory experiments (Table 38) performed in Tasks 3 and 5 (Abdelouas et al., 2022). All of them were modelled in a simplified 1D geometry using a computational mesh of linear elements for the transport equations and quadratic elements for the electric potential (first order accuracy of the potential gradient), with element sizes ranging from 0.05 mm near the metal surface to 0.5 mm in the bulk. An initial time step of 10^{-9} s was set due to the initial transient of the corrosion model and the fast kinetics of some of the radiolytic reactions.

The model, taking profit from the coupling between the corrosion model, the transport equations and the radiolysis of water and chloride implemented in COMSOL on one side, and the geochemistry of the bentonite-iron system in PhreeqC on the other (Fig. 1), is intended to describe the joint evolution of the corrosion potential and rate, together with the porewater composition and the precipitation of corrosion products (film formation). In all cases for compacted bentonite (Table 2), the diffusion of corrosion products into the buffer was analysed.

Table 38. Tentative list of simulations from Tasks 3 and 5 for the validation the numerical model.

Test No.	Author	Material	Buffer	T	Duration	Liquid sat.	Corrosion products	Irradiation
1	KIT	SGI	MX-80 slurry (100 g/L)	25°C	3 months	100%	NO	NO
2	KIT	SGI	MX-80 slurry (100 g/L)	50°C	3 months	100%	NO	NO
3	KIT	SGI	MX-80 slurry (100 g/L)	25°C	3 months	100%	α-Fe_2O_3 (0.5 wt. %)	NO
4	KIT	SGI	MX-80 slurry (100 g/L)	50°C	3 months	100%	α-Fe_2O_3 (0.5 wt. %)	NO
5	CIEMAT	Carbon steel	FEBEX (1.4 g/cm³)	25°C	8 days	100%	NO	NO
6	CIEMAT	Carbon steel	FEBEX (1.4 g/cm³)	25°C	8 days	100%	NO	66 Gy/h
7	CIEMAT	Carbon steel	FEBEX (1.4 g/cm³)	25°C	8 days	60%	NO	66 Gy/h
8	CIEMAT	Carbon steel	FEBEX (1.4 g/cm³)	80°C	8 days	100%	NO	NO

6.2.1.2 Adding microbial activity to geochemical models (UFZ)

Microbiology

Microorganisms are known to participate and accelerate chemical reactions and thereby largely contribute to geo-chemical processes occurring in the repository. One of the aspects to be considered is microbially influenced corrosion (MIC) of the canister material, which can occur under anoxic conditions either by direct uptake of electrons from metals acting as canister material, e.g. methanogenic archaea (Tamisier et al., 2022), or by secondary corrosion due to the corrosive action of hydrogen sulphide released by sulphate-reducing bacteria (e.g. Feron and Crusset, (2014), King et al., (2021), Tamisier et al., (2023)) or methanogenic microbes (Leupin et al., (2017), Mijnendonckx et al., (2019), Tamisier et al., 2022). At the same time MIC has an effect on the partial pressure of hydrogen (as it is used as an electron donor by most of the corrosive microbes), carbon dioxide / carbonate (which serves as a carbon source for corrosive microbes and can also precipitate as protective crust at the surface of the corroded canister material) and methane (which is produced by corrosive and other methanogens).

Mathematical description of microbes as chemically reactive particles

To add microbiology to the geochemical reactive-transport models, the structure and physiology of microbes need to be simplified to the extent that critical processes can be handled mathematically. To achieve that, our concept is to model them as colloid-like chemically reactive particles, which can then be treated like chemical compounds in the reactive-transport models. Within ConCorD, the UFZ developed the software package *mibisim*, which is particularly designed for that purpose. The concepts and assumptions employed therein are depicted in Figure 58.

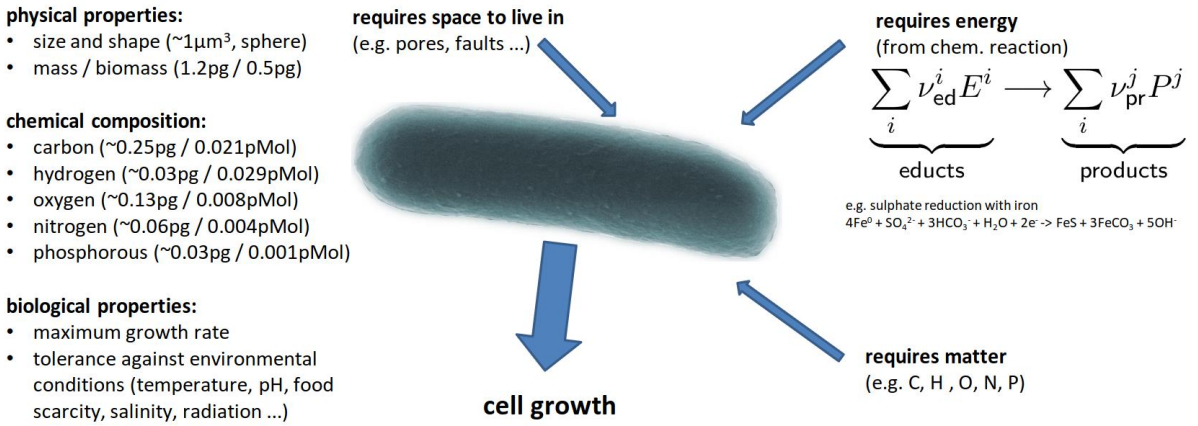

Figure 58. Illustration of the mathematical model of a microbe as a colloid-like reactive particle as implemented in the software package *mibisim*.

Physical properties

Since the morphology of a microbe depends not solely on its genetic determination but also on the physiological state of the microbe (for example, cells may elongate before division or shrink due to starvation), we assume microbes to be spheres with a single parameter R_c being their radius (typical radii would be 0.5 µm to 1.5 µm) to control size and volume. That given, their volume and maximum concentration (assuming either a hexagonally-close-packed structure or jammed-sphere-packing with fill-factors ~0.74 and ~0.49, respectively) can be calculated.

The cells are modelled to consist of water and biomass, with the latter assumed to be a mixture of mainly hydrogen, carbon, nitrogen, oxygen and phosphorous. To get realistic ratios between carbon, nitrogen and phosphorus in microbes, typical Redfield ratios could be used (A.C. Redfield, James Johnson Mem. Vol. (1934)). A more recent averaged elemental composition of a microbial cell is given by Roden and Jin (2011) as H:C:N:O:P = 5:7:2:1:0.2. Using literature values for a microbial dry matter contents of about 0.41 (Bratbak and Dundas, 1984)) the mass and biomass of a microbial cell are of the order of 1 to 9 pg and 0.41 to 3.69 pg, respectively.

Chemical and metabolic properties

Microbes drive chemical reactions to extract matter and energy from their environment in order to live and divide themselves, which is termed cell growth. Every microbial strain can potentially employ multiple different types of metabolic pathways in order to adapt to particular environmental conditions, a possibility that is accounted for in the model. Each of the possible metabolic activities is characterised by its chemical reactions:

$$\underbrace{\sum_i \nu^i_{\mathrm{ed}} E^i}_{\text{educts}} \longrightarrow \underbrace{\sum_j \nu^j_{\mathrm{pr}} P^j}_{\text{products}}$$

with a set of chemical compounds acting as reactants (educts), E, and products, P, which in turn, via the microbially driven changes in their concentrations, feed back into the geochemical model. The energy that is made available to the microbe by this reaction is calculated from the Gibb's potential of the reaction (depending on temperature, concentration of reactants and products, etc.).

With respect to canister corrosion, we focused on the process of dissimilatory sulphate reduction, which is known to be the most critical microbially influenced corrosion due to sulphate reduction occurs under anoxic conditions, either electrochemically by direct electron uptake from the metal:

$$4Fe(0) + SO_4^{2-} + 3HCO_3^- + H_2O \rightarrow FeS + 3FeCO_3 + 5OH^-$$

or by using the hydrogen produced by the chemical oxidation of Fe(0) by the produced sulphide:

$3Fe + 4H_2O \rightarrow Fe_3O_4 + 4H_2$ (under anoxic conditions via $Fe(OH)_2$, (Schütz et al. (2015))

$4H_2 + SO_4^{2-} \rightarrow S^{2-} + 4H_2O$ ($\Delta G'$=-22.8kJ/mol, (Hoehler et al. FEMS (2001))

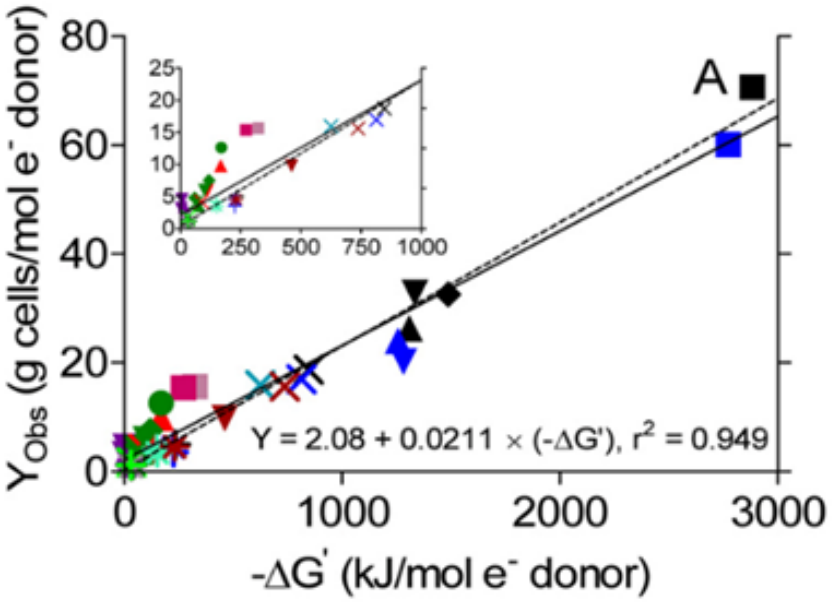

Figure 59. The relationship between the change in Gibb's free energy during the chemical reaction driven by metabolising microbes and the biomass production yield according to Roden and Jin, (2011) (Graphics reproduced with permission).

The microbial growth dynamics, which describe the time evolution of the number of cells in the system, can be calculated from the rates of growth, μ_g, and death, $\bar{\mu}_c$ of the cells. In *mibisim* the growth rate is modelled as a maximum growth rate, $\mu_{c,max}$, which is hampered by environmental conditions. To model the hampering, growth activity functions, A_i, with a value range [0 .. 1], are introduced for each environmental parameter (e.g. temperature, pH or concentration of chemical compounds required for microbial metabolism). Those conditions are assumed to be independent of each other, for the sake of simplicity, such that they can be chained together by simple multiplication, but also because experimental data for growth activity hampered by combinations of different parameters are almost unavailable.

The model considers several cardinal factors for growth activity hampering. Those factors are expressed as activities functions returning numbers in the range of 0 (growth completely hampered) to 1 (no hampering). The considered cardinal factors for growth activity hampering are:

- Temperature, modelled as suggested by Van Derlinden and Impe (2010) (with maximum temperature estimation according to Rosso et al. (1993))
- pH, using the model given by Biesta-Peters et al. Appl. Env. Microbiol. (2010)
- oxygen concentration (Couvert et al. Food Microbiol. (2019))
- water activity (Nyhan et al. Food Microbiol. (2018))
- swelling pressure (assumed to be linearly decreasing from 1 (p=0 MPa, growth not hampered) to 0 (p=2 MPa, no growth possible)).

The activity functions are displayed in Figure 60.

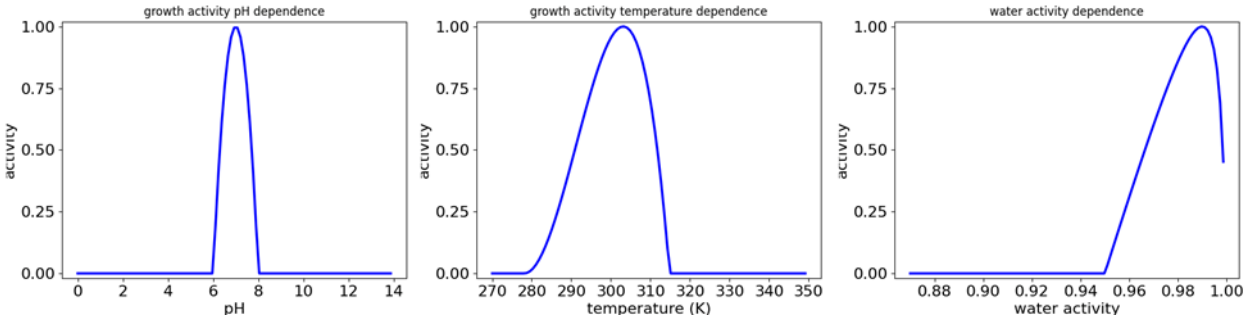

Figure 60. Microbial growth activity hampering by environmental parameters modelled as activity functions in *mibisim*. (These data are used for modelling the *Desulfosporosinus*-like microbe in the test-case below.)

To model the case of growth activity hampering by limited substrate availability, in other words low concentrations of chemical compounds required by the microbes' metabolisms, a half-growth rate concentration, N_{half}, model was used:

$$A_{met} = \prod_i \frac{N_{ed}^i}{N_{half}^i + N_{ed}^i}$$

with N_{ed} being the concentrations of the reactants (substrate) required for the particular metabolic pathway and A_{met} being the growth activity hampering factor resulting from substrate limitation.

Furthermore, a novel concept was introduced in order to treat the problem of one microbial strain having different possible metabolic pathways available[5]. (In a chemical language this means that, depending on the concentrations of the available chemical compounds, the microbes can choose between different chemical reactions that they can catalyse in order to gain energy.) To avoid hard switches from one metabolic pathway to another, for instance based on comparisons of concentrations of substrate chemical compounds required by one or the other, ΔG is evaluated for all metabolic pathways under the present conditions. Then, in an analogy to parallel resistors in electric circuits, the (normalised) partial activities of the different pathways are summed. Overall, the calculation of the microbial activity hampering in *mibisim* is sketched in the figure below.

[5] This is normally the case because the possibility to adapt to different environments is a precondition for microbial resilience.

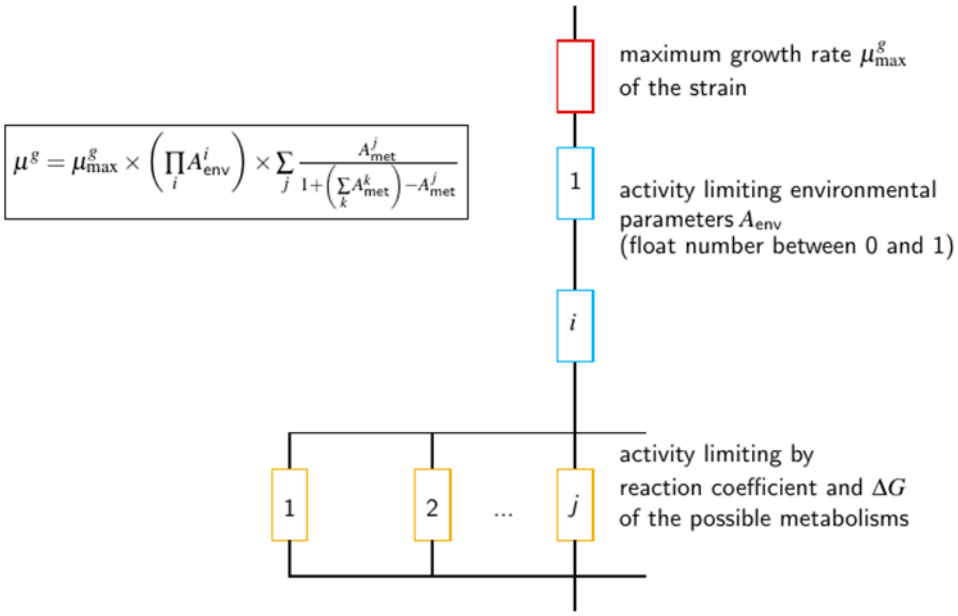

Figure 61. Modelling the microbial growth rate hampering by activity functions (expressed as floating point numbers between 0.0 and 1.0) for environmental parameters and metabolic pathways hampering substrate limitation.

Ordinary differential equations describing the time evolution of the microbial population

To calculate the time evolution of the system it is necessary to numerically solve the set of coupled ordinary differential equations for the concentration of microbial cells (N_c), chemical compounds being reactants (educts) (N^i_{ed}) and products (N^j_{pr}) in microbial metabolic pathways as well as the sources of carbon, nitrogen and phosphorus that are required for microbial growth (N^k_{src}).

$$
\begin{aligned}
\frac{\mathrm{d}N_\mathrm{c}}{\mathrm{d}t} &= \underbrace{\mu^g(t)N_\mathrm{c}(t)}_{\text{growth}} - \underbrace{\mu^d(t)N_\mathrm{c}(t)}_{\text{death}} \\
\frac{\mathrm{d}N^i_\mathrm{ed}}{\mathrm{d}t} &= -\frac{\nu^i_\mathrm{ed}}{Y}\mu^g(t)N_\mathrm{c}(t) \\
\frac{\mathrm{d}N^j_\mathrm{pr}}{\mathrm{d}t} &= +\frac{\nu^j_\mathrm{pr}}{Y}\mu^g(t)N_\mathrm{c}(t) \\
\frac{\mathrm{d}N^k_\mathrm{src}}{\mathrm{d}t} &= -M^k_\mathrm{c}\mu^g(t)N_\mathrm{c}(t) + M^k_\mathrm{c}\mu^d(t)N_\mathrm{c}(t) \qquad k = \{\mathrm{C},\mathrm{N},\mathrm{P}\}
\end{aligned}
$$

Test case: chemical microbially influenced corrosion by sulphate-reducing bacteria (SRB)

For a number of fast-growing and easily culturable microbes, data on maximum growth rates, optimum temperature and pH ranges, possible metabolic pathways and alike are available and in some cases even conveniently summarised in review papers (in the case of Escherichia coli for instance in Basavaraju and Gunashree, 2022). However, in the context of long-term nuclear waste repositories, a complete description of the entire parameter set of all microorganisms present in the surrounding environment, or merely a single strain that could serve as being representative of the microbial community, is not readily available and difficult to access since most underground microorganisms cannot be isolated and cultivated to date (Stewart et al., 2012). That being said, the task in this work was to review the available literature to develop a formulation of a model microbe that is a close-to-realistic organism of relevance for microbial corrosion processes in a nuclear waste repository.

As a basis for such a model organism, the genus *Desulfosporosinus* was chosen as its affiliated species are spore-forming sulphate-reducing bacteria. *Desulfosporosinus* has been detected in the microbial communities present in bentonites that are also used as barrier materials in nuclear waste repositories with (most probable) cell numbers of about 400 cells per gram bentonite (Haynes et al. (2018)). *Desulfosporosinus* species are strictly anaerobic as "[o]xygen tolerance has not been reported for *Desulfosporosinus* isolates" (Karnachuk et al. (2015)). *Desulfosporosinus burensis*, for instance, is an SRB that was isolated from a deep clay environment in France for which many of the required properties have been described (Mayeux et al. (2013)). Whilst *D. burensis* itself is not able to oxidise hydrogen (with CO_2 as the carbon source), some of its closest relatives (e.g. *D. lacus*) have the ability to do so (Ramamoorty et al. 2006). *D. burensis* and *D. lacus* are described as being rod-shape cells of about 3 µm and 5 µm length with diameters of about 0.6 µm and 1.0 µm, respectively, (Ramamoorty et al. 2006, Mayeux et al. (2013)). With respect to volume, such cells can be modelled as spheres of 2 µm to 3 µm diameter. The physical parameters for the simulation are given in Table 39. Under optimum conditions, the maximum growth rate was determined to be about 0.09 hr^{-1}. The reported temperature range for growth stretches from 5°C to 42°C with an optimum between 25°C and 30°C and the tolerable pH range is 6 to 8. Some of the *Desulfosporosinus* species appear to exhibit a remarkable tolerance against radiation. Data from a gamma irradiated commercial bentonite sample provided by Haynes et al. (2018) suggest that about one third of the *Desulfosporosinus* cells that were initially present in the sample could still be detected after a 1000 Gy irradiation (dose rate 24.17 Gy min^{-1}). From the same publication it becomes clear that owing to the ability to form resistant endospores, *Desulfosporosinus* cells also exhibit a certain tolerance against heat as even after a 24 hr exposure to 90°C, about 3% of the cells initially present were detected. In turn, for the repository, this means that after the near-field of the canister has cooled to about 40°C, *Desulfosporosinus* spores would transform into actively growing cells and microbially influenced corrosion is to be expected.

radius of the cell	r_c	1.25 µm
volume - expressed by radius	V_c	8.181 μm^3
mass	m_c	8.54 pg
biomass	mcb	3.50 pg
dry-matter content	µcd	0.41 --
maximum cell density	C_c^{max}	2.49E+11 cells/mL
	$Cc_{,mol}^{max}$	4.14E-13 mol/L
chemical composition (wet)		$C_5H_7O_2N_1P_{0.12}$:n_w H_2O

Table 39. Description of a Desulfosporosinus sp. cell as a reactive particle in *mibisim*, physical parameters and derived geometrical constraint for the maximum cell density.

Besides temperature and pH, swelling pressure of the bentonite and water activity are parameters hampering microbial growth, and thus affecting the microbially influenced canister corrosion. To the best of our knowledge, no data on the relation between microbial growth and swelling pressure are available; however, it is well accepted that microbial growth is only possible up to a pressure, p_s, of 2 MPa. Therefore, the growth activity is assumed to decrease linearly from 1 at p_s = 0 MPa to 0 at p_s = 2 MPa. The water activity, aw, of the porewater is expected to be around 0.99 but it is certainly greater than 0.98, which is the water activity of sea-water (Pedersen, (1995)). The dependence of microbial growth activity on aw is modelled by the model suggested by Nyhan et al. (2018). However, swelling pressure and water activity are entangled parameters. The dependence of aw on p_s is modelled according to Equation 9 in Nagra (1986). It is important to mention that if by increasing the swelling pressure, the water activity can be lowered below 0.96, likely resulting in efficient suppression of microbial activity, and thus microbial canister corrosion (Stroes-Gascoyne et al., 2010)).

The parameters used to model the growth dynamics of the *Desulfosporosinus*-derived model microbe are given in Table 40.

parameter	minimum	optimum	maximum
temperature	278K	303K	315K (calculated)
pH	6	7	8
O2 concentration	0.0%	0.0%	0.0%
water activity	0.95	0.99	0.99999

Table 40. Parameters used to model the growth activity hampering of the *Desulfosporosinus*-derive model microbe.

In order to gain an insight into the capability of cells of a *Desulfosporosinus* species located in a void in the bentonite barrier to produce hydrogen sulphide (by consuming H_2), which in turn leads to chemical canister corrosion, sulphate reduction by H_2 as electron donor and CO_2 as the carbon source is assumed. The Gibb's free energy per mol of consumed sulphate is –22.8kJ (Hoehler et al. (2001)).

The figure below shows four test cases in which sulphate is initially provided at a concentration of 0.01 M, which is to be expected in the bentonite barrier (Fernandez et al. (2001)). In order not to run into a limitation of the electron acceptor, hydrogen is kept at a constant concentration of 0.1 mM, which is 7 times below the solubility limit. The pH value was set to 7.29.

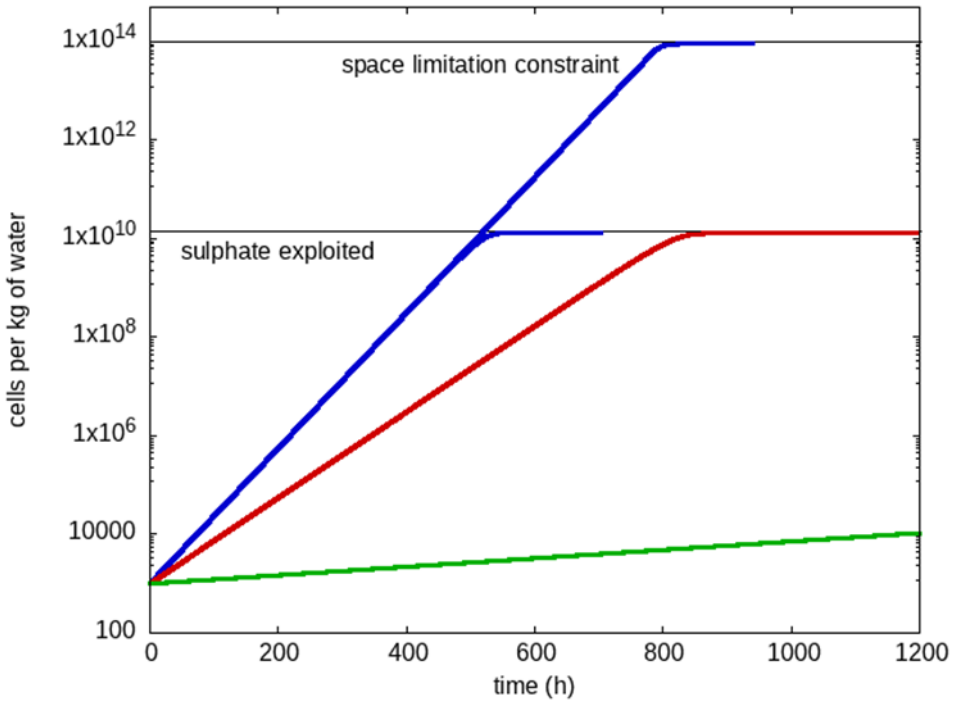

Figure 62. Simulated cell growth of the sulphate-reducing Desulfosporosinus-derived model organism under space- and sulphate-limiting conditions.

The water activity for the red data (T=20°C) and blue data (T=30°C) was set to 0.99, such that it does not limit growth. The results demonstrate how the growth rate depends on temperature. Growth stops when either sulphate is consumed or, in the case that it is constantly delivered, when there is no space left in which the cells can grow. The green line shows the same simulation as displayed in blue (T=30°C)

but at a decreased water activity of 0.952, which is supposed to result from compaction and swelling pressure. The test case confirms that a high compaction of the bentonite barrier leads to space limitation as well as low water activity, which would both strongly hamper microbial growth. The software *mibisim* is now ready to be integrated into OpenGeoSys.

6.2.1.3 Repository scale modelling of sulphide (University of Bern)

A 1D cylindrical model has been previously developed to model the sulphide evolution in the near-field and sulphide corrosion on copper canisters in the Swiss DGR (Cloet et al., 2017). In this task, this 1D model was further improved by implementing more recent designs of the Swiss DGR and a more advanced geochemical conceptual model (Posiva, 2021) including scavenging sulphide by the iron system in the bentonite (Figure 63). It was also extended to estimate sulphide corrosion on both copper and steel canisters under different repository settings, such as with "badly-emplaced buffer" or including a concrete liner around the buffer. Furthermore, a 2D model was developed to investigate the impact of anisotropic diffusion in the host rock. Specific subtasks are detailed below. All calculations were carried out using reactive transport code PFLOTRAN (www.pflotran.org/).

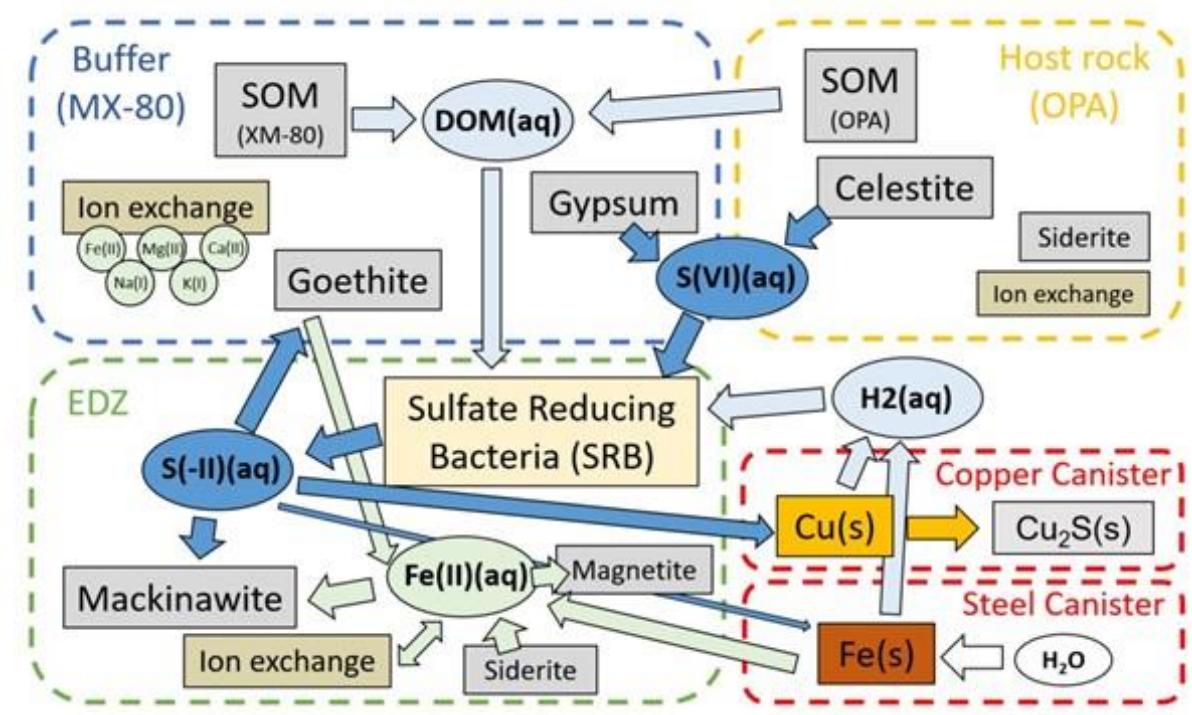

Figure 63: Schematic of main processes considered in the conceptual biogeochemical model (J. Ma et al., 2022). SOM: Solid organic matter, DOM: dissolved organic matter, EDZ: excavation-damaged zone, OPA: Opalinus Clay.

(1) Reference cases

1D and 2D (isotopic) reference cases were calculated using a model geometry as shown in Figure 64(a) and (b), respectively. The physical parameters of the model are listed in Table 41. The initial porewater and mineral compositions for the Opalinus clay (OPA) were documented in Cloet et al., 2017, whereas those for the buffer were documented in Posiva, 2021 (see Appendix A Table A1).

Table 41: Physical parameters used for different regions of the reference case.

	Buffer	EDZ	OPA
Dry density	1450 kg/m^3	2450 kg/m^3	2450 kg/m^3

	Buffer	EDZ	OPA
Porosity	0.48	0.14	0.11
Effective diffusion coefficient	2E-12 m^2/s	1E-11 m^2/s	2E-12 m^2/s
Permeability	1E-20 m^2	1E-20 m^2	1E-20 m^2

(2) The effect of "badly-emplaced" buffer

The evolution of the near-field sulphide system was calculated considering a "badly-emplaced" buffer, which has reduced density and hosts active SRB. Both 1D and 2D models (Figure 64(a) and (b)) were used for the calculation, assuming a buffer with a 10× faster diffusion coefficient compared to the reference case (Cloet et al., 2017) and SRB activity compared to the EDZ.

(3) The effect of anisotropic diffusion

Anisotropic effective diffusion coefficients, D_e, were used for the OPA host rock in the 2D model (Figure 64 (b)), assuming a 5x faster diffusion in the horizontal direction compared to the reference case. The results were compared to the 2D reference case to investigate the effect of anisotropic diffusion and to estimate the maximum corrosion depth on the copper and steel canisters.

(4) The effect of concrete liner

A layer of concrete liner was considered at the interface between the buffer and the EDZ (Figure 64 (c)). The composition of the concrete was calculated after a full hydration process of the mixture (Appendix A Table A2 & A3). The concrete layer induces an alkaline plume into the bentonite and the OPA. The effect on the montmorillonite stability and on the sulphide fluxes in the NF was investigated.

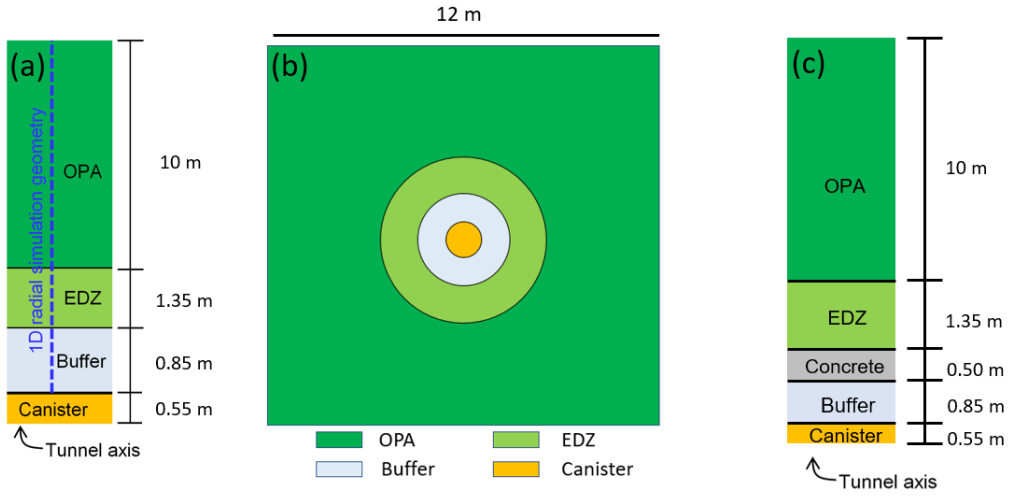

Figure 64:Geometry of the 1D and 2D model used in Task A: (a) 1D model reference case, (b) 2D model reference case, (c) 1D model with concrete liner.

Reference cases of the 1D model

Copper canister

For the reference case, solid organic matter (SOM) remained largely in excess, thus not limiting SRB activity over the 1 Myr modelling period, both in the buffer and in the OPA (Figure 65a). Although gypsum was rapidly depleted in the buffer after 12 kyr, celestite in the OPA functioned as an additional sulphate source that lasted for one million years. The distribution of sulphide generally displayed four temporal phases (Figure 66): 1) direct use of sulphate in the EDZ with high sulphide production within the EDZ (<ca.8 kyr); 2) sulphate mainly supplied by gypsum dissolution in the buffer with relatively high sulphide

production near the buffer-EDZ interface (ca. 9-15 kyr); 3) lower fluxes of sulphate supplied by residual sulphate in the buffer porewater and celestite dissolution from the host rock (ca. 16-28 kyr); 4) low fluxes of sulphate supplied only by celestite dissolution from the host rock(>ca. 28 kyr). Goethite (α-FeOOH) was depleted after about 600 kyr. After 1 Myr, 5,693 mol of sulphide was produced per canister unit, of which almost 100% was produced via the dissolved organic matter (DOM) pathway, while the contribution of the H_2 pathway remained negligible. About 95% of the produced sulphide precipitated as mackinawite ($Fe_{1+x}S$, where x=0 to 0.11) and only 0.4% reached the copper canister (Figure 65b). After 1 Myr, the corrosion depth of the copper canister is 0.1 mm.

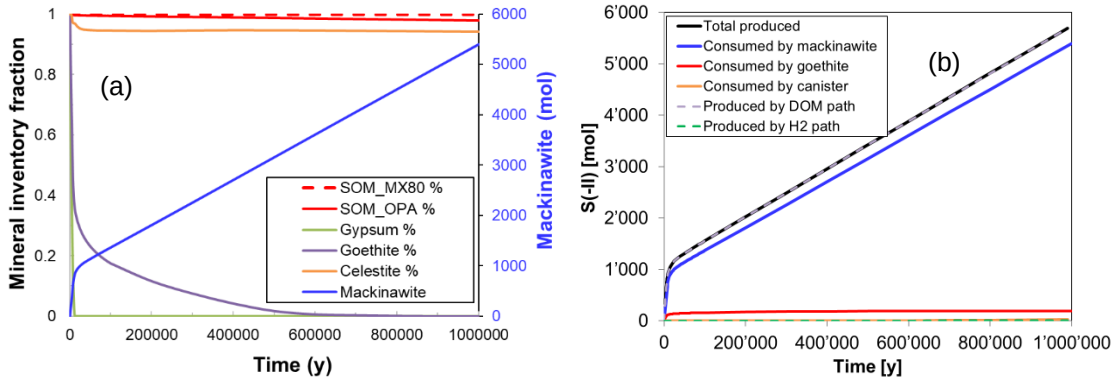

Figure 65: (a) Evolution of mineral inventories (reference case with copper canister). Left axis was normalised by the initial inventory. (b) Evolution of the produced sulphide via the SOM or H_2 pathway, and the consumed sulphide by goethite dissolution or mackinawite precipitation (reference case with copper canister).

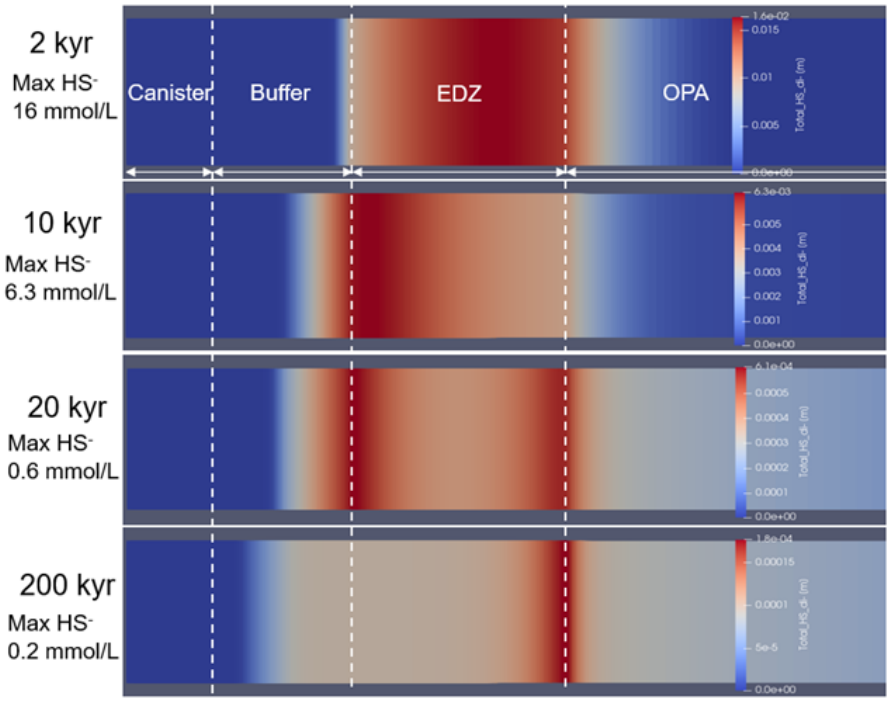

Figure 66: Phases of sulphide distribution in the reference case (copper canister).

Steel canister

In the case of a steel canister, the main corrosion process was water corrosion (i.e. anaerobic corrosion) and the sulphide system had little impact on this corrosion process. The 14 cm thick steel was depleted after 460 kyr, assuming a nearly constant corrosion rate of 0.3 μm yr^{-1} by water. Meanwhile, only 0.5 μm

of the canister was corroded by sulphide, which was significantly attenuated by Fe^{2+} near the canister. The released Fe^{2+} mostly precipitated as magnetite in the first 500 kyr and a small amount (about 8% after 1 Myr) precipitated as mackinawite as a result of the produced sulphide (Figure 67a). Due to the Fe-rich environment, goethite in the buffer was not depleted after 1 Myr.

In terms of the sulphide system, about similar amounts of sulphide (5,642 mol) were produced after 1 Myr compared to the copper canister. The H_2 pathway was responsible for more than half of the sulphide production in the first 600 kyr due to H_2 released from steel corrosion. Then, following the depletion of the steel canister, the DOM pathway became more dominant, contributing to about 61% of the total sulphide production after 1 Myr (Figure 67b).

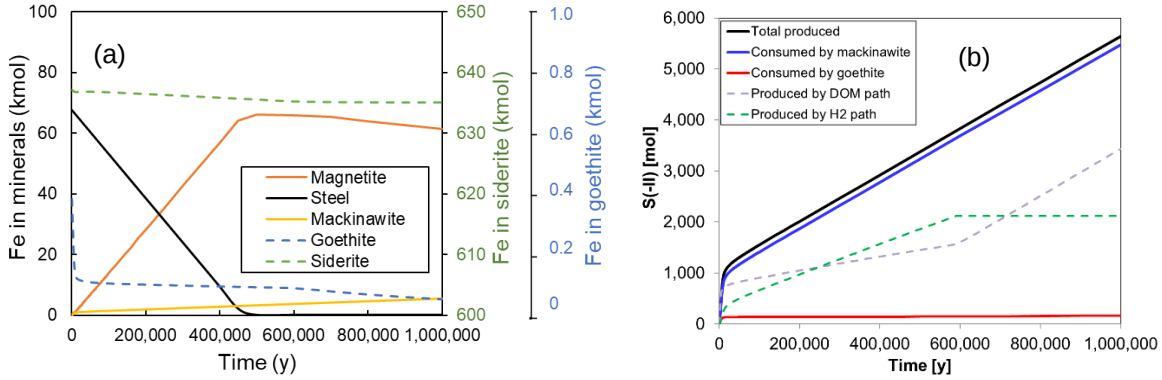

Figure 67: (a) Evolution of iron minerals (reference case with steel canister). (b) Evolution of the produced sulphide, via the SOM or H_2 pathway, and the consumed sulphide by goethite dissolution or mackinawite precipitation (reference case with steel canister).

Effect of "badly-emplaced" buffer

SRB activity in the buffer facilitated very fast sulphide production in the first few thousand years, when sulphate and DOM were locally accessible (Figure 68). Consequently, gypsum and goethite in the buffer were depleted much more rapidly compared to the reference case. For example, in the copper case, gypsum and goethite were depleted within 2 kyr (instead of 12 kyr) and 24 kyr (instead of 600 kyr), respectively. The consumption of SOM in the buffer reached about 59%, which was significantly higher than in the reference case (Figure 69a). Compared to the reference case, the corrosion depths of the canister were strongly enhanced. After 1 Myr, the corrosion depth was 2.19 mm, whereas only 0.1 mm was predicted for the reference case.

In addition, more sulphide was produced from the H_2 pathway due to the H_2 released from canister corrosion being used directly in the buffer. After 1 Myr, a total of 5,682 mol sulphide was produced, from which about 2% was produced via the H_2 pathway, while the rest was produced via the DOM pathway. Most (86%) of the produced sulphide precipitated as mackinawite, about 3% was consumed via the goethite reaction and 9% contributed to canister corrosion (Figure 69a).

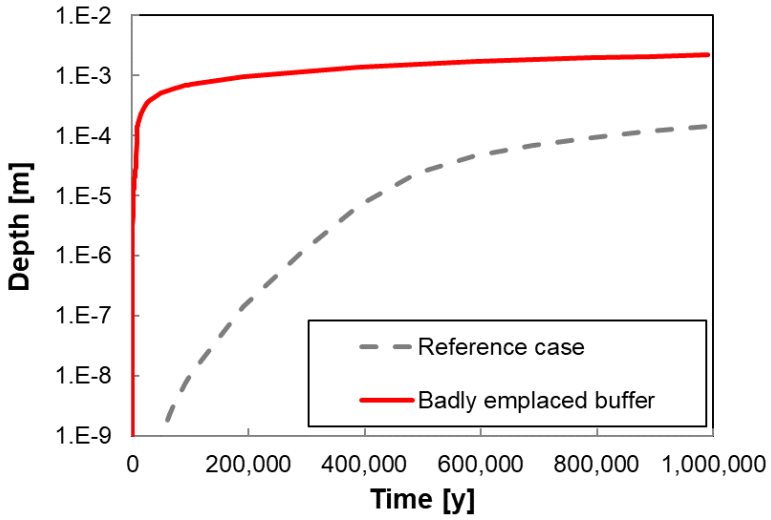

Figure 68: Comparison of copper canister corrosion depth evolution with the reference case and the "badly-emplaced" buffer case.

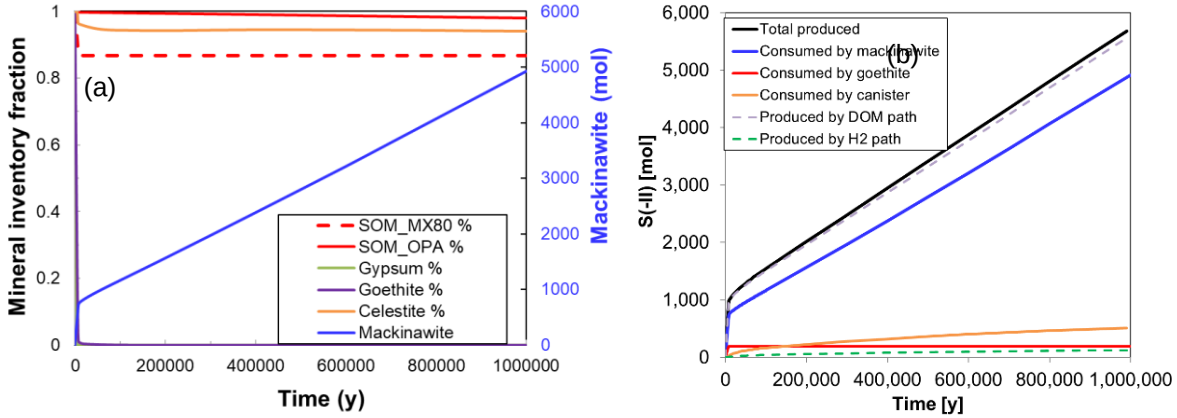

Figure 69: (a) Evolution of mineral inventories for the "badly-emplaced" buffer case. Left axis was normalised by the initial inventory. (b) Evolution of the produced sulphide via the SOM or H_2 pathway and the consumed sulphide by goethite dissolution or mackinawite precipitation ("badly-emplaced" buffer case with copper canister).

In the steel canister case, the SRB activity in the buffer did not significantly affect the overall iron and sulphide systems and thus the corrosion rates. About 50 µm of the canister was corroded by sulphide, while the 14 cm thick steel canister was completely corroded by reaction with water after about 460 kyr.

Effect of anisotropic diffusion

Before applying the 2D anisotropic model, a 2D isotropic case was prepared as a reference case. As shown in Figure 70, the canister corrosion depths agrees very well between the 2D isotropic (97.7 µm) and the 1D models (101 µm), demonstrating the consistency between the two models. In particular, the smaller thickness of the host rock in the 2D model has little impact on the results.

With the implementation of anisotropic diffusion, a faster transport in the horizontal direction was assumed. This first led to more precipitation of mackinawite, due to faster sulphide and Fe(II) transport (Figure 72a), and subsequently slower corrosion of the canister in the first tens of thousands of years (ca. 90 kyr in the reference case and ca. 50 kyr in the "badly-emplaced buffer" case) (Figure 70). Later, the faster diffusion of DOM led to a higher sulphide production, which also caused depletion of SOM

near the EDZ. The depletion of SOM eventually limited the sulphide fluxes, particularly in the horizontal direction (Figure 72b), after ca. 500 kyr (with “well-emplaced” buffer) to 600 kyr (with “badly-emplaced” buffer). After 1 Myr, the average corrosion depth remained similar to the reference for the “well-emplaced” buffer case (91.0 µm vs 97.7 µm), but it was enhanced for the “badly-emplaced” buffer case (5.66 mm vs 2.15 mm).

In addition, the anisotropic diffusion also led to a somewhat higher corrosion depth in the horizontal direction compared to the vertical direction. After 1 Myr, the corrosion depths in the horizontal and vertical directions were 98.3 µm and 84.8 µm, respectively, for the “well-emplaced buffer” case, and 5.82 mm and 5.49 mm, respectively, for the “badly-emplaced buffer” case (Figure 73).

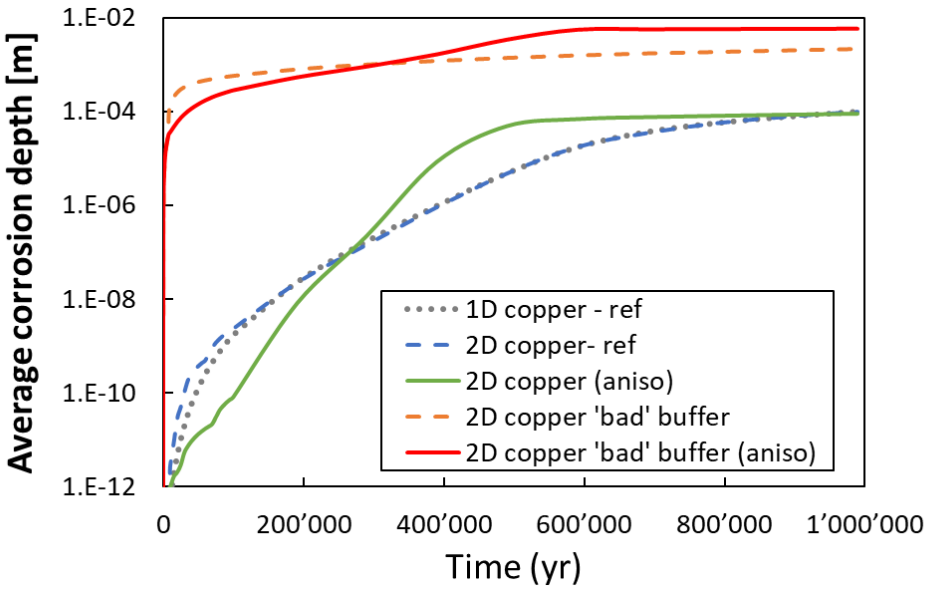

Figure 70. Average copper canister corrosion depths in the 1D and 2D reference cases, and in the anisotropic rock cases with tight or badly-emplaced buffer.

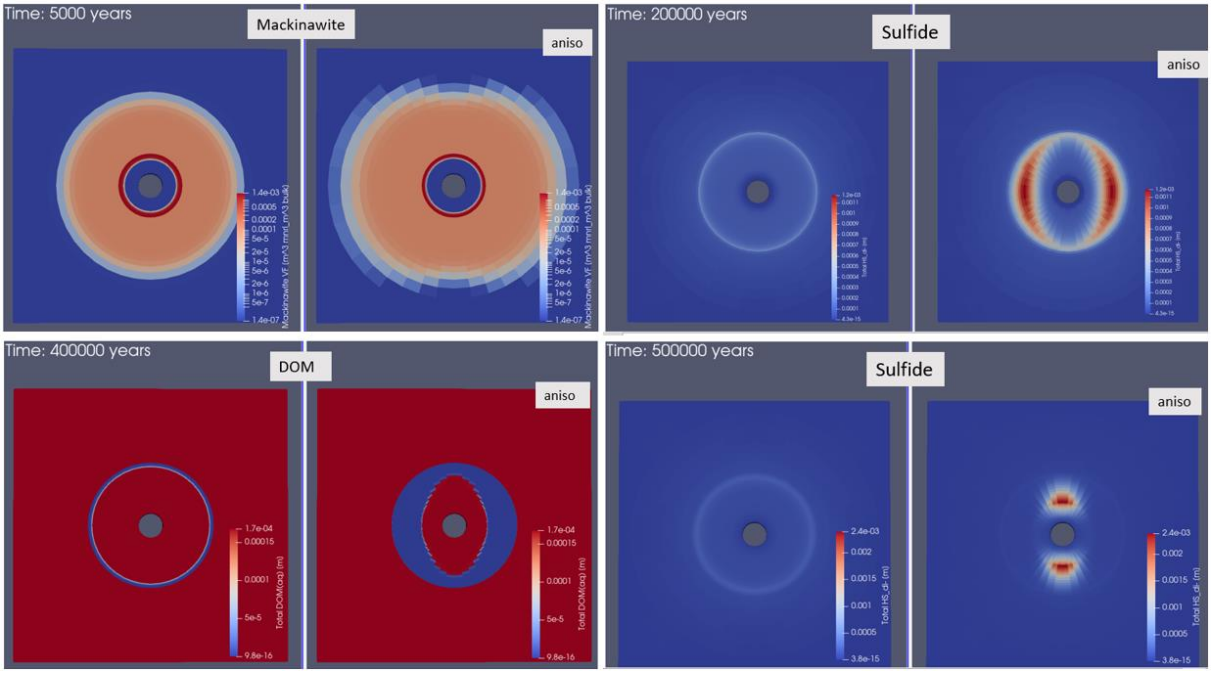

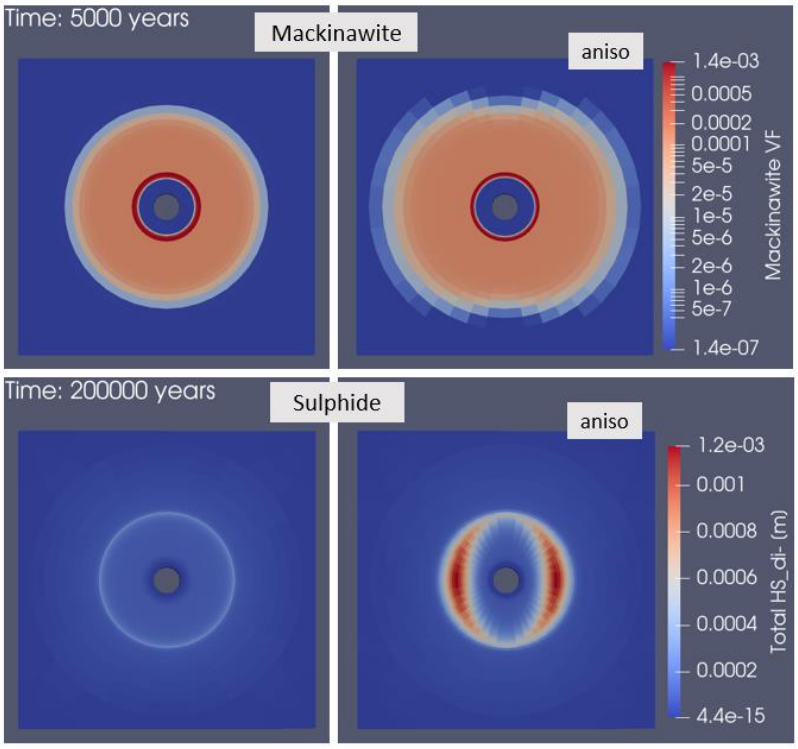

Figure 71a. Distribution of mackinawite (vol.%), and concentrations of sulphide at selected times (copper canister reference case).

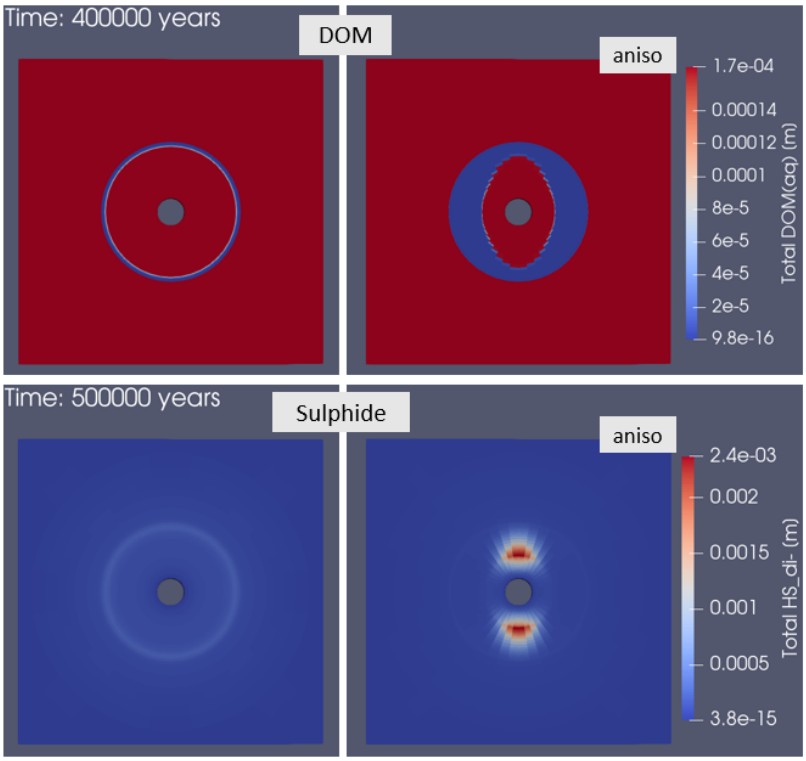

Figure 72b. Distribution of concentrations of sulphide and DOM (mol/L) at selected times (copper canister reference case).

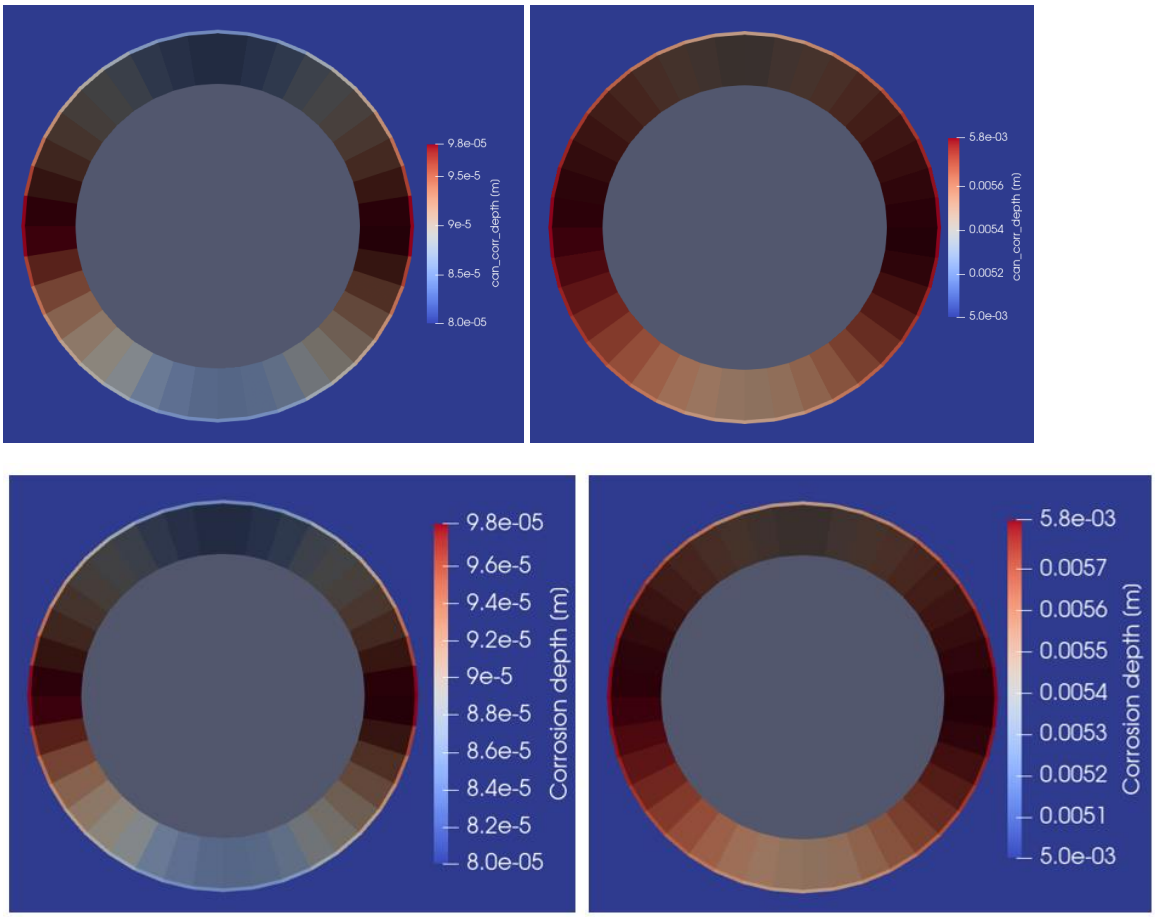

Figure 73. Anisotropic corrosion depth at the copper canister surface. Left: reference case, right: "badly-emplaced" buffer case.

For the steel canister, anisotropic diffusion did not affect the canister corrosion due to the rapid reaction with water. However, sulphide production and mackinawite precipitation processes were enhanced in the horizontal direction.

Effect of concrete liner

The high pH plume from the concrete liner resulted in montmorillonite (MMT) dissolution near the liner. The first centimeter of MMT was dissolved after 500 years, whereas the second centimeter was dissolved after 5,000 years. After 1 Myr, 4 cm of MMT were completely dissolved, 65 cm of buffer still had more than half of the initial MMT and 85% of the MMT remained undissolved near the canister. Overall, about 34% of the MMT in the buffer was transformed. In the long term, transformation of MMT towards illite and beidellite was predicted. Calcite precipitated inside the liner towards the EDZ, whereas dolomite precipitated inside the liner towards the buffer.

Sulphide was produced in the EDZ. With the additional sulphate in the liner, more sulphide was produced in total. However, the higher pH enhanced mackinawite precipitation, which significantly reduced sulphide corrosion of the copper canister (Figure 75). After 1 Myr, almost no copper was corroded due to 98% of the produced sulphide precipitating as mackinawite.

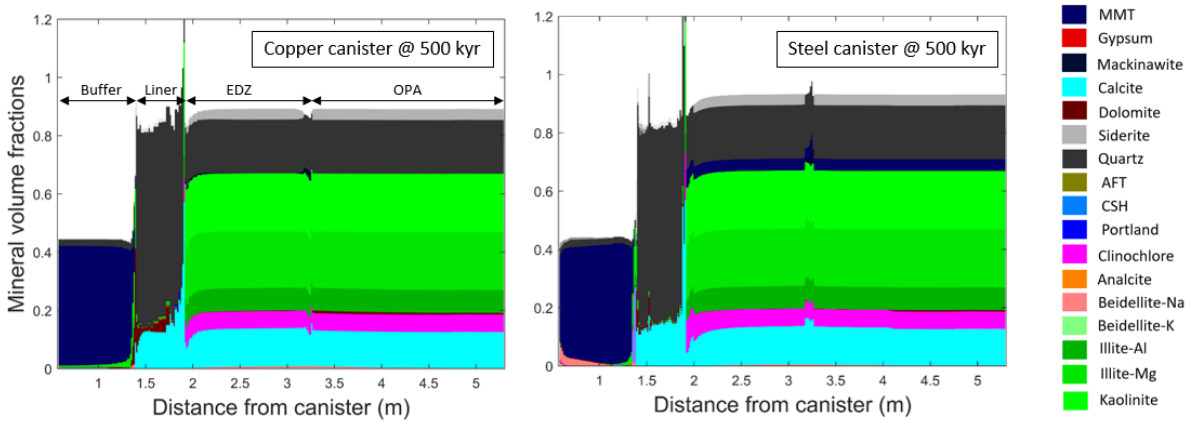

Figure 74. Mineral compositions at 500 kyr in the 1D model with concrete liner. Left: copper canister, right: steel canister.

Considering the significant dissolution of MMT in the buffer, an additional case with SRB inside the buffer was prepared for the concrete liner scenario. The evolution of the major mineral composition was similar to the case without SRB inside the buffer. A higher corrosion depth was predicted compared to the case without SRB in the buffer, but it was still lower than the reference case at 1 Myr (29 µm vs 98 µm).

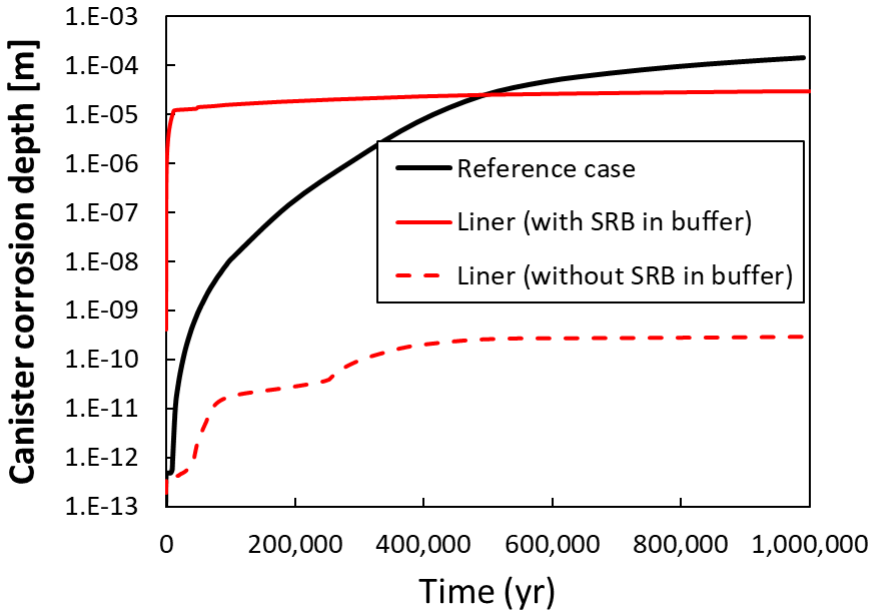

Figure 75. Copper canister corrosion depth in the case with concrete liner (with and without 10%SRB in the buffer).

Similar MMT dissolution near the liner surface was predicted in the steel canister case. Moreover, additional MMT dissolution was predicted near the steel canister due to slightly higher pH conditions at the steel surface (Figure 74). Overall, about 26% of the MMT in the buffer was transformed.

Uncertainties

The biogeochemical model was developed using relatively pessimistic parameters and conservative assumptions. Due to the lack of relevant experimental data, uncertainties in the parameterisation remain. For example, the long-term dissolution rates of the SOM, the reaction rates of goethite with sulphide, and more importantly, the SRB activity and sulphate reduction rates under various geochemical conditions are not well known. Some sensitivity calculations are presented in the Appendix

(Figure A1), showing that although varying these parameters affected the evolution of copper canister corrosion, the corrosion depths after 1 Myr were rather well constrained due to the limited mineral inventory and slow solute transport rates.

Conclusions from the repository scale model

Copper canister

Sulphide corrosion is an important long-term process for copper canisters. Both the 1D and 2D model predicted a corrosion depth of ca. 0.1 mm after 1 Myr. The evolution of the sulphide system varied significantly for different repository settings. The corrosion depths in the simulated cases are summarised in Table 42. A "badly-emplaced" buffer led to very high sulphide production rates in the first tens of thousands of years. Consequently, it significantly enhanced the corrosion depths by more than 20 times after 1 Myr. Anisotropic diffusion (5× faster in the horizontal direction) in the host rock induced somewhat heterogeneous corrosion with a variation of ±3-8% of the average corrosion depth. It also enhanced the average corrosion depth by a factor of two in the "badly-emplaced" buffer case. The concrete liner induced a high pH plume, which led to dissolution/alteration of about 34% of the MMT in the buffer after 1 Myr. Transformation of MMT into illite and beidellite was predicted in the long-term. Moreover, the high pH enhanced the precipitation of mackinawite and significantly reduced sulphide corrosion of the canister.

Table 42. Summary of average corrosion depths for copper canisters after 1 Myr.

Scenario	Average corrosion depth at 1 Myr
Reference case 1D	1.01×10^{-4} m
Reference case 2D	9.77×10^{-5} m
"Badly-emplaced" buffer 1D	2.19×10^{-3} m
"Badly-emplaced" buffer 2D	2.15×10^{-3} m
Anisotropic diffusion ("well-emplaced" buffer)	9.10×10^{-5} m (8.48×10^{-5} – 9.83×10^{-5} m)
Anisotropic diffusion ("badly-emplaced" buffer)	5.66×10^{-3} m (5.49×10^{-3} – 5.82×10^{-3} m)
Concrete liner	2.87×10^{-10} m
Concrete liner with SRB in the buffer	2.90×10^{-5} m

Steel canister

On the other hand, the model suggested that water is the dominant corroding agent for the steel canister, even in the case of elevated sulphide fluxes. The 14 cm thick steel canister was completely corroded after about 460 kyr (with the assumption of a corrosion rate of 0.3 µm yr^{-1}). Most of the released Fe^{2+} precipitated as magnetite, which continued to function as an Fe source and attenuated sulphide in the long term. The variant cases displayed changes in the mineral evolution to some extent, but the canister corrosion rate remained the same. In the case with a concrete liner, transformation of the MMT was predicted near both the canister and the liner.

6.2.2 Subtask 6.2: Integration for performance assessment

6.2.2.1 Application of novel materials in future performance assessments.

Current performance assessments associated with carbon steel and copper containers base the design life on the corrosion of the container wall. For corrosion allowance materials such as carbon steel, continued loss of material beyond the corrosion allowance reduces the load carrying capacity of the container making it more susceptible to plastic collapse and fracture. For materials such as copper, corrosion of the outer surface does not significantly affect the load carrying capacity, which is provided by an inner support (as in the coated NWMO concept), and the design life is based on the time taken for it to be penetrated by corrosion.

For alternative metallic materials that are slight variations on more established container materials, such as HCP copper, performance assessment is expected to mirror that adopted previously, and therefore will not require innovation. It is anticipated that a key aspect of evaluating the extent to which HCP copper can be used in place of OFP copper will be demonstrating that comparable performance can be achieved over the range of permissible chemical compositions that are covered in the alloy specification. The aim of such a program would be to determine the thresholds in the chemical composition that lead to a deterioration in performance of the alloy and to then demonstrate that the composition of HCP copper is sufficiently far from those thresholds that the desired performance can be assured.

For ceramic bulk materials, such as silico-aluminate sealing materials and alumina containers, substantial work is envisioned to produce a performance assessment that addresses the expected failure mechanisms of the material, not just in isolation but also in conjunction with the whole disposal system. For ceramic containers, thickness loss due to corrosion is expected to occur at a substantially lower rate than for metallic containers and is therefore not expected to dominate the design life. A key factor in performance assessment of ceramic materials is the susceptibility to fracture owing to the lower fracture toughness when compared to metals. Factors such as the porosity and presence of defects in the bulk and the sealing material are expected to be key parameters that will need to be evaluated during performance assessment. Furthermore, compatibility of novel materials with current buffers will need to be established to determine whether there is a need for the development of complementary novel buffer systems to use in conjunction with them.

For novel coating materials, performance assessment will need to address the behavior of the material both in isolation and in conjunction with the substrate. A key parameter that is envisioned to impact design life is the extent to which the coating can remain adhered to the substrate. With the vast array of coating technologies available and the range of conditions under which a specific coating can be applied, there is a need to demonstrate the efficacy with which a specific coating can be applied to the substrate to ensure the desired performance. Factors such as the uniformity of the coating thickness, absence of porosity or other potential defects are expected to be key parameters that will need to be evaluated to determine tolerable limits regarding durability. It is feasible that to thoroughly evaluate the extent to which both metallic and ceramic materials can be used as coatings for containers during geological disposal, novel testing methods and modelling approaches may need to be developed to give confidence in their long-term performance.

A key challenge associated with the performance assessment of novel materials, in particular ceramics and modern engineering alloys, is demonstrating how they will perform in the long term in the absence of empirical data and experience. The advantage of using traditional materials such as carbon steel and copper is the vast amount of experience that has been accrued with their use as engineering materials. For traditional materials the availability of archeological analogues adds a further layer of confidence in their anticipated long-term behavior and can be used to validate mechanistic arguments relating to their performance. For novel materials, new approaches to long-term performance assessment may be required to overcome the absence of data or suitable analogues at present. However, if these challenges

can be overcome, the use of novel materials may lead to more robust safety cases owing to the potential for very long-term durability and other advantages that arise as a result of the optimization of their production methods.

6.2.2.2 Application of radiation corrosion results in performance assessments

Results from ConCorD support the exclusion of radiation effects on the corrosion of carbon steel in performance assessment provided the dose rate is below a critical level where no significant effect is anticipated. Results from experiments performed at a range of dose rates suggest this threshold is around 10 Gy hr^{-1} in a fully aqueous system, which is considered to be pessimistic compared to the disposal environment owing to the observation of a lower impact of radiation on corrosion in the presence of compacted bentonite.

For copper, it is necessary to account for the effects of radiolysis regardless of the dose rate, because no lower limit was established when tested under fully aqueous conditions. Therefore, it may be appropriate to account for radiolysis effects for the entire service life of the canister (e.g. up to 1 million years), not just for the period of highest dose rate (i.e. the first 300 years). However, this may be pessimistic as it does not take credit for possible consumption of radiolysis products by bentonite and should be investigated further to avoid over-conservatism.

Under unsaturated conditions, irradiation may induce corrosion at a lower relative humidity than under unirradiated conditions. This observation requires further study, and may apply to both copper and carbon steel, although it has only been investigated for steel and at dose rates exceeding the maximum dose rates anticipated at the container surface.

In compacted bentonite at elevated temperature, the presence of radiation at representative dose rates led to a reduction in corrosion rate of carbon steel compared to unirradiated conditions but the magnitude of the effect was influenced by both temperature and type of bentonite. With a larger effect occurring at higher temperature and in the presence of Czech bentonite compared to MX-80. These findings suggest the need for improved mechanistic understanding of both the interactions between radiolytically generated species and bentonite, and the impact of porewater chemistry on radiolytic yield.

6.2.2.3 Application of microbial activity studies in performance assessments

A key assumption underpinning performance assessment of metallic containers in bentonite is that microbial activity, namely sulphate reduction, can be suppressed by the bentonite at a sufficiently high dry density. However, findings from ConCorD showed that corrosion rates in FEBEX bentonite were greater when supplemented with sulphate reducing and iron reducing bacteria, even at a high dry density of 1.6 Mg m^{-3}. Although these findings do not prove that microbial activity was taking place under the saturated test conditions, they do invite further investigation of the relationship between bentonite density and microbial activity. Fortunately, development of experimental methodologies within ConCorD have laid the groundwork for performing further validation tests that can be used to evaluate the threshold densities for microbial activity in various bentonites, which are anticipated to feed directly into future performance assessments.

It was found that increasing the temperature to 90°C and 150°C was sufficient to lead to a dramatic loss of viability and cultivability of indigenous bentonite microorganisms, with similar effects observed in both BCV and MX-80 bentonite. This implies that where such temperatures arise near the canister surface, the microbial activity will be suppressed. These findings can be used in performance assessment when considering the scenarios under which a biofilm could form at the container surface e.g., prior to saturation, or following loss of the buffer.

6.2.2.4 Application of corrosion during transient studies in performance assessments

Temperature was found to have a big impact on the corrosion rate of carbon steel in bentonite, with significantly higher corrosion rates observed at 90 °C and 150 °C. This is relevant to performance

assessments that rely on the use of empirically determined corrosion rates for carbon steel that are typically measured under steady state conditions at borehole temperatures, and may indicate a need to consider a potentially higher corrosion rate under initial conditions when the canister surface is at elevated temperature.

Corrosion rates were higher in FEBEX bentonite which was attributed to the high salinity porewater when compared to the other bentonites (SWy-3 and Czech). Whilst this is not directly applicable to performance assessment, it serves to demonstrate that empirically determined corrosion rates for carbon steel are only applicable under representative conditions i.e., in conjugation with the exact buffer.

6.2.2.5 Application of new modelling tools in in performance assessments

Carbon steel corrosion model

Development of a carbon steel corrosion model as discussed in Section 6.1.1 has relevance to performance assessments for disposal concepts involving carbon steel containers emplaced within a bentonite buffer, namely those proposed by Nagra, Surao and NUMO. Current methods of evaluating the long-term performance of carbon steel involve the interpretation of empirical data in support of mechanistic arguments. If performance of the corrosion model could be validated over its range of applicable operating conditions, it could be used to underpin and extrapolate empirical measurements of the corrosion rate of carbon steel with time. Another benefit to employing this model is the ability to explore other variables that are not as widely evaluated in current experimental programs such as the impact of transients in temperature, eh, pH and radiation dose rate on expected corrosion performance and to interpolate between experimental data points. Due to the incorporation of electrochemical behaviour of the steel, the model could also be used to underpin existing mechanistic arguments such as the reasoned exclusion of specific mechanisms e.g., localised corrosion. At present, the major limitation associated with the deployment of such a model is validating it, since it is not currently known to what extent processes that are excluded from it lead to under or overly-pessimistic predictions in the corrosion rate.

Microbial activity model

The microbial activity model that was developed as discussed in Section 6.1.1.2 is designed to be implemented within existing geochemical models such as the reactive transport sulphide model described in Section 6.1.1.3. The benefit that this model could bring to performance assessment is the ability to predict whether microbial activity is reduced under specific environmental stressors and to help underpin empirical data. A key assumption that underpins performance assessment of metallic containers in bentonite buffers is that sulphate reducing bacteria can be supressed by having a sufficient swelling pressure in the bentonite leading to low water activity and limited porosity. The microbial model could be used to extrapolate between empirical measurements to better define the thresholds for which microbial activity will take place. However, the ability to deploy this model is limited by the requirements for good quality data relating to the tolerance of the various relevant strains of microbe to the different environmental stressors, and such data is currently lacking.

Repository scale modelling of sulphide

Of the three modelling tools developed in Task 6, the repository scale sulphide model discussed in Section 6.1.1.3 is the most suitable for use in performance assessment as it represents the latest iteration in a model that has been developed and refined for over a decade. The recent updates in the model enable the influence of a wider range of variables and specific scenarios to be evaluated on the corrosion of both copper and carbon steel. A key finding of the model was that the influence of an order of magnitude increase in diffusion rate (that could arise due to a fault in the emplacement of the buffer) is expected to lead to a significant increase in the corrosion loss for copper containers. Whereas the impact of anisotropic diffusion (e.g., 5x faster in the horizontal direction) is only predicted to cause a

significant increase in the corrosion loss of copper containers when it is also combined with the increase in overall diffusion rate associated with a badly emplaced buffer. Another major finding was the impact of a concrete liner, which was shown to greatly attenuate the extent of corrosion of copper from sulphide due to enhanced mackinawite precipitation.

These additions to the model support mechanistic arguments made regarding the impact of sulphate reduction on the corrosion of copper and highlight the sensitivity of the corrosion rate to specific assumed parameters such as diffusivity. For carbon steel, the model demonstrates that corrosion due to sulphide is expected to be insignificant even at durations vastly exceeding the design life of the canister, which can be used to support the reasoned exclusion of sulphide driven corrosion as a major degradation mechanism for carbon steel in performance assessment.

7. References

Abdelouas A., Alonso U., Bernier-Latmani R., Bosch C., Cherkouk A., Dobrev D., Fernández A.M., Finck N., Gaggiano R., Havlová V., Hesketh J., Idiart A., Mijnendonckx K., Montoya V., Muñoz A.G., Padovani, C., Pont A., Rajala P., Riba O., Sarrasin, L., Sayenko S., Smart N., Texier-Mandoki N., Wersin P. (2022): Initial State-of-the-Art of WP ConCorD. Final version as of 17.08.2022 of deliverable D15.1 of the HORIZON 2020 project EURAD. EC Grant agreement no: 847593.

Abdelouas, A., Fernández, A.M., Cherkouk A., Muñoz A.G., Idiart A., Pont, A., Singh, A.R., Bosch, C., Padovani, C., Dobrev, D., Hesketh, J., Černá, K,. Mijnendonckx, K., Sarrasin, L., Matulová M., Merroun, M., Texier-Mandoki, N., Smart, N., Finck, N., Riba, O., Wersin, P., Rajala, P., Bernier-Latmani, R., Gaggiano, R., Šachlová, Š., Sayenko, S., Alonso, U., Havlová, V., Montoya, V.: Updated State-of-the-Art of WP ConCorD. Final version as of #xx.04.2024 of deliverable D15.2 of the HORIZON 2020 project EURAD. EC Grant agreement no: 847593.

Aoki, K., Sugita, Y., Chijimatsu, M., Tazaki, K. (2010): Impacts of thermo-hydro-mechanical experiments on the microbial activity in compacted bentonite at the Kamaishi Mine, Northeast Japan, in Appl. Clay Sci., vol. 47, p. 147–154.

ASTM (2011): ASTM-G1: Standard Practice for Preparing, Cleaning, and Evaluating Corrosion Test Specimens. ASTM International, West Conshohocken, PA, USA.

Bagnoud A., Chourey K., Hettich R. L., de Bruijn I. and Andersson A. F., Leupin O.X., Schwyn B., Bernier-Latmani R. (2016): Reconstructing a hydrogen-driven microbial metabolic network in Opalinus Clay rock, in Nature Communications, vol. 7, p. 12770.

Basavaraju M., Gunashree B.S. (2022): Escherichia coli: An overview of main characteristics. doi: 10.5772/intechopen.105508.

Bell E., Lamminmäki T., Alneberg J., Andersson A., Qian C., Xiong W., Hettich R., Frutschi M., Bernier-Latmani R. (2020): Active sulfur cycling in the terrestrial deep subsurface, ISME Journal, vol. 14(5), p. 1260-1272. doi: 10.1038/s41396-020-0602-x.

Bengtsson A., Pedersen K. (2017): Microbial sulphide-producing activity in water saturated Wyoming MX-80, Asha and Calcigel bentonites at wet densities from 1500 to 2000 kg m^{-3}, in Applied Clay Science vol. 137, p. 203–212.

Bevas, C., Hesketh J., Rance A., Stevenson L-A, Uthayakumaran S., Pateman B., Padovani C., Šachlová S., Kašpar V., Dobrev D., Götz D., Kolomá K., Večerník P. (2024): Elucidation of critical irradiation parameter, Final version as of 06/02/2024 of deliverable D15.7 of the HORIZON 2020 project EURAD. EC Grant agreement no: 847593.

Biesta-Peters E.G., Reji M.W., Gorris L.G.M., Zwietering M.H. (2010): Comparing nonsynergistic gamma models with interaction models to predict growth of emetic bacillus cereus when using combinations of pH and individual undissociated acids as growth-limiting factors, in Applied and Environmental Microbiology, vol. 76(17), p. 5791-5801. doi: 10.1128/AEM.00355-10.

Bildstein O., Trotignon L., Perronnet M.,Jullien M. (2006): Modelling iron–clay interactions in deep geological disposal conditions, in Physics and Chemistry of the Earth, Parts A/B/C, vol. 31(10–14), pages 618-625, doi:10.1016/j.pce.2006.04.014

Bratbak G., Dundas I. (1984): Bacterial dry matter content and biomass estimations, in Applied and Environmental Microbiology, vol. 48(4), doi: 10.1128/aem.48.4.755-757.1984.

Burzan N., Murad Lima R., Frutschi M., Janowczyk A., Reddy B., Rance A., Diomidis N., Bernier-Latmani R. (2022): Growth and persistence of an aerobic microbial community in Wyoming bentonite MX-80 despite anoxic in situ conditions, in Front. Microbiol, doi: 10.3389/fmicb.2022.858324.

Cai, P., Huang Q., Zhu J., Jiang D., Zhou X., Rong X. and Liang W. (2007): Effects of low-molecular-weight organic ligands and phosphate on DNA adsorption by soil colloids and minerals, in Colloids Surf B Biointerfaces, vol. 54, p. 53-59.

Černá, K., Černoušek, T., Polívka, P., Ševců, A. (2019): Survival of microorganisms in bentonite subjected to different levels of irradiation and pressure, EU MIND Project Deliverable 2.15.

Červinka R., Vašíček R., Večerník P., Kašpar V. (2018): SÚRAO report no. 419/2019: Complete characterization of the BCV 2017 bentonite (in Czech). SURAO, Prague, Czech Republic.

Charpentier D., Devineau K., Mosser-Ruck R., Cathelineau M., Villiéras F. (2006): Bentonite–iron interactions under alkaline condition: An experimental approach, in Applied Clay Science, vol. 32, p. 1–13.

Chi Fru, E., Athar R. (2008): In situ bacterial colonization of compacted bentonite under deep geological high-level radioactive waste repository conditions, in Applied Microbiology and Biotechnology, vol. 79, p. 499-510.

Cloet V., Pekala M., Smith P., Wersin P., Diomidis N. (2017): An evaluation of sulphide fluxes in the near-field of a HLW repository, Nagra Technical Report 17-04.

Couvert O., Divanach M.-L., Lochardet A., Thuault D., Huchel V. (2019): Modelling the effect of oxygen concentration on bacterial growth rates, in Food Microbiology, vol. 77, p. 21-25. doi: 10.1016/j.fm.2018.08.005.

Van Derlinden E., Van Impe J.F. (2012): Modeling microbial kinetics as a function of temperature: Evaluation of dynamic experiments to identify the growth/inactivation interface, in Journal of Food Engineering, vol. 2012(1), p. 201-210. doi: 10.1016/j.jfoodeng.2011.03.037.

Ebert, W. L., Hoburg, R. F., & Bates, J. K. (1991): The sorption of water on obsidian and a nuclear waste glass, in Physics and Chemistry of Glasses, vol. 32(4), p. 133-137.

Engel, K., Coyotzi, S., Vachon, M. A., McKelvie, J. R., Neufeld, J. D. (2019): Validating DNA extraction protocols for bentonite clay, in MSphere, vol. 4(5). https://doi.org/10.1128/msphere.00334-19.

Fernández A.M., Alonso U., Nieto P., Mingarro M, Missana T., Muñoz A., Finck N., Müller N., Schild D., Singh A.R., Šachlová S., Kašpar V., Dobrev D., Gõtz D., Kolomá K., Večerník P., Zuna M., Matulová M. (2024): Final version as of 29.04.2024 of deliverable D15.12 of the HORIZON 2020 project EURAD. EC Grant agreement no: 847593.

Fernández, A.M., Marco, J.F., Nieto, P., León, F.J., Robredo, L.M., Clavero, M.A., Cardona, A., Fernández, S., Svensson, D., Sellin, P., (2022): Characterization of Bentonites from the in situ ABM5 heater experiment at Äspö Hard Rock Laboratory, Sweden, in Minerals, vol. 12(4), p. 471, doi.org/10.3390/min12040471.

Fernández A.M., Alonso U., Nieto P., Mingarro M, Missana T., Muñoz A., Finck N., Müller N., Schild D., Singh A.R., Šachlová S., Kašpar V., Dobrev D., Gõtz D., Kolomá K., Večerník P., Zuna M., Matulová M. (2024): Final version as of 29.04.2024 of deliverable D15.12 of the HORIZON 2020 project EURAD. EC Grant agreement no: 847593.

Fernández, A.Mª., Baeyens, B., Bradbury, M., Rivas, P., (2004): Analysis of the pore water chemical composition of a Spanish compacted bentonite used in an engineered barrier, in Physics and Chemistry of the Earth, vol. 29(1), p. 105-118.

Fernández, A.M., Rivas, P., (2005): Pore water chemistry of saturated FEBEX bentonite compacted at different densities, in: Advances in understanding Engineered Clay Barriers. A.A. Balkema Publishers, Leiden, Alonso, E.E., Ledesma, A. (eds.), p. 505-514.

Féron D., Crusset D. (2014): Microbial induced corrosion in French concept of nuclear waste underground disposal, in Corrosion Engineering, Science and Technology, vol. 49(6), p. 540-547. doi: 10.1179/1743278214Y.0000000193.

Finck, N., Morelová, N., Schlegel, M.L., Schild, D., Reguer, S., Dardenne, K., Geckeis, H., (2023): Corrosion of austenitic stainless steel at 90°C under highly saline and anoxic conditions: A microscopic study, in Corros. Sci. vol. 220, p. 111265.

Frankl, M., Wittel M., Diomidis N., Vasiliev A., Ferroukhi H., Pudollek S., (2023): Criticality assessments for long-term post-closure canister corrosion scenarios in a deep geological repository, in Annals of Nuclear Energy vol. 180, 109449.

Gaggiano, R., Debelle, A., Rossignol F., Cornu, I., Bosch, C., Ganster, P., Dias, R. De C. C. D., Sayenko, S., Kuprin, A., Trentin, A., Vaari J., Pakarinen, J. (2024): Deliverable 15.6: Novel materials and processes for the optimisation of long-term container performance. Final version as of 06.05.2024 of deliverable D15.6 of the HORIZON 2020 project EURAD. EC Grant agreement no: 847593.

Hadi, J., Wersin, P., Serneels, V., Grenèche, J.-M., (2019): Eighteen years of steel–bentonite interaction in the FEBEX in situ test at the Grimsel Test Site in Switzerland Clays, in Clay Miner. Vol. 67, p. 111-131.

Haynes H.M., Pearce C.I., Boothman C., Lloyd J.R. (2018): Response of bentonite microbial communities to stresses relevant to geodisposal of radioactive waste, in Chemical Geology, vol. 501, p. 58-67, doi: 10.1016/j.chemgeo.2018.10.004.

Hedin, A., Johansson, A.J., Lilja, C., Boman, M., Berastegui, P., Berger, R., Ottosson, M., (2018): Corrosion of copper in pure O_2-free water?, in Corros. Sci. vol. 137, p. 1-12.

Hesketh, J., Haynes, H., Reddy, B., Rance, A., Bevas, C., Padovani, C., Diomidis, N., (2023): Carbon steel corrosion in a bentonite buffer: A comparison between in situ exposure and lab based experiments, in Mater. Corros., vol. 74, p. 1728-1745.

Hollmark, H.M., Keech, P.G., Vegelius, J.R., Werme, L., Duda, L.-C., (2012): X-ray absorption spectroscopy of electrochemically oxidized Cu exposed to Na_2S, in Corros. Sci. vol. 54, p. 85-89.

Huang Y., Shao H., Wieland E., Kolditz O., Kosakowski G. (2021): Two-phase transport in a cemented waste package considering spatio-temporal evolution of chemical conditions, in Materials Degradation vol. 5, p. 1–4, doi: 10.1038/s41529-021-00150-z.

Huertas, F., P. Fariña, J. Farias, J.L. García-Siñeriz, M.V. Villar, A.M. Fernández, P.L. Martín, F.J. Elorza, A. Gens, M. Sánchez, A. Lloret, J. Samper, M.A. Martínez (2006): Full-scale Engineered Barriers Experiment. Updated Final Report 1994-2004. Publicación Técnica ENRESA, Vol. 05-0/2006, 590 pp.

Jonsson, M., Emilsson, G., Emilsson, L., (2018): Mechanical design analysis for the canister. Posiva SKB Report 04, July 2018. SKB ID 1524476, Posiva ID RDOC-104919. ISSN 2489-2782.

Karnachuk O.V., Kurganskaya I.A., Avakyan M.R., Frank Y.A., Ikkert O.P., Filenko R.A., Danilova E.V., Pimenov N.V. (2015): An acidophilic Desulphosporosinus isolated from the oxidized mining wastes in the Transbaikal area, in Microbiology, vol. 84, p. 677-686, doi: 10.1134/S0026261715050112.

Karnland, O., (2010): Chemical and mineralogical characterization of the bentonite buffer for the acceptance control procedure in a KBS-3 repository., SKB Report technical report TR-10-60.

Kašpar, V., Šachlová, Š., Hofmanová, E., Komárková, B., Havlová, V., Aparicio, C., Černá, K., Bartak, D., Hlaváčková, V. (2021): Geochemical, geotechnical, and microbiological changes in Mg/Ca bentonite after thermal loading at 150°C, in Minerals vol. 11, p. 965. https://doi.org/10.3390/min11090965.

Kaufhold, S., Dohrmann, R., (2008): Detachment of colloidal particles from bentonites in water, in Appl. Clay Sci., vol. 39, p. 50-59.

Kaufhold, S.; Dohrmann, R.; Sandén, T.; Sellin, P.; Svensson, D. (2013): Mineralogical investigations of the first package of the alternative buffer material test – I. Alteration of bentonites, in Clay Minerals, vol. 48(2), p. 199–213. doi:10.1180/claymin.2013.048.2.04.

Kaufhold, S., Dohrmann, R., Klinkenberg, M., Noell, U. (2015): Electrical conductivity of bentonites, in Appl. Clay. Sci. vol. 114, p. 375-385.

Kaufhold S., Hassel A. W., Sanders D., Dohrmann R. (2015b): Corrosion of high-level radioactive waste iron-canisters in contact with bentonite, in Journal of Hazardous Materials, vol. 285, p. 464–473.

Kaufhold, S., Dohrmann, R., Gröger-Trampe, J. (2017): Reaction of native copper in contact with pyrite and bentonite in anaerobic water at elevated temperature, in Corros. Eng. Sci. Technol., vol. 52, p. 349-358.

Kaufhold, S., Klimke, S., Schloemer, S., Alpermann, T., Renz, F., Dohrmann, R. (2020): About the corrosion mechanism of metal iron in contact with bentonite, in ACS Earth Space Chem., vol. 4, p. 711-721.

King F., (2008): Corrosion of carbon steel under anaerobic conditions in a repository for SF and HLW in Opalinus Clay, Nagra Technical Report 08-12, Nagra, Switzerland.

King F., Kolář M., Puigdomenech I., Pitkänen P., Lilja C. (2021): Modeling microbial sulfate reduction and the consequences for corrosion of copper canisters, in Materials and Corrosion, vol. 72(1-2). p. 339-347, Doi: 10.1002/maco.202011770.

King, F., Padovani, C., (2011). Review of the corrosion performance of selected canister materials for disposal of UK HLW and/or spent fuel, in Corros. Eng. Sci. Technol. Vol. 46, p. 82-90.

Landolt, D., Davenport, A., Payer, J., and Shoesmith, D. (2009): A review of materials and corrosion issues regarding canisters for disposal of spent fuel and high-level waste in Opalinus clay, Nagra Technical Report 09-02.

Laskowska, E., Kuczyńska-Wiśnik, D. (2020): New insight into the mechanisms protecting bacteria during desiccation, in Curr. Genet., vol. 66, p. 313-318. https://doi.org/10.1007/s00294-019-01036-z.

Laufek, F., Hanusová, I., Svoboda, J., Vašíček, R., Najser, J., Koubová, M., & Mašín, D. (2021): Mineralogical, Geochemical and Geotechnical Study of BCV 2017 Bentonite - The Initial State and the State following Thermal Treatment at 200° C, in Minerals, vol. 11(8), p. 871.

Leupin O.X., Bernier-Latmani R., Bagnoud A., Moors H., Leys N., Wouters K., Stroes-Gascoyne S. (2017): Fifteen years of microbiological investigation in Opalinus clay at the Mont Terri rock laboratory (Switzerland). In Swiss J. Geosci., vol. 110(Supp 1), p. 343–354. doi: 10.1007/s00015-016-0255-y.

Madejova´ J., Pentra´k M., Pa´lkova´ H. & Komadel P. (2009): Near-infrared spectroscopy: a powerful tool in studies of acid-treated clay minerals, in Vibrational Spectroscopy, vol. 49, p. 211218.

Martinez-Moreno, M.F., Povedano-Priego, C., Morales-Hidalgo, M., Mumford, A.D., Ojeda, J.J., Jroundi, F., Merroun, M.L. (2023): Impact of compacted bentonite microbial community on the clay mineralogy and copper canister corrosion: a multidisciplinary approach in view of a safe deep geological repository of nuclear wastes, in J. Hazard Mater, vol. 458, 131940. https://doi.org/10.1016/j.jhazmat.2023.131940.

Matschiavelli, N., Kluge, S., Podlech, C., Standhaft, D., Grathoff, G., Ikeda-Ohno, A., Warr, L.N., Chukharkina, Arnold, T., Cherkouk, A. (2019): The year-long development of microorganisms in uncompacted Bavarian bentonite slurries at 30 and 60°C, in Environmental Science and Technology, vol. 53, 10514–10524. https://doi.org/10.1021/acs.est.9b02670.

Matulová M., Hausmannová L., Malina J., Šatura L. (2023): Waste disposal package for spent nuclear fuel in the Czech Republic, MS SÚRAO Report, TZ 665/2023, Prague.

Mayeux B., Fardeau M.-L., Bartoli-Joseph M., Casalot L., Vinsot A., Labat M. (2013): Desulfosporosinus burensis sp. Nov., a spore-forming, mesophilic, sulfate-reducing bacterium isolated from a deep clay environment, in International Journal of Systematic and Evolutionary Microbiology, vol. 63(2), Doi: 10.1099/ijs.0.035238-0.

Mijnendonckx, K., Van Gompel, A., Coninx, I., Bleyen, N., Leys, N., (eds), (2018): Radiation and microbial degradation of bitumen, EU MIND Project Deliverable D1.3.

Mijnendonckx K., Miroslav H., Wang L., Jacops E., Provoost A., Mysara M., Wouters K., De Craen M., Leys N. (2019): An active microbial community in boom clay porewater collected from piezometers impedes validating predictive modelling of ongoing geochemical processes, in Appl. Geochem, vol. 106, p. 149–160. doi: 10.1016/j.apgeochem.2019.05.009.

Mijnendonckx, K., P. Monsieurs, K. Černá, V. Hlaváčková, J. Steinová, N. Burzan, Bernier-Latmani R., Boothman C., Miettinen H., Kluge S., Matschiavelli N., Cherkouk A., Jroundi, F. (2021): Chapter 4 in Molecular techniques for understanding microbial abundance and activity in clay barriers used for geodisposal, in The Microbiology of Nuclear Waste Disposal. J. R. Lloyd and A. Cherkouk (eds), Elsevier, p. 71-96, doi: 10.1016/B978-0-12-818695-4.00004-6.

Mijnendonckx K. (2023): Training Materials of WP15 ConCorD. Final version as of 22.03.2023 of deliverable D15.3 of the HORIZON 2020 project EURAD. EC Grant agreement no: 847593.

Mijnendonckx, K., Smoldersn C., Bartak, D., Morales-Hidalgo, M., Povedano-Priego, C., Jroundi, F., Merroun, M., Leys, N., Černá, K. (2024): DNA extraction in MX-80 bentonite: a comprehensive inter-laboratory investigation. Environmental Microbiology (in revision).

Morales Hidalgo, M., Povedano Priego, C., Martinez Moreno, M.F., Jroundi, F., Merroun, M.L., Alonso, U., Fernández, A.M., García-Gutiérrez, M., Mingarro, M., Missana Jesus Morejón, T., Nieto, P., Valdivieso, P.P., Bartak, D.S., Říha, J., Černá, K., Šachlová, S., Kašpar, V., Dobrev, D., Večerník, P., Jakus, N., Jermann, E., Bena, P., Zarkali, C., Bernier-Latmani, R., Wei, T., Sushko, V., Cherkouk, A., Smolders, C., Kursten, B., Mijnendonckx K. (2024): Integration of the findings on the impact of irradiation, dry density and particle size on the microbial community. Final version as of 04/04/2024 of deliverable D15.9 of the HORIZON 2020 project EURAD. EC Grant agreement no: 847593.

Morco R.P. (2020): Gamma-radiolysis kinetics and its role in the overall dynamics of materials degradation, PhD Thesis, The University of Western Ontario (Canada), Electronic Thesis and Dissertation Repository. 7248, https://ir.lib.uwo.ca/etd/7248.

Neff D., Saheb M., Monnier J., Perrin S., Descostes M., LHostis V., Crusset D., Millard A., Dillmann P. (2010): A review of the archaeological analogue approaches to predict the long-term corrosion behaviour of carbon steel overpack and reinforced concrete structures in the French disposal systems, in J. Nucl. Mat. Vol. 402, p. 196–205.

Nixon, S., Bassil, N.M., Lloyd, J.R. (eds) (2017): Effects of radiation and microbial degradation of ILW organic polymers, MIND Project Deliverable D1.2.

Nyhan L., Begley M., Mutel A., Qu Y., Johnson N., Callanan M. (2018): Predicting the combinatorial effects of water activity, pH and organic acids on Listeria growth in media and complex food matrices, in Food Microbiology, vol. 74, p. 75-85, doi: 10.1016/j.fm.2018.03.002.

Padovani, C., King F., Lilja C., Féron D., Necib S., Crusset D., Deydier V., Diomidis N., Gaggiano, R., Ahn T., Keech P.G., Macdonald D.D., Asano H., Smart N.R., Hall D.S., Hänninen H., Engelberg D., Noël J.J., Shoesmith D.W. (2017): The corrosion behaviour of candidate container materials for the disposal of high-level waste and spent fuel – a summary of the state of the art and opportunities for synergies in future R&D in Corrosion Engineering, Science and Technology, vol 52:sup1, p. 227-231.

Patel, R., Punshon, C., Nicholas, J., Bastid, P., Zhou, R. C., Schneider, N., Bagshaw, D., Howse, E., Hutchinson, R., Asano, King F: (2012): “Canister design concepts for disposal of spent fuel and high level waste, Nagra Technical Report, NTB 12-06.

Pedersen, K., Motamedi, M., Karnland, O. (1995): Survival of bacteria in nuclear waste buffer materials - The influence of nutrients, temperature and water activity, SKB technical Report TR--95-27.

Pitonzo, B.J., Amy, P.S., Rudin, M. (1999): Effect of gamma radiation on native endolithic microorganisms from a radioactive waste deposit site, in Radiation Research, vol. 152(1), p. 64-70. https://doi.org/10.2307/3580050.

Posiva (2021): Sulphide fluxes and concentrations in the spent nuclear fuel repository at Olkiluoto - 2021 update. POSIVA Working Report WR 2021-07.

Pospíšková I., Dobrev D., Kouril M., Stoulil J., Novikova D., Kotnour P., Matal O. (2017): Czech national programme and disposal canister concept, in Corrosion Engineering, Science and Technology, 201752, 1_suppl, p. 6-10.

Povedano-Priego, C., Jroundi, F., Lopez-Fernandez, M., Shrestha, R., Spanek, R., Martín-Sánchez, I., Villar, M.V., Ševců, A., Dopson, M., Merroun, M.L. (2021): Deciphering indigenous bacteria in compacted bentonite through a novel and efficient DNA extraction method: Insights into biogeochemical processes within the Deep Geological Disposal of nuclear waste concept, in Journal of Hazardous Materials, vol. 408, 124600. https://doi.org/10.1016/j.jhazmat.2020.124600.

Povedano-Priego, C., Jroundi, F., Solari, P.L., Guerra-Tschuschke, I., Abad-Ortega, M. del M., Link, A., Vilchez-Vargas, R., Merroun, M.L. (2023): Unlocking the bentonite microbial diversity and its implications in selenium bioreduction and biotransformation: Advances in deep geological repositories, in Journal of Hazardous Materials vol. 445, 130557. doi.org/10.1016/j.jhazmat.2022.130557.

Puigdomenech, I., Taxén, C., (2000): Thermodynamic data for copper. Implications for the corrosion of copper canister under repository conditions. SKB Technical Report TR-00-13.

Ramamoorty S., Sass H., Langner H., Schumann P., Kroppenstedt R.M., Spring S., Overmann J., Rosenzweig R.F. (2006): Desulfosporosinus lacus sp. Nov., a sulfate-reducing bacterium isolated from pristine freshwater lake sediments, in International Journal of Systematic and Evolutionary Microbiology, vol. 56(12). p. 2729-2736, doi: 10.1099/ijs.0.63610-0.

Reddy, B., Padovani, C., Rance, A.P., Smart, N.R., Cook, A., Haynes, H.M., Milodowski, A.E., Field, L.P., Kemp, S.J., Martin, A., Diomidis, N., 2020. The anaerobic corrosion of candidate disposal canister materials in compacted bentonite exposed to natural granitic porewater containing native microbial populations, in Mater. Corros., vol. 72, p. 361-382.

Roden E.E., Jin Q. (2011): Thermodynamics of microbial growth coupled to metabolism of glucose, ethanol, short-chain organic acids, and hydrogen, in Applied and Environmental Microbiology, vol. 77(5), doi: 10.1128%2FAEM.02425-10.

Rosso L., Lobry J.R., Flandrois J.P. (1993): An Unexpected Correlation between Cardinal Temperatures of Microbial Growth Highlighted by a New Model, in Journal of Theoretical Biology, vol.162(4), p. 447-463, doi: 10.1006/jtbi.1993.1099.

Sarrasin L., Tisyadi M.F., Abdelouas A., Šachlová Š., Kašpar V., Dobrev D., Götz D., Kolomá K., Večerník P., Zuna M., Alonso U., Diéguez M., Soto C., Fernández A.M., Gutiérrez M.G., Valdivieso P., Missana T. (2024): Synthesis of irradiation results under repository conditions. Final version as of 13.05.2024 of deliverable D.15.8 of the HORIZON 2020 project EURAD. EC Grant agreement no: 847593.

Schlegel, M.L., Necib, S., Daumas, S., Labat, M., Blanc, C., Foy, E., Linard, Y., (2018): Corrosion at the carbon steel-clay borehole interface under anoxic alkaline and fluctuating temperature conditions, Corros. Sci., vol 136, p. 70-90.

Schütz M.K., Schlegel M.L., Libert M., Bildstein O. (2015): Impact of Iron-Reducing Bacteria on the Corrosion Rate of Carbon Steel under Simulated Geological Disposal Conditions, in Environmental Science and Technology, vol. 49(12), p. 7483-7490. doi: 10.1021/acs.est.5b00693.

Selzer Ph., Shao H. et al. (2024): The value of simplified models of radionuclide transport for the safety assessment of nuclear waste repositories, to be submitted to Journal of Contaminant Hydrology.

Senior, N.A., Newman, R.C., Artymowicz, D., Binns, W.J., Keech, P.G., Hall, D.S., (2019): Communication – A method to measure extremely low corrosion rates of copper metal in anoxic aqueous media, in J Electrochem. Soc. Vol. 166, p. C3015-C3017.

SKB, (2022): Post-closure safety for the final repository for spent nuclear fuel at Forsmark Fuel and canister process report, PSAR version, SKB Technical Report TR-21-02.

Smart N. R., Rance A., Reddy B., Fennell P., Winsley R. (2012): Analysis of SKB MiniCan Experiment 3. SKB Technical report TR-12-09.

Steward E.J. (2012): Growing Unculturable Bacteria, in Journal of Bacteriology, vol. 194(16), doi: 10.1128/jb.00345-12.

Stoulil J., Kaňok J., Kouřil M., Parschová H., Novák P. (2013): Influence of temperature on corrosion rate and porosity of corrosion products of carbon steel in anoxic bentonite environment, in J. Nucl. Mat., vol. 443(1–3), p. 20-25, doi:10.1016/j.jnucmat.2013.06.031.

Stoulil J., Mukhtar S., Lhotka M., Bureš R., Kašpar V., Šachlová Š., Dobrev D., Večerník P., Zuna M., Němeček J., Němeček J. (2023): Processing of samples from corrosion experiments – Corrosion products 2, SÚRAO technical report TZ 700/2022.

Stroes-Gascoyne, S., West, J.M. (1997): Microbial studies in the Canadian nuclear fuel waste management program, in FEMS Microbiol. Rev. vol. 20, p. 573–590. doi.org/10.1111/j.1574-6976.1997.tb00339.x.

Stroes-Gascoyne, S. (2010): Microbial Occurrence in Bentonite-Based Buffer, Backfill and Sealing Materials from Large-Scale Experiments at AECL's Underground Research Laboratory, in Appl. Clay Sci., vol. 47(1), p. 36–42.

Stroes-Gascoyne S., Hamon C.J., Maak P., Russel S. (2010): The effects of the physical properties of highly compacted smectitic clay (bentonite) on the culturability of indigenous microorganisms, in Applied Clay Science, vol. 47(1-2), p. 155-162, doi: 10.1016/j.clay.2008.06.010.

Stucki, J.W., (2011): A review of the effects of iron redox cycles on smectite properties, in Comptes Rendus Geoscience, vol. 343(2–3), p. 199-209.

Svensson, D.; Sandén, T.; Olsson, S.; Dueck, A.; Eriksson, S.; Jägerwall, S.; Hansen, S., (2011): Alternative buffer material status of the ongoing laboratory investigation of reference materials and test package 1. SKB Technical report TR-11-06.

Tamisier M., Schmidt M., Vogt C., Kümmel S., Stryhanyuk H., Musat N., Richnow H.-H., Musat F. (2022): Iron corrosion by methanogenic archea characterized by stable isotope effects and crust mineralogy, in Environmental Microbiology, vol. 24(2), p. 583-595, doi: 10.1111/1462-2920.15658.

Tamisier M., Musat F., Richnow H.-H., Vogt C., Schmidt M. (2023): On the corrosion of ductile cast iron by sulphate-reducing bacteria – implications for long-term nuclear waste repositories, in Frontiers in Geochemistry, vol. 1., doi: 10.3389/fgeoc.2023.1244283.

Timkina, E., Drábová, L., Palyzová, A., Řezanka, T., Maťátková, O., Kolouchová, I. (2022): Kocuria Strains from Unique Radon Spring Water from Jachymov Spa, in Fermentation vol. 8, p. 35., doi.org/10.3390/fermentation8010035.

van Gerwen, S. J. C., Rombouts, F. M., van't Riet, K., Zwietering, M. H. (1999): A data analysis of the irradiation parameter D10 for bacteria and spores under various conditions, in J. Food Prot. 62, 1024–1032.

Van Loon, L., Soler, J.M., M.H. Bradbury (2003): Diffusion of HTO, $36Cl^-$ and $125I^-$ in Opalinus Clay samples from Mont Terri: Effect of confining pressure, in Journal of Contaminant Hydrology, vol. 61(1-4), p. 73-83.

Vehling F., Kosakowski G., Shao H. (2024): Two-Phase Reactive Transport Modelling of Heterogeneous Gas Production in Low- and Intermediate-level Radioactive Waste Repository, to be submitted to Applied Clay Science.

Wersin, P., Kumpulainen, S. & Juvankoski, M. (2017): Definition of reference buffer characteristics for TURVA-2020 (v. 26 July 2017). Internal Posiva memorandum POS-032716.

Wersin, P., Hadi, J., Kiczka, M., Jenni, A., Grenèche, J.-M., Diomidis, N., Leupin. O.X., Svensson, D., Sellin, P., Reddy, B., Smart, N., Zhang, Z., (2023): Unravelling the corrosion processes at steel/bentonite interfaces in in situ tests, in Mater. Corros. Vol 74(11-12), p. 1716-1727, oi.org/10.1002/maco.202313755.Wilson, J., (2017): FEBEX-DP: Geochemical Modelling of Iron-Bentonite Interactions, Quintessa Report QRS-1713A-R3 (v1.3)).

Zuna M., Steinová J., Šachlová Š., Dobrev D., Mendoza Miranda A. N., Kolomá K., Kašpar V., Jankovský F., Večerník P. (2023): Corrosion test in natural granitoid environment – involvement in the MaCoTe project. Final report. SURAO Technical report no. 712/2023, SÚRAO, Prague, Czech Republic.

Appendices

Appendix A. Modelling sulphide corrosion in the Swiss HLW repository under various settings (University of Bern)

Input parameters

Table A43: Input parameters of the modelled cases. (1) Dissolved organic matter (DOM) is assumed to have the generic molecular formula of CH_2O, (2) Presence of montmorillonite was considered for surface reactions (surface protonation and cation exchange) only, (3) Generic exchanger (with composition reported in Mäder (2009)) was considered for Opalinus Clay (OPA), (4) Solid organic matter (SOM) in the MX-80 buffer, (5) Solid organic matter (SOM) in the Opalinus Clay and EDZ, (†) Initially absent, but allowed to precipitate if over-saturated.

	Buffer	**OPA and EDZ**
pH	7.31	7.27
pe	-3.24	-3.08
Eh (mV vs SHE)	-191	-182
Total aq. components [mol L^{-1}]		
Na	3.27E-01	1.67E-01
Mg	8.13E-03	5.80E-03
Ca	1.18E-02	8.08E-03
Sr	3.21E-04	3.10E-04
K	1.56E-03	1.64E-03
Fe	4.71E-05	3.85E-05
Si	1.82E-04	1.82E-04
Cl	1.60E-01	1.60E-01
CO_3	3.44E-03	2.95E-03
S(VI)	1.03E-01	1.72E-02
S(-II)	8.66E-10	8.70E-10
H_2	1.00E-06	1.00E-06
(1)DOM	1.67E-04	8.33E-05
Minerals [volume fraction]		
(2)MX-80_exchanger	4.74E-01	0.00
(3)OPA_exchanger	0.00	4.90E-01
Calcite	4.44E-03	1.23E-01
Dolomite	(†)0.00	5.50E-03
Siderite	(†)0.00	3.71E-02
Celestite	(†)0.00	3.70E-04
Gypsum	6.73E-03	(†)0.00
Quartz	2.08E-02	1.84E-01
Goethite	1.529E-03	(†)0.00
(4)SOM_MX-80	2.78E-04	0.00
(5)SOM_OPA	0.00	1.23E-03
Mackinawite	(†)0.00	(†)0.00

Table A44: Composition of the concrete liner.

Component	**Kg m^{-3}**
CEM II/B-LL 32.5 R	180
Bentonite	30
Quartzsand	670
Limestone powder	300
Microsilika	6.5
Water	560

		Proposed System
	kg per m3 of comp. A	**At 30 °C**
Comp. A	CEM II/B-LL 32.5R	180 kg
	Bentonite	30 kg
	Quartzsand (coarse)	670 kg
	Limestone powder (fine)	300 kg
	Microsilika	6.5 kg
	Water	560 kg
	Retarder	4.0 kg
	Sum for 1m3 Comp. A	**1750 kg = 1000 L**
	Marsh time initial (s)	51
	Bleeding 24h (%)	3.0
Comp. B	Sodium silicate (water glass)	110 kg
	Gel time (s)	10
	Needle penetration 1h (MPa)	3.8
	UCS 24h (MPa)	1.62
	UCS 28d (MPa)	3.7
	Elastic Modulus 28d (MPa)	1800

Table A45: Klinker recipe for the hydration calculation.

Alite (vol.%)	2.16
Belite (vol.%)	0.54
Aluminate (vol.%)	0.04
Ferrite (vol.%)	0.46
Gypsum (vol.%)	0.05
Silica fume (vol.%)	0.26
Limestone (vol.%)	13.3
Water (vol.%)	57.1
Sand (vol.%)	25.8

Table A46: List of secondary minerals in the concrete liner (as defined in the Thermochimie thermodynamic database v.9b0 – www.thermochimie-tdb.com) allowed to form, if over-saturated, due to interactions between the bentonite buffer and the cementitious leachates.

Considered Secondary Minerals			
MSH150	Celadonite-Fe	Tobermorite-14A	Kaolinite
Nontronite-Ca	Celadonite-Mg	Gyrolite	Clinochlore
Nontronite-Na	Illite-Al	Celestite	Microcline
Nontronite-Mg	Illite-FeIII	Katoite	Anorthite
Nontronite-K	Illite-Mg	Dolomite	Aragonite
Mordenite	Beidellite-Ca	Siderite	Cristobalit
Clinoptilolite_Ca	Beidellite-K	Brucite	Talc
Clinoptilolite_K	Beidellite-Mg	Hydrotalcite	Pyrophyllite
Clinoptilolite_Na	Beidellite-Na	Ettringite	Barite
Saponite-FeCa	Albite-low	Ettringite-Fe	Analcime
Saponite-FeK	Tobermorite-11A	Gibbsite	Syngenite

Sensitivity calculations

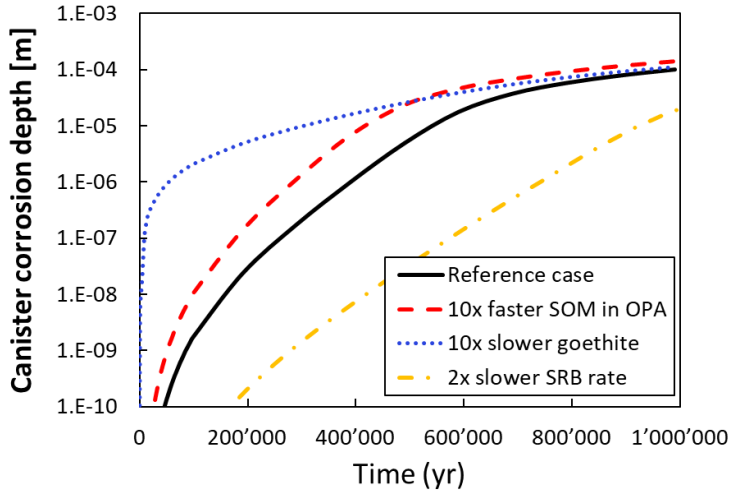

Figure A76: Sensitivity calculations compared to the copper reference case (see Section 6.2.1.3 in main text).

Appendix B. Reactive transport modelling of steel corrosion in bentonite – additional information (Amphos 21)

Chloride radiolysis modelling

[1]

Reactions	$M^{-1}\cdot s^{-1}$ or s^{-1}	Reactions	$M^{-1}\cdot s^{-1}$ or s^{-1}
$H_2O \rightarrow H^+ + OH^-$	k= 2.60E-05	$H + O_2^- \rightarrow HO_2^-$	k= 2.00E+10
$H^+ + OH^- \rightarrow H_2O$	k= 1.43E+11	$H + HO_2 \rightarrow H_2O_2$	k= 8.50E+09
$H_2O_2 \rightarrow H^+ + HO_2^-$	k= 3.56E-02	$H + H_2O_2 \rightarrow H_2O + OH$	k= 4.20E+07
$H^+ + HO_2^- \rightarrow H_2O_2$	k= 2.00E+10	$H + O_2 \rightarrow HO_2$	k= 2.10E+10
$E^- + H_2O \rightarrow H + OH^-$	k= 1.90E+01	$HO_2 + HO_2 \rightarrow H_2O_2 + O_2$	k= 8.40E+05
$H + OH^- \rightarrow E^- + H_2O$	k= 2.20E+07	$HO_2 + O_2^- \rightarrow O_2 + HO_2^-$	k= 9.60E+07
$OH + OH^- \rightarrow H_2O + O^-$	k= 1.30E+10	$OH + O^- \rightarrow HO_2^-$	k= 1.80E+10
$O^- + H_2O \rightarrow OH + OH^-$	k= 1.80E+06	$O + O \rightarrow O_2$	k= 1.00E+09
$HO_2 \rightarrow H+ + O_2^-$	k= 8.00E+05	$H_2O_2 \rightarrow H_2O + O$	k= 3.80E-04
$H+ + O_2^- \rightarrow HO_2$	k= 5.00E+10		
$E^- + H^+ \rightarrow H$	k= 2.30E+10		
$E^- + E^- \rightarrow H_2 + OH^- + OH^-$	k= 5.50E+09		
$E^- + H \rightarrow H_2 + OH^-$	k= 2.50E+10		
$E^- + O_2^- \rightarrow HO_2^- + OH^-$	k= 1.30E+10		
$E- + HO_2 \rightarrow HO_2^-$	k= 2.00E+10		
$E^- + H_2O_2 \rightarrow OH + OH^-$	k= 1.10E+10		
$E^- + O_2 \rightarrow O_2^-$	k= 1.90E+10		
$E^- + HO_2^- \rightarrow O^- + OH^-$	k= 3.50E+09		
$OH + OH \rightarrow H_2O_2$	k= 5.50E+09		
$OH + E^- \rightarrow OH^-$	k= 3.00E+10		
$OH + H \rightarrow H_2O$	k= 9.70E+09		
$OH + HO_2 \rightarrow H_2O + O_2$	k= 6.60E+09		
$OH + O_2^- \rightarrow O_2 + OH^-$	k= 1.00E+10		
$OH + H_2O_2 \rightarrow HO_2 + H_2O$	k= 2.70E+07		
$OH + H_2 \rightarrow H + H_2O$	k= 3.40E+07		
$OH + HO_2^- \rightarrow HO_2 + OH^-$	k= 7.50E+09		
$H + H \rightarrow H_2$	k= 7.80E+09		

[2]

G Values (units of Molecules / 100 eV)

species	γ rays
$G(e^-_{aq})$	2.60
$G(H)$	0.66
$G(H_2)$	0.45
$G(OH)$	2.70
$G(H_2O_2)$	0.70
$G(HO_2)$	0.02
$G(H^+)$	3.10
$G(OH^-)$	0.50

[1] Kelm, M., Bohnert, E. 2004. A kinetic model for the radiolysis of chloride brine, its sensitivity against model parameters and a comparison with experiments, Forschungszentreum Karlsruhe, FZKA 6977.
[2] Pastina, B., & LaVerne, J. A. (2001). Effect of molecular hydrogen on hydrogen peroxide in water radiolysis. *The Journal of Physical Chemistry A*, *105*(40), 9316-9322.

[3]

Reactions and Rate Constants Involving Chloride			
	Chemical Reaction		rate constant* (25 °C) ($M^{-1}\cdot s^{-1}$ or s^{-1})
6.41	$\cdot OH + Cl^- \rightarrow \cdot ClOH^-$		4.3×10^{9}
6.42	$\cdot OH + HClO \rightarrow \cdot ClO + H_2O$		9×10^{9}
6.43	$\cdot OH + HClO_2 \rightarrow \cdot ClO_2 + H_2O$		6.3×10^{9}
6.44	$\cdot e_{aq}^- + \cdot Cl \rightarrow Cl^- + H_2O$		1×10^{10}
6.45	$\cdot e_{aq}^- + \cdot Cl_2^- \rightarrow 2Cl^- + H_2O$		1×10^{10}
6.46	$\cdot e_{aq}^- + \cdot ClOH^- \rightarrow Cl^- + OH^- + H_2O$		1×10^{10}
6.47	$\cdot e_{aq}^- + HClO \rightarrow \cdot ClOH^- + H_2O$		5.3×10^{10}
6.48	$\cdot e_{aq}^- + Cl_2 \rightarrow \cdot Cl_2^-$		1×10^{10}
6.49	$\cdot e_{aq}^- + Cl_3^- \rightarrow \cdot Cl_2^- + Cl^- + H_2O$		1×10^{10}
6.50	$\cdot e_{aq}^- + HClO_2 \rightarrow \cdot ClO + OH^- + H_2O$		4.5×10^{10}
6.51	$\cdot e_{aq}^- + HClO_3 \rightarrow \cdot ClO_2 + OH^- + H_2O$		4.0×10^{9}
6.52	$\cdot H + Cl \rightarrow Cl^- + H^+$		1×10^{10}
6.53	$\cdot H + \cdot Cl_2^- \rightarrow 2Cl^- + H^+$		8×10^{9}
6.54	$\cdot H + \cdot ClOH^- \rightarrow Cl^- + H_2O$		1×10^{10}
6.55	$\cdot H + Cl_2 \rightarrow \cdot Cl_2^- + H^+$		7×10^{9}
6.56	$\cdot H + HClO \rightarrow \cdot ClOH^- + H^+$		1×10^{10}
6.57	$\cdot H + Cl_3^- \rightarrow \cdot Cl_2^- + Cl^- + H^+$		1×10^{10}
6.58	$\cdot HO_2 + \cdot Cl_2^- \rightarrow 2Cl^- + O_2 + H^+$		4×10^{9}
6.59	$\cdot HO_2 + Cl_2 \rightarrow \cdot Cl_2^- + O_2 + H^+$		1×10^{9}
6.60	$\cdot HO_2 + Cl_3^- \rightarrow \cdot Cl_2^- + Cl^- + O_2 + H^+$		1×10^{9}
6.61	$\cdot O_2^- + \cdot Cl_2^- \rightarrow 2Cl^- + O_2$		2×10^{10}
6.62	$\cdot O_2^- + HClO \rightarrow \cdot ClOH^- + O_2$		7.5×10^{6}
6.63	$H_2O_2 + \cdot Cl_2^- \rightarrow 2Cl^- + \cdot O_2^- + 2H^+$		1.4×10^{5}
6.64	$H_2O_2 + Cl_2 \rightarrow \cdot Cl_2^- + \cdot HO_2 + H^+$		1.9×10^{2}
6.65	$H_2O_2 + HClO \rightarrow Cl^- + O_2 + H^+ + H_2O$		1.7×10^{5}
6.66	$\cdot Cl_2^- + OH^- \rightarrow \cdot ClOH^- + Cl^-$		7.3×10^{6}
6.67	$Cl_2 + OH^- \rightarrow HClO + Cl^-$		3.88×10^{11}
6.68	$\cdot ClOH^- + H^+ \rightarrow \cdot Cl + H_2O$		2.1×10^{10}
6.69	$Cl_2O_2 + H_2O \rightarrow HClO + HClO_2$		2×10^{2}
6.70	$Cl_2O_2 + H_2O \rightarrow HClO + H^+ + Cl^- + O_2$		1×10^{3}
6.71	$Cl_2O + H_2O \rightarrow 2\,HClO$		1×10^{2}
6.72	$Cl_2O_4 + H_2O \rightarrow HClO_2 + HClO_3$		1×10^{2}
6.73	$Cl_2O_4 + H_2O \rightarrow HClO + Cl^- + H^+ + O_4$		1×10^{2}
6.74	$O_4 \rightarrow O_2 + O_2$		1×10^{5}
6.75	$Cl^- + \cdot Cl \rightarrow Cl_2^-$		2.1×10^{10}
6.76	$Cl^- + \cdot ClOH^- \rightarrow \cdot Cl_2^- + OH^-$		9×10^{4}
6.77	$Cl^- + HClO \rightarrow Cl_2 + OH^-$		1×10^{10}
6.78	$Cl^- + Cl_2 \rightarrow Cl_3^-$		1×10^{4}
6.79	$\cdot ClOH^- \rightarrow \cdot OH + Cl^-$		6.1×10^{9}
6.80	$\cdot Cl_2^- \rightarrow Cl + Cl^-$		1.1×10^{5}
6.81	$\cdot Cl_2^- + \cdot Cl_2^- \rightarrow Cl^- + Cl_3^-$		7×10^{9}
6.82	$Cl_3^- \rightarrow Cl_2 + Cl^-$		5×10^{4}
6.83	$\cdot ClO + \cdot ClO \rightarrow Cl_2O_2$		1.5×10^{10}
6.84	$\cdot ClO_2 + \cdot ClO_2 \rightarrow Cl_2O_4$		1×10^{2}
6.85	$Cl_2O_2 + HClO_2 \rightarrow HClO_3 + Cl_2O$		1×10^{3}

[3] Morco, R. P. (2020). *Gamma-Radiolysis Kinetics and Its Role in the Overall Dynamics of Materials Degradation* (Doctoral dissertation, The University of Western Ontario (Canada)).

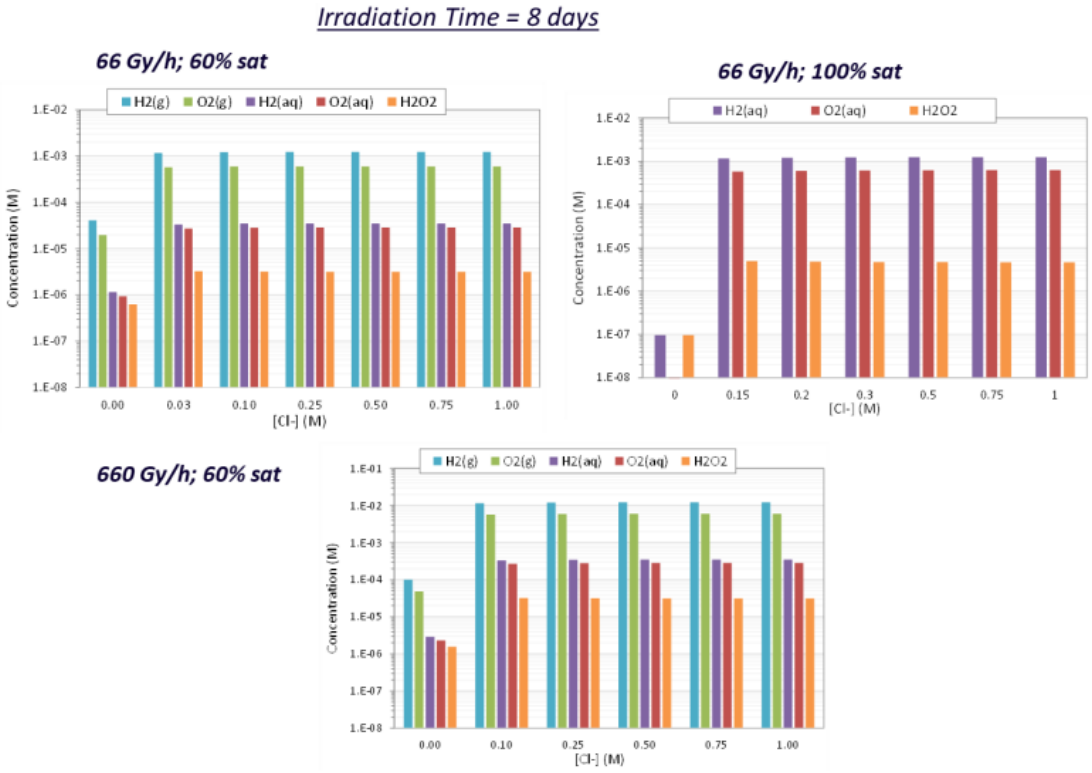

Carbon steel corrosion modelling

NUMERICAL MODEL. CARBON STEEL CORROSION MODEL

- **Anodic current**

$$j_{ct,Fe} = j_{0,Fe} \times e^{\frac{(\varphi - E_{rev,i})}{b}}$$

$$j_{0,Fe} = j_{0,Fe}^{ref} \times e^{\frac{-\Delta H_{Fe}}{K}\left(\frac{1}{T} - \frac{1}{T_{Fe}^{ref}}\right)}$$

$$E_{rev,Fe} = E_{rev,Fe}^{0} + b\log(C_{Fe2+})$$

$j_{corr} = j_{Fe} = j_{O_2} + j_{H^+} + j_{H_2O}$ at $\varphi = E_{corr}$

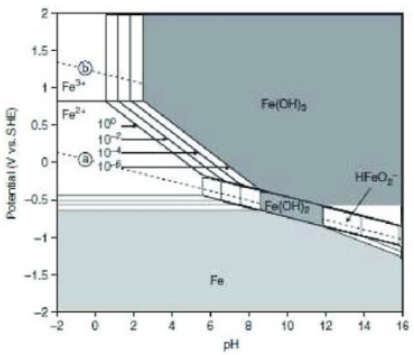

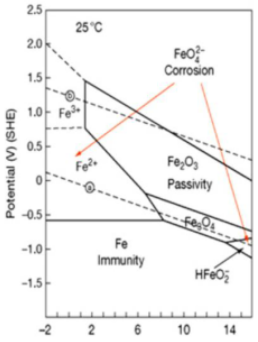

- **Parametrization**

Symbol	Value	Unit
Standard potential (vs. SHE)		
$E^0_{rev,Fe}$	-0.447	V
E^0_{rev,O_2}	0.401	V
E^0_{rev,H^+}	0	V
E^0_{rev,H_2O}	-0.828	V

Reference exchange current density		
$j^{ref}_{0,Fe}$	1.0×10^{-3}	A/m²
j^{ref}_{0,O_2}	1.4×10^{-3}	A/m²
j^{ref}_{0,H^+}	0.03	A/m²
j^{ref}_{0,H_2O}	1.4×10^{-5}	A/m²

Active enthalpy for exchange		
ΔH_{Fe}	37,500	J/mol
ΔH_{O_2}	23,200	J/mol
ΔH_{H^+}	30,000	J/mol
ΔH_{H_2O}	30,000	J/mol

Reference temperature		
T^{ref}_{Fe}	298.15	K
$T^{ref}_{O_2}$	303.15	K
$T^{ref}_{H^+}$	298.15	K
$T^{ref}_{H_2O}$	293.15	K
T^{ref}_{μ}	293.15	K
Reference physical parameters		
$C^{ref}_{H^+}$	0.1	mol/m³

NUMERICAL MODEL. CARBON STEEL CORROSION MODEL

- **Electric potential** (φ) is calculated with **Poisson's equation** assuming **electroneutrality**. Corrosion potential is used as Dirichlet boundary condition on the metal surface
- **Electrochemical boundary conditions**: the **cathodic currents** are used as **Neumann fluxes** on the metal surface in the transport equations
- **Nernst-Planck equation** is being solved for H^+ and OH^-. Electromigration will be extended to all relevant charged species in PhreeqC including Fe^{2+}.

$$\frac{\partial c_i}{\partial t} + \nabla \cdot \mathbf{N}_i + R_i = 0$$

$$\mathbf{N}_i = -D_i \nabla c_i - z_i u_{m,i} F c_i \nabla \phi_i$$

NUMERICAL MODEL. LIMITATIONS

- Only general corrosion.
- Bentonite alteration due to irradiation has not been considered.
- Porosity and transport properties have not been coupled with the precipitation/dissolution of corrosion products for numerical stability (conservative approach).
- This feature will be implemented for the simulation of long-term scenarios.
- Initial oxic conditions have not been reproduced yet.
- Sudden Eh, pH jumps in PhreeqC can lead to numerical instabilities in COMSOL.
- PhreeqC does not allow for electrochemical boundary conditions (fluxes). Ferrous iron must be produced via a domain source. An **infinitesimal steel domain** has been considered.
- A **pure electrochemical** model would be possible, provided that all relevant reactions are implemented in COMSOL
  - Not feasible in bentonite, but could be affordable in metal-water systems

APPLICATION TO CARBON STEEL COUPONS EMBEDDED IN COMPACTED BENTONITE

- Setup based on CIEMAT's radiolytic cells with Nagra carbon steel coupon
- FEBEX bentonite (dry density: 1.4 g/cm^3)
- Liquid degree of saturation: 100%
- Dose Rate (DR): 0, 66 and 660 Gy/h. Irradiation Time: 9 days
- Radiolysis of water and chloride
- ThermoChimie database
- 1D approximation
- 50 elements: from 0.02 to 0.5 mm.

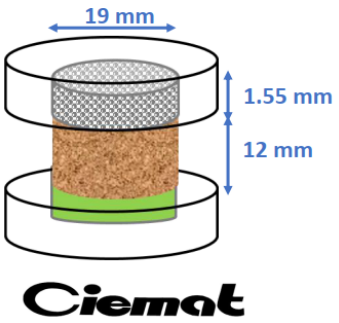

APPLICATION TO CARBON STEEL COUPONS EMBEDDED IN COMPACTED BENTONITE

- **Non-irradiated cell: results at the steel-bentonite interface**

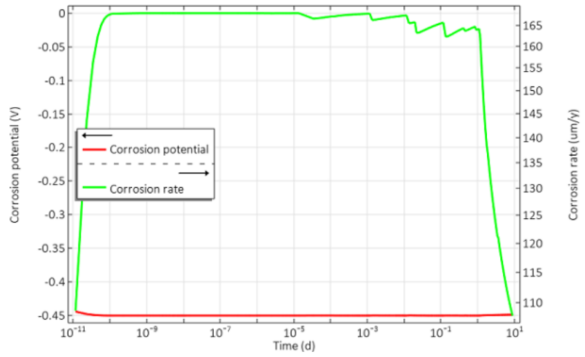

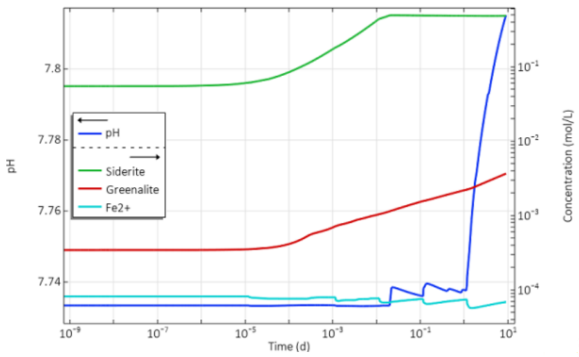

- No corrosion products further than Siderite and Greenalite due to the presence of Si and carbonates in bentonite.
- Highly reductive environment. Corrosion highly sensitive to pH.

APPLICATION TO CARBON STEEL COUPONS EMBEDDED IN COMPACTED BENTONITE

- **Irradiated cell (66 Gy/h): results at the steel-bentonite interface**

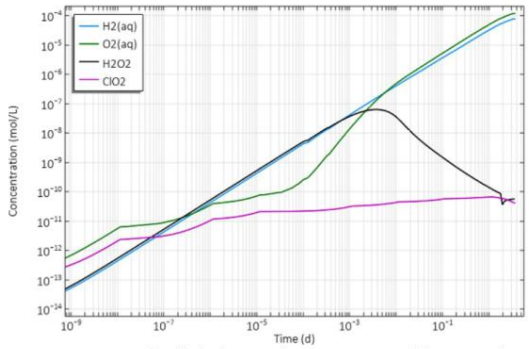

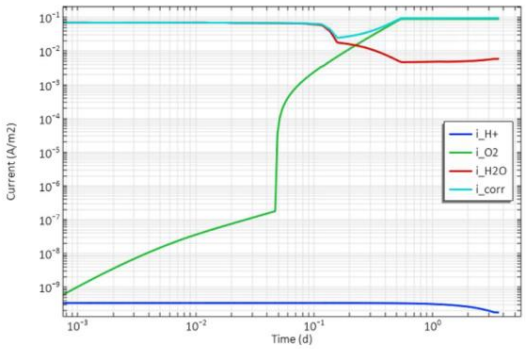

- Radiolytic species are approaching steady state after 3 days.
- Oxic corrosion soon dominates over the anoxic one.
- Oxic corrosion steady state after reaching the solubility limit (non-hermetic cell)

APPLICATION TO CARBON STEEL COUPONS EMBEDDED IN COMPACTED BENTONITE

- **Irradiated cell (66 Gy/h)**

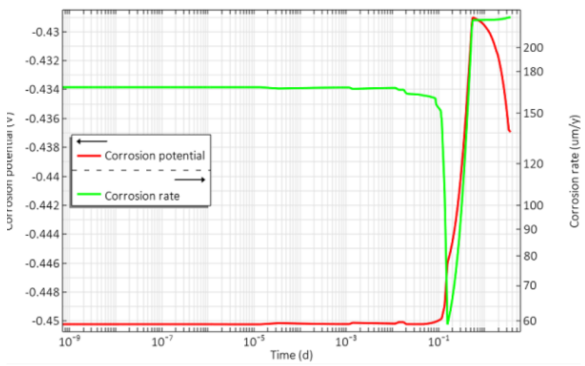

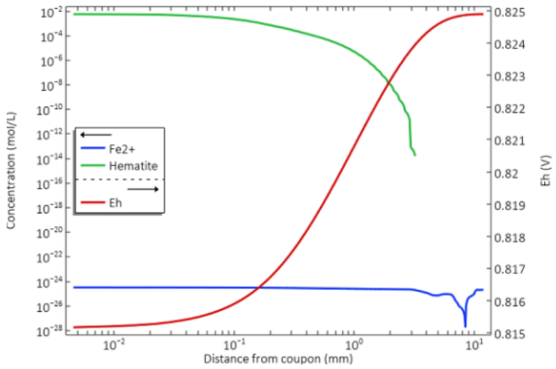

- Corrosion rate slightly increases when oxic corrosion becomes dominant, but not significantly.
- Oxidating conditions in the whole cell. Ferrous iron concentration becomes negligible, and the system becomes dominated by the precipitation of hematite.

APPLICATION TO CARBON STEEL COUPONS EMBEDDED IN COMPACTED BENTONITE

- **Irradiated cell (66 Gy/h)**

  - The sudden precipitation of hematite causes a steep (Eh, pH) adjustment, leading to non-convergence of the solver.
  - The progressive evolution of the system towards more oxidating regions suggests a future precipitation of goethite, as found by CIEMAT.

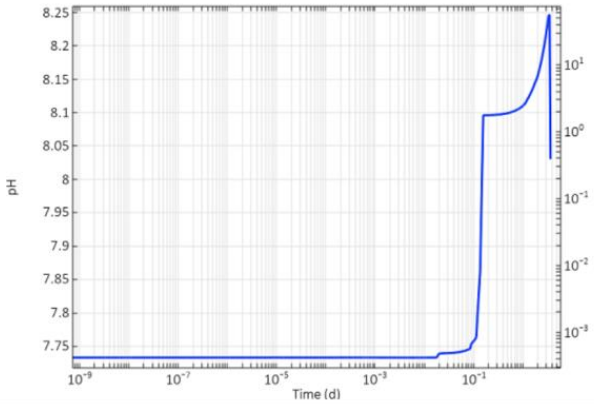

APPLICATION TO CARBON STEEL COUPONS EMBEDDED IN COMPACTED BENTONITE

- **Irradiated cell (660 Gy/h)**
  - Oxic corrosion steady state is reached one order of magnitude earlier, as observed in the Jacobs' case.
  - Similar corrosion rate.